# Understanding Catchment Ecohydrological Processes and Their Interactions Across Multiple Spatiotemporal Scales: A Darwinian Approach

by

**Guta Wakbulcho Abeshu**

A dissertation submitted to the Department of Civil and Environmental Engineering,
Cullen College of Engineering
in partial fulfillment of the requirements for the degree of

Doctor of Philosophy

in Civil Engineering

Chair of Committee: Dr. Hong-Yi Li
Committee Member: Dr. Keh-Han Wang
Committee Member: Dr. Mostafa Momen
Committee Member: Dr. Hyongki Lee
Committee Member: Dr. Murugesu Sivapalan

University of Houston
May 2022

# Dedication

*… in memory of my brother and best friend Sagni Wakbulcho*

*… for my dad Wakbulcho Abeshu*

*… for my mum Tajitu Jirata*

*… for my brothers and sisters*

## Acknowledgments

I would like to express my deepest gratitude to my research advisor Dr. Hong-Yi Li for his valuable guidance and continuous support throughout my time at The University of Houston and Montana State University before that. His motivation, sincerity, trust, and friendship have helped me to carry out the research and prepare this dissertation. I am extremely grateful that you provide me with the opportunity to do my research under your supervision.

My stay at the University of Houston and going forward have been positively affected by the modesty of my lab mates and friends, Dr. Wondimagegn Yigzaw (Wondie), Fasil Worku, and Taher Chegni. I did not realize how the presence of Wondie made me comfortable until he left the University of Houston; I am always grateful to him and his family. I want to thank Fasil for always having time to listen to my qualms and for his encouragement. I am thankful to Taher Chegni for all the fruitful academic and non-academic discussions we had over the past four years.

Most of all, I would like to thank my parents, Wakbulcho Abeshu and Xejitu Jirata, and siblings, Sagni, Tujuba, Dinka, Hawi, Bontu, Ugume, and Sena, for the unconditional love, support, and guidance they provided throughout my life.

# Abstract

The ecohydrological system is a complex adaptive system. Climatic signals propagation through this system takes nonunique pathways, creating nonlinear interactions between climate, soil, water, and vegetation. The synthesis of the links between these components can be approached by a detailed physics-based process understanding or based on emerging patterns and common functionalities across space and time. This dissertation develops a mechanistic understanding of hydrological and ecological processes interactions at the catchment scale based on the latter approach. It has five main objectives: (1) to develop a simple diagnostic framework for exploring links between water balance and vegetation dynamics, (2) to establish a scale-independent function for carbon-water coupling, (3) to explore hydrological processes underpinning vegetation carbon uptake seasonality, (4) to develop and implement a simple dynamic vegetation model global scale, and (5) to enhance global hydrologic model (Xanthos) by adding some aspects of water management. The dissertation begins with the development and validation of two functions. The first function is an analytical framework for the Horton index, derived based on the generalized proportionality hypothesis. The function helped depict the critical role vegetation plays in hydrologic partitioning. It also explained the space-time similarity of the catchment hydrologic state. The second function is a two-parameter linear relationship between carbon uptake and water balance. It simulated seasonal vegetation carbon uptake at catchment and patch levels reasonably. It is also valuable for understanding the catchment transpiration to vaporization ratio. Exploratory data analysis is performed for objective (3). Hysteresis between water supply and productivity and atmospheric demand and productivity was explained by the efficiency of catchment water, energy, and carbon

use. It also reveals that vegetation in catchments oscillating between water- and energy-limited states are under hydrologic stress during the peak growing period. Functions from objectives (1) and (2) were coupled with Xanthos. Simulation with this model captured the seasonality and magnitudes of carbon uptake reasonably. Xanthos is further enhanced by adding a water management module that treats irrigation, hydropower, and flood-control reservoirs differently. It is the first attempt to represent hydropower reservoirs in a global model. The model performance is improved significantly in reproducing observed streamflow.

# Table of Contents

# List of Tables

# List of Figures

## List of Abbreviations

| | |
|---|---|
| C | Reservoir storage capacity |
| CAMELS | Catchment Attributes and MEteorology for Large-sample Studies |
| AVHRR | Advanced very-high-resolution radiometer |
| AVP($e_a$) | Actual vapor pressure |
| CL/NVM | Croplands/Natural vegetation mosaic |
| $CO_2$ | Carbon dioxide |
| CONUS | Contagious US |
| CUE | Carbon Uptake Efficiency |
| DBF | Deciduous Broadleaf Forests |
| E (ET) | Evapotranspiration |
| EAI | Ecological Aridity Index |
| Ec | Continuing vaporization |
| EEMT | Effective energy and mass transfer |
| EF | Evergreen Forest |
| EFI | Evaporative Fraction Index |
| Eo | Initial vaporization |
| Eobs | Observed Evapotranspiration |
| Ep(PET) | Potential vaporization |
| Esim | Simulated evapotranspiration |
| FLUXNET | Flux Network |
| GCAM | Global Change Analysis Model |
| GHM | Global Hydrologic Model |
| GL | Grasslands |
| GRDC | Global Runoff Data Center |
| GPCC | Global Precipitation Climatology Centre |
| GPH | Generalized Proportionality Hypothesis |
| GPP | Gross Primary Productivity |
| GRanD | Global Reservoirs and Dams |
| GVF | Green Vegetation Fraction |
| HI | Horton Index |
| ISIMIP | Inter-Sectoral Impact Model Intercomparison Project |
| KGE | Kling Gupta Efficiency |
| LAI | Leaf Area Index |
| LHS | Latin hypercube sampling |
| M | Melt (The ***abcd*** model) |
| MF | Mixed Forests |
| MRTM | Modified River Transport Model |
| NRMSE | Normalized Root Mean Squared Error |

| | |
|---|---|
| P | Precipitation |
| PCA | Principal Component Analysis |
| PR | Precipitation's rain component (The ***abcd*** model) |
| PS | Precipitation's snow component (The ***abcd*** model) |
| Q | Streamflow |
| Qb | Baseflow |
| QB | Slow runoff(The ***abcd*** model) |
| QD | Fast runoff (The ***abcd*** model) |
| Qs | Surface runoff(The ***abcd*** model) |
| R | Water available |
| RE | Recharge (The ***abcd*** model) |
| RH | Relative humidity |
| RMSE | Root Mean Squared Error |
| $R'_{m,y}$ | Reservoir provisional release |
| $R_{m,y}$ | Reservoir final release |
| S | Storage |
| SAC-SMA | Sacramento Soil Moisture Accounting Model |
| SCE-UA | Shuffled Complex Evolution |
| SDI | Standardized Discharge Index |
| SCS-CN | Soil Conservation Service Curve Number |
| SDP | Stochastic Dynamic Programming |
| SI | Seasonality Index |
| SM | Soil Moisture |
| SP | Snow Pack(The ***abcd*** model) |
| SVP($e_s$) | Saturation vapor pressure |
| SW | Shortwave radiation |
| T | Temperature |
| TBM | Terrestrial Biosphere Model |
| USGS | United States Geological Services |
| VIF | Variance Inflation Factor |
| VPD | Vapor Pressure Deficit |
| W | Wetting |
| WATCH | WATer and global CHange |
| WFDEI | WATCH Forcing Data methodology applied to ERA-Interim |
| WS + SL (WSSL) | Woody Savannas and Shrublands |
| $\alpha$ | Intercept coefficient of a linear function |
| $\beta$ | The slope of a linear function |
| $\Delta S$ | Storage change |
| $\kappa$ | Reservoir capacity reduction coefficient |
| $\lambda$ | Initial vaporization to total vaporization ratio |
| $\upsilon$ | Velocity adjustment coefficient |

# 1 Introduction

## 1.1 Motivation

The ecohydrological system is a complex adaptive system consisting of hydrological and ecological processes. The propagation of climatic signals through this system is non-stationary and generates heterogeneous feedback. Hydrologic fluctuations are responsible for ecological process dynamics. Hence, it is responsible for some of the fundamental differences between various ecosystems' space-time patterns and processes (Eagleson, 2002; Porporato and Rodriguez-Iturbe, 2013). Soil water storage is the hydrologic system's primary link to the ecosystem. The plant hydraulic transport system links the soil water storage to the carbon-water exchange at the leaf surface. Both components of the carbon-water exchange (i.e., carbon uptake and transpiration) are dominant driving factors in land-atmospheric interactions. The plant carbon uptake is the primary driver of the land carbon sink, and evapotranspiration is the largest terrestrial water flux (Maxwell and Condon, 2016; Spielmann et al., 2019; Trenberth et al., 2014).

Observation data primarily drive understanding of the plant-water interactions, which is generally available at the site, patch, or stand scales. Understandings generated at these levels are often applied at larger scales with little to no modifications. This has led many state-of-the-art global models to struggle to capture patterns and characteristics seen in observation data, such as evapotranspiration partitioning (Schlesinger & Jasechko, 2014). For instance, while the global mean transpiration to evapotranspiration ratio is >64% per observation data, global models persistently estimate below 40% (Good et al., 2015; Schlesinger and Jasechko, 2014). One major contributing factor to such mismatch is the lack of an effective mechanism to upscale site/patch scale understandings to larger scales. This dissertation proposes generating a new understanding of hydrologic and ecologic systems interactions at the catchment scale as a bridge between site/patch and global scale implementations for three major reasons. First, catchments are often made up of multiple ecosystems, and this resembles the spatial characteristics of the global model's grid. Second, like gridded scales, catchments can be represented in lumped, semi-distributed, or distributed forms. Lastly, relative to site scale, understanding how vegetation production responds to water balance at a spatial unit like a catchment is essential for designing and implementing land management plans.

Synthesis of the links between soil water storage dynamics and processes at vegetation leaves surface (i.e., evapotranspiration and carbon uptake) can be approached through two schools of thought. Focusing on individual biomes in isolation with a detailed physics-based representation (Newtonian) or based on emerging spatiotemporal patterns/laws among a population of catchments (Darwinian). The Newtonian approach employs universal laws to build a mechanistic model, often without ties to a particular landscape. Underlying assumptions and model parameters strongly condition that the solutions characterize a given landscape (Blöschl et al., 2011; Wang and Tang, 2014). The Darwinian synthesis starts from observations of individual behavior and builds a theory that explains the collective dynamics (Pástor et al., 2016). It then seeks to describe patterns of variability and their process (Blöschl et al., 2011; Sivapalan, 2005; Sivapalan et al., 2011a; Wang and Tang, 2014). Regardless of the pathways, a synthesis should be based on a simple and falsifiable framework (Harte, 2002). It should go beyond the emerging spatial/temporal patterns and identify the actual mechanisms at work. Ultimately, the pursuit of such mechanistic understanding is to apply the fundamental knowledge we garner to solve real-world problems involving ecohydrological systems.

Ecohydrological systems' self-organizing behaviors often do not manifest themselves in mathematical forms. Hence, embracing the science of places is very important rather than investigating specific biome in isolation (Harte, 2002). Embracing the science of places here means using a population of catchments to examine the action of vegetation on the water balance and vice versa. Data-driven explorations of the dynamic interaction amongst the components of ecohydrological systems are generally limited to patch scales since observation data are primarily available at that level. The scaling issue, the inability to establish a smooth connection between the patch- and catchment-scale soil-water-vegetation dynamics, hinders the extension of most patch-scale synthesis to catchment-scale.

On the other hand, most catchment-scale hydrologic models are partially coupled with ecosystem processes. These models objectively introduce catchment ecosystems only to aid a more realistic simulation of the hydrologic processes. Fully coupled models are often process-based; hence they can solve hydrological and vegetation dynamics over space and time explicitly and simultaneously. Unfortunately, the involved numerous adjustable parameters generally make them unfalsifiable, drawing a curtain on the opportunity to learn from the multitudes of wrong predictions. Hence, there is a need for simple and falsifiable frameworks, an approach with limited complexity that can directly link catchment water balance and vegetation dynamics at multi-temporal scales. A framework for detecting patterns and laws among a population of catchments, which in turn help develop theories and further our capability to synthesize catchment ecohydrology as a single adaptive unit.

The overarching goal of this dissertation is to develop methods for linking catchment water balance and vegetation dynamics at multi-scales. Specifically to develop and validate macroscopic functional frameworks that are simple enough and yet sufficiently exact in revealing the mechanisms at work. Here, these approaches are referred to as *Fermi-type macroscopic approaches*, hoping to implement a simplified problem-solving approach of Enrico Fermi[1] to catchment ecohydrology(Harte, 2002). This dissertation also aims to use the developed functional forms and understandings to enhance an existing global hydrologic model. To achieve this goal, the subtasks of this research follow the Darwinian school of thought to develop the functions. The main objectives include: i) developing a simple mathematical diagnostic framework for exploring multi-scale links between catchment water balance and vegetation dynamics, ii) establishing a unified functional framework for the catchment scale carbon-water coupling, iii) exploring the hydrological processes underpinning the distinct space-time patterns of carbon uptake among various biomes, iv) combining approaches developed in "i-iii" and existing hydrologic model to develop a simple dynamic vegetation model and apply at the global scale, and vi) integrating the human influences into the global hydrologic model to further enhance its streamflow simulation.

## 1.2 Methodological Framework

The dissertation undertakes the objectives described in the preceding section as an independent primary research task with specific objectives. Methodological developments for these tasks follow the Darwinian school of thought individually and collectively to achieve the overarching goal of the dissertation, except for the global scale analysis. The Darwinian school of thought emphasizes population thinking rather than typological. It embraces that populations consist of uniquely different individuals, and patterns manifesting from their individual and collective behavior lead to a generalized explanatory interpretation. The functions development and process understanding at the catchment level is followed by implementation into an existing global hydrologic model to enhance its capacity for simulating vegetation dynamics. This dissertation also develops a generic global water management module to improve human influence on the river system. The summary of each research task and the overall methodological framework (Figure 1-1).

**1) The link between soil water storage dynamics and evapotranspiration**

*To develop a conceptual framework for exploring multi-scale links between water balance and vegetation dynamics*

This task investigates vegetation influence on the second stage of the now universally accepted hydrologic portioning framework. Most analyses concerning such influence are data-driven and do not provide a mechanistic generalizable understanding across space and time, especially at an intra-annual scale. Under this task, we developed a new conceptual framework for exploring multi-scale links between catchment water balance and vegetation dynamics based on the Generalized Proportionality Hypothesis. The framework is then validated over catchments across the contiguous United States and with various climate, vegetation, soil, and topographic conditions, focusing primarily on the monthly scale. We use the new analytical framework to understand the mechanisms underpinning the emergent patterns of water-vegetation interactions at inter-and intra-annual variability.

**2) Catchment level link between evapotranspiration and carbon uptake:**

*To develop a functional relationship between catchment water balance and vegetation carbon uptake*

Under various climate and landscape conditions, seasonal vegetation dynamics, and hydroclimatic variables, we evaluate water balance and vegetation dynamics data from a population of natural catchments distributed across the contiguous United States. Based on the observed emerging patterns, we developed a universal functional relationship between vegetation carbon uptake and catchment water balance. The relationship is a two-parameter linear function, and the parameters could be estimated a prior as functions of catchment climate and landscape conditions. Further, we explore the landscape and hydroclimatic variables controlling the parameters, thereby the type of the linear function.

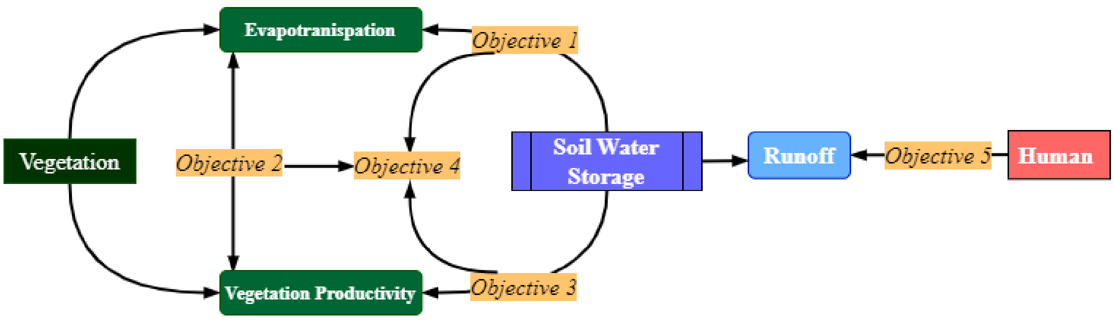


Figure 1-1: Methodological Framework

**3) The effect of soil water storage and atmospheric dryness on vegetation:**

*To provide a mechanistic understanding of catchment wetness /vegetation carbon uptake and atmospheric dryness/vegetation carbon uptake hysteresis.*

Hysteric behaviors are common in a system that can recharge and discharge. Vegetation takes up carbon at the expense of water hydraulically lifted from the soil; the lag between them creates a hysteresis. Observation data showed several emerging patterns, including the wide/narrow and clockwise/anti-clockwise hysteric behaviors. We explore hydrological processes underpinning these patterns using water, energy, and carbon uptake efficiency indicators and provide a mechanistic understanding of the patterns. Ultimately, understanding these seasonal co-dynamics can help improve the understanding of how intermittent natural disturbances like droughts constrain the carbon cycle and water use.

**4) Enhancing a simple hydrologic models capacity beyond simulating hydrologic releases**

*To develop a simple empirical model for vegetation carbon uptake model*

Catchments are closed spatial units, and most global hydrologic models use gridded spatial units. Here, we tested whether the understanding we generated based on small to medium-sized catchments can be applied globally. We integrate the previously developed functions with a conceptual hydrologic model and develop a simple but dynamic vegetation model to simulate monthly water balance and dynamics. We use the ***abcd*** model (Martinez and Gupta, 2010), which is also a basis for Xanthos (an existing distributed global hydrologic model and part of the Global Change Intersectoral Modeling System framework) (Liu et al., 2018). We underpinned both model's actual evapotranspiration estimations with the new conceptual framework (objective 1) and the carbon uptake with the unified relationship (objective 2). The model is applied globally at half-degree resolution and evaluated against a recent observation-based global product.

**5) Human interference with the hydrologic release**

*To enhance Xanthos by including human influence on hydrologic systems*

Human decision-making, such as surface and groundwater withdrawal and surface water management, can affect both vertical (e.g., through land management such as irrigation) and horizontal (e.g., through shifting natural water availability patterns) hydrologic fluxes. Human influences on these components propagate to the carbon cycle as the vegetation's carbon uptake characteristics vary with land management practices and the natural variability of water available. One of the main features of surface water management is the surface water reservoirs, which provide a critical human response to natural variability and short-term environmental influences such as droughts. Reservoirs also have the potential to alter the long-term co-evolution of energy-water-land systems. Understanding the future role of reservoirs in shaping the co-evolution of energy-water-land systems at a global scale requires carefully representing reservoirs and their multiple purposes—such as irrigation, hydropower, and flood control—in global hydrologic models. The resulting dynamics emerging from global hydrologic models can then be used to inform the dynamics in global integrated human-earth system models such as the Global Change Analysis Model (GCAM). As a first step toward this goal, this study aims to develop a water management module for Xanthos, an existing distributed global hydrologic model that is part of the Global Change Intersectoral Modeling System framework, by adding local surface water extraction and reservoir operation.

## 1.3 Guiding Philosophy

The dissertation's first three chapters are focused on a data-based mechanistic understanding of the links between vegetation and catchment water balance. Those sections guiding framework is shown in Fig. 1-2. The enhancement of the global hydrologic model to simulate vegetation dynamics is based on these chapters, while the human influence representation, to a certain extent, also aims to follow a simple framework of process understanding.

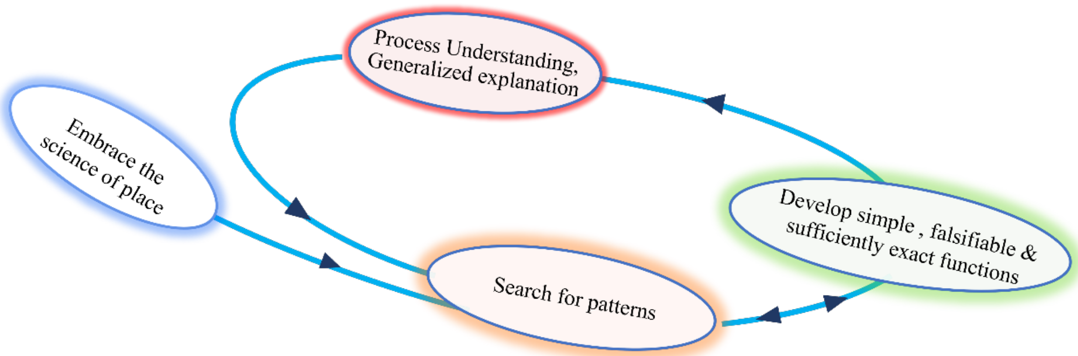


Figure 1-2: Major steps in the exploratory data analysis and functions development

## 1.4 Dissertation Structure

The dissertation is organized into seven chapters. Chapters 2 and 3 present the two parts of vegetation actions on the hydrologic partitioning study: the development of the conceptual framework for exploring multi-scale links between water balance and vegetation dynamics and the unified functional framework for vegetation carbon uptake and water balance relationship. Chapter 4: presents findings on the hydrologic processes that underpin the hysteric behavior between catchment water balance and vegetation carbon uptake. Chapters 5 and 6: present the simple dynamic vegetation model and the development of the water management modules for a global hydrologic model. Chapter 7 presents conclusions and implications of the results presented in this dissertation, followed by future works.

# 2 Soil Water Storage Relationship with Evapotranspiration[1]

## 2.1 Introduction

Horton Index, a dimensionless ratio of catchment vaporization (total evapotranspiration) to wetting (the portion of precipitation that wets canopy, ground surface, and soil), has been a valuable signature in revealing the links between catchment water balance and vegetation dynamics (Brooks et al., 2011; Horton, 1933; Sivapalan et al., 2011; Tang & Wang, 2017; Troch et al., 2009; Voepel et al., 2011). Horton (1933) found that the HI calculated over the growing period (May to October) at a pristine catchment shows a remarkable constancy between years despite substantial inter-annual precipitation variability. He postulated that the reason for this constancy might be that vegetation maximizes productivity relative to available water, echoing back to the concept of maximum possible actual evapotranspiration (Ol'dekop, 1911). Based on his hydrologic partitioning theory, L'vovich (1979) also confirmed a maximum attainable actual evapotranspiration for a given soil wetting magnitude, hence recognizing the role of soil-vegetation interactions in hydrologic partitioning.

It was not until decades later that Troch et al. (2009) revisited HI and its between-year constancy using 89 catchments distributed across different ecoregions. Using this index, Troch et al. (2009) revealed a space-time symmetry between the inter-catchment and inter-year variability of HI, which they suggested might be underpinned by a similarity across biomes in short- and long-term adaptation strategies of vegetation to climate variability.

[1] Abeshu, G. W., & Li, H. Y. (2021). Horton Index: Conceptual framework for exploring multi-scale links between catchment water balance and vegetation dynamics. Water Resources Research, 57(5), 1–24. https://doi.org/10.1029/2020WR029343

Inspired by Troch et al. (2009), there have been many data-driven studies evaluating the impacts of climate, soil, and topographic conditions on HI variations over the past decade. For example, Voepel et al. (2011) found that climate conditions exerted a first-order control on the HI variations, e.g., there was a power-law relationship between HI and Aridity Index, while topographic characteristics such as topographic slope and mean elevation only exerted a secondary control. Using 86 of the 89 catchments utilized by Troch et al. (2009), Rasmussen (2012) related the HI to effective energy and mass transfer (EEMT). Here, the EEMT represents energy that can perform work on the subsurface and has two components, the energy flux associated with effective precipitation and the energy flux from net primary production. The result showed a strong negative correlation between EEMT and HI, indicating that water-limited catchments correspond to lower EEMT. Zapata-Rios et al. (2016) examined HI characteristics over high-elevation catchments. They reported that snowpack conditions explained over 95% of the HI variability and that, in turn, influenced annual vegetation greening. They also found that the topographic aspect did influence the magnitude of HI but only during wet years.

Moreover, HI has been used as a valuable diagnostic signature for catchment water balance under the influences of climate, soil, and biomes. Guardiola-Claramonte et al. (2010) used annual HI as one of the objective functions to calibrate and validate their catchment water balance simulations. Brooks et al. (2011) and Voepel et al. (2011) showed that HI could be a good predictor of inter-annual changes in vegetation cover and greenness. Harman et al. (2011) derived analytical expressions that relate the flow elasticities to long-term mean HI. Thompson et al. (2011) showed the scale-dependence of catchment water balance partitioning on a hierarchical flow path network with a scale-dependent expression of HI.

Wang & Tang  (2014) and Tang & Wang (2017) parameterized their Budyko-type models directly or indirectly with HI. Arciniega-Esparza et al. (2017) and Troch et al. (2018) found that HI was a highly efficient predictor of the spatial variability of average maximum deep storage, low flows, and groundwater recharge in ungauged catchments with different types of climate, soils, geology, and vegetation cover.

The aforementioned HI-related studies are nevertheless mostly data-driven i.e., without providing a mechanistic, generalizable understanding across space and time. The only exceptions are Sivapalan et al. (2011) and Schaefli et al. (2012). Sivapalan et al. (2011) derived a functional formula of HI as a function of two dimensionless similarity variables (rescaled annual precipitation and aridity index) based on the two-stage hydrologic partitioning theory (L'vovich, 1979; Ponce & Shetty, 1995a, b). They then revealed a space-time symmetry of inter-catchment (regional) and inter-annual variability of $HI$. Schaefli et al. (2012) derived an analytical expression for HI as a function of available storage in the atmospheric column and a constant k (the ratio of maximum potential evaporation to maximum runoff). They confirmed the power-law relationship between HI and AI as suggested by Voepel et al. (2011).

However, neither Sivapalan et al. (2011) nor Schaefli et al. (2012) examined HI's intra-annual variability. In fact, most of the data-driven HI-related studies have also focused on the annual scale by neglecting soil moisture storage change. The importance of intra-annual variability of $HI$ has nevertheless not been fully explored, particularly over the growing season (Horton, 1933; Troch et al., 2009). There is substantial seasonal variability in the dynamics of most vegetation types. For example, in the U.S., for most vegetation types, a calendar year can be divided into a growing season and a dormant season (Kukal and Irmak, 2018).

Vegetation typically acquires and consumes much more water via transpiration during the growing season than during the dormant season (Schlesinger & Jasechko, 2014; Wang et al., 2014; Zhou et al., 2016). It is thus necessary to incorporate intra-annual variability to improve the understanding of $HI$ variability and the role of vegetation that cannot be effectively captured at the annual scale (Sivapalan et al., 2011; Troch et al., 2009).

The mathematical derivation of Sivapalan et al. (2011) was directly based on the two-stage hydrologic partitioning theory pioneered by L'vovich (1979) and later on theoretically proven by Ponce & Shetty (1995a, b). The two-stage hydrologic partitioning theory quantifies the partitioning of precipitation into fast flow and wetting (1st-stage) and then partitioning wetting into baseflow and vaporization (2nd-stage). The 2nd-stage partitioning is directly relevant to HI. Ponce & Shetty (1995a, b) provided the theoretical foundation of this hydrologic partitioning theory by generalizing the Proportionality Hypothesis underpinning the Soil Conservation Service Curve Number (SCS-CN) method (SCS, 1985). Given that $Z$ is a certain amount of water that can be portioned into X and Y (e.g., precipitation portioned into soil retention and excess runoff, or catchment wetting partitioned into vaporization and baseflow), the Generalized Proportionality Hypothesis (GPH) states that

$$\frac{\mathrm{X}-\mathrm{X}_0}{\mathrm{X}_\mathrm{p}-\mathrm{X}_0}=\frac{\mathrm{Y}}{\mathrm{Z}-\mathrm{X}_0}. \qquad (2\text{-}1)$$

Here $\mathrm{X}_p$ is the potential of X, and $\mathrm{X}_o$ is the initial fraction of X (e.g., initial soil abstraction or initial vaporization). Ponce & Shetty (1995a, b) showed that GPH could be used to theoretically derive the functional formulas for both stages of the two-stage hydrologic partitioning. For the 2nd-stage partitioning, applying GPH leads to

$$\frac{E - E_0}{E_p - E_0} = \frac{Q_b}{W - E_0}. \tag{2-2}$$

Where $E$ is total vaporization. $E_0$ is initial vaporization. $E_p$ is potential vaporization. $Q_b$ is baseflow. $W$ is total wetting. Note that Eqn. (2-2) is for long-term catchment water balance; hence storage change is neglected (Sivapalan et al., 2011; Tang & Wang, 2017; Wang et al., 2015).

Interestingly, Wang & Tang (2014) showed that GPH could also be used to derive the Budyko-type formula theoretically. A Budyko-type formula is essentially quantifying a one-stage hydrologic partitioning, i.e., total precipitation partitioned into total runoff (including fast flow and baseflow) and vaporization. By applying GPH to this one-stage partitioning, Wang & Tang (2014) derived a generic, one-parameter expression of the Budyko model for long-term catchment water balance and suggested that the original deterministic Budyko curve (Budyko, 1974) and Fu's equation (Fu, 1981) are just two specific forms of this generic expression.

More importantly, Wang et al. (2015) later proved that GPH could be theoretically derived from the thermodynamic principle, i.e., Maximum Entropy Production. In particular, they showed that the 2nd-stage partitioning at the long-term scale could directly result from the Maximum Entropy Production principle. Wang (2018) was then able to theoretically derive the proportionality relationship used in the SCS-CN method following a different route than the Maximum Entropy Production principle, i.e., by proposing a new probability density function for the spatial distribution of soil water storage capacity. Hooshyar & Wang (2016) also demonstrated the physical basis of the SCS-CN proportionality hypothesis by deriving it from Richard's equation but for relatively specific conditions, i.e., coarse-textured soil, shallow water table, and an early stage of ponded infiltration.

So far, GPH has been validated empirically (SCS, 1985), indirectly by Ponce & Shetty (1995a, b) and Wang & Tang (2014), and theoretically by Wang et al. (2015), Hooshyar & Wang (2016), and Wang (2018). It appears to be a very powerful theoretical framework not only underpinning the now well-accepted two-stage hydrologic partitioning theory and Budyko hypothesis but also facilitating new hydrologic theoretical explorations.

Our objectives are, therefore, three-fold: 1) Developing a new analytical framework of HI applicable at multi-temporal scales based on the Generalized Proportionality Hypothesis; 2) Validating the analytical framework over a large number of catchments with various climate, vegetation, soil, and topographic conditions with a main focus on the monthly scale; and 3) Using the new analytical framework to help understand the mechanisms underpinning the emergent patterns of HI's inter- and intra-annual variability. The rest of this paper is organized as follows: Section 2.2 introduces the analytical framework. Section 2.3 describes the validation of it at both annual and monthly scales. Section 2.4 presents the emergent patterns in the $HI$'s spatial (inter-catchment) variability and temporal (inter- and intra-annual) variability and interprets them using the analytical framework. Section 2.5 closes with a summary and further discussion.

## 2.2 Analytical Framework of Horton Index

### 2.2.1 General Horton Index Definition

So far, at annual and long-term scales, HI has been mostly defined and used as the ratio of catchment vaporization to catchment wetting (Horton, 1933; Troch et al., 2009) without accounting for the effects of storage carryover between years. Troch et al. (2009) suggested accounting for storage carryover from winter into spring for using HI. For multi-scale applicability, we thus adopt a general definition of HI as

$$\mathrm{HI} = \frac{\mathrm{E}}{\mathrm{W} - \Delta\mathrm{S}} \;. \tag{2-3}$$

Where $E$ is catchment vaporization (or actual evapotranspiration), $W - \Delta S$ is catchment wetting accounting for the storage change. We hereafter consider $(W - \Delta S)$ as effective catchment wetting, which is the amount of water available for vaporization and baseflow at any time scale. Effective catchment wetting can also be viewed as the maximum water supply for vegetation use. The definition in Eqn. (2-3) can thus be applied at any time scale. In this study, we define and examine HI on the long-term, annual, and monthly scales. For the long-term scale, HI is defined as the ratio of long-term average evapotranspiration to long-term average catchment wetting and denoted as long-term HI hereinafter. For the annual scale, HI is defined as the ratio of annual total evapotranspiration to annual effective catchment wetting for any specific calendar year and denoted as annual HI. For the monthly scale, HI is defined as the ratio of monthly total evapotranspiration over monthly effective catchment wetting for any month and denoted as monthly HI.

### 2.2.2 Mathematical Derivations

At the catchment scale, total liquid precipitation (rainfall + snowmelt), $P$, can be partitioned into total surface runoff ($\mathrm{Q_s}$) and catchment wetting ($W$). W includes total infiltration and interception by vegetation canopy and surface depressions (see Figure 2-1a). The first stage of precipitation partitioning is expressed as

$$\mathrm{P} = \mathrm{Q}_{\mathrm{s}} + \mathrm{W}. \tag{2-4}$$

Catchment wetting occurs in two phases: initial wetting ($W_o$) due to interception by vegetation and ground surface depressions and continuing wetting ($W_c$) due to soil infiltration. Catchment wetting can then be further partitioned into catchment vaporization (E), base flow ($Q_b$) and soil water storage change ($\Delta S$) (see Figure 2-1b).

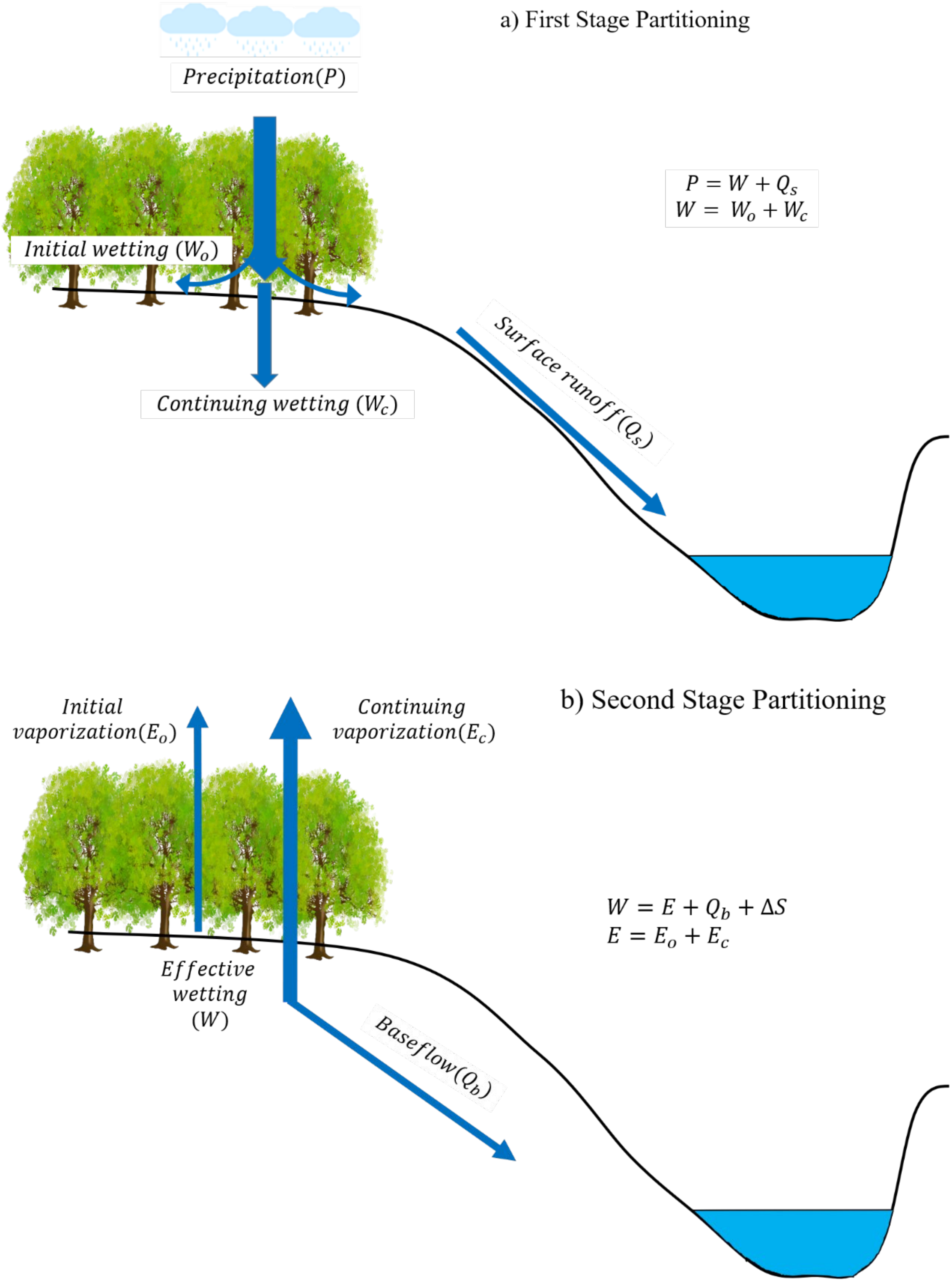


Figure 2-1: Conceptual-level two-stage hydrologic partitioning scheme, (a) First-Stage Partitioning for effective precipitation partitioning and (b) Second-Stage Partitioning for effective catchment wetness partitioning.

Hence, the second stage of precipitation partitioning is given by

$$W = E + Q_b + \Delta S. \tag{2-5}$$

We now apply GPH to the 2nd-stage partitioning at the monthly scale, which yields

$$\frac{E - E_o}{E_p - E_o} = \frac{Q_b}{W - \Delta S - E_o}. \tag{2-6}$$

$E_0$ is the portion of vaporization that occurs at the initial stage, i.e., evaporation from canopy interception and surface depression ponding and transpiration from shallow water storage (mostly in the unsaturated zone). Note that with Eqn. (2-6) here, we only assume that GPH is valid for the 2nd-stage partitioning at the monthly scale. Whether it is valid at finer time scales is beyond the scope of this study. Rearranging Eqn. (2-6) for $Q_b$, we obtain

$$\frac{Q_b}{W - \Delta S} = \frac{\left(\frac{E}{W - \Delta S} - \frac{E_o}{W - \Delta S}\right)\left(1 - \frac{E_o}{W - \Delta S}\right)}{\frac{E_p}{W - \Delta S} - \frac{E_o}{W - \Delta S}}. \tag{2-7}$$

Similar to the SCS-CN method (SCS, 1985), Ponce & Shetty (1995a, b), and Wang & Tang (2014), we consider the whole vaporization process occurs in two stages: an initial stage followed by a continuing stage,

$$E = E_0 + E_c\,, \tag{2-8a}$$

$$\text{where} \quad E_0 = \lambda E\,. \tag{2-8b}$$

$E_c$ is the portion of vaporization that occurs after the initial stage, mostly transpiration from deeper soil water storage that is very close to or below the groundwater table. $\lambda$ is a dimensionless fraction parameter. We provide a more detailed discussion on $E_0$ and $\lambda$ later in Section 2.4. From Eqn. (2-7) and (2-8), we get

$$\frac{Q_b}{W-\Delta S}=\frac{(1-\lambda)\frac{E}{W-\Delta S}-(\lambda-\lambda^2)\left(\frac{E}{W-\Delta S}\right)^2}{\frac{E_p}{W-\Delta S}-\lambda\frac{E}{W-\Delta S}}. \tag{2-9}$$

When $\lambda > 0$, Eqn. (2-10) is a typical quadratic equation for $(E/(W-\Delta S))$. Solving it yields

$$\frac{E}{W-\Delta S}=\frac{\left(1+\frac{E_p}{W-\Delta S}\right)\pm\sqrt{\left(1+\frac{E_p}{W-\Delta S}\right)^2-4(2\lambda-\lambda^2)\frac{E_p}{W-\Delta S}}}{2(2\lambda-\lambda^2)}. \tag{2-12}$$

If taking the plus sign in Eqn. (2-12), one will always obtain $\frac{E}{W-\Delta S}\geq 1.0$, while $\frac{E}{W-\Delta S}$ should always be no larger than 1.0 (Eqn. 2-5). So in Eqn. (2-12) we take the minus sign and obtain

$$\frac{E}{W-\Delta S}=\frac{1}{2(2\lambda-\lambda^2)}\left\{\left(1+\frac{E_p}{W-\Delta S}\right)-\left[1+(2-8\lambda+4\lambda^2)\frac{E_p}{W-\Delta S}+\left(\frac{E_p}{W-\Delta S}\right)^2\right]^{0.5}\right\}. \tag{2-13}$$

Eqn. (2-13) is thus an analytic expression of HI, which applies to the long-term, annual, and monthly scales.

Hereafter we refer to the ratio of potential evapotranspiration to effective catchment wetness as the ecological aridity index (EAI), which quantifies the interaction between monthly energy supply and water supply for plant water use at the catchment scale. Note for convenience, we define EAI at the long-term, annual, and monthly time scales similarly to HI, and hereinafter denote them as long-term, annual, and monthly EAI, respectively. Compared to the well-known aridity index (AI), defined as the ratio of potential evapotranspiration to total precipitation, EAI is overall larger since it excludes surface runoff from the water supply for vaporization. Intuitively it is more physically meaningful from the plant water use point of view since surface runoff will rarely be available for vaporization in the real world. Figure 2-2(a) provides a conceptual diagram of Eqn. (2-13), which includes a theoretical upper-bound of HI when $\lambda = 1.0$ (solid blue line) and a theoretical lower-bound when $\lambda = 0$ (dashed blue line). When $EAI < 1.0$, the water supply for vaporization is larger than the evaporative energy demand, and the catchment is in an energy-limited or ecologically wet state. When $EAI > 1.0$, the water supply for vaporization is less than the energy supply, and the catchment is in a water-limited or ecologically dry state.

From Eqn. (2-5) and (2-9), we get

$$(2\lambda - \lambda^2)\left(\frac{\mathrm{E}}{\mathrm{W} - \Delta\mathrm{S}}\right)^2 - \left(1 + \frac{\mathrm{E_p}}{\mathrm{W} - \Delta\mathrm{S}}\right)\left(\frac{\mathrm{E}}{\mathrm{W} - \Delta\mathrm{S}}\right) + \frac{\mathrm{E_p}}{\mathrm{W} - \Delta\mathrm{S}} = 0. \tag{2-10}$$

When $\lambda = 0$, Eqn. (2-10) gives

$$\frac{\mathrm{E}}{\mathrm{W} - \Delta\mathrm{S}} = \frac{\frac{\mathrm{E_p}}{\mathrm{W} - \Delta\mathrm{S}}}{1 + \frac{\mathrm{E_p}}{\mathrm{W} - \Delta\mathrm{S}}}. \tag{2-11}$$

One can also see that the changing rate of HI is gradually decreasing with EAI, suggesting that HI variability might be decreasing when a catchment is moving from an ecologically-wetter state to an ecologically-drier state. To quantify the changing rate of HI with EAI, we take the derivative of Eqn. (2-13), and obtain

$$\frac{\mathrm{d(HI)}}{\mathrm{d(EAI)}} = \frac{1}{2(2\lambda - \lambda^2)}\left\{1 - \left(1 - 4\lambda + 2\lambda^2 + \frac{\mathrm{E_p}}{\mathrm{W} - \Delta\mathrm{S}}\right)\left[1 + (2 - 8\lambda + 4\lambda^2)\frac{\mathrm{E_p}}{\mathrm{W} - \Delta\mathrm{S}} + \left(\frac{\mathrm{E_p}}{\mathrm{W} - \Delta\mathrm{S}}\right)^2\right]^{-0.5}\right\}. \tag{2-14}$$

This $d(HI)/d(EAI)$ is thus capturing the gradually decreasing slope of the HI~EAI curve, as shown in Figure 2-2(b). $d(HI)/d(EAI)$ is overall more than 0.3 when a catchment is ecologically humid, i.e., $EAI < 1.0$, suggesting a relatively large variability of $HI$ between humid catchments (spatially variability) or humid years (temporal variability). When a catchment is ecologically dry, i.e., $EAI > 1.0$, $d(HI)/d(EAI)$ drops quickly and is mostly below 0.1 when $EAI > 2.0$, suggesting that HI remains constant among dry catchments (spatial variability) or dry years (temporal variability).

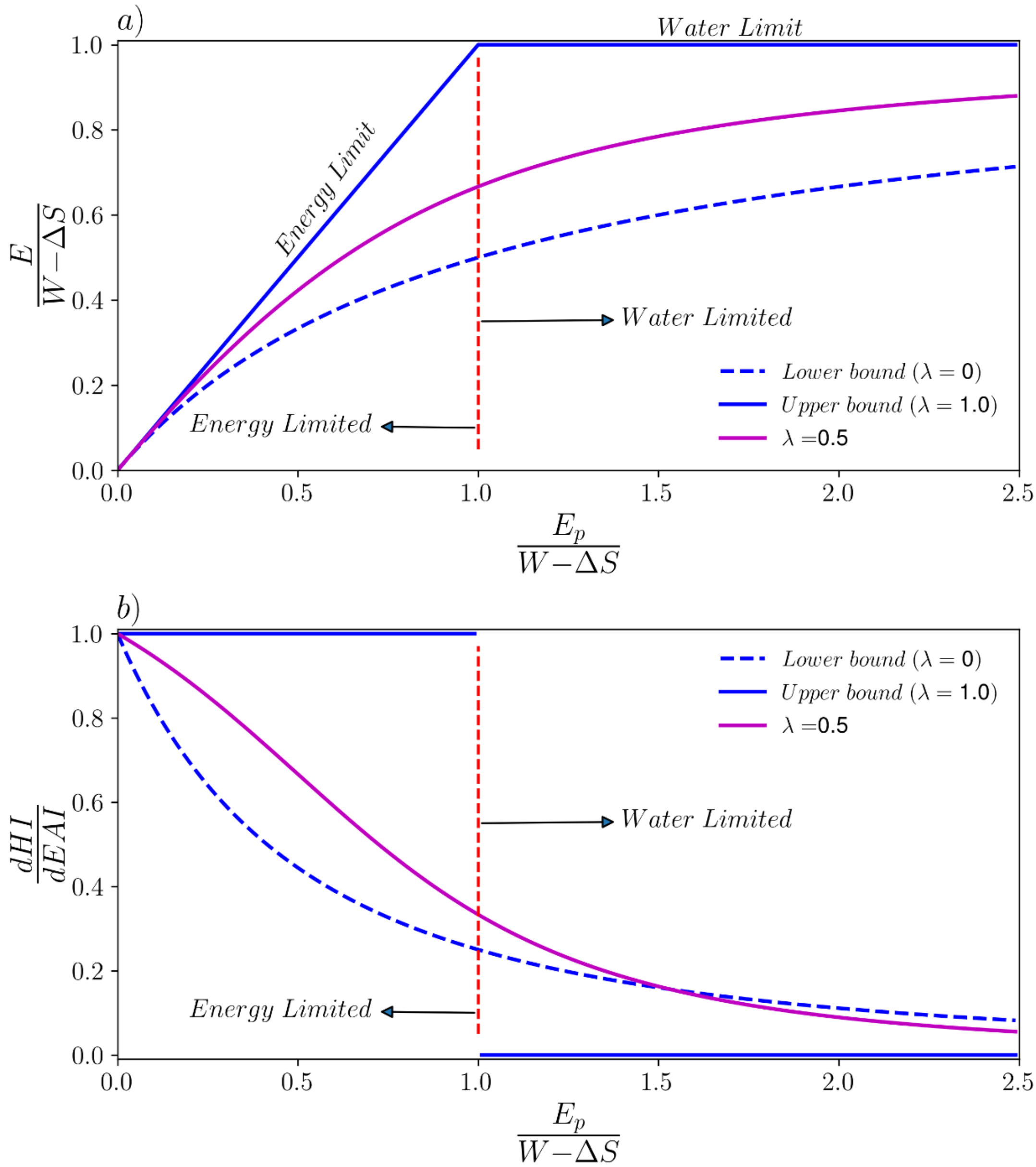


Figure 2-2: Theoretical bounds of the new Horton Index functional framework (Eqn. 2-13). The model parameter, λ, which is defined as the ratio of initial vaporization to total vaporization, varies between 0 and 1.

This small spatiotemporal variability of HI is consistent with the previous empirical findings that HI is relatively constant in dry years or arid catchments (Horton, 1933; Troch et al., 2009).

## 2.3 Validation of the Analytical Framework

### 2.3.1 CAMELS Dataset

The data used in this study are mainly from the Catchment Attributes and MEteorology for Large-sample Studies (CAMELS) dataset (Addor et al., 2017; Newman et al., 2015). CAMELS includes 671 small to medium-sized, nearly pristine catchments distributed across biomes, climatic, and topographic gradients of the contiguous United States. CAMELS provides observed daily precipitation, streamflow, and maximum and minimum temperature data for each catchment from 1980 to 2014. It also offers topographic, soil, and vegetation attributes such as elevation, mean topographic slope, soil hydraulic conductivity, soil depth, porosity, dominant vegetation cover, monthly leaf area index (LAI), root depth, etc. Besides the observed data, CAMELS also provides model simulated hydrologic variables such as actual and potential evapotranspiration, a by-product of streamflow simulation using the coupled Snow-17 and SAC-SMA models, which have been validated against the observed streamflow data (Addor et al., 2017). For analysis purposes, we perform the following filtering and post-processing steps of CAMELS data.

1) In some CAMELS catchments, there are missing records in the observed streamflow data. We exclude those catchments without complete daily streamflow records from 1982 to 2012.
2) Model simulated evapotranspiration data from CAMELS is essential for our analysis, but there has been uncertainty (Newman et al., 2015). To minimize the impacts of modeling uncertainty, we adapt a criterion expressed as $|\bar{E}_{obs} - \bar{E}_{sim}| <$

$10\% * \bar{E}_{obs}$. Here $\bar{E}_{sim}$ is the long-term average of simulated evapotranspiration from 1982 to 2012. $\bar{E}_{obs}$ is calculated as the long-term average of observed precipitation subtract the long-term average of observed streamflow. We exclude those catchments that do not satisfy this criterion.

3) Each catchment's dominant vegetation type is available within the CAMELS vegetation attributes, along with the percentage of catchment area it covers. The dominant cover fraction percentage ranges from 31.45% to 100% for the entire dataset. Here, we consider specific vegetation cover the dominant vegetation cover if it takes more than 50% of the total catchment area. Thus, we further exclude those catchments without vegetation cover, taking more than 50% of the catchment areas, i.e., no dominant vegetation cover.
4) We select 343 CAMELS catchments after Steps 1~3. The CAMELS catchments belong to eleven different dominant vegetation cover types, as shown in Figure 2-3a. For convenience, we further group them into six vegetation cover types: Croplands and Croplands/Natural vegetation mosaic (denoted as CL/NVM, 99 catchments), Deciduous Broadleaf (denoted as DBF, 82 catchments), Evergreen Needleleaf and Broadleaf Forest (denoted as EF, 22 catchments), Mixed Forests (denoted as MF, 50 catchments), Grasslands (denoted as GL, 40 catchments) and Savannas, Woody Savannas and Open/Closed Shrublands (denoted as WS + SL, 50 catchments). Figure 2-3b show that most forested catchments (DBF, EF, and MF) are located in the humid or semi-humid climate regions, as indicated by the aridity index (AI, here defined as the ratio of long-term average potential evapotranspiration over precipitation) values less than 1.0. Those non-forested catchments (CL/NVM, GL, and WS+SL) are located in the arid or semi-arid climate regions.

5) Note that the final precipitation data employed in this study are essentially daily rainfall + snowmelt time series, which are directly taken from the CAMELS dataset.

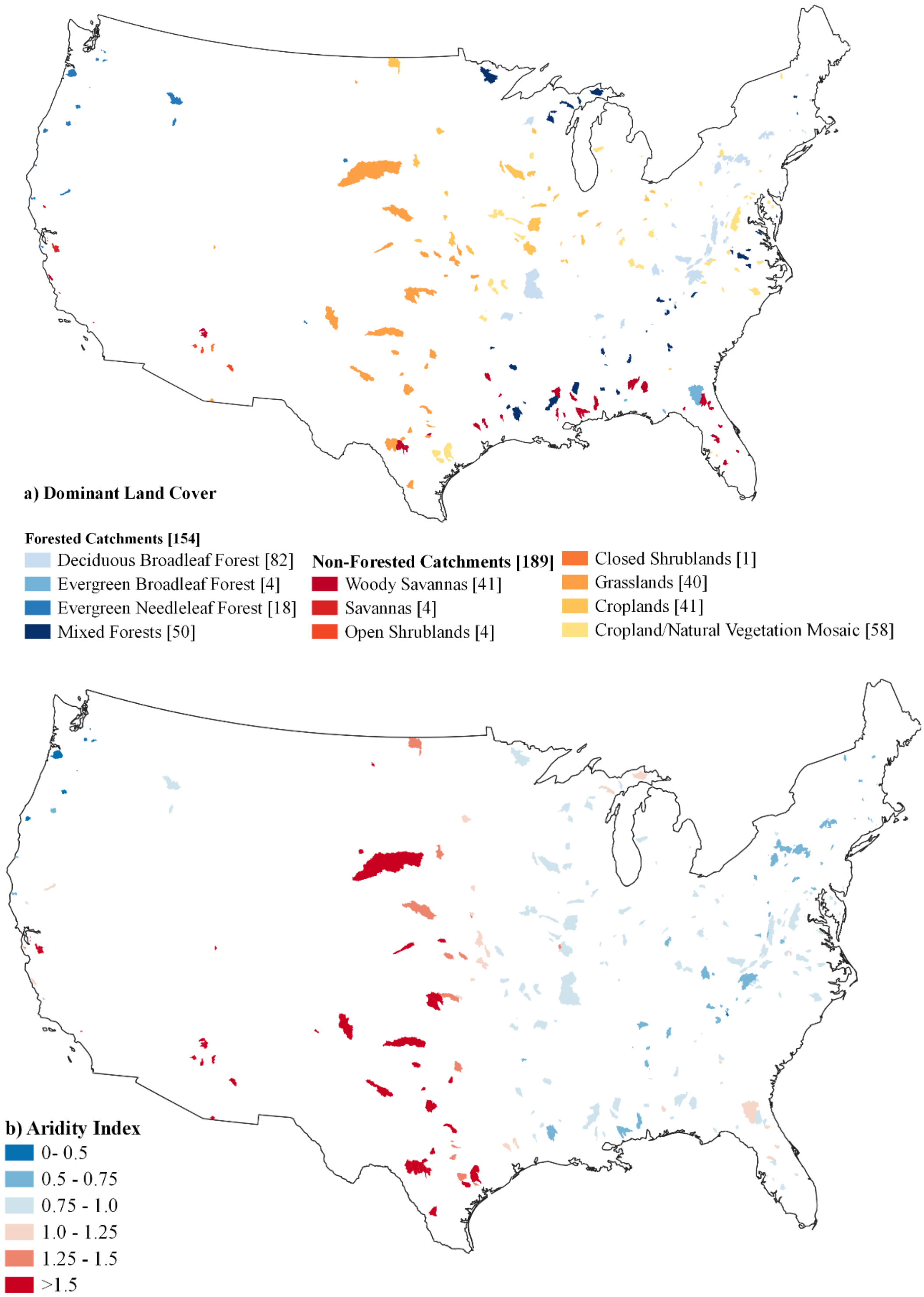


Figure 2-3: Selected 343 CAMELS catchments: a) Dominant biomes, b) Aridity Index(Ep/P)

6) The observed daily streamflow time series is separated into daily surface runoff and baseflow time series at each selected catchment using the one-parameter recursive digital filtering method (Nathan and McMahon, 1990).

### 2.3.2 Validating the Analytical Framework

To evaluate the analytical framework, we first estimate the monthly HI time series at each catchment directly using the CAMELS data. $E$ is taken from the CAMELS simulated daily evapotranspiration time series. $W - \Delta S$ is calculated indirectly as $E + Q_b$. According to Eqn. (5). We hereafter denote those HI values calculated using the CAMELS dataset as "estimated" for easy reading and those derived using the analytical framework as "analytical". For evaluating the closeness between the "estimated" and "analytical" HI series, we use the Kling-Gupta Efficiency (KGE) (Gupta et al., 2009) and Normalized Root Mean Square Error (NRMSE). Overall, the higher the KGE value, the closer the "estimated" and "analytical" HI series, and KGE = 1.0 means a perfect match. Similarly, the smaller the NRMSE, the closer the "estimated" and "analytical" HI series and NRMSE = 0.0 means a perfect match. At each catchment, we calibrate the $\lambda$ value at the monthly scale in the calibration period 1982-2001 to reach the best match between the "estimated" and "analytical" monthly HI time series, as indicated by the optimal KGE value. The optimal KGE values are no less than 0.5 and 0.8 for over 95% and 87% of the 343 catchments, respectively (as shown in Figure 2-4a and 2-4b), suggesting the promising predicting power of the analytical framework.

The resulted $\lambda$ values from this calibration process are hereinafter denoted as the "calibrated." We then apply the calibrated $\lambda$ value corresponding to each catchment in the validation period 2002-2012, 90% and 82 % of the catchments have the KGE values no less than 0.5 and 0.8, respectively, indicating the representativeness of the calibrated $\lambda$ values over the whole study period 1982-2012. The NRMSE values between the "estimated" and "analytical" HI monthly time series are mostly less than 0.1 in both the calibration and validation periods (as shown in Figures 2-4c and 2-4d), again indicating good prediction power of the analytical framework. Note that since the normalizing factor (i.e., long-term HI) is always ≤ 1, NRMSE ≥ RMSE.

Regarding specific vegetation types, the analytical framework performs very well at the CL/NVM, MF, DBF, and WS+SL dominated catchments, but only reasonably well at the GL (according to KGE), and EF (according to NRMSE) dominated catchments. By looking into the details of those individual catchments where the analytical framework does not perform well, we find that poor KGE results are partially related to the weak seasonal variability of estimated HI. We use the coefficient of variation (CV, the ratio of the standard deviation to mean) to compute the variability of the estimated HI. In total, only 39 catchments have KGE values less than 0.75, of which 34 have CV values less than 10%. Visual inspection of these catchments shows that the low KGE values do not necessarily imply model incapability. Instead, since the estimated HI index is slightly invariable, the framework's small overestimation/underestimation is somehow exaggerated by the KGE metric, which is evident by the NRMSE box-plots in Figures 2-4(c) and (d), i.e., the NRMSE values are mostly less than 0.1, except for the EF dominant catchments.

To illustrate more detailed HI variations at individual catchments, we select two representative catchments out of each of the six biome regimes, i.e., CL/NVM, DBF, EF, MF, GL, and WS+SL, based on Figure 2-4. Within each biome regime, there are a number of catchments under various climate conditions, i.e., a range of AI values. For each biome regime, we select one catchment with relatively higher AI value and another with relatively lower AI values. Figure 2-5 shows the "estimated" (blue lines) and "analytical" (red lines) monthly HI time series at the representative catchments. Each row is for one biome. The left column is for the catchments with relatively higher AI values. Overall, the analytical framework reproduces the monthly HI time series quite well in most catchments.

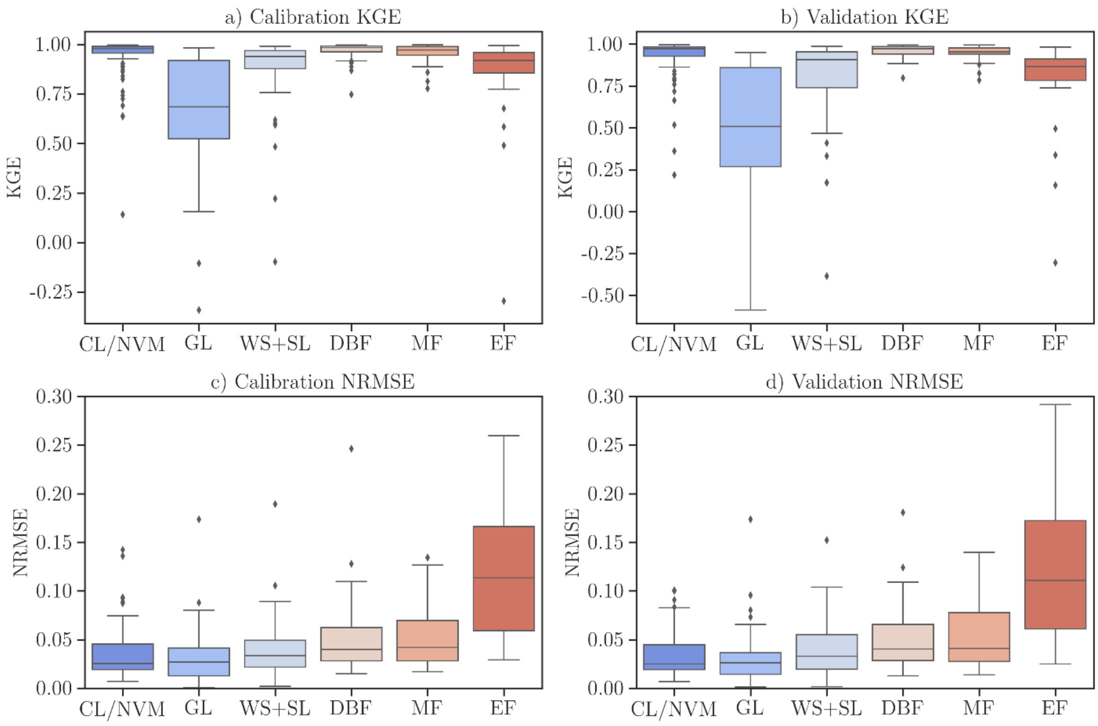


Figure 2-4: Performance of the analytical formula. Box-plots of (a). KGE values for different vegetation types in the calibration period; (b). KGE values in the validation period; (c). NRMSE values in the calibration period; (d).

Nevertheless, there are noticeable biases in the peak HI values, for example, at the EF and GL catchments, as indicated by the relatively low KGE values (for the GL dominant catchments) and high NRMSE values (for the EF dominant catchments). There are several possible reasons for the biases: 1) The NRMSE values for the EF dominant catchments are slightly higher than others, primarily because of the model's slight overestimation of seasonal peak values for this type of catchments. During most of the year, these catchments are in an energy-limited state. However, most of them become water-limited during a couple of growing-season months with peak HI values.

The slight overestimation of the peak value possibly arises from a failure to capture the transition into and out of this short period since the calibration is dominated by those months in an energy-limited state with relatively high HI values. 2) Temperature and precipitation (magnitude, frequency, and timing) exert strong controls on grassland ecosystems' productivity and water use (Hufkens et al., 2016). Hence, growth and productivity are highly dynamic even at a sub-monthly temporal scale, i.e., weekly or daily, and this sub-monthly variation may have led to strong inter-annual variability of growth and productivity (Hufkens et al., 2016). Therefore, the biases of monthly HI estimation in the GL dominant catchments are likely because the analytical framework is not well capturing the sub-monthly timescale characteristics, which is an essential factor in the strong inter-year variability of grassland dormant-season water use.

Figure 2-5 shows that the analytical framework reproduces the HI seasonal variations quite well across biomes despite the biases. In each catchment, the drier months can be further grouped into a growing season (on average, May to October for the contiguous United States) when plan transpiration is high. The wetter months can be grouped into a dormant season (November to April) when plant transpiration is much less. HI's seasonal variation is stronger at those catchments under more humid climates, i.e., lower AI values. Particularly, during the dormant season (including late fall, winter, and early spring), the monthly HI values in the relatively humid catchments are significantly lower than those in relatively arid catchments. This difference can be attributed to the different climate conditions (see Fig. 2-3).

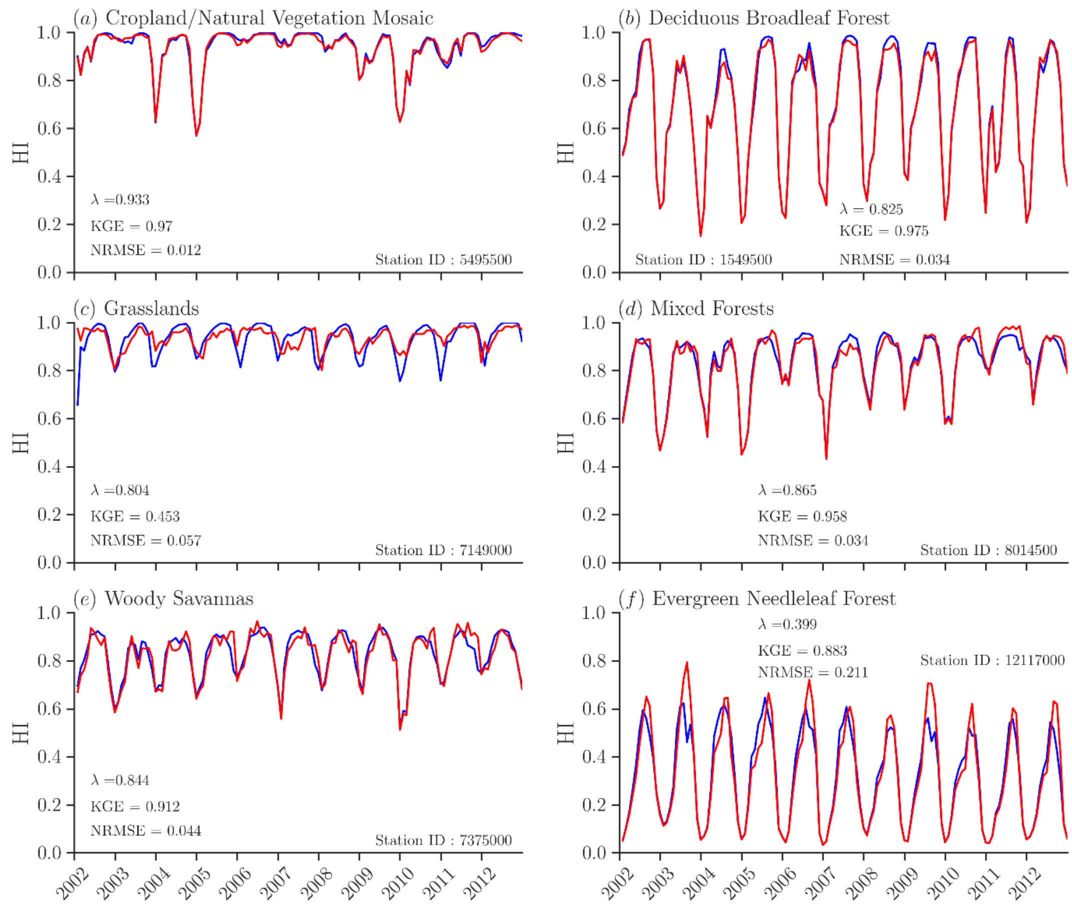


Figure 2-5: Horton Index monthly time series over the analytical framework validation period (2002-2012) for selected catchments. The blue and red lines are for the estimated and analytical HI time series, respectively.

Most forested catchments are located in the relatively humid climate regions, where the water supply for vaporization (precipitation) is overall no less than the evaporative energy demand (potential evapotranspiration). In fact, in these forested catchments, the monthly total vaporization ($E$) is mostly less than the monthly catchment wetness ($W - \Delta S$). In the dormant season, at the forested catchments, the total vaporization is small owing to minimum evaporative energy demand, and the catchment wetness remains a fair amount; while at the non-forested catchments, the total vaporization is at a similar level as those forested catchments, but the catchment wetness is small since it has been depleted by relatively larger vaporization in the growing season.

The difference in the monthly HI values among the catchments can also be attributed to different vegetation phenology among various biomes. In most forested catchments, usually, there is a dense understory and a litter layer, which help reduce soil evaporation during the dormant season by blocking soil moisture from the atmosphere, hence not only reducing vaporization and surface runoff but also increasing catchment wetness (Gomyo and Kuraji, 2016; Sakaguchi and Zeng, 2009; Song et al., 1997). In the broadleaf forests, most leaves fall off in the dormant season leading to not only a thicker litter layer but also significantly reduced transpiration from leaves. In the evergreen forests, the leaves largely remain on the trees even during the dormant season, but the trees lower their carbon utilization rate (i.e., downregulation of photosynthetic capacity) in response to the low-temperature conditions (Adams et al., 2004; Öquist and Huner, 2003). A reduced photosynthetic activity means much of the radiation absorbed by leaves cannot be utilized for the photosynthetic fixation of $CO_2$. Hence, the likelihood of water escaping through the stomatal opening (i.e., transpiration) during the carbon uptake process is significantly reduced. In non-forested areas such as grasslands, such a litter layer is usually not developed. In the U.S., cropland residues are often left on the field after harvesting and can be as effective as the forest litter layer. However, the removal of crops after harvesting increases wind speed by reducing ground surface roughness and thus increases the effective evaporation rate. Another possible reason for the different HI values between the forested and non-forested catchments is the hydraulic redistribution mechanism. With deeper root systems, in the dormant season, trees are able to transport excess water from topsoil down to deeper soil, particularly during nights, hence increasing catchment wetness (Amenu & Kumar, 2008; Brooks et al., 2002; Prieto et al., 2012).

## 2.4 Further Discussion of the Analytical Framework

$\lambda$ is the only parameter in our analytical framework which is closely related to the partitioning of total vaporization (E) into initial ($E_0$) and continuing vaporization ($E_c$). In this study, the lambda values are obtained from the monthly HI time series calibration and applied to the multi-scale analysis. Recall that $E_0$ corresponds to three primary sources where water is easily available for vaporization: direct evaporation from interception (canopy and litter interception), direct evaporation from the soil surface, and temporally stored water in surface depressions, and transpiration from the shallow root zone. The contribution from interception loss accounts for 10–50% of gross precipitation, depending on vegetation types, canopy density, and meteorological conditions (Levia et al., 2011; Miralles et al., 2010; Miralles et al., 2016; Roth et al., 2007; Wang et al., 2007)(Levia et al., 2011; Miralles et al., 2010; Roth et al., 2007; Wang et al., 2007)(Levia et al., 2011; Miralles et al., 2010; Roth et al., 2007; Wang et al., 2007). Thus, it is not unreasonable to infer that direct evaporation from interception contributes to more than 10-50% of total vaporization. Direct evaporation from surface depressions is a spatiotemporally heterogeneous process mainly driven by surface microtopography (Kamphorst et al., 2000). Surface depressions here mainly refer to those small, unmanaged water bodies embedded either within uplands or river floodplains. They are small yet abundant at the catchment or on larger scales(Wu et al., 2019). The temporally stored water in these surface depressions thus plays an important role in catchment hydrological processes, including evaporation (Alexander et al., 2018; Cohen et al., 2016; Golden et al., 2017; Lane et al., 2018; Rajib et al., 2020; Yu and Harbor, 2019). The transpiration component of initial vaporization corresponds to the fast transpiration, which only draws on the upper 50cm of the soil layer where most root biomass is located, and most transpiration occurs (Savenije, 2004). In the U.S., Addor et al. (2017) derived catchment-average root-depth data for 671 catchments based on a global vegetation root distribution model by Zeng (2001) and suggested that, for all catchments (excluding the missing values, 24 of 671 catchments), 50% of root biomass is located within the top 25cm soil layer. Globally, Schenk & Jackson (2002b) analyzed 475 profiles for 209 sites in 15 biomes and showed that ~90% of the root system is in the upper 30cm soil layer across all sites. Initial transpiration from this upper soil layer is thus not trivial and at least comparable to direct evaporation from interception. Overall, each of these three sources of $E_0$ is nontrivial. $E_0$ is therefore expected to be a significant, even dominant portion of total vaporization. The value of $\lambda$, although it may vary from one catchment to another, should be nontrivial in most catchments. Figure 2-6 shows the box-plot of calibrated $\lambda$ values for different biome regimes. The calibrated $\lambda$ values are more than 0.5 for most catchments, consistent with the above discussion.

What is more interesting from Figure 2-6 is that the calibrated $\lambda$ values are relatively lower in the forested catchments, particularly in those EF dominant catchments. The average of calibrated $\lambda$ values within each biome regime is 0.876, 0.875, 0.886, 0.799, 0.807 and 0.686 for CL/NVM, GL, WS+SL, DBF, MF and EF respectively. The lower $\lambda$ values in the forested catchments are very likely due to the deeper root systems, which facilitate access to deeper soil water for continuing vaporization. Although overall forest biomes have more interception owing to higher LAI values and understory vegetations, the denser canopy often reduces evaporation from the soil surface by blocking more incoming evaporative (solar) energy and increasing the aerodynamic resistance or vaporization. On the other hand, non-forest biome regimes usually have shallower root systems, which allow for quicker responses to incoming rainfall but less access to deeper soil water for continuing vaporization

(Fan et al., 2017; Rore and Stern, 1967). For example, typical root length densities for crop plants are about 6 cm /cm3 and 1 cm / cm3  in the surface soil layer and a 50-100 cm deep soil layer, respectively (Glinski and Lipiec, 2018). The GL catchments in this study are mostly located in the Great Plains of North America (Fig. 2-3) and generally fall under water-limited ecosystems (EAI > 1.0 for 49 out of 50 GL catchments).

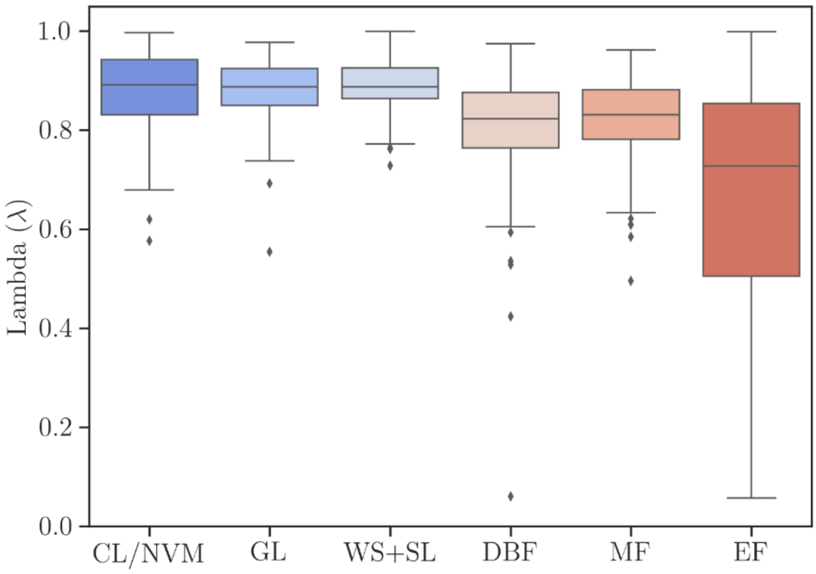


Figure 2-6: Bot-plot of λ values calibrated at the monthly scale for different vegetation types.

In a water-limited biome, root systems are shallower and wider in dry climates and deeper and narrower in cold and wet climates (Schenk and Jackson, 2002b). Hence, GL catchments in this study can be characterized by a shallow and wide root system type. Schenk & Jackson's (2002b) data for CONUS grasslands (34 root profiles) show that 90% of the sites have 50% of the root distribution within the top 20cm. A more recent isotopic evapotranspiration partitioning experiment on tallgrass prairie in the Great Plains of North America by (Sun et al., 2021) found that the top 10cm soil layer is a major source of the total evapotranspiration during the initial drying periods. Like croplands, high water volume is extracted for transpiration from the topsoil layer; thus, the initial vaporization is a dominant component.

The between-catchment variability of calibrated $\lambda$ values within each biome regime appears to be higher in the forested catchments, i.e., the coefficients of variance are 10.0%, 9.44%, 7.5%, 12.93%, 16.64%, and 33.08% for CL/NVM, GL, WS+SL, DBF, MF, and EF dominant catchments respectively. This between-catchment variability within each biome regime may be caused by several reasons. First, the difference in the non-dominant proportion of the catchment land cover may be a contributing factor. In each of the 343 selected catchments, we define the dominant cover as the biome type covering > 50% of the catchment. For instance, a catchment with 100% DBF cover will behave differently from another with only 60 % DBF cover, although both are classified into the same biome regime in this study. Second, the between-catchment variability difference between the forested and non-forested catchments is likely because non-forest biome regimes are often intensive water users featured by high water use efficiency. As such, their behavior (e.g., partitioning of E into $E_0$ and $E_c$) is more alike and converging towards optimal rain use efficiency despite the different climate, soil, and topographic conditions (Huxman et al., 2004; Troch et al., 2009). Third, the different root systems between the forested and non-forested regimes. In the forested catchments, $E_c$ is usually larger than the non-forested due to deeper roots and easier access to deeper soil water, and thus more sensitive to climate variations because deeper roots allow trees to better cope with climate variations. Last but not least, the variability in type and density of the understory vegetation in the forested catchments may also contribute to this between-catchment variability. The types of understory can be trees, shrubs, or herbaceous vegetation. For instance, if trees dominate the understory, more water is likely to be extracted from deeper soil (especially during the summer season) than an understory dominated by nonperennial herbaceous vegetation with shallow roots. Moreover, the understory also affects soil evaporation since a denser understory will more likely block solar radiation from reaching the soil surface.

## 2.5 Emergent Patterns and Theoretical Insights

Upon successful validation, we further investigate the analytical framework's capacity to help detect and explain emergent patterns in HI's spatiotemporal variations at different temporal scales. Note here that we define space-time similarity as the similarity between a spatial (between-catchment) variability and a temporal (within-catchment but between different years or months) trend.

### 2.5.1 Space-Time Similarity in HI Trends

Figure 2-7(a) shows that the analytical framework can well capture HI's inter-catchment variability, i.e., the increasing trend of HI from wetter to drier catchments. Here each dot in Figure 2-7(a) represents a pair of estimated long-term HI and EAI values for one of the 343 catchments. The magenta line is the "analytical" curve fitted using Eqn. (2-13), with a calibrated $\lambda$ value of 0.774 and an NRMSE value of 0.075. Moreover, the analytical framework also captures the between-year variability of HI very well, i.e., the increasing trend of HI from wetter to drier years, as shown in Figure 2-7(b). Here each dot represents a pair of "estimated" annual HI and EAI values for one catchment and one year from 1982 to 2012. The analytical curve is fitted again using Eqn. (2-13), achieving a calibrated $\lambda$ value of 0.783, and the NRMSE value is 0.08. The calibrated $\lambda$ value at the long-term scale, 0.774, is quite close to that at the annual scale, 0.783, suggesting a space-time similarity of HI increasing trend from wetter catchments (years) to drier catchments (years).

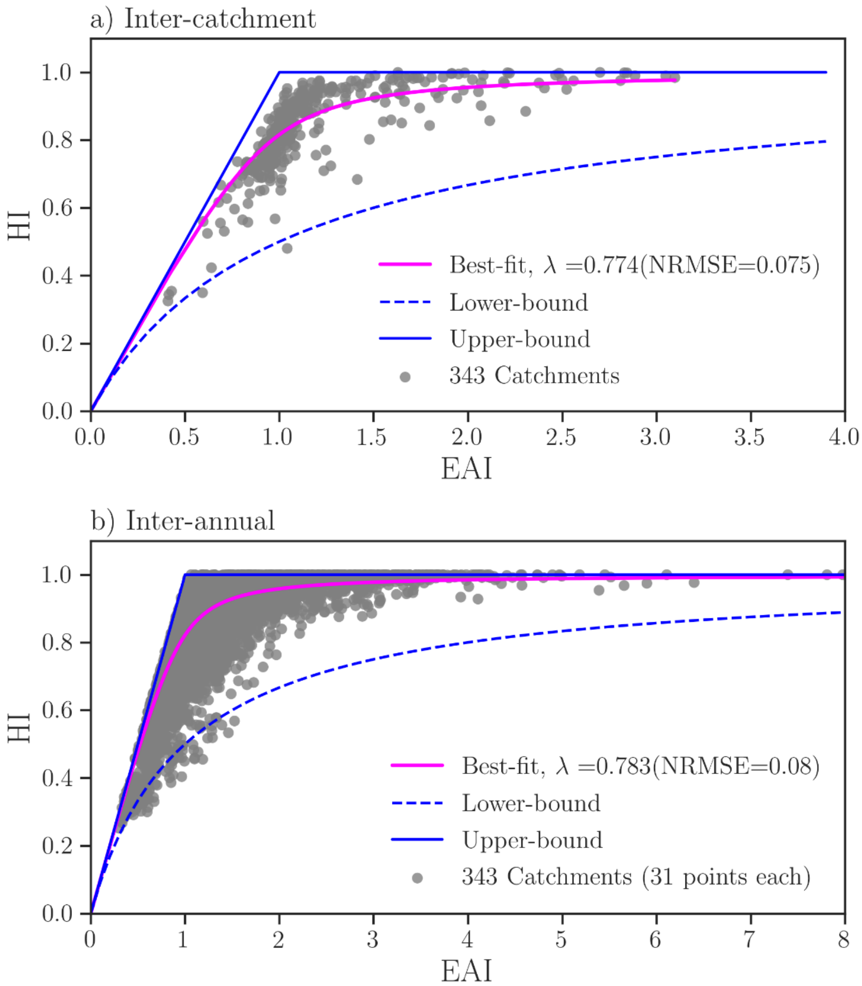


Figure 2-7: Space-time similarity of HI~EAI relationships. (a) Inter-catchment (spatial) variability of HI. Each dot represents one catchment. (b) inter-annual variability of HI. Each dot represents one year (31 dots per catchment).

Figure 2-8 further explores this space-time similarity for different biome regimes. Again, the closeness between the long-term and annual calibrated $\lambda$ values across different vegetation types confirms the space-time similarity both empirically and theoretically. It appears that most non-forest catchments are in an ecologically dry state, i.e., EAI > 1.0 for both between-catchment and between-year cases. Under such a dry state, these non-forest biome regimes tend to operate toward the optimal water use efficiency, leading to the convergence of HI values towards 1.0. The variability of HI in these non-forested catchments is thus small. The forested catchments nonetheless do not have such a preference, i.e., their EAI values spread around 1.0. The DBF catchments have the narrowest range of EAI values, followed by the MF and then EF dominant catchments. Overall, the variability of annual HI decreases from wetter to drier states, as shown in Figure 2-9(a).

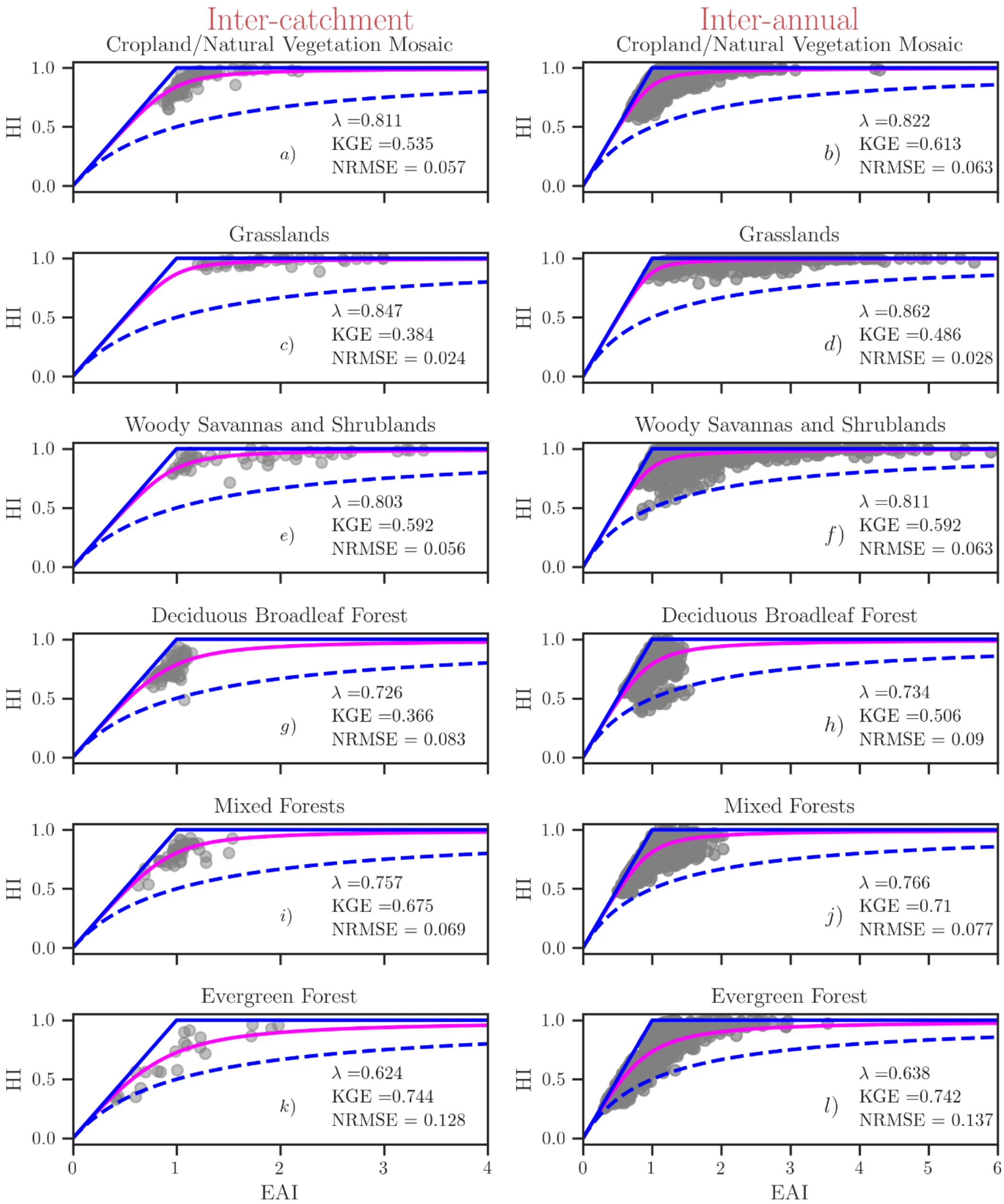


Figure 2-8: Space-time similarity of HI~EAI relationships. The left column is for inter-catchment (spatial) variability, one dot per catchment. The right column is for inter-annual variability, and each catchment has 31 dots.

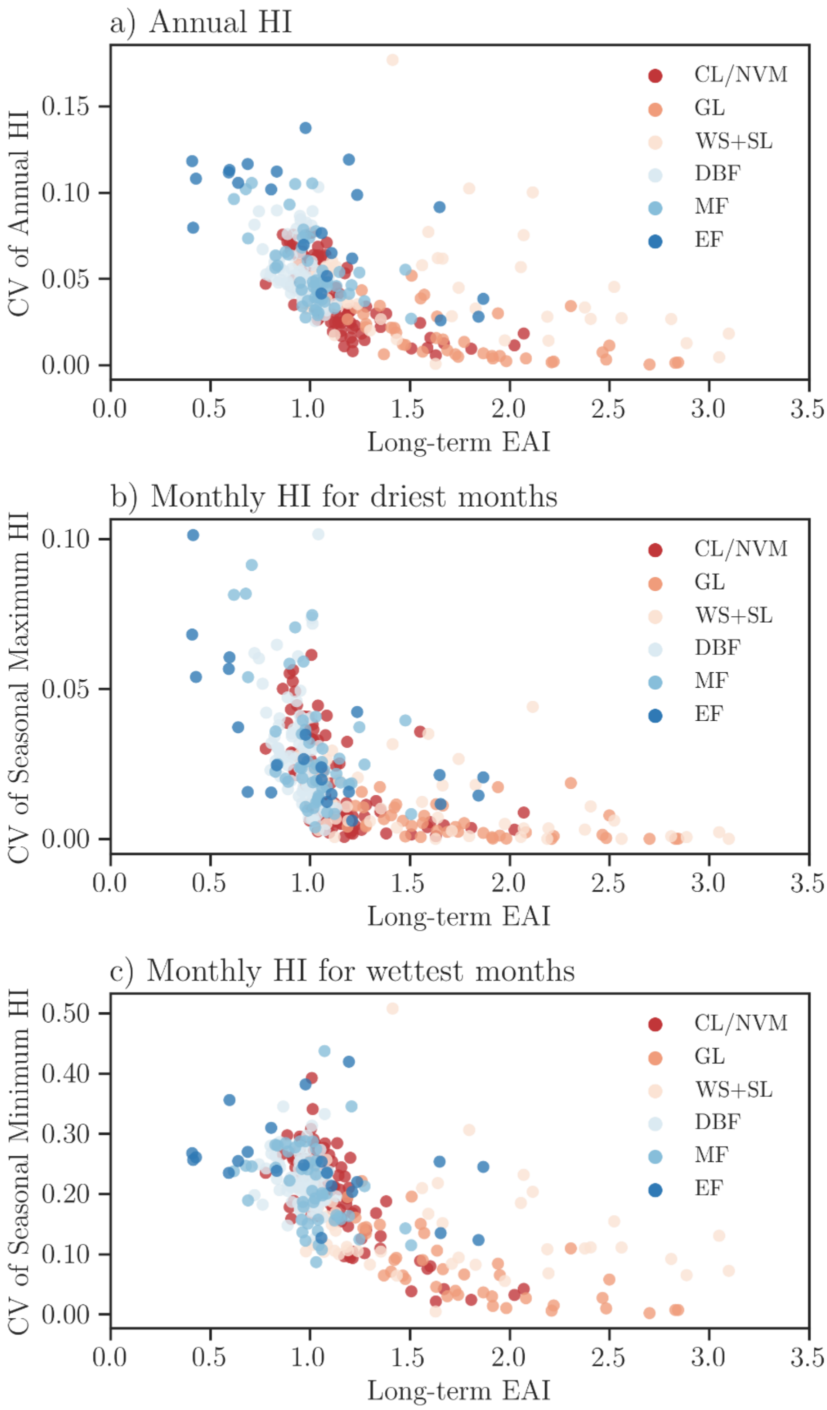


Figure 2-9: Inter-annual variability of a) annual HI, b) monthly HI but for the driest month only from each year, and c) monthly HI values but for the wettest month only from each year. Each dot here represents one catchment.

More interestingly, the above space-time similarity exists not only at the annual scale but also at the monthly scale, as shown in Figures 2-10 and 2-11. Figure 2-10 shows that the monthly HI values increase from the wetter to drier months as captured by both the empirical data points and theoretical curves at each representative catchment. Overall, the evapotranspiration in the growing season is higher than in the dormant season and is dominated by plant transpiration over evaporation from soil and interception. Correspondingly, the monthly HI values in the growing season are generally higher than those in the dormant season.

Figure 2-11 confirms this trend of intra-annual variability across all 343 catchments. The twelve subplots in Figure 2-11 correspond to the twelve months in a calendar year. Each dot represents one catchment; e.g., in Figure 2-10(a), the January HI value for a catchment is calculated as a ratio of the average of January precipitation in 1982-2012 over the average of January catchment wetting. This way, HI's intra-annual variability manifests as the difference between the subpanels in Figure 2-11. Overall, in the growing season, particularly July-September, the HI values are preferentially distributed in the ecologically dry state, i.e., EAI >1; hence the variability of monthly HI values is relatively small, as more clearly shown in Figure 2-9(b). In the dormant season, particularly December-February, the HI values are more distributed in the ecologically wet state, and the variability of monthly HI values is relatively larger, as also shown in Figure 2-9(c).

Within each panel in Figure 2-11, the between-catchment variability is well captured by the theoretical curves. For example, in the subpanel corresponding to May, the HI values increase from those catchments with a drier May to those with a wetter May in an average sense. Within each subpanel, a calibrated $\lambda$ value is chosen to best capture the inter-catchment variability. The calibrated $\lambda$ values are quite similar among the subpanels, i.e., varying in a very narrow range of 0.81- 0.86, suggesting similar inter-catchment variability across different seasons.

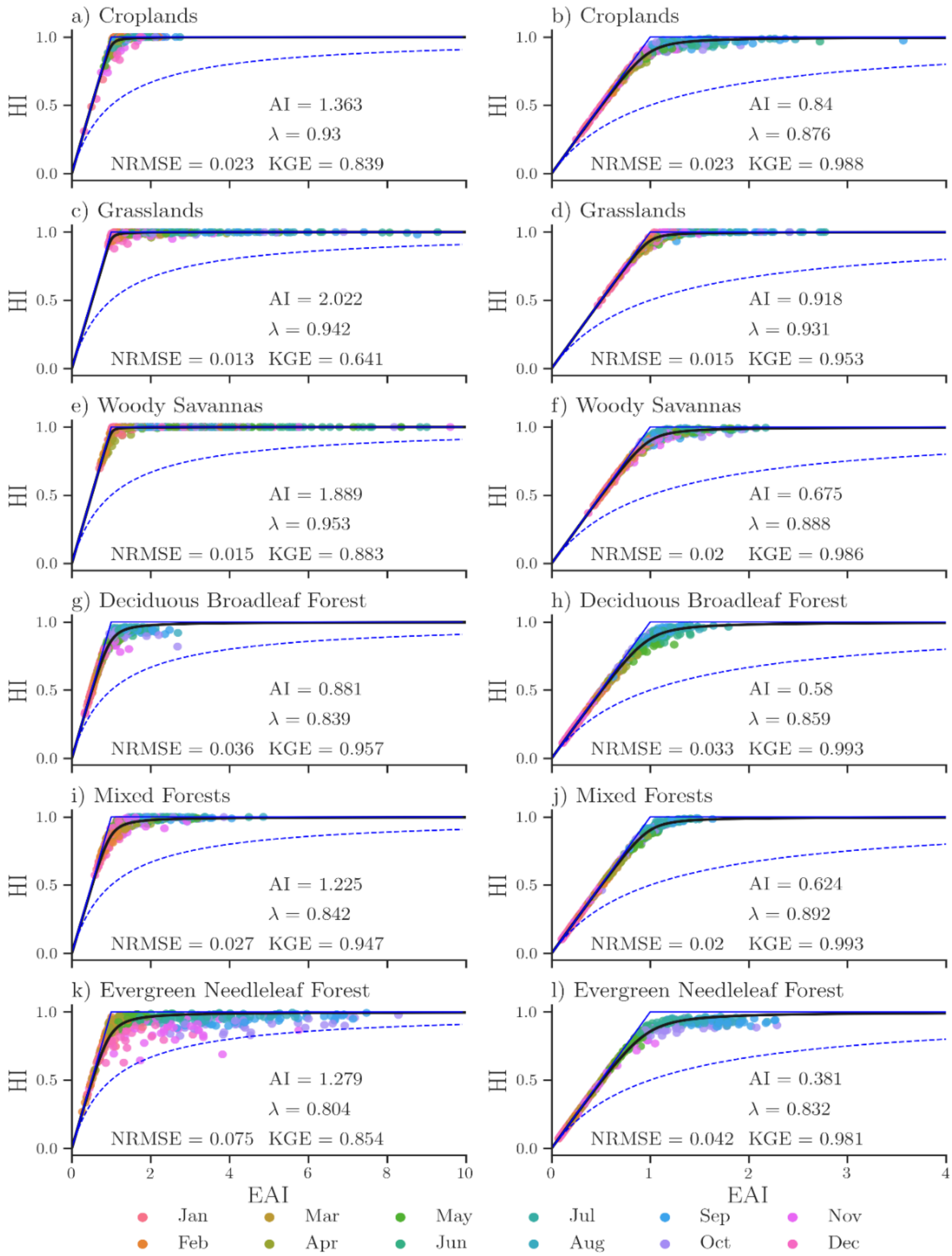


Figure 2-10: Intra-annual variability of monthly HI within individual catchments in 1982-2012. The black, solid blue, and dashed blue lines correspond to the best-fitted, upper-bound, and lower bound from Eqn. (2-13) respectively.

The corresponding USGS gage ID for the catchments are, a) 5123400, b) 3241500, c) 6447000, d) 6917000, e) 9505350, f) 2481000, g) 3173000, h) 1413500, i) 2212600, j) 1162500, k) 11162500, and l) 14325000.

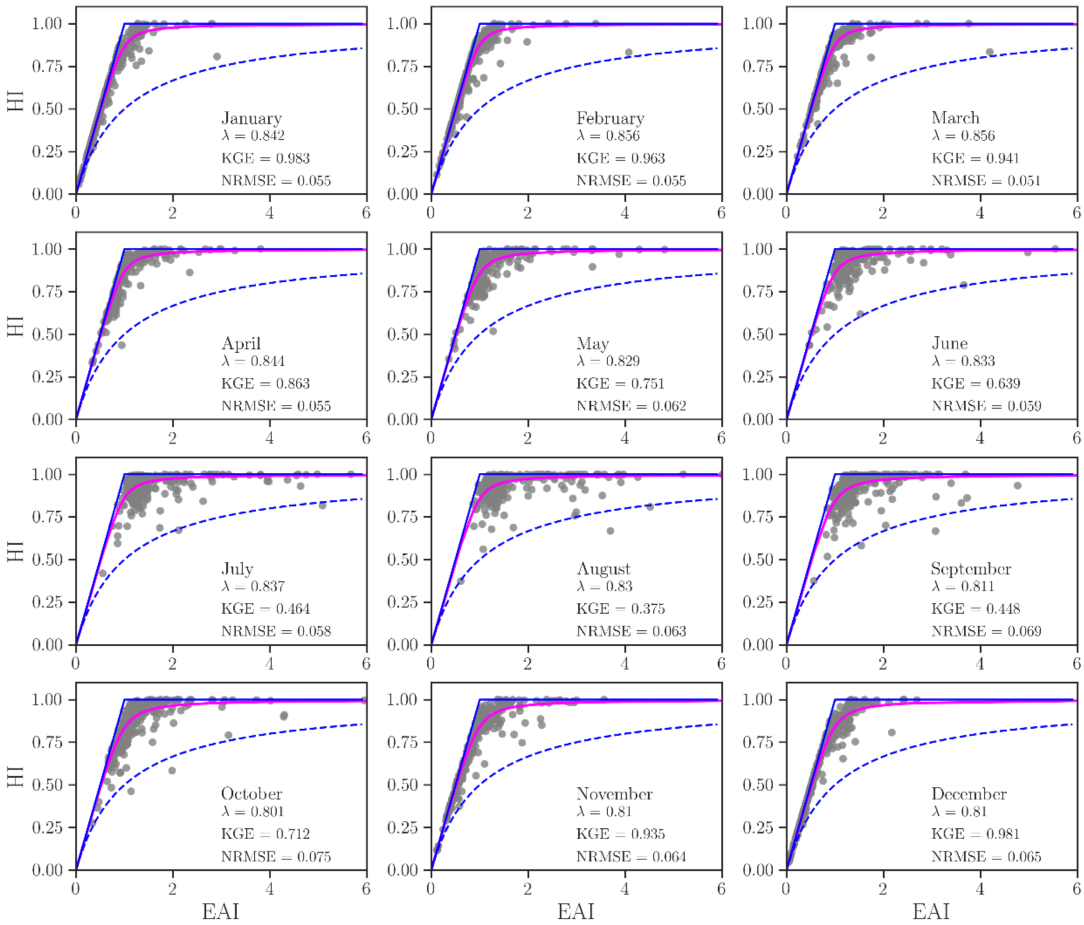


Figure 2-11: Intra-annual variability of mean-monthly HI between catchments. The magenta, solid blue, and dashed blue lines correspond to the best-fitted, upper-bound, and lower bound curves using Eqn. (2-13) respectively.

### 2.5.2 Space-Time Similarity in the Increasing Rate of HI with EAI

So far, we have verified the increase of $HI$ with $EAI$ both theoretically (based on Eqn. (2-13)) and empirically (using the "estimated" $HI$ and $EAI$ values) with a space-time similarity. Next, we examine the spatiotemporal variability of the changing rates of $HI$, or the slopes in the $HI\sim EAI$ relationships, quantified using $d(HI)/d(EAI)$ as in Eqn. (2-14).

Figure 2-12 shows the $d(HI)/d(EAI)$, or slope values of the $HI\sim EAI$ relationships at the long-term or annual scales corresponding to Figure 2-7. We first divide all the "estimated" $HI\sim EAI$ values in Figure 2-7 into several bins, each bin containing ten pairs of "estimated" $HI \sim EAI$ values. We then perform a linear regression within each bin, and the resulting slope is used as the estimated $d(HI)/d(EAI)$ value, shown as one dot in Figure 2-12. Note that we test the bin size from 5 to 10 for different data sizes, and the patterns remain similar. We, therefore, use a bin size of ten in the rest of the Figures. The theoretical curves in Figure 2-12 are derived based on Eqn. (2-12) using the same $\lambda$ values as in Figure 2-7.

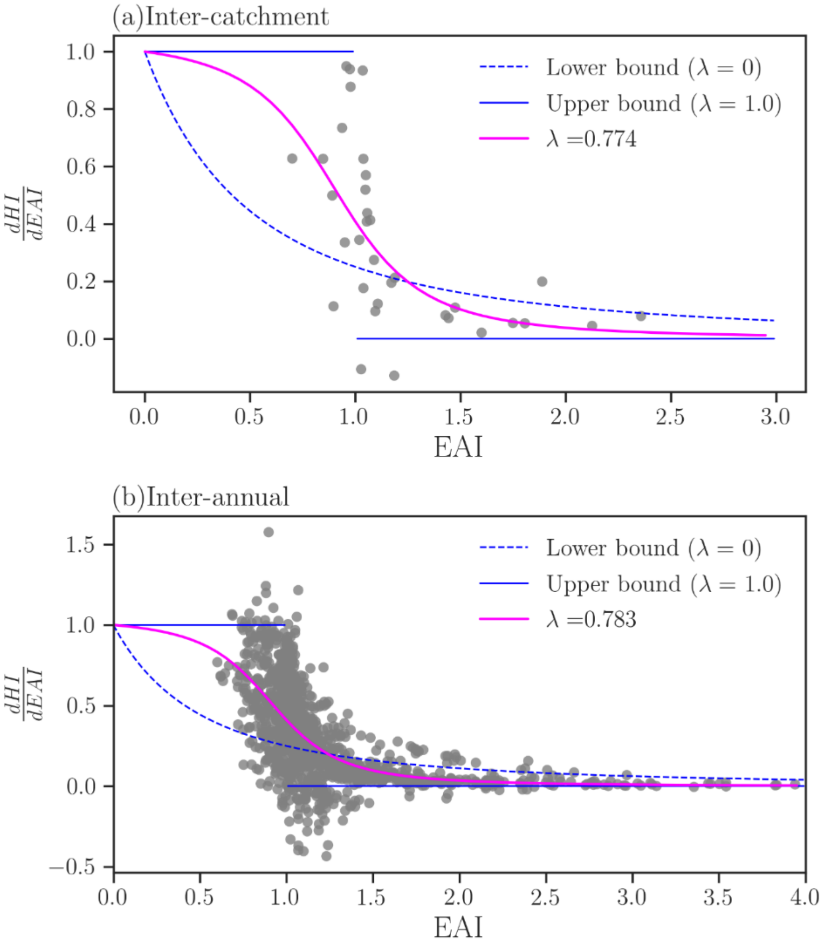


Figure 2-12: Space-time similarity of d(HI)/d(EAI)~EAI relationships at the annual scale across different climatic, topographic, and vegetation regimes. (a) between-catchment (spatial) variability. (b) between-year (inter-annual) variability.

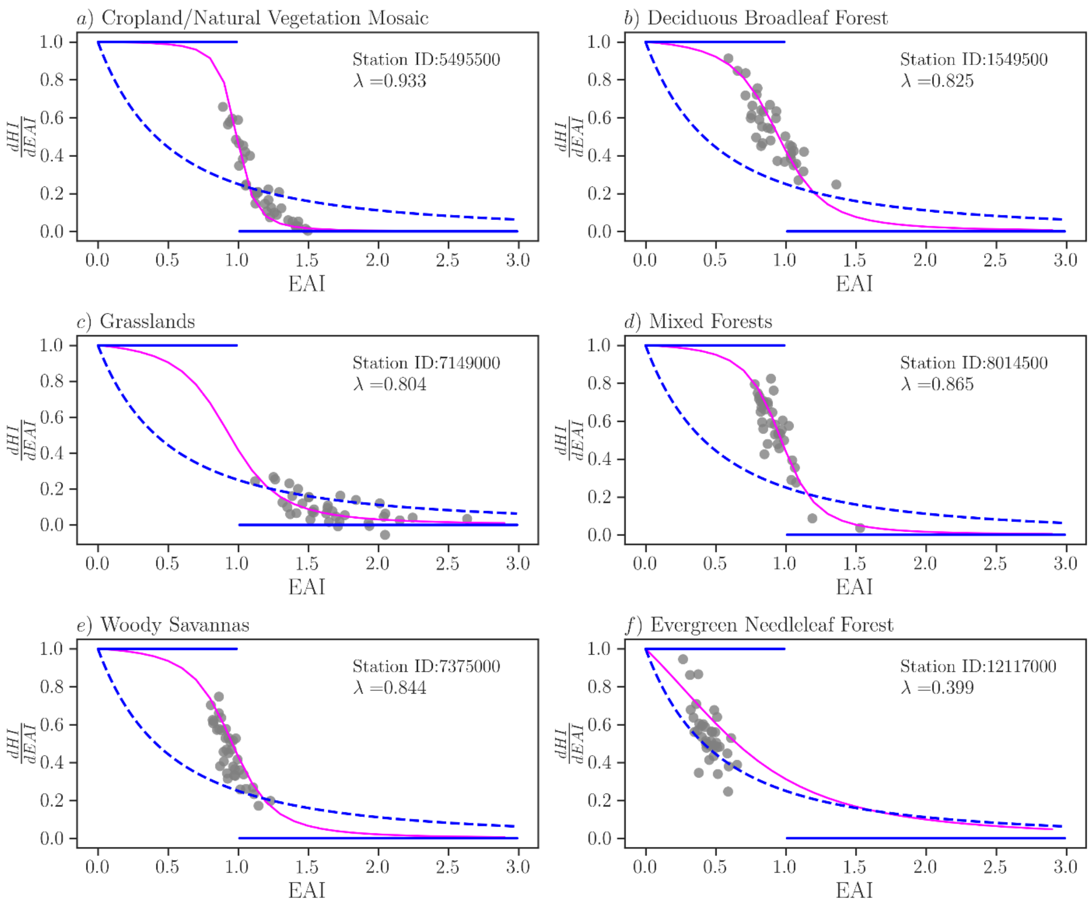


Figure 2-13: d(HI)/d(EAI)~EAI relationships at the monthly scale. A bin size of ten is used to compute the empirical d(HI)/d(EAI). The best-fitted (magenta), upper-bound (solid blue), and lower bound (dashed blue) curves.

Figure 2-12 suggests that $d(HI)/d(EAI)$ decreases with $EAI$ in a space-time similar way, i.e., it decreases both from wetter to drier catchments and from wetter to drier years, but following the same decreasing pattern. This $d(HI)/d(EAI)$ decreasing pattern can be roughly characterized as an S-shape and divided into three stages: 1) $d(HI)/d(EAI)$ decreases slowly and remains relatively high for $0 \leq EAI < \sigma_1$; 2) $d(HI)/d(EAI)$ decreases quickly for $\sigma_1 \leq EAI < \sigma_2$; and 3) $d(HI)/d(EAI)$ decreases slowly but remains relatively low for $EAI > \sigma_2$. $\sigma_1$ and $\sigma_2$ are divisions between the three stages and cannot be accurately defined since the transitions from Stage 1 to 2 and from State 2 to 3 are both gradual instead of abrupt. There are some dots in Figure 2-12 beyond the theoretical upper ($d(HI)/d(EAI) = 1$) or lower ($d(HI)/d(EAI) = 0$)

limits, and we attribute these to the uncertainties embedded in the CAMELS data. We do not produce a $d(HI)/d(EAI)$ plot corresponding to Figure 2-8 using the same binning method because the number of $HI \sim EAI$ pairs is too small.

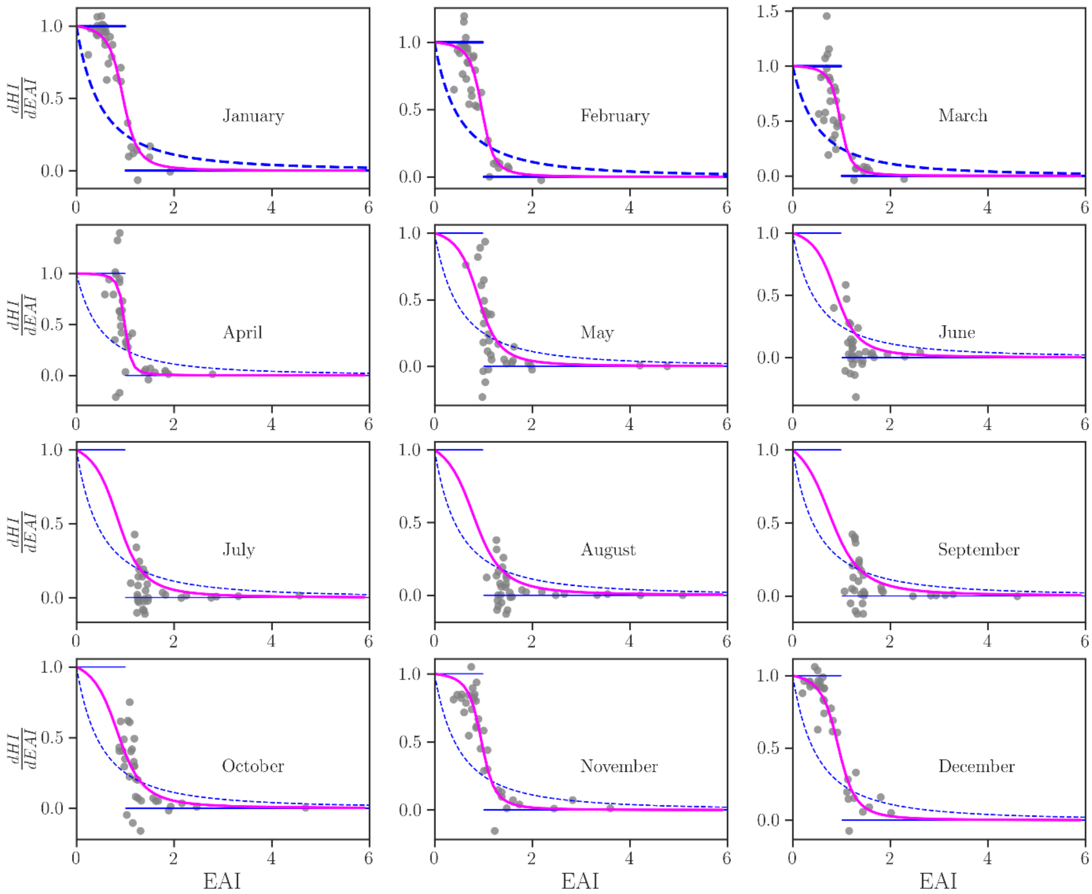


Figure 2-14: Space-time similarity: d(HI)/d(EAI)~EAI of monthly means of the HI across spaces. A bin size of ten is used to compute the empirical d(HI)/d(EAI). The best-fitted (magenta), upper-bound (solid blue), and lower bound (dashed blue) curves.

Figures 2-13 and 2-14 examine the $d(HI)/d(EAI)$, or slope values of the $HI \sim EAI$ relationships at the monthly scale corresponding to Figures 2-10 and 2-11, respectively. Similar to Figure 2-12, the $d(HI)/d(EAI)$ values decrease with $EAI$ following an S-shape pattern across both time (Figure 2-13) and space (Figure 2-14), hence suggesting a space-time similarity at the monthly scale.

## 2.6 Summary and Conclusions

In this study, we present an analytical framework of HI as a single function of ecological aridity index (EAI) (see Figures 2-1 to 2-2) based on the Generalized Proportionality Hypothesis. We successfully validate it over the long-term, annual, and monthly scales across various regimes of climate, vegetation, soil, and topography (see Figures 2-3 to 2-6). $\lambda$, as a direct indicator of catchment wetting (or effective water storage) partitioning, is no less than 0.5 over most of the 343 catchments over the contiguous United States, indicating the importance of catchments' initial responses to storm events in the form of direct evaporation from vegetation interception and ground surface and transpiration from the shallow root zone. We suggest that different biome regimes exert different levels of control on not only partitioning of catchment wetting (or total water storage) into vertical vaporization and lateral baseflow but also partitioning of vaporization into initial and continuing components.

Facilitated with this analytical framework, we find that there is an emergent space-time similarity between the regional (inter-catchment) and intra-annual variability of HI, expressed in terms of the $HI{\sim}EAI$ relationships. The space-time similarity of HI's intra-annual variability appears to resemble that of HI's inter-annual variability (see Figures 2-7 to 2-10), suggesting that HI increases from wetter to drier places, years, or months in a similar fashion. The analytical framework can explain these space-time similarity patterns in a unified way, i.e., HI increases with EAI following a similar curve provided by Eqn. (2-13). More interestingly, we find that this space-time similarity also exists in the slopes of the $HI{\sim}EAI$ relationships, quantified by an S-shaped curve of $d(HI)/d(EAI){\sim}EAI$ relationship given by Eqn. (2-14). Under very dry conditions, HI approaches its theoretical maximum, 1.0, but with decreasing regional or temporal (inter-and intra-annual) variability in a space-time symmetric fashion. Eqn. (2-14) thus shed some light on the previous finding of HI's inter-catchment and inter-year constancy (Horton, 1933; Troch et al., 2009) under dry conditions and further extend it to HI's intra-annual variability for different biome regimes.

This analytical framework opens the door and/or paves the way to many exciting opportunities to advance our understanding of water-plant-soil-climate interactions, including but not limited to:

- HI is a better indicator than AI for vegetation water use. HI captures the partitioning of soil moisture storage, which is directly available to vegetation. AI (in the framework of the Budyko formula) captures the partitioning of precipitation into runoff and E, and the runoff part includes surface runoff which is not available to vegetation. The analytical framework of HI can thus be a useful tool to explore quantitative connections between ecohydrology and hydrology at the catchment scale (e.g., over a few catchments) or regional scale (e.g., over a large number of catchments in a region).
- In this study, we assume that GPH is valid at the monthly scale for the partitioning of catchment wetting into vaporization and baseflow. We validate this assumption by showing empirical evidence that our analytical framework has successfully reproduced intra-annual variability of HI across over 340 catchments. It is nevertheless worthy to further explore to what extent GPH can be applied. Given the fact that the SCS-CN method is essentially applicable at the event scale, it is feasible to explore whether and how GPH can be applied to the 2$^{nd}$-stage of hydrologic partitioning at the event scale and how vegetation may play a role in it.
- This analytical framework can be used as a first-order constraint to the simulated ecological and hydrological responses from the hydrological, land surface, and

earth system models, helping prompt a balanced, effective representation of hydrological and ecological processes and their interactions and hence reducing the simulation uncertainties.

- Our analytical framework may be used to improve the parameterization of hydrologic models due to its common theoretical basis with the SCS-CN method, i.e., GPH. Furthermore, the SCS-CN method is suggested to have a similar physical basis to the *abcd* model (Wang and Tang, 2014) and Variability Infiltration Model (Wang, 2018). There is thus a promising potential to help better estimate the runoff parameters, for instance, according to dominant vegetation cover in each of the spatial units in these models.
- The emergent space-time similarity patterns may be used as empirical evidence to advance our understanding of Horton's hypothesis that vegetation practices maximization of productivity relative to available water (Horton, 1933). Despite the highly nonlinear vegetation dynamics and spatiotemporal heterogeneity in climate, soil, and topographic conditions, it appears that vegetation maximum productivity may function as an organizing principle and lead to a convergence of plant-soil-atmosphere interactions, which manifests in the form of emergent patterns presented here.

We suggest that the analytical framework and emergent patterns have important implications for improving the understanding and modeling of ecological and hydrological processes and their interactions at the catchment and larger scales. More broadly, the findings from this study suggest the promising potential of the Horton Index as a conceptual yet quantitative framework for exploring the links between catchment water balance and vegetation dynamics across multiple scales in space (catchment to regional scales) and time (event to long-term scales).

# 3 Evapotranspiration and Vegetation Carbon-Uptake Relationship at Catchment Scale[2]

## 3.1 Introduction

The carbon and hydrological cycles are tightly coupled via ecosystem processes of photosynthetic carbon assimilation and evapotranspiration (ET), a process mediated directly by stomatal conductance (Fatichi et al., 2016; Gentine et al., 2019; Luke Smallman and Williams, 2019). Gross primary production (GPP) is the carbon production rate of photosynthesis, which needs solar energy, carbon dioxide ($CO_2$), and water. ET consists of plant transpiration, evaporation from canopy intercepted water, evaporation from open water surfaces and soil, and cycles precipitation back to the atmosphere. Photosynthesis needs access to $CO_2$, which is controlled by leaf stomata. Stomatal opening results in $CO_2$ and water exchanges between leaves and the ambient atmosphere and the coupling between carbon and water interactions of plants(Fatichi et al., 2016). The water loss through transpiration depends on accessible soil moisture, which is associated with root biomass and the vertical profile of roots. In other words, plant carbon–water coupling is also related to the soil–root interface. Thus, the GPP and ET relationship is an indicator of ecosystem function and meaningful to the predictions of the terrestrial ecosystems in response to global environmental changes(Bonan and Doney, 2018).

State-of-the-art terrestrial biosphere models (TBMs), which solve radiative transfer, stomatal conductance, and electron transport, provide a process-oriented representation of the coupling between carbon and water cycles at the leaf scale(Harper

[2] This work is in preparation to be submitted for publication to Water Resources Research as: Abeshu, G. W., Li, H., Shi M., Brookshire, J., Tang, J., Xu, C, McDowell, N., and Leung, L.R., A unified functional relationship for linking catchment water balance and vegetation carbon-uptake

et al., 2016; Oleson et al., 2010; Smallman et al., 2013). However, scaling carbon and water fluxes from leaf level to canopy level is increasingly complex due to the non-linear variations of light, temperature, momentum, water, $CO_2$, and other factors(Bonan et al., 2018; Nolan et al., 2017). These non-linear interactions could also induce the carbon and water estimate uncertainty of TBMs. Further, performing TBM simulations at varied temporal and spatial resolutions to understand carbon–water interactions consumes significant time and computational resources. Given that flux tower measurement (Baldocchi et al., 2001; Novick et al., 2018; Pastorello et al., 2020), measurements at watershed scales (Addor et al., 2017), and satellite observations(Joiner and Yoshida, 2020; Jung et al., 2019; Robinson et al., 2018) are increasingly providing carbon and water flux related products. It is essential to use the existing tremendous amount of data to estimate the GPP and ET relationships in ecosystems with varied stomatal and root dynamics.

The studies of GPP–ET interaction at the catchment scale and varied temporal resolutions are essential to understanding carbon–water dynamics but are limited. Previous studies across different sites confirm that GPP and ET are linearly related(Beer et al., 2009; Zhang et al., 2016; S. Zhou et al., 2014). Establishing this GPP–ET relationship at tree and patch scales is less limited because observational data at these scales have consistent observational timing and temporal resolutions. Mechanistic understanding of GPP–ET relationships at larger scales (e.g., catchment or regional scales) is limited by increased surface complexity, which is associated with the spatial heterogeneity of vegetation cover.

Catchments adapt to the climate through soil-water-vegetation coevolution. At the inter-annual scale, fundamental biome-defining features such as vegetation, soil, and geology exert less control on the soil water partitioning process, while climate imposes first-order control (Abeshu & Li, 2021; Budyko, 1974; Horton, 1933; Troch et al., 2009). Hence, the static nature of vegetation representation, which is often a type of vegetation, could be considered sufficient for annual and intra-annual scale process understanding. The importance of physical factors influencing temporal vegetation dynamics, including climate, vegetation types, and topographic characteristics, manifests at the sub-annual scales. Hence, vegetation dynamics influence is also noticeable at sub-annual scales. Intra-annually, vegetation is dynamic, and transpiration is its first-order physiological link to the hydrologic partitioning process. Intra-annually, vegetation is dynamic, and transpiration is its first-order physiological link to the hydrologic partitioning process. Temporal patterns of the carbon taken up at the expense of water hydraulically lifted from the soil escaping through stomata govern vegetation's dynamic nature (Katul et al., 2012; Zhang et al., 2016b). However, these characteristics are rarely reflected in most simple hydrologic models.

There are three approaches to advance the understanding of GPP–ET interactions: (i) develop theoretical/empirical functions linking water balance and carbon uptake directly at the catchment scale, (ii) establish a scaling framework between patch- and catchment- scales, and (iii) the combination of (i) and (ii). While the availability of extensive observation data in recent decades makes the first approach a possibility, the lack of understanding of whether site-level water-carbon processes behave similarly at a catchment scale or not makes it a difficult task to undertake. Thus, we have three primary goals in this study. The first goal is to evaluate the linearity between GPP and ET at the catchment scale using an exploratory data analysis of 380 catchments distributed across climate and landscape gradients of contagious US. Second, we want to develop a unified functional framework between GPP and ET and then explore methods of estimating the function parameters from catchment characteristics, thereby avoiding calibration. Finally, we will use the unified functional framework, which can provide a generalized explanation of GPP–ET variations, seasonality, spatially, and factors controlling GPP–ET interactions. The remainder of this chapter is organized as follows: Section 3.2 describes the data, and Section 3.3 introduces the unified functional framework. Section 3.4 describes the validation results and the emergent patterns of functional frameworks. Sections 3.5 and 3.6 are discussions and conclusions, respectively.

## 3.2 Data

This study uses the catchments information from the Catchment Attributes and Meteorology for Large-Sample Studies (CAMELS) dataset (Addor et al., 2017; Newman et al., 2015). CAMELS dataset provides hydrometeorological observations, such as precipitation, actual vapor pressure, shortwave solar radiation, minimum temperature, maximum temperature, and streamflow for more than three decades (1982 to 2014). It also comprises the ET product covering the same period; it is an output from the integrated Snow-17/SAC-SMA model(Burnash, 1995; Addor et al., 2017). Catchment attributes, including dominant vegetation type, the cover fraction of this type, and Green Vegetation Fraction (GVF) difference, are also available from CAMELS. GVF difference is the difference between the maximum and minimum monthly mean of the vegetation cover fraction of a catchment.

Catchment GPP is from Landsat GPP product over CONUS (Robinson et al., 2018). We preferred Landsat GPP because it has a 36-year observational time period (1986-2021), and the time coverage overlaps with the CAMELS dataset for 29 years. Landsat GPP has a spatial resolution of 30 meters and a temporal resolution of 16-days. The vegetation phenology data is from USGS-AVHRR; it has a spatial resolution of 1 km and is available annually from 1989 to 2010. Figure 3-1 provides a summary of catchment data used in this study, and the following nine steps describe the processes of data preparation and quality control:

1) The CAMELS dataset provides an integrated Snow-17/SAC-SMA model output for ten optimal parameter sets. We collected the daily ET produced with each parameter set and computed the daily ensemble mean ($ET_{ensemble}$).

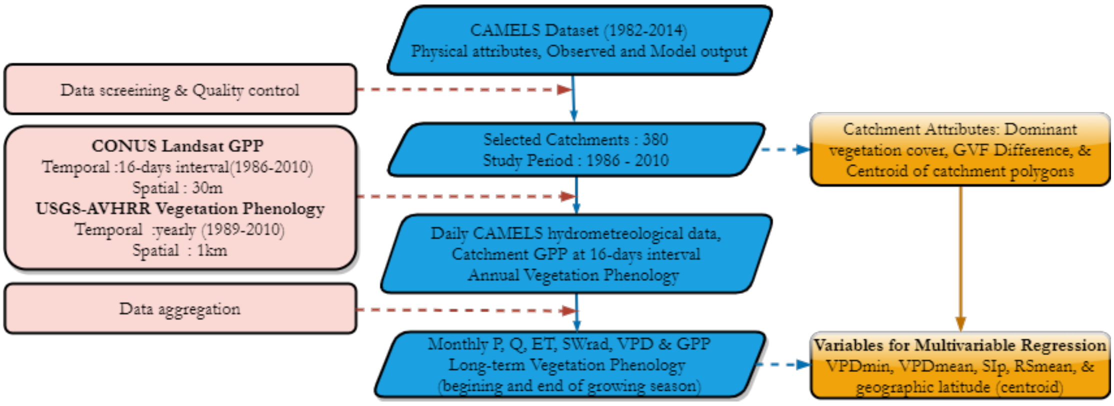


Figure 3-1: Catchment data used in this study

2) The ensemble annual mean ET ($\overline{ET}_{ensemble}$) is then compared against observed annual mean ET ($\overline{ET}_{obs}$) using percent error. Observed annual mean ET is annual mean precipitation minus annual mean runoff. Runoff is the flow rate ($m^3/s$) converted to depth (mm/day). Percent error is the ratio of model output bias ($|\overline{ET}_{obs} - \overline{ET}_{ensemble}|$) to $\overline{ET}_{obs}$ in percent. Catchments with less than ten percent error are declared usable for our objectives.

3) Using drainage area polygons, we masked the LandSat GPP spatial maps from 1986 to 2014 (only for catchments selected in (2)). This yielded a time series of GPP spatial maps for each catchment at 16-days intervals. Catchment scale GPP is computed as the spatial average, and we converted the 16-day sum time series to a monthly one, assuming each day contributed to the 16-days sum equally.

4) We identified 1986-2010 as the study period during which all hydroclimatic variables and Landsat GPP data are continuously available (i.e., no missing data) for most of the catchments selected in (2). Filtering out catchments with missing data, we obtained 392 catchments.
5) We define a dominant vegetation cover as a single vegetation type covering at least 50% of the drainage area. Hence, we excluded catchments that do not meet this criterion and obtained 380 catchments with drainage areas ranging from 6.25 to 25,818 $km^2$ (Fig. 3-2).
6) The USGS-AVHRR vegetation phenology data (the start and end of the growing period) are available from 1989 to 2010. To generate the long-term phenology map of CONUS, we used the median values of the start and end of the growing period in each data pixel (1 km) from 1980 to 2010. We then apply the drainage area polygons of catchments from (5) to the CONUS phenology map. We use the $30^{th}$ and $70^{th}$ percentile across the catchment phenology map pixels to decide a single start and end of the growing period, respectively. The $30^{th}$ percentile for the start of the growing period map implies that the growing period has started for at least 30% of the catchment area. In contrast, the $70^{th}$ percentile for the end of the growing period map indicates that the growing period has ended for at least 70% of the catchment area.
7) For convenience, we grouped the 380 catchments into six groups based on dominant vegetation type, resulting in three forested and three non-forested catchment groups (Table 3-1). Forested catchments comprise Deciduous Broadleaf (DBF) (89), Evergreen Forest (Needle leaf + Broadleaf) (EF) (25), and Mixed Forests (MF) (50) dominated catchments. Croplands plus Croplands/Natural Vegetation Mosaic (CL/NVM) (109), Grasslands (GL) (47), and a combination of Savannas, Woody

Savannas, and Open/Closed Shrublands, hereafter WS-SL catchments (60) make up the three non-forested catchments.

Table 3-1: Catchments group based on dominant vegetation type.

| Group | Vegetation type(Count) | Group Name | Count |
|---|---|---|---|
| 1 | Deciduous Broadleaf(89) | DBF | 89 |
| 2 | Evergreen Neadleaf Forest(22)<br>Evergreen Broadleaf Forest(3) | EF | 25 |
| 3 | Mixed Forests(50) | MF | 50 |
| 4 | Croplands(46)<br>Croplands/Natural Vegetation Mosaic(63) | CL/NVM | 109 |
| 5 | Savannas(4)<br>Woody Savannas(46)<br>Open Shrublands(7)<br>Closed Shrublands(3) | WS-SL | 60 |
| 6 | Grasslands(47) | GL | 47 |

8) Vapor Pressure Deficit (VPD) represents the difference between actual and saturation vapor pressure, and we calculate VPD to study the water deficit of plants. The daily actual vapor pressure data is from the CAMELS dataset, and we calculated the saturation vapor pressure with Magnus' formula (Parish and Putnam, 1977). Input for the Magnus formula is air temperature. We computed the daily saturation vapor pressure as a mean of saturation vapor pressure at maximum and minimum air temperatures.
9) Further, we use flux tower GPP and latent heat flux for site-level validations of the developed functions. Data within the CONUS were collected from the FLUXNET dataset (Pastorello et al., 2020). We selected 14 stations with a minimum of ninety-six months of GPP and latent heat data. The latent heat flux is converted to ET for consistency with catchment data. A description of the fourteen sites is provided in Table 3-2.

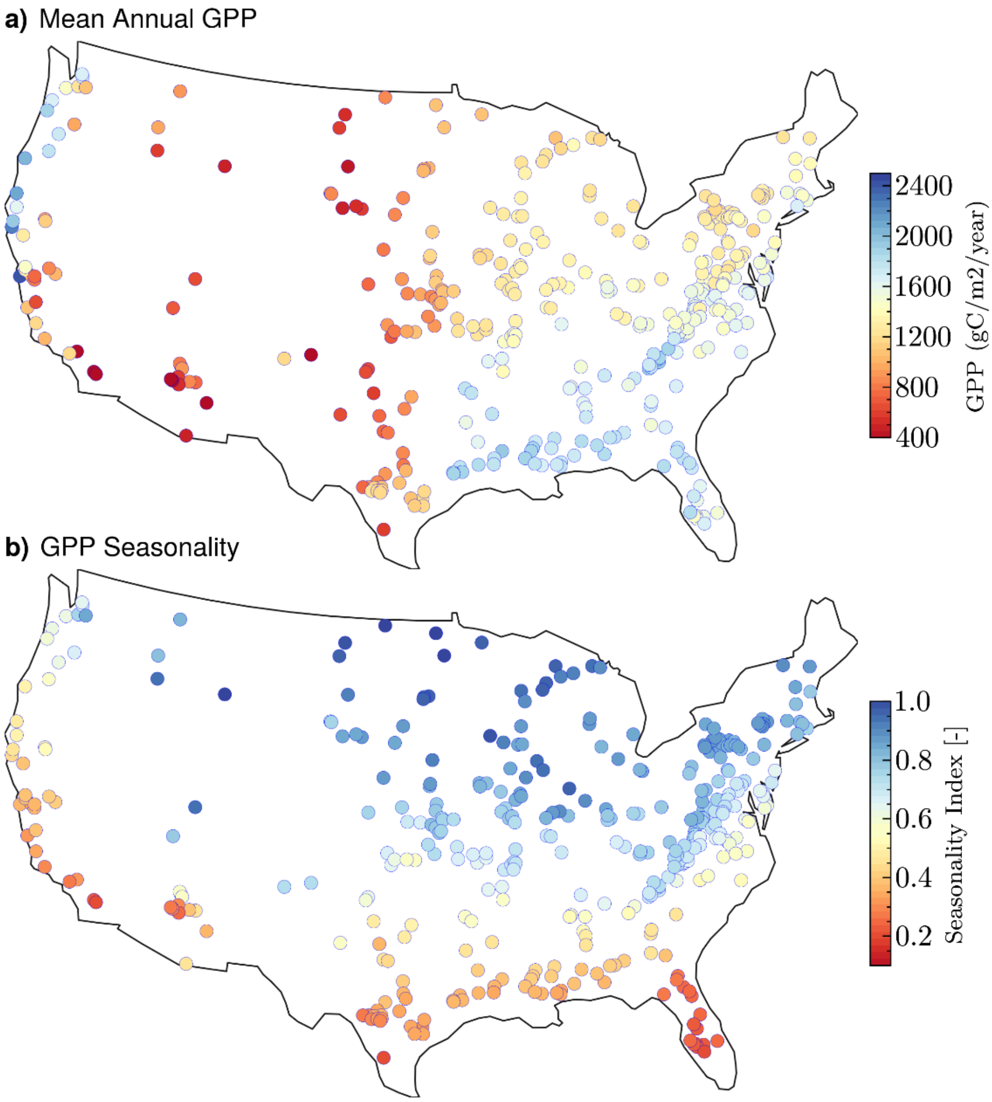


Figure 3-2: Catchments long-term GPP characteristics: (a) long-term annual carbon uptake computed from 25 years (1986-2010) of Landsat GPP data, (b) GPP seasonality computed from long-term mean monthly.

Table 3-2 : FLUXNET2015 sites used in this study

| | Lat | Lon | ID | Vegetation Cover | Period of Record |
|---|---|---|---|---|---|
| 1 | 36.606 | -97.488 | US-ARM | Croplands | 2003-2012 |
| 2 | 41.165 | -96.477 | US-Ne1 | Croplands | 2001-2012 |
| 3 | 41.165 | -96.47 | US-Ne2 | Croplands | 2001-2012 |
| 4 | 41.180 | -96.44 | US-Ne3 | Croplands | 2001-2012 |
| 5 | 41.841 | -88.241 | US-IB2 | Grasslands | 2004-2011 |
| 6 | 38.413 | -120.95 | US-Var | Grasslands | 2002-2013 |
| 7 | 31.737 | -109.94 | US-Wkg | Grasslands | 2004-2014 |
| 8 | 31.821 | -110.87 | US-SRM | Woody Savannas | 2004-2014 |
| 9 | 38.432 | -120.97 | US-Ton | Woody Savannas | 2001-2014 |
| 10 | 38.895 | -120.63 | US-Blo | Evergreen Needleleaf Forests | 1997-2007 |
| 11 | 44.452 | -121.56 | US-Me2 | Evergreen Needleleaf Forests | 2002-2014 |
| 12 | 41.555 | -83.844 | US-Oho | Deciduous Broadleaf Forests | 2004-2013 |
| 13 | 31.744 | -110.05 | US-Whs | Open Shrublands | 2007-2014 |
| 14 | 39.323 | -86.413 | US-MMS | Deciduous Broadleaf Forests | 1999-2014 |

## 3.3 Methods

### 3.3.1 Unified GPP- ET Functional Framework at Catchment Scale

To develop a universal functional between GPP and ET at the catchment scale, we make two fundamental assumptions; i) the GPP and ET have a robust linear relationship at the catchment scale, and ii) for a given catchment, the magnitudes of GPP and ET normalized by their corresponding climatological mean are reasonably close. We develop a functional relationship between GPP and ET based on these assumptions. The validity of our assumptions will be evaluated using exploratory data analysis before further use of the functional relationship. We normalized both monthly GPP and ET with their corresponding long-term mean to remove the effect of differences in catchment vegetation covers. Then, based on our assumptions, we generalize that the normalized magnitudes are approximately equal and described as

$$\frac{\mathrm{GPP_m}}{\overline{\overline{\mathrm{GPP}}}} \cong \frac{\mathrm{ET_m}}{\overline{\overline{\mathrm{ET}}}}. \tag{3-1}$$

The subscript $\boldsymbol{m}$ indicates the month, and the over-line (i.e., $\overline{GPP}$, $\overline{ET}$ ) indicates the long-term mean. We can utilize the expected immerging patterns between the two ratios relationships to transform the Eqn. (3-1) approximation sign to equality. First, because all linear relationships have a y-intercept, we introduce parameter $\boldsymbol{b}$ as the intercept; this will serve two scenarios; a relationship where intercept zero and nonzero. Secondly, ET is an aggregate of plant, soil, and open-surface vaporization. Plant contribution (i.e., transpiration) is only a fraction of ET. We represent transpiration as $\boldsymbol{a}ET$, where $\boldsymbol{a}$ is the vaporization partitioning coefficient and ranges 0-1. The bounds 0 and 1 imply no contribution and total contribution by vegetation, respectively. Substituting the two adjustments in Eqn. (3-1) and rearranging for $GPP_m$, we get

$$\mathrm{GPP_m} = \frac{\overline{\mathrm{GPP}}}{\overline{\mathrm{ET}}}(\mathrm{aET}_{\mathrm{m}} + \mathrm{b}\overline{\mathrm{ET}}). \tag{3-2}$$

The ratio of $\overline{GPP}\ to\ \overline{ET}$ is universally known as the long-term ecosystem water use efficiency at a monthly scale; we designated it as $c$ and obtained

$$\mathrm{GPP_m} = \mathrm{acET_m} + \mathrm{bc}\overline{\mathrm{ET}}. \tag{3-3}$$

We further represent $ac$ and $bc$ as $\beta$ and $\alpha$, respectively. Which yields a functional model with all the uncertainties compressed into the two parameters as

$$\mathrm{GPP_m} = \beta\mathrm{E_m} + \alpha\overline{\mathrm{E}}. \tag{3-4a}$$

Equation-3-4a represents a two-parameter functional model representing all catchments, including those where intercept is not essential; hence the name ***unified GPP-ET*** functional relationship. If $\alpha = 0\ and\ \boldsymbol{a} = 1$, it reduces to the traditional ecosystem model for monthly time scale and given by

$$\mathrm{GPP_m} = \beta\mathrm{ET_m}. \tag{3-4b}$$

Where $\beta$ is water use efficiency. Here, we need to define the parameter's value ranges to utilize these functions correctly. Since $\boldsymbol{a} \geq 0$ and $\boldsymbol{c} > 0$, the theoretical lower bound of parameter $\beta$ is 0. We can estimate the upper bound for $\beta$ as the product of maximum $\boldsymbol{a}$ ($a_{max}$=1) and maximum $\boldsymbol{c}$ ($c_{max}$) values, which yields $c_{max}$. The second term, $\alpha\overline{ET}$ is the intercept and can be expressed as $\alpha\overline{E} = bc\overline{ET} = b\overline{GPP}$ . The intercept can be greater or less than zero; however, it generally corresponds to ET=0 (i.e., the dormant period). GPP is generally less than the long-term mean during the dormant months. Hence, one can conclude that the absolute value of the intercept is always less than the long-term mean, and it is reasonable to state that $-\overline{GPP} < b\overline{GPP} < \overline{GPP}$. Dividing all sides by $\overline{GPP}$ we get, $-1 < \boldsymbol{b} < 1$. Taking extreme ends of both $\boldsymbol{b}$ and $\boldsymbol{c}$, we can describe the lower and upper bounds of $\boldsymbol{bc}$ as $-c_{max} < \boldsymbol{bc} < c_{max}$ . The ranges for both parameters are therefore summarized as

$$0 < \beta \leq c_{max} \tag{3-5a}$$

$$\text{and } -c_{max} < \alpha < c_{max} \; . \tag{3-5b}$$

We can determine the maximum long-term ecosystem water use efficiency from a population of observation data. In order to avoid specific catchments with larger magnitudes deciding the overall upper bound, the upper bounds should be computed for each vegetation class. Based on the 380 catchments, we obtained rounded values of 3.70 for DBF, 2.80 for MF, 4.10 for EF, 3.40 for WS-SL, 1.70 for GL, and 2.30 for CL/NVM.

In order to depict the improvement Eqn. (3-4) brings compared to the traditional GPP-ET model where $\alpha = 0$, we simulated GPP with two types of models. Without and with $\alpha$, a one-parameter and two-parameter functions, respectively. For readability, hereafter, we refer to the one-parameter function as ***Model-I*** and the two-parameter function as ***Model-II***. Both functions were calibrated using two-thirds of the data (1986-

2002) and validated over the study period's last one-third (2003-2010). We use Kling-Gupta Efficiency (KGE)(Gupta et al., 2009) as the goodness-of-fit measure.

### 3.3.2 Parameters of the Linear Function

Environmental factors, such as climate, soil, topography, and vegetation, are responsible for some of the fundamental differences in carbon and water dynamics in different ecosystems. Parameters of the proposed function (i.e., function-I and function-II) contain the long-term characteristics of these environmental factors. Hence, the type of GPP-ET linearity for a given catchment might manifest long-term catchment characteristics, including dominant vegetation cover seasonal characteristics and climatic factors as it exerts first-order control on water balance. One can expect the following three cases of relationships between GPP and ET based on the dormant period characteristics, i) intercept < 0 (GPP = 0 & ET > 0), ii) intercept > 0 (GPP > 0 & ET = 0), and iii) intercept = 0 (GPP = ET = 0). The emergence of these characteristics, however, may not be random. Therefore, we aim to identify catchment characteristics responsible for these differences.

More importantly, we can use these environmental factors to develop a multivariable linear regression equation for slope and intercept, which allows us to estimate the parameters a priori and avoid calibration. However, it is also essential to keep the input data required for the regression model minimal to apply the functions in data-limited regions. Therefore, we rely on readily available climatic characteristics, including precipitation, solar radiation, and vapor pressure deficit. Given that geographic locations also manifest through vegetation types and their seasonal patterns, we included the centroid of the catchment polygons as an additional variable. The downside of having closely related variables such as solar radiation and geographic locations is that the regression equation could suffer from multicollinearity. Here, we test for multicollinearity and apply remedial measures if necessary.

### 3.3.3 Statistical Methods

*Seasonality Index (SI)*: The GPP and precipitation seasonality is computed using Walsh & Lawler (1981). SI represents the degree of variability in monthly flux within a year. It is described as the sum of the absolute deviations of the mean monthly value from the monthly mean divided by the mean annual value. The SI value ranges between 0 and 1.83. A value of 0 indicates that all 12 months contribute equally to the annual total, and 1.83 indicates that only one month contributed to the annual total.

*Pearson correlation coefficient (Pearson's r)*: *Pearson's r* is a statistical measure of the strength of a linear relationship between paired data. Its value ranges from −1 to +1, indicating perfect positive and negative association, respectively, while 0 indicates no association. The interpretation according to Evans, (1996) are as follows: $< 0.2$–Very weak, 0.2 to 0.4 – Weak, 0.4 to 0.6 – Moderate, 0.6 to 0.8 – Strong, $\geq 0.8$–Very strong.

*Kling-Gupta Efficiency (KGE)*: We use KGE (Gupta et al., 2009) as the goodness-of-fit measure for calibrating and validating *function-I* and *function-II*. The KGE value ranges between $-\infty$ to +1. KGE = 1 implies a perfect agreement between observed and simulated data.

*Spearman's correlation (Spearman's ρ)*: Spearman's correlation is a statistical measure of the strength and direction of a monotonic relationship between paired data. Its magnitude ranges from −1 to +1, indicating perfect negative and positive monotonic relationships. The general rule of thumb for interpreting Spearman ρ is that 0 to ±0.20 is negligible, ± 0.21 to ± 0.40 is weak, ± 0.41 to ± 0.60 is moderate, ± 0.61 to 0.80 is strong, and ± 0.81 to ± 1.00 is very strong.

*Principal Component Analysis (PCA)*: we use PCA to measure how much of the within vegetation types variability of parameters, **β,** and **α**, can be explained by the collective characteristics of catchment climatic and geographic variables.

*Variance Inflation Factor(VIF)*: Multicollinearity between components of our regression equation is tested using the VIF method (Neter et al., 1983). Generally, a VIF > 5 indicates multicollinearity, and a remedial measure is necessary if any of the variables used in the regression score VIF > 5. In case such issues are detected in our regression, we apply one or both of the following two approaches to resolve it: i) a mean centering approach, where variables mean is subtracted from each catchment's actual values, and ii) we combine variables with high VIF, for instance, by representing them with their arithmetic product.

## 3.4 Results

### 3.4.1 Empirical Evidence of GPP-ET Linearity at Catchment Scale

Catchment vegetation carbon uptake is linked linearly to water balance across climatic and landscape gradients (Fig. 3-3). Evaluation over a 25-year monthly record showed a *Pearson's r* of $\geq 0.6$ and $\geq 0.8$ for 97% and 89% of the 380 catchments, respectively (Fig. 3-3a). Reasons for lower than 0.6 *Pearson's r* values are more likely to indicate one or both of the following, i) the uncertainty in ET estimation from the SAC-SMA model, and ii) the increase in the relative importance of vaporization components other than transpiration. For the growing period (Fig. 3-3b), *Pearson's r* significantly changed (i.e., changed by ± 5% compared to the result from the monthly time series) for 78 catchments only. One would expect *Pearson's r* values to equal or be higher than the time series for the growing period. Primarily because of relatively increased vegetation-water interaction during the growing period. Here, about 67% of the 78 catchments showing significant deviation have higher *Pearson's r* for the growing period. Most of the catchments were the growing period *Pearson's r* decreased relative to that of time series belong two vegetation types: EF (11 catchments) and WS-SL (8 catchments). These vegetation types maintain much of the leaves during the dormancy period. The average GVF difference for these two vegetation types is less than 0.2. Therefore, for these groups, the decrease in the growing period *Pearson's r* compared to the time series could be attributed to the decreased sample size due to dormant season months exclusion.

Overall, the results confirmed that catchment water balance is linked linearly to vegetation carbon uptake to the highest degree, regardless of size, climate, topography, and vegetation type. Verifying that site scale understanding of the GPP-ET relationship can be extended to the catchment scale. On this basis, we present results from the GPP-ET functional models developed in the following section.

### 3.4.2 Unified GPP-ET Functional Model

The two GPP-ET functional relationships were derived based on two basic assumptions: i) the GPP and ET have a solid linear relationship at the catchment scale, and ii) the magnitudes of GPP and ET normalized by their corresponding climatological mean are reasonably close. With the confirmation of the first assumption (see section 3.4.1), the next step is to justify the second assumption. The goodness-of-fit between the normalized GPP and ET time series showed that less than ten percent of the 380 catchments scored $KGE < 0.5$. This result indicates that the normalized ET can reasonably well estimate the normalized GPP across gradients of vegetation types at a monthly scale, validating our second assumption.

However, the KGE between normalized GPP and ET time series is less than 0.8 for ~60% of the catchments. This is statistically insufficient to generalize that the normalized relationship between GPP and ET (Eqn. (3-1)) could represent any given catchment for GPP simulation. Therefore, improvements to Eqn-1 are necessary for using the relationship as a catchment GPP estimator. These validate the steps we took to extend the normalized GPP and ET relationship (Eqn. (3-1)) to *function-I* and *function-II*. We evaluate the performances of the two functions (Eqn. (3-4)and Eqn. (3-5)) during calibration and validation processes. Figure 3-4 presents the results at 380 catchments, with a Cumulative Distribution Function (CDF) plot describing the percent of the 380 catchments at any given KGE value. For example, CDF at KGE = 0.5 indicates the percentage of the 380 catchments with KGE ≤ 0.5.

Overall, *function-I* calibration and validation results show that the function can reasonably well estimate catchment vegetation carbon uptake on a monthly scale (Fig. 3-4a). It performed reasonably well over the validation period with KGE ≥ 0.5 and ≥ 0.8 for ~96% and ~40% of the 380 catchments, respectively. Further, validation period KGE of > 0.5 for 12 of the 14 FLUXNET sites suggests that *function-I* is scale-independent (Fig. 3-4b). However, nearly 60% of our catchment's goodness-fit score (i.e., KGE) is less than 0.8, implying that we cannot conclusively suggest that this function can sufficiently estimate catchment GPP at the monthly scale for any given catchment.

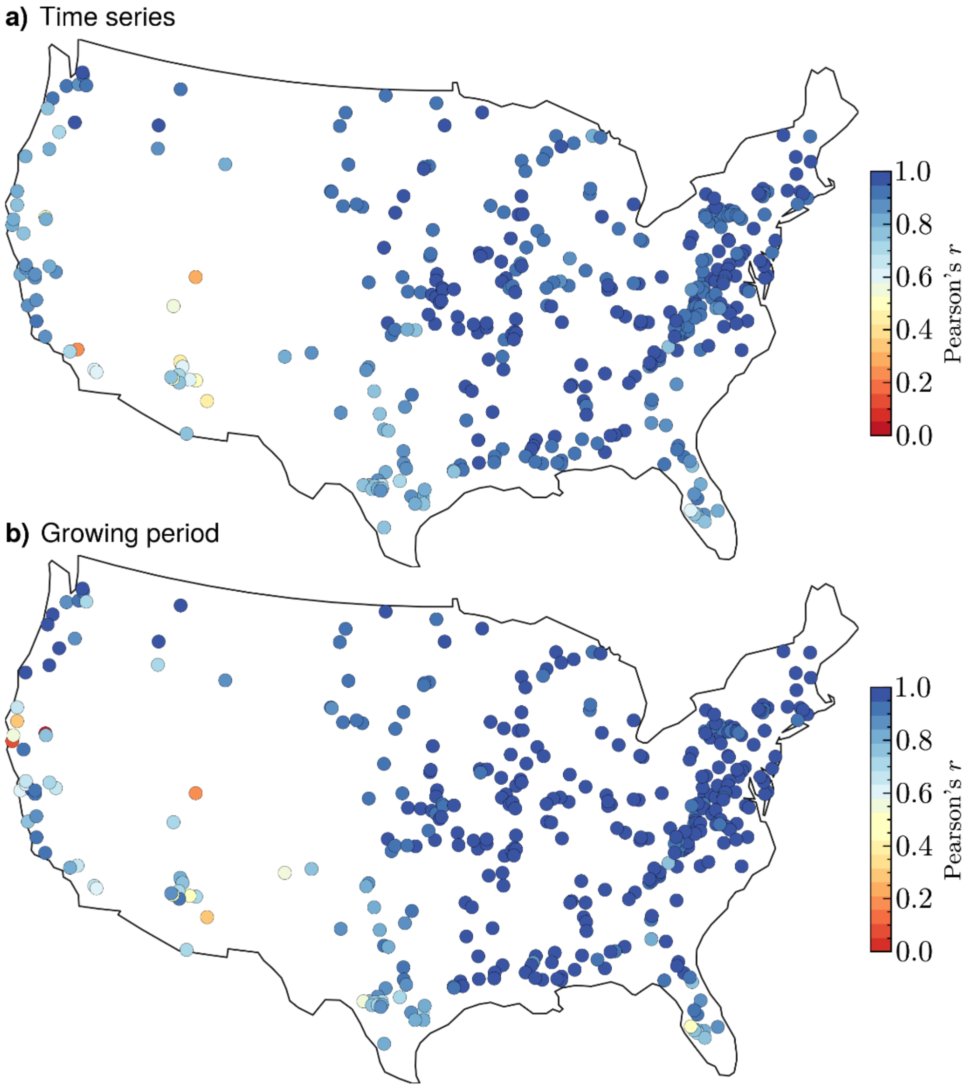


Figure 3-3: Pearson correlation coefficient between GPP and ET from (a) 25 years of monthly data and (b) for growing periods of the 25 years.

With additional components, *function-II* improved *function-I* predicaments significantly, achieving KGE ≥ 0.8 for 85% of our catchment population and increasing the total number of catchments with KGE ≥ 0.9 from just 38 for *function-I* to 200 catchments. The validation KGE for FLUXNET sites is also > 0.6 except for one site (Fig. 3-4b). The performance of *function-II* is temporally and spatially promising. To understand the similarity and differences of the function's properties across different vegetation types, we further explore the physical meaning of the function's parameters and the factors that control the parameters of *function-II*. The following section explores the parameter variability within and across different vegetation types.

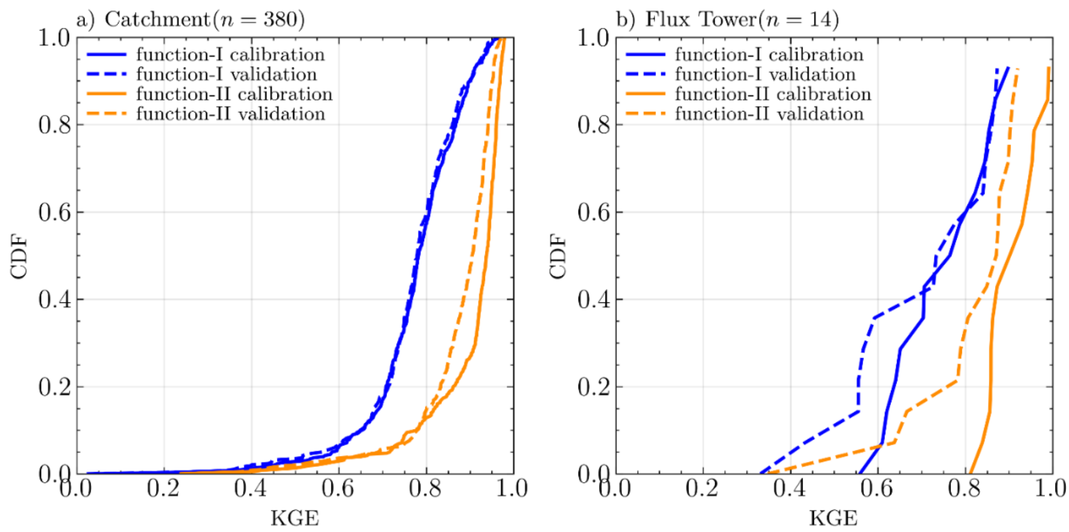


Figure 3-4: Cumulative Distribution Function (CDF) plot of function-I and function-II performance for (a) catchments and (b) at FLUXNET sites.

### 3.4.3 Emerging Patterns

#### a) Variability of GPP-ET relationship: between vegetation types

The two functions comparison showed that introducing the intercept improved the GPP estimates significantly, which is indicated by the increase in catchments with KGE $\geq$ 0.8 from 158 for *function-I* to 333 for *function-II*. Since *Pearson's r* values are positive and generally very strong ($\geq$ 0.8), based on that, we can generalize that the *function-II* intercept corresponds to the dormant period (i.e., low GPP and low ET season). The functions slope represents the gram of carbon taken up by vegetation in one square meter at the expense of one millimeter of water. The spatial patterns of the two parameters agree with the total annual GPP and GPP seasonality (Fig. 3-5). To explore catchment characteristics underlying the magnitudes of the parameters, we group them per dominant vegetation cover type and display their distribution with a boxplot (Fig. 3-6).

From Fig. 3-6a and b, one can notice the differences among vegetation types for both parameters (β and α). For convenience, we classify the slope into four classes as mild ($\beta \leq 1.5$) (93 catchments), moderate ($1.5 < \beta \leq 2.25$)(122 catchments) , steep (2.25

< β ≤ 3.0) (103 catchments) and very steep (β > 3.0) (74 catchments) using the natural breaks in the data as a guide. Excluding the CL/NVM vegetation type (as humans may influence the seasonal patterns of green cover for this type to a certain degree), all non-forested catchments are in the mild to moderate slope class. In contrast, 70% of the forested catchments have β > 2.25, hence fall in the steep to very steep categories. DBF catchments dominate the steep to very steep ranges among the forested catchments, while the EF is mainly characterized by mild to moderate slopes. The MF catchments are reasonably placed between the two (as they represent a mixture of EF and DBF), dominating the moderate – steep ranges. Though CL/NVM catchments are distributed across the four slope classes, two classes account for ~77% of the catchments: ~43% in steep slopes and another ~34% in moderate class. The intercept coefficient varies based on vegetation type (Fig. 3-6b). Since linear relationships intercept are generally correlated with the slope, we analyze the intercept ranges for each slope class. For mild and moderate slope classes, the intercept coefficient is > 0 for ~79% and ~23% of the catchments, respectively. Similarly, ~93% of the steep slope catchments and ~96% of the very steep ones have intercept coefficients less than zero.

GVF difference, a proxy for spatio-temporal vegetation characteristics, explains the differences among vegetation types (Fig. 3-6c). Catchments with a high GVF difference (i.e., significant expansion and contraction of green catchment cover within a year) have a very steep slope. The *function-II* slope is mild in catchments where the GVF difference is low (i.e., only a slight difference between the peak time and dormant period green cover extent). For instance, DBF types possess thick cover at the peak of the growing period but lose their leaves during the dormant period, hence a relatively large green cover difference between peak and dormant season (GVF difference > 0.4).

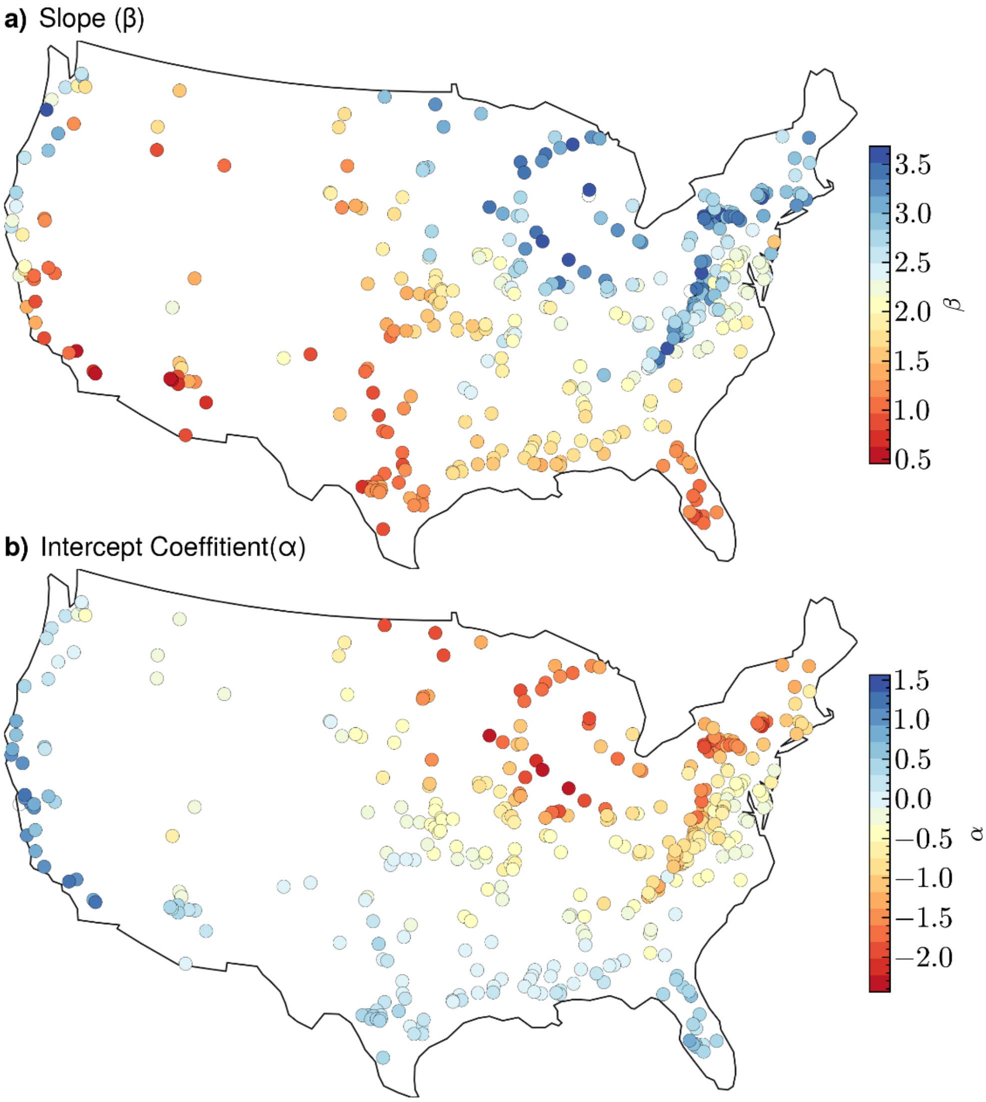


Figure 3-5: Spatial patterns for *function-II* parameters estimated through calibration: a) slope and b) intercept coefficient.

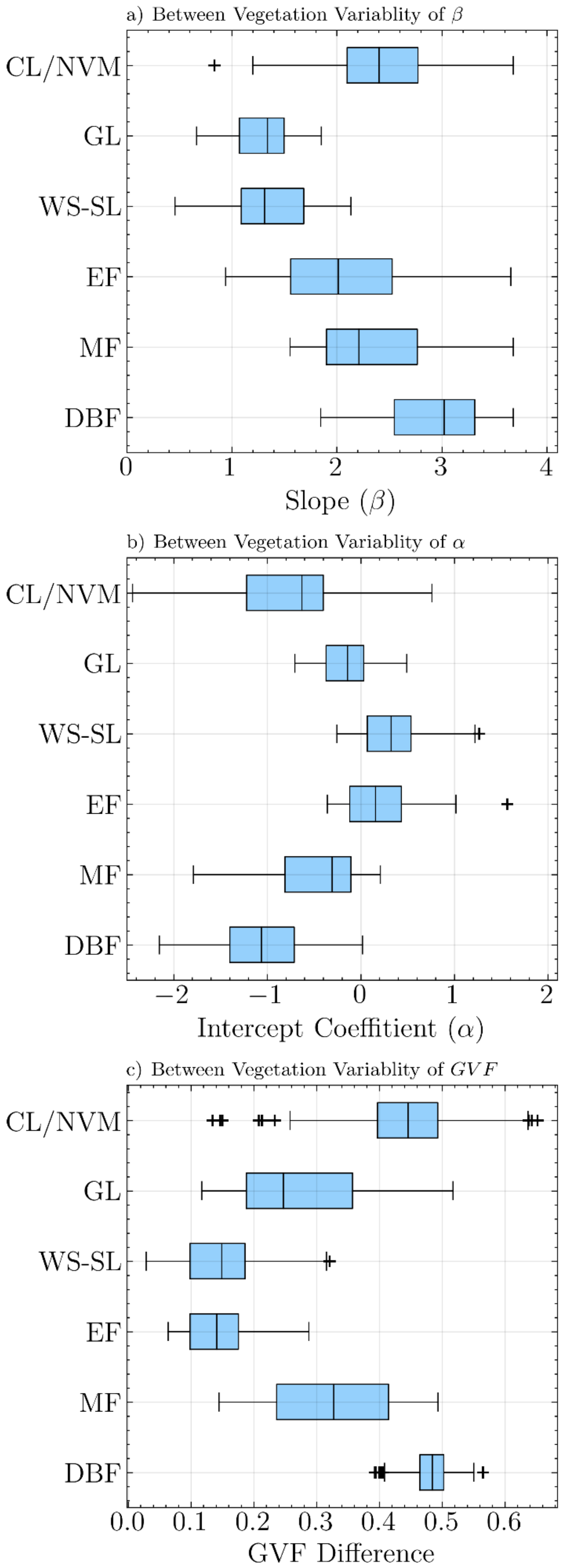


Figure 3-6: Vegetation seasonal dynamics relationship with the parameters of the unified function estimated through calibration.

Hence, the GPP-ET relationship in catchments dominated by DBF is characterized by a steep to a very steep slope and intercept coefficient < 0, this is true for 88 of the 89 DBF catchments. On the other hand, EF and WS-SL retain most of their cover during the dormant periods, hence low GVF difference (GVF difference < 0.2 for 80% of EF and 83% of the WS-SL). These catchments are characterized by intercept coefficients closer to zero and mild to moderate slope classes. Similarly, attributed to the harvesting cycle, cropland-dominated catchments (CL/NVM) have higher GVF differences ( > 0.4 for 79 of the 109 catchments), correspondingly moderate to a steep slope, and intercept coefficient < 0 for >75% of the catchments. GL catchments have a wide range of GVF differences. The low GVF difference (< 0.2 for 30% of the catchments) and the high values (> 0.4 for ~20% of the catchments) could be attributed to perennial and non-perennial grasses respectively.

**b) Variability of GPP-ET relationship: within vegetation types**

The preceding section showed that vegetation phenology (i.e., GVF difference) explains most of the variability in β and α between vegetation types. Further, one can see the systematic similarity in patterns of GVF difference and that of the parameters β and α (Fig. 3-6). This suggests that common underlying factors may be responsible for the patterns. Hence, it is essential to explore factors that control the variability of β and α within each vegetation type.

To explain the within vegetation type variability, we explored environmental and physical factors that affect carbon–water interactions in different ecosystems. These include solar radiation, precipitation, VPD, and the catchment's geographic location. These climatic factors' mean monthly values were summarized using seasonality index, minimum, and mean values. For each parameter (i.e., β and α), we choose those indices that resulted in relatively higher correlation coefficients when evaluated against the parameters of the linear function. Accordingly, we used precipitation seasonality index ($SI_P$), monthly mean shortwave solar radiation (SWrad), monthly mean VPD (VPDmean), and geographic latitude in radian (Latitude) to explore slope characteristics. The same indices are used for the intercept coefficient, except that the monthly mean VPD is substituted with a minimum of the mean monthly VPD (VPDmin). *Pearson's r* values indicate that *function-II* parameters are strongly associated with climatic factors (Fig. 3-7). The regressions are generally linear, suggesting that the selected climatic factors could develop a multilinear regression equation for *function-II* parameters prediction.

Using Spearman's correlation coefficient, we explored if long-term climatic factors ($SI_P$, VPDmin, VPDmean, and SWrad) and geographic location (Latitude) and *function-II* parameters (β and α) show a detectable monotonic relationship. Results show that the importance of the climatic factors varies between vegetation types(Fig. 3-8). For instance, the slope parameter does not show a significant monotonic association with latitude ($|Spearman\ \rho| < 0.4$) for EF and WS-SL, and only slopes of GL and WS-SL catchments showed significant relation to $SI_P$($|Spearman\ \rho| > 0.4$) (Fig. 3-8a). The slope-SWrad relationship showed $|Spearman\ \rho| > 0.4$ for all vegetation types except DBF. Similarly, the intercept coefficient showed a weak to a negligible relationship ($|Spearman's\ \rho| < 0.4$) with SWrad for MF, EF, and WS-SL (Fig. 3-8b). Except for SWrad and WS-SL vegetation type, all variables vary strongly with the intercept coefficient ($|Spearman\ \rho| > 0.6$). Overall, though the importance of these variables differs between vegetation types, we can generalize that their collective characteristics are responsible for the variability of *function-II's* slopes and intercept coefficients in each vegetation type.

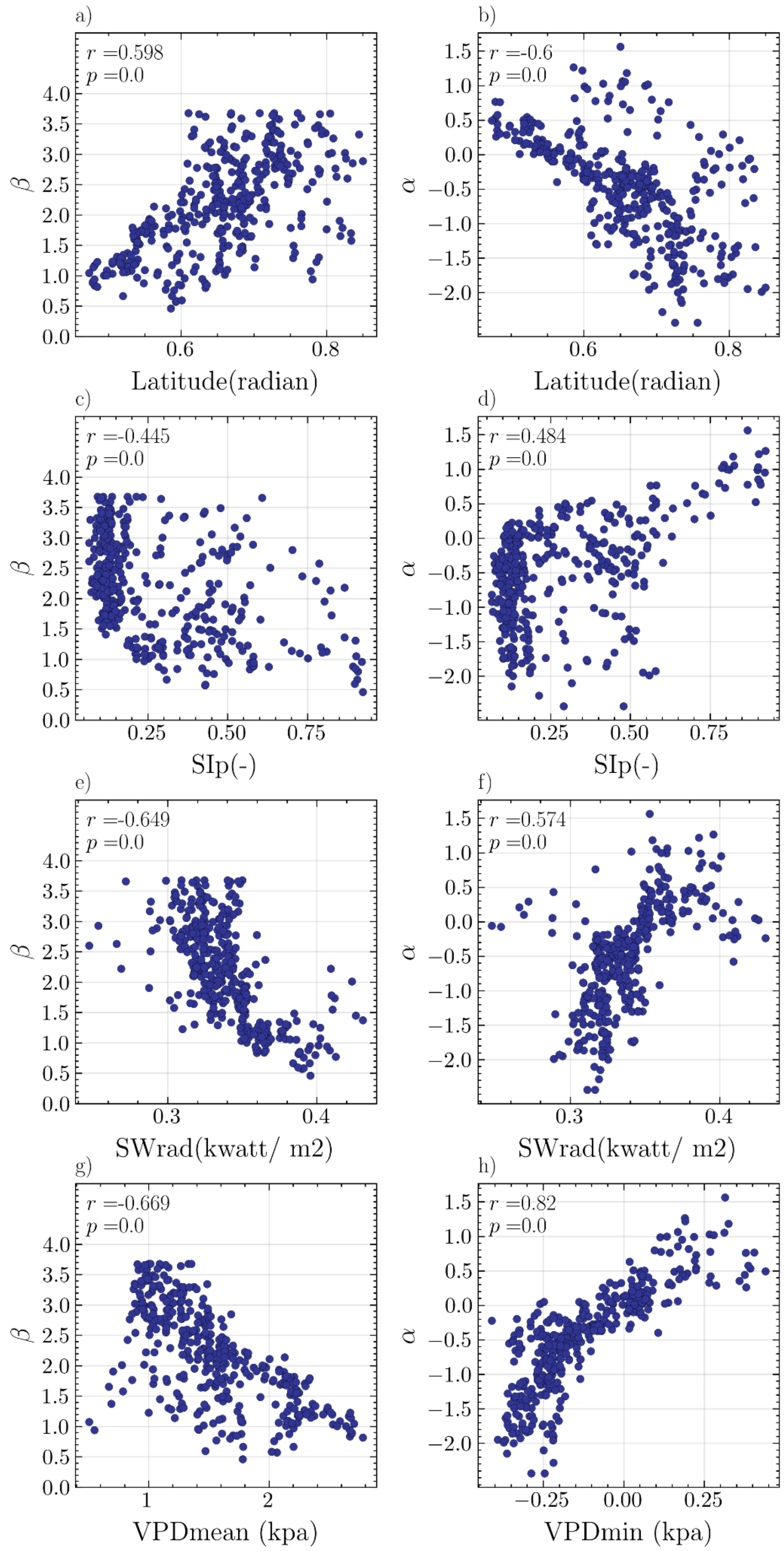


Figure 3-7: Long-term climatic characteristics and geo-location relationship with the parameters of the unified function estimated through calibration: β left column rows and α right column rows.

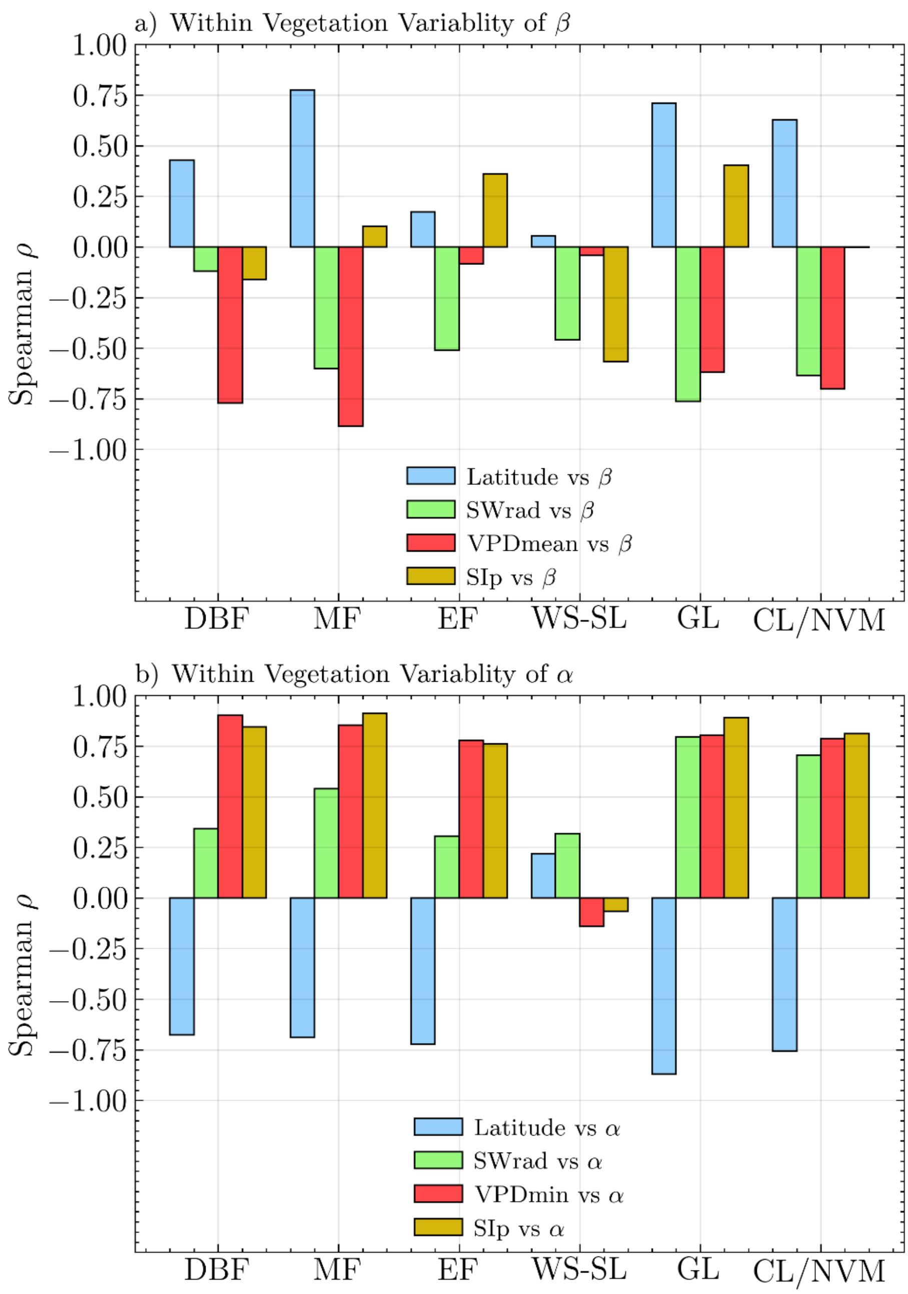


Figure 3-8: Spearman's ρ computed between precipitation seasonality, vapor pressure deficit , solar radiation and geographic latitude, and the calibrated linear functions parameters for each vegetation group: (a) for β and (b) for α.

Further, we performed a PCA to evaluate if the variables presented in Fig. 3-7 explain *function-II* slope and intercept parameters variability within vegetation types(Fig. 3-9). It showed that the first two components of PCA explain more than 80% of both slopes and intercept variability in each vegetation type. This indicates that the difference in slope and intercept values for catchments dominated by the same vegetation type is due to long-term climatic characteristics and geographic location.

Based on the above analysis, we summarize that the combined properties of these variables (i.e., variables from Fig. 3-7) could sufficiently predict *function-II* parameters (β and α). Therefore, we developed two separate multilinear regression equations for each parameter.

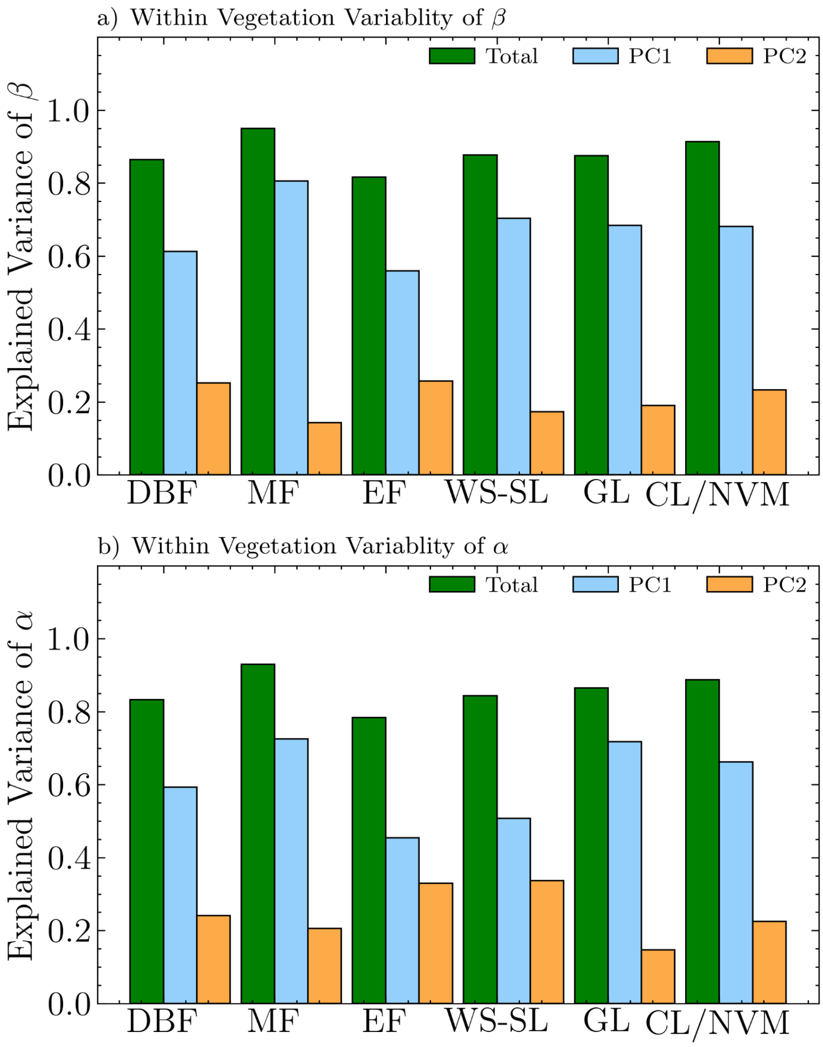


Figure 3-9: Percent of variance explained, a Principal Component Analysis (PCA) between variables from Fig.6 against the calibrated parameters: (a) for the parameter β and (b) for the parameter α.

**c) Estimating slope and intercept of *function-II***

The multivariable regression's direct use of $SI_P$, SWrad, VPDmean, VPDmin, and Latitude resulted in multicollinearity. Hence, we first applied a mean centering approach (section 3.3.4), which significantly improved the VIF scores of all variables. However, the VIF score for some variables remained > 5. Specifically for Latitude and

SWrad for the slope regression and Latitude and VPDmin for the intercept coefficient regression. Thus, we merged these variables and represented them with their arithmetic product, which reduced the VIF to ≤ 5 for all cases. Two multilinear regressions were developed after the two remedial measures (Fig. 3-10 a and b). Parameters (β and α) predicted using the regression equations showed a good agreement when compared against parameters(β and α) that are estimated through calibration (Fig. 3-10a and b). We then used the predicted β and α to simulate monthly GPP over the entire study period and for all catchments. Validation against Landsat GPP showed KGE ≥ 0.5 and ≥ 0.80 for 92% and 60% of the catchments, respectively (Fig. 3-10c), indicating that readily available climatic variables can reasonably predict *function-II* parameters.

**d) Catchment transpiration to vaporization ratio**

The slope coefficient comprises two components (Eqn. 3-3), the long-term mean ecosystem water use efficiency and vaporization partitioning coefficient. The partitioning coefficient represents the fraction of vaporization contributed through plant transpiration. Slope and intercept coefficients are collinear, and during parameter estimations, we only control the upper bound of the arithmetic product of **a** and **c**. Therefore, the vaporization partitioning coefficient could not be computed effectively from the slope, and long-term mean ecosystem water-use efficiency because there is no guarantee that it will yield a value between 0 to 1. The upper bound of β (i.e., $\mathbf{a_{max}}$*$\mathbf{c_{max}}$) is known for each vegetation type. Hence, we can estimate the lower bound of the long-term mean transpiration to vaporization ratio by dividing the estimated slope values by the upper bounds of β (Fig. 3-11).

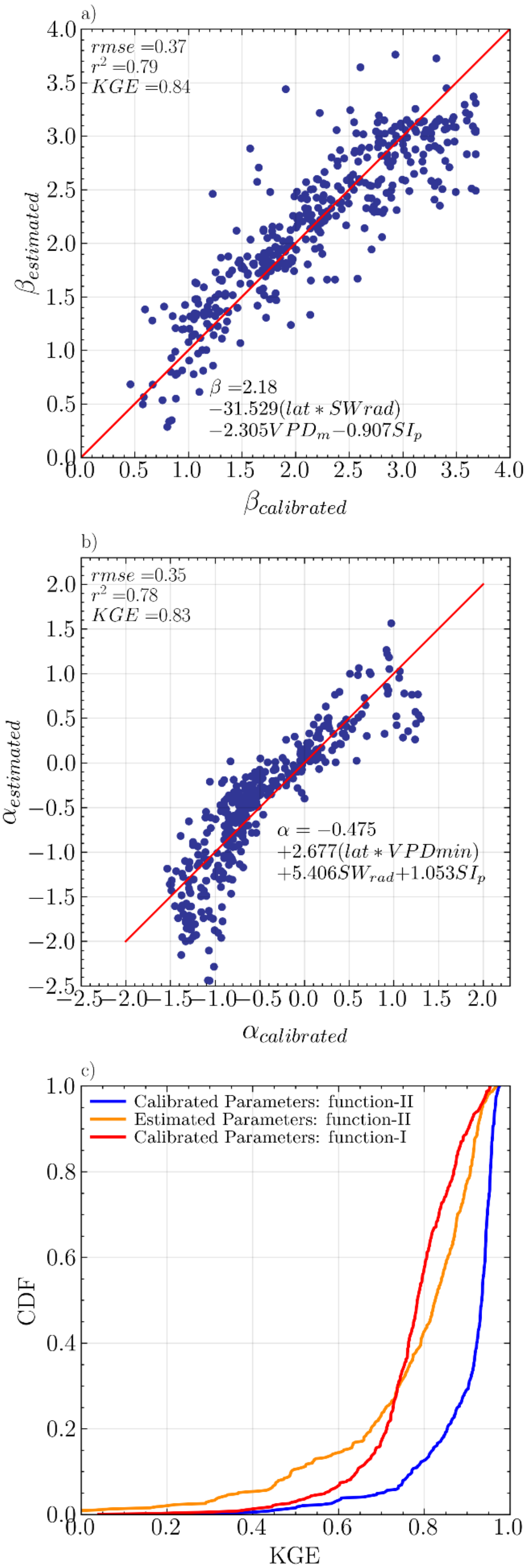


Figure 3-10: Multivariable linear regression: (a) for the parameter β, (b) for the parameter α and model performance with the predicted parameters (c).

The result shows that catchment vegetation contribution to total vaporization is generally highest in CL/NVM and forested catchments (i.e., DBF, MF) and lower in GL and WS-SL. The lower bound for EF showed a wide range (~0.25 – 1.0), while half of them are in the 0.25 – 0.5 range. This could be attributed to the difference in canopy density and understory vegetation types.

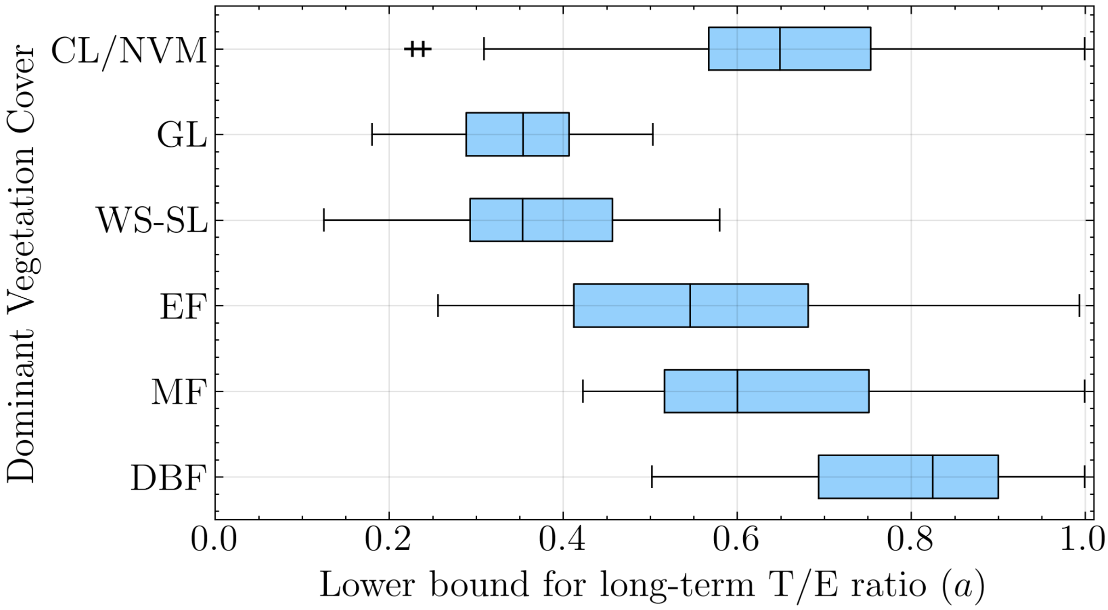


Figure 3-11: Lower bound of catchment vaporization partitioning coefficient for six dominant vegetation classes.

## 3.5 Discussions

This study provides the first-time evidence of the GPP–ET relationship at the catchment scale with an extensive amount of data. Based on this evidence from a large number of catchments, our work provides two generalized overviews of the connection between catchment carbon and the water cycle on a monthly time scale. Firstly, results from 380 catchments affirm that catchment GPP is linearly linked to ET at the catchment scale(Fig. 3-2), and the ratio of ET to long-term mean ET is a reasonable initial estimate for GPP to long-term mean GPP. These characteristics establish a basis for developing a functional relationship between catchment water balance and carbon uptake dynamics. Secondly, this study develops and validates two GPP–ET functional relationships, (i) a one-parameter linear function (Eqn. 3-5) and (ii) a two-parameter linear function (Eqn. 3-4). The functions directly link catchment water balance to photosynthetic carbon assimilation. In addition, these functions could be applied to any catchment without calibration as the parameters can be estimated from climatic and geographic variables and are easy to couple with catchment water balance models.

The linearity between GPP–ET is closely related to the dominant vegetation types. For instance, the variation of the slope values and the negative–a positive shift of intercepts is demonstrably driven by the green vegetation fraction difference (Fig. 3-5), which implies the role of the leaf area expansion and contraction across seasons in catchment spatial area. Catchments with substantially seasonal leaf areas expansion demonstrate a linear function with a steeper slope ($\beta > 2.25$) and an intercept < 0 (e.g., DBF catchments). On the other hand, a linear function for catchments with limited seasonal leaf area variations (e.g., EF and WS-SL catchments) generally has intercept values larger than zero and relatively mild to moderate slopes ($\beta \leq 2.25$). These findings demonstrate that water balance models should be informed by vegetation phenology to represent plant contribution to ET effectively. Thus, it is meaningful for future studies to consider the representation of ET in a lumped but semi-distributed model (e.g., the probability distribution models) in a similar way we represent spatial variability of soil moisture, which is supported by recent findings by Yao & Wang, (2022). In such a way, GPP–ET interactions could be well quantified in deterministic conceptual hydrologic models.

The two developed functions demonstrated adequate capacity in estimating GPP at site and catchment scales. The two-parameter function performs better in most catchments (Fig. 3-4). Hence, the function can be used to explore the interactions between catchment carbon uptake and water balance. It can also be rearranged to estimate ET with certain GPP products. The simplicity of the function and the availability of variables needed (i.e., SWrad, VPD, $SI_P$, and latitude) for estimating the parameters (β and α) a priori make this method an appealing tool to link with deterministic conceptual hydrologic models. Thus, it can help provide an advanced understanding of the GPP–ET relationships at annual, inter-annual, and intra-annual scales.

The multilinear regression in this study predicted the parameters of the linear function sufficiently, indicating that calibration is not a necessity (Figs. 3-8, 3-9, and 3-10). However, this does not suggest that the variables used in the regression are dominant controlling factors or the only factors. Here, we simply opt to develop a regression equation based on readily available data. Therefore, it is possible that a regression function made up of other seasonal and physical characteristics indicators could be equivalently well. For instance, one can use the frequency of dry days (precipitation < 1mm/day), frequency of freezing days (minimum temperature < 0), and frequency of days where VPD is less than the minimum threshold for plant transpiration (VPD < ~650 Pascal), and topographic elevation to list a few.

Transpiration measurements are often unavailable at catchment and ecosystem scales, and most ET products provide ET instead of its components. Data limitation constrains the understanding of ET partitioning at varied spatial scales. Despite the differences in parametrizations, a commonly used framework in lumped hydrologic models is partitioning catchment precipitation at two stages. The first stage separates precipitation into total wetting and overland flow, and the second stage partitions total wetting into ET, soil moisture, and subsurface flow. Such models rarely go beyond the second stage and partition ET into its components. This study provides the lower bound estimation for transpiration at the catchment level, which may help in improving these drawbacks. Here, a lower bound for the transpiration contribution to ET (Fig. 3-11) is estimated from *function-II* calibrated slope parameter and long-term mean ecosystem water use efficiency. The results indicated that the contribution from transpiration is high in DBF and MF catchments, relatively lower in EF among forested catchments, and lower in GL and WS-SL catchments, which agrees with global findings by Zhou et al. (2016) and Purdy et al. (2018). Given that it is a lower bound, the result is comparable to actual stand-level ratios (Maxwell & Condon, 2016; Schlesinger & Jasechko, 2014). Thus, this research result could benefit the terrestrial biosphere model community, in which the estimates of GPP and transpiration are essential to the surface carbon, water, and energy flux representations.

In summary, the developed functions and the corresponding parameters could be used for several purposes with observational data and hydrologic process understanding. Given that the parameters can be easily estimated from climatic inputs and geographic locations, the functions can be applied to data gap filling of GPP and ET products and to extend historical GPP or ET records during which observational data are not available (especially for GPP). With regards to hydrologic process understanding, the functions can be primarily used for two research purposes: 1) using GPP products and the functions to estimate ET, which can be used to diagnose the impacts of vegetation phenology on streamflow; 2) coupling these functions with deterministic hydrologic models such as the ***abcd*** model, Budyko framework, and probability distribution models to estimate GPP seasonality. All this research could benefit the calibration of hydrologic models at regional and global scales.

## 3.6 Conclusions

This study uses monthly GPP data from Landsat and hydrometeorological data from the CAMELS dataset at 380 catchments distributed across CONUS to answer three main questions: 1) Does the GPP–ET linearity hold at the catchment scale? 2) Can we establish a functional relationship between GPP and ET? and 3)What controls the characteristics of the linear relationship, such as the slope and intercept? The GPP–ET linearity is confirmed. A two-parameter unified functional relationship is proposed for estimating GPP from ET. Catchment vegetation spatial cover seasonal dynamics drive differences in GPP–ET linearity among vegetation types. Long-term climate and geographic location are responsible for differences in linearity type within a given vegetation type.

Vegetation carbon uptake and water balance have a strong linear relationship across vegetation types. The proposed two-parameter GPP-ET functional relationship is validated and is sufficiently exact in simulating monthly GPP at any given catchment. The function's parameters (i.e., $\beta$ and $\alpha$) are strongly linked to environmental factors, geographic location, and the seasonal dynamics of catchment green vegetation cover. Linear functions for catchments dominated by vegetations demonstrating strong seasonal dynamics (i.e., high GVF difference) are characterized by steep ($2.25 < \beta \leq 3.0$) to very steep ($\beta > 3.0$) slopes and an intercept coefficient of less than zero (e.g., DBF, some of the MF, and some of the CL/NVM catchments). Whereas linear functions with milder slopes ($\beta \leq 1.5$) and intercept coefficient > 0 are found in catchments dominated by vegetation types whose green cover is maintained through growing and dormancy periods (e.g., EF, WS-SL). Environmental factors, including precipitation seasonality, long-term vapor pressure deficit, long-term solar radiation, and catchment physical setting such as geographic latitude, are responsible for the within-vegetation type variability of the linearity type. These variables explain more than 80% of the within vegetation type variability of GPP-ET linearity type (i.e., mild, moderate, steep, or very steep). The importance of these variables is different across vegetation types. For instance, vapor pressure deficit and precipitation seasonality have a weak relationship with the slope parameters for catchments dominated by EF and CL/NVM vegetation types. The differences in long-term climate characteristics, precipitation seasonality strength, vapor pressure deficit, solar radiation, and physical setting explain more than 80% of the variability in linearity form within vegetation types. A multilinear regression equation developed based on these factors predicted the slope and intercept parameters with sufficient accuracy. GPP simulated with the predicted parameters compared reasonably well against Landsat GPP. The slope parameter for the two-parameter function combined with the long-term ecosystem water use efficiency provided a simple way to estimate the T/ET ratio at the catchment scale. The estimates provided in this study represent the lower bound.

# 4 Soil Water Storage and Atmospheric Dryness Dynamics Effects on Seasonality of Vegetation Carbon Uptake[3]

## 4.1 Introduction

Catchment wetness (i.e., water available for vegetation use) and atmospheric dryness (i.e., vapor pressure deficit) are critical variables in the intra-annual variability of vegetation carbon uptake (i.e., gross primary productivity). Catchment wetness refers to total liquid precipitation (rain + melt) subtracting the lateral surface runoff that exited the catchment. It includes total infiltration and water stored on land surface (e.g., streams, lakes, swamps, and surface depressions). Vapor pressure deficit (VPD) is the difference between saturation and actual water vapor pressure at a given temperature. While an increase in VPD means increased atmospheric demand for water, it can also induce stomatal closure (tiny pores at the leaf surface responsible for carbon-water exchange), thereby constraining plant carbon uptake(Gentine et al., 2019). The Gross Primary Production (GPP) is the total carbon uptake by plants through photosynthesis, an ecosystem signature, and the dominant carbon flux between terrestrial ecosystems and the atmosphere. Catchment wetness and atmospheric dryness are vital abiotic factors controlling water and carbon fluxes. Understanding the catchment vegetation carbon uptake intra-annual response to the intra-annual variability of catchment wetness and atmospheric dryness is crucial for assessing the impacts of climatic and hydrologic signals propagation toward catchment vegetation.

Soil moisture is an essential factor that optimizes and regulates both water and carbon fluxes(Gentine et al., 2019; Green et al., 2019; Zhou et al., 2019b). Processes at

[3] This work is in preparation to be submitted for publication as: Abeshu, G. W., Li, H., & Shi M., The effects of atmospheric dryness and catchment wetness on seasonality of vegetation carbon uptake

the leaf surfaces interact with hydrologic systems through Xylem, a plant hydraulic transport system. Hence, the available soil water can determine the amount of water lifted hydraulically by plants and escape through stomata during the carbon-water exchange. Plant structural and physiological characteristics regulatory mechanisms, including the stomata and the hydraulic transport, help them regulate the changes in soil moisture (Martínez-Vilalta et al., 2014). In order to avoid damage to the hydraulic transport system, plants partially close their stomata when they detect a decrease in available soil water (Gentine et al., 2019; Martínez-Vilalta et al., 2014; Zhou et al., 2019a). The nonlinear response of carbon fluxes to soil moisture is among the essential factors on which the long-term capacity of our continents to act as a future carbon sink critically depends(Green et al., 2019). Under drought conditions, soil moisture feedback to the atmosphere enables extreme atmospheric aridity, influencing the plant carbon uptake(Zhou et al., 2019a).

Vapor pressure deficit is an essential driver of plant system function and determinant for plant-water relations as it regulates stomata(Grossiord et al., 2020). The atmospheric demand for water increases with VPD. However, this does not directly translate to increased transpiration, as plant regulatory mechanisms can limit response to increased VPD(Massmann et al., 2019). While stomata are fully open under low VPD, a high VPD or rapid increase in VPD triggers plants to close their stomata to minimize water loss and avoid hydraulic transport system failure (Grossiord et al., 2020; McAdam and Brodribb, 2015). Over the recent decades, the temperature has been increasing across the globe, resulting in increased VPD(Hatfield and Prueger, 2015). The projected increase in temperatures and decrease in relative humidity is expected to increase future VPD (Byrne and O'Gorman, 2013). Hence, understanding the degree of influence VPD exterts on catchment ecohydrologic system is essential.

Vegetation water use and productivity can be limited by catchment wetness and atmospheric dryness independently but also concurrently during periods of hydrologic stress (Grossiord et al., 2020; Liu et al., 2020). The compound effect of a concurrent increase in VPD and low soil water availability can be a source of extremely dry events (Zhou et al., 2019a). Understanding the relative contribution of the two components is complicated by the difficulty of disentangling soil moisture and VPD as they are coupled processes connected by plant hydraulic transport systems. A recent study shows that soil moisture is a dominant driver of ecosystem production under dryness stress, especially in semi-arid ecosystems(Liu et al., 2020). The two components are essential factors in understanding the intra-annual variability of catchment vegetation uptake. However, although catchment wetness has been linked to catchment vegetation dynamics indicators such as leaf area index at annual and intra-annual scales, it has not been directly linked to carbon uptake dynamics. Similarly, VPD is among the overlooked variables in understanding catchment water fluxes.

This study uses a data-based exploratory analysis to investigate vegetation carbon uptake response to catchment wetness and atmospheric dryness. Specifically, we ask three essential questions, 1) when is catchment vegetation under seasonal hydrological stress? 2) how does catchment vegetation respond to atmospheric demand and hydrological variations? 3) what are the factors underlying catchment vegetation carbon uptake seasonal dynamics? To address these questions, we investigate the intra-annual variability and connectedness between catchment wetness, VPD, and GPP with data from 380 catchments distributed across gradients of climate, vegetation, and topography of contagious US. The remainder of this paper is organized as follows: Sections 4.2 and 4.3 introduce the data and methods. Section 4.4 presents the results. Section 4.5 and 4.6 discuss and summarize the findings.

## 4.2 Data

Providing generalized understanding following the classical comparative hydrological approach requires having many catchments distributed across gradients of landscape and climate. The Catchment Attributes and MEteorology for Large-sample Studies (CAMELS) provides a dataset for 671 unimpaired catchments distributed across the contiguous US(Addor et al., 2017; Newman et al., 2015). The dataset comprises daily observed/observation-based hydrometeorological datasets and model outputs, including actual evapotranspiration (ET) from the integrated Snow-17/SAC-SMA model(Addor et al., 2017). Catchment attributes, including dominant vegetation cover characteristics and dominant cover fraction, are also available from CAMELS. The daily data we used in this study includes precipitation (rain + melt), maximum and minimum temperature, actual vapor pressure, actual and potential evapotranspiration, and stream discharge. The potential evapotranspiration (PET) is estimated with the Priestly-Taylor method. The daily baseflow was computed from the observed discharge using the one-parameter recursive digital filtering with three passes (Nathan and McMahon, 1990). GPP data is obtained from the Landsat GPP dataset for the contiguous US (Robinson et al., 2018). It has a spatial and temporal resolution of 30 meters and 16 days, respectively. The catchment polygons were used to mask the Landsat GPP spatial maps over the study period. We then generated a time series of catchment average GPP at 16-days intervals, which we later converted to monthly series. We performed data quality control following two criteria: i) no missing data in both simulated and observation data, and ii) the relative percent error between the simulated annual mean of model output ET and observed ET (calculated as annual mean precipitation subtract annual mean discharge). This yielded 380 catchments distributed across the contiguous US. These catchments can be summarized under six vegetation groups: Deciduous Broadleaf (DBF) (89), Evergreen Forest (Needle leaf + Broadleaf) (EF) (25), and Mixed Forests (MF) (50), Croplands plus Croplands/Natural Vegetation Mosaic (CL/NVM) (109), Grasslands (GL) (47), and a combination of Savannas, Woody Savannas, and Open/Closed Shrublands, hereafter WS-SL catchments (60).

## 4.3 Methods

### 4.3.1 Catchment Wetness

Precipitation partitioning at annual or sub-annual scales is significantly modified by storage carryover. Hence, accounting for the inputs and outputs that affect catchment water surface and subsurface storage dynamics (Fig. 4-1), water balance at a monthly scale is given by

$$P - ET - Q_b - Q_s = \Delta S. \tag{4-1}$$

Where P is precipitation, ET is actual evapotranspiration, $Q_b$ is baseflow, $Q_s$ is surface runoff, and ΔS is the net change in water storage. ΔS comprises changes in water stored at the surface (i.e., streams, lakes, swamps, and surface depressions) and subsurface storage changes. Total wetting (W ) represents precipitation that wetted the catchment, excluding precipitation that becomes quick runoff. It includes total infiltration and water stored on land surface (i.e., river, lakes, swamps, surface depressions) and is given by P - $Q_s$. Substituting this into Eqn. (4-1) yields

$$W - \Delta S = E + Q_b = W_c. \tag{4-2}$$

Where $W_c$ is catchment wetness. The ΔS effectively acts as either an additional source for the second stage partitioning to evaporative and advective outputs (i.e., $\Delta S < 0$) or precipitation held in the catchment storage components (i.e., $\Delta S > 0$) that competes with the other second stage partitioning components (i.e., ET and $Q_b$). Wc represents total water available for plant use.

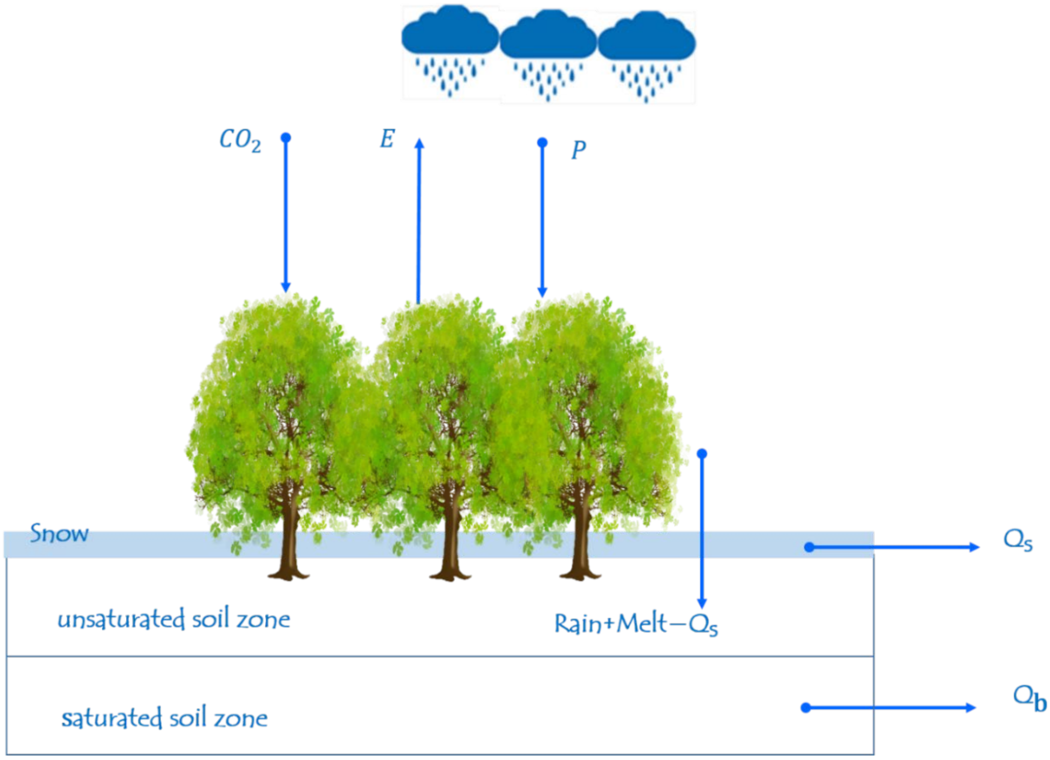


Figure 4-1: Hydrologic partitioning conceptual diagram. In the first stage, precipitation portions into soil wetting and surface runoff. The soil-wetting plus storage carryover further partitions into evapotranspiration and baseflow.

### 4.3.2 Catchment Atmospheric Dryness

Terrestrial plants regulate water loss and maximize carbon gain primarily through a stomatal response to atmospheric dryness. The atmospheric dryness is characterized by VPD, the difference between actual vapor pressure (AVP) and saturation vapor pressure (SVP). We used the mean daily AVP from the CAMELS dataset and computed the mean daily SVP with the Magnus formula, which is given by

$$SVP = 0.6108 \, . exp \left(\frac{17.27T}{237.3 + T}\right). \tag{4-3}$$

Substituting air temperature (°C) yields SVP in kPa. The mean daily SVP is calculated as SVP at daily maximum and minimum air temperatures.

### 4.3.3 Catchment Hydroclimatic and Vegetation Dynamics Indices

Understanding the seasonal co-evolution of climatic and hydrological demand-supply interactions is essential to synthesize the hydrologic system's controls on catchment vegetation carbon uptake seasonal dynamics. We characterize the seasonal variation of climatic demand-supply interactions using the ecological aridity index, the hydrologic demand-supply interaction using the Horton Index, and the energy demand-supply state interaction using the evaporation fraction. We also characterized catchment vegetation production efficiency by the actual to potential carbon uptake ratio. Below here is the summary of these indices:

1. The ecological Aridity Index (EAI) is computed as the potential evapotranspiration to catchment wetness ratio(Abeshu and Li, 2021). It indicates interactions between catchment energy supply and water supply for plant water use. The seasonal EAI magnitude for a given climatic condition can range from $0\ to\ \infty$, with a wet climate corresponding to smaller EAI. It is given by

$$\mathrm{EAI} = \frac{\mathrm{PET}}{\mathrm{W} - \Delta S}. \tag{4-4}$$

2. Horton Index (HI): HI is evapotranspiration as a fraction of the precipitation available for catchment vegetation use (Abeshu and Li, 2021). HI ranges between 0 and 1, indicating absolute hydrologic wetness and dryness conditions, respectively. HI is expressed as

$$\mathrm{HI} = \frac{\mathrm{ET}}{\mathrm{W} - \Delta S}. \tag{4-5}$$

3. Evaporative Fraction Index (EFI): We computed EFI as an actual to potential evapotranspiration ratio. We use it as an indicator of the efficiency of catchment energy use. EFI values range between 1 and 0, implying the most and least efficient catchments. EFI is defined as

$$\mathrm{EFI} = \frac{\mathrm{ET}}{\mathrm{PET}}. \tag{4-6}$$

4. Carbon Uptake Efficiency (CUE): Robinson et al. (2019) parametrizes the 16-day sum GPP from Landsat as

$$\mathrm{GPP} = \varepsilon_{\mathrm{max}} * (\mathrm{T}_{\mathrm{scalar}} * \mathrm{W}_{\mathrm{scalar}}) * \mathrm{APAR}. \tag{4-7}$$

Where $\varepsilon_{max}$ is the maximum radiation conversion efficiency (kg $^0$C $MJ^{-1}$) specific to vegetation type, which is downregulated by temperature limitation($T_{scalar}$) and water stress ($W_{scalar}$) to yield actual radiation conversion efficiency, $\varepsilon = \varepsilon_{max} * T_{scalar} * W_{scalar}$, and APAR is the absorbed photosynthetically active radiation. Both $T_{scalar}$ and $W_{scalar}$ reflect the climatic limits of carbon uptake. Hence, under no limiting conditions (i.e., $T_{scalar} = W_{scalar} = 1$) Eqn. 4-7 leads to estimates of potential GPP as

$$\mathrm{GPP}_{\mathrm{potential}} = \varepsilon_{\mathrm{max}} * \mathrm{APAR}. \tag{4-8}$$

The ratio of actual to potential GPP, hereafter referred to as Carbon Uptake Efficiency (CUE), can be expressed as

$$\mathrm{CUE} = \frac{\mathrm{GPP}}{\mathrm{GPP}_{\mathrm{potential}}} = \mathrm{T}_{\mathrm{scalar}} * \mathrm{W}_{\mathrm{scalar}}. \tag{4-9}$$

CUE ranges between 0 and 1. Mean monthly $T_{scalar}$ is estimated from the mean monthly temperature and Biome-Property-Look-Up-Table( Robinson et al., 2019). Whereas $W_{scalar}$ is determined using mean monthly VPD and a Biome-Property-Look-Up-Table( Robinson et al., 2019). Under atmospheric demand < catchment water supply condition, CFE=1 shows the peak productivity under an energy-limited state. Conversely, CF = 1 under atmospheric demand > catchment water supply condition represents peak productivity under a water-limited state. When atmospheric demand approaches catchment water supply and maximum demand, CFE = 1 implies the maximum productive use of both energy and water.

### 4.3.4 Statistical Analysis

**Circularity statistics**: Circular (directional) statistics summarize the intra-annual variability of fluxes (Dingman, 2015; Fisher, 1993; Markham, 1970). To apply circular statistics, first, we need to construct circular data by representing the mean monthly data as vector quantities. The vector magnitude corresponds to the flux amount for the month, and the vector direction is the month expressed in a unit of arc. Direction for a given month is the median date of the month measured from January 1$^{st}$ in a clockwise direction. An ordinary year has 365 days, and one day is equivalent to $\theta = 360/365 = 0.986^o$ on a circle. This factor adjusts the day of the year to give the corresponding angular direction on a circle. For instance, the median day for February measured from January 1$^{st}$ is 31 days (January) + 14.5 (median of February days) = 45.5$^{th}$ day of the year. The corresponding angle on a circle ($\phi$) is $45.5*\theta = 44.9^o$. The vector components of any catchment fluxes with positive magnitudes are determined as

$$C = \sum_{m=1}^{12} \overline{X}_m \cos \phi_m \tag{4-10}$$

and

$$S = \sum_{m=1}^{12} \overline{X}_m \sin \phi_m \ . \tag{4-11}$$

The Seasonality Index (SI), which expresses a given catchment flux's concentration in time, is the resultant vector's magnitude normalized with the annual mean value (Markham, 1970) and is given by

$$SI = \frac{X_R}{\bar{X}}. \tag{4-1}$$

Where $X_R$ is the resultant vector given by $\sqrt{C^2+S^2}$ and $\bar{X}$ is the annual mean. SI ranges between 0 and 1, indicating an intra-annually uniformly distributed flux and a flux concentrated in a single month, respectively. The average time of occurrence ($\overline{\phi}$) is the angular direction corresponding to the resultant vector, which is given by

$$\overline{\phi} = \begin{cases} arctan(S/C) & if\ S > 0\ and\ C > 0 \\ arctan(S/C) + \pi & if\ C < 0 \\ arctan(S/C) + 2\pi & if\ S < 0\ and\ C > 0. \end{cases} \tag{4-13}$$

For $\overline{\phi}$ January 1st represents the north (0°), April 1st represents the east direction (90°), July 1st represents the south direction (180°), and October 1st represents the west direction (270°). We compute the seasonality index and average time of occurrence for GPP (denoted as $SI_{gpp}$ and $\phi_{gpp}$), Wc ( denoted as $SI_{wetness}$ and $\phi_{wetness}$), and VPD ($SI_{vpd}$ and $\phi_{vpd}$).

**Spearman's correlation (ρ)**: Spearman's correlation is a metric for quantifying the degree of association between paired data. Its ranges from −1 to +1. The magnitude indicates the strength agreement between the paired data, and the sign indicates whether it is a direct (+) or inverse (−) association. Generally, $0 < \rho \leq \pm 0.20$ is considered negligible, $\pm 0.21 < \rho \leq \pm 0.40$ is weak, $\pm 0.41 < \rho \leq \pm 0.60$ is moderate, $\pm 0.61 < \rho \leq 0.80$ is strong, and $\pm 0.81 < \rho \leq \pm 1.00$ is very strong.

**Granger Causality**: Granger causality characterizes the dependence relation between paired time-series data(Stokes and Purdon, 2017). Granger's statistical causality depends on two principles: i) cause occurs before effect, and ii) knowledge of a cause improves the prediction of its effect (Granger, 1969). The hypothesis is that a given time series $X_t$ is Granger causal of another time series $Y_t$ if the inclusion of the history of X improves the prediction of Y over knowledge of the history of Y alone(Stokes and Purdon, 2017). The hypothesis is rejected when the probability value is less than the predefined significance level.

## 4.4 Results

Vegetation plays a vital role in the intra-annual variability of lateral (i.e., surface and subsurface runoff) and vertical (i.e., evapotranspiration, groundwater recharge) hydrologic releases. Conversely, catchment water storage and atmospheric demand mediate vegetation productivity and efficiency. Hence, establishing a connection between catchment water supply, atmospheric demand, and vegetation productivity can help synthesize the catchment hydrologic variation's role in the seasonal dynamics of terrestrial vegetation carbon uptake. Before all else, we performed two separate cross-correlation analyses: i) between catchment wetness and vegetation carbon uptake (i.e., Wetness-GPP) and ii) between atmospheric dryness and vegetation carbon uptake (i.e., VPD-GPP) at 380 catchments using 25 years of monthly data. Catchment wetness and GPP showed their best association at zero lag for 57% of the catchments and GPP lags by one month for another 37%. The maximum correlation coefficient at the corresponding lags is ≥ 0.8 for all catchments. Similarly, VPD-GPP cross-correlation analysis showed maximum correlation coefficients ≥ 0.86 at zero lag and one month lag (i.e., VPD lags behind GPP) for 14.5% and 73% of the catchments, respectively. This suggests that catchment supply-productivity and demand-productivity cause and effect interactions happen within a maximum span of two months (i.e., ±1 month from GPP). Furthermore, the Granger Causality test also showed that catchment wetness is partially responsible for the patterns of vegetation primary productivity. In the following subsections, we examine the intra-annual variability of supply-demand-productivity interactions at the catchment level.

### 4.4.1. Intra-Annual Variability of Catchment Wc, VPD, and GPP

We used circularity statistics to summarize the intra-annual variability in monthly catchment wetness ($W_C$), atmospheric demand (VPD), and vegetation productivity (GPP). It provides two essential statistics, the degree of seasonality (SI) and the average time of occurrence ($\phi$). SI varies with geographic latitude (Fig. 4-2). For a given longitudinal frame, the strength of seasonality increases from south to north for all three variables. The $SI_{gpp} > SI_{wetness}$ for 86% of the catchments and $SI_{gpp} > SI_{vpd}$ for 92 % of the catchments, which indicates that intra-annually catchment vegetation's productivity is more variable than both water supply and atmospheric demand. The $SI_{wetness} > SI_{vpd}$ for 66 % of the catchments, indicating the atmospheric demand is the less variable component among the three. The average time of occurrences, $\phi_{wetness,}$ and $\phi_{gpp}$ when converted to month matches for 73% of the catchments and $\phi_{gpp}$ delays by at least one month for another 23% of the catchments. The $\phi_{vpd}$ differs by at least +1 month from $\phi_{gpp}$ and $\phi_{wetness}$ for 91% and 95% of the catchments, respectively.

For each vegetation type, we explored supply-productivity (i.e., Wetness-GPP) and demand-productivity (i.e., VPD-GPP) relationships for each month separately using mean monthly values. For the Wetness-GPP, a strong-positive association ($\rho > 0.6$) is found in WSSL and GL catchments (Fig. 4-3a). This is reasonable given that these vegetation types are associated with water-limited environments. The association is also significant and positive ($\rho > 0.4$) for CL/NVM and DBF, except during the peak carbon uptake periods (Jun-Aug). A significant relationship is detected only during months of dormant periods for EF (4 months) and MF (5months) (Fig.4-3a). Similarly, the VPD-GPP result showed a significant positive relationship ($\rho > 0.4$) during most of the greening period (January – March) and most browning period (October – December) for all vegetation types except WSSL (Fig. 4-3b). On the contrary, the relationship is significant and negative ($\rho < -0.4$) during the peak growing season (June-August). This is because VPD is high during these months, and higher VPD is known to induce stomatal closure, reducing carbon uptake.

The detected significant positive association for both Wetness-GPP and VPD-GPP for the earlier and later part of a year implies the importance of catchment water supply and atmospheric demand during the greening and browning periods. The insignificant Wetness-GPP association during the peak period (except for WSSL and GL) combined with a strong negative association of VPD-GPP implies that catchment vegetation may be in some form of optimal state.

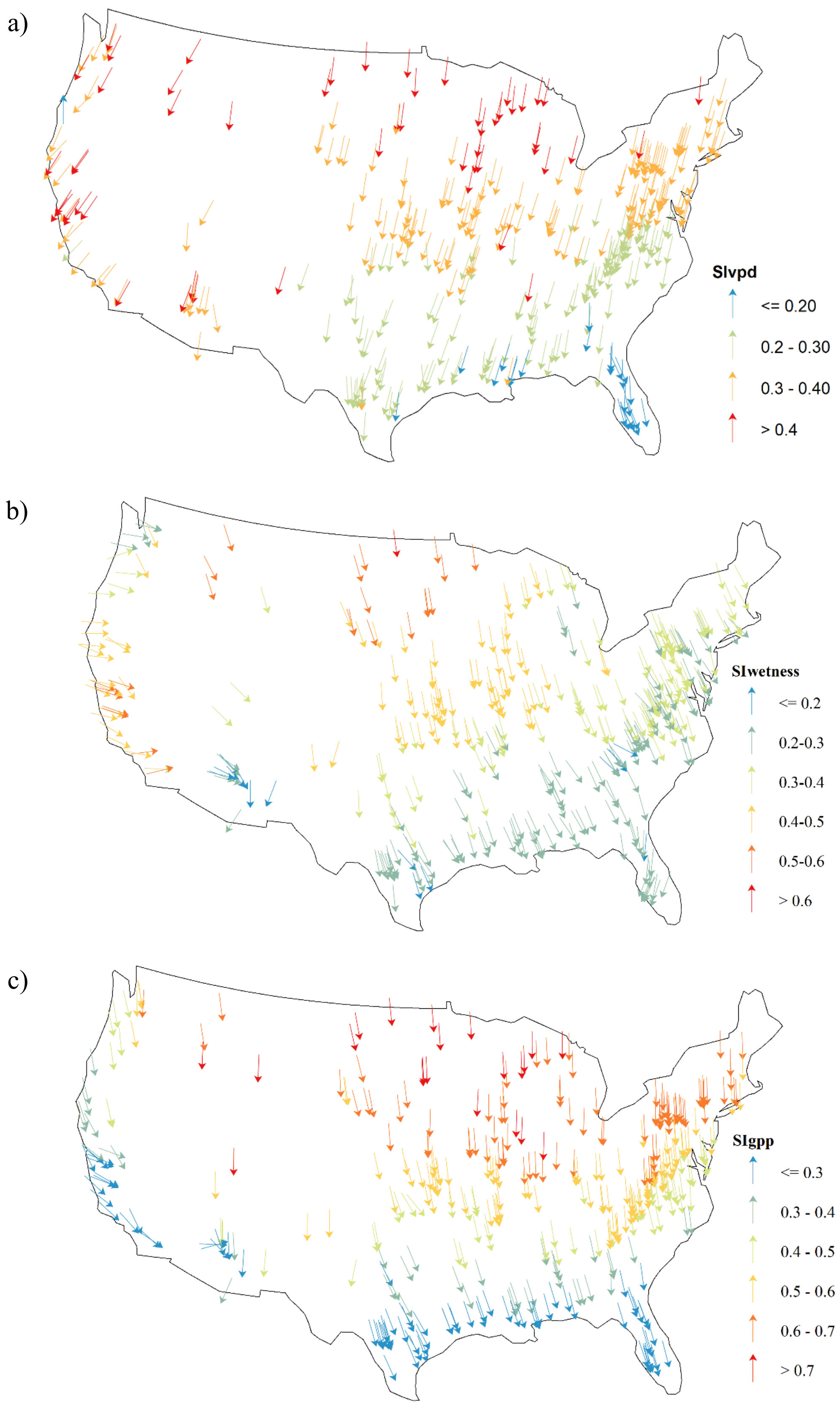


Figure 4-2: Seasonality strength and direction for catchment wetness (a), atmospheric dryness (b), and GPP (c). The direction of the arrow is judged with the north as a reference and in a clockwise direction.

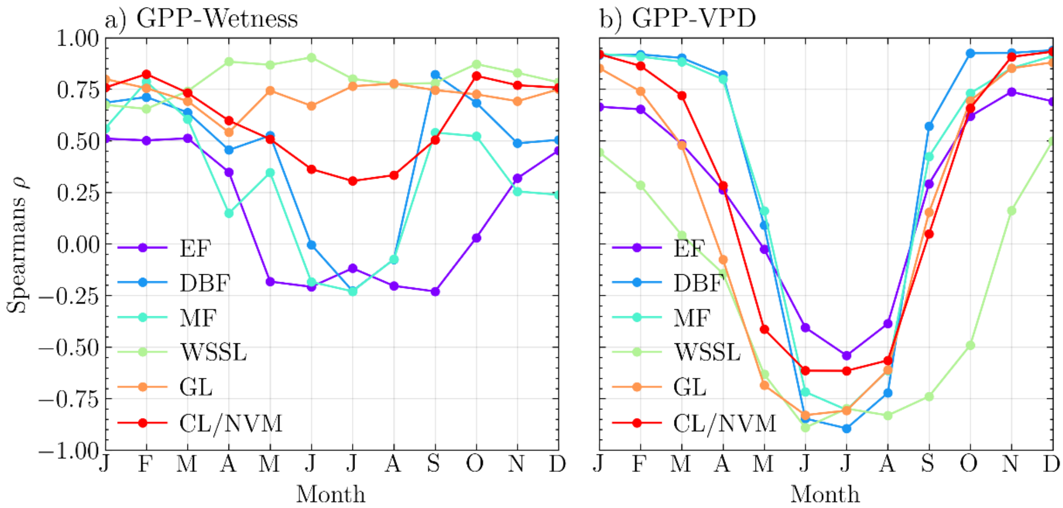


Figure 4-3: Association between intra-annual variability of GP-Wetness(a) and GPP-VPD relationship (b)

Further, the strength of seasonality for GPP and wetness combined with the lag in vegetation response to catchment water supply creates a hysteresis phenomenon, GPP-Wetness hysteresis (i.e., hysteresis between catchment water supply and vegetation productivity). Similarly, the lag between GPP and VPD creates the GPP-VPD hysteresis (i.e., hysteresis between atmospheric demand and vegetation productivity). Figures 4-4 and 4-5 depict the six vegetation types' GPP-Wetness and GPP-VPD hysteresis. For convenience, all variables (i.e., GPP, VPD, and Wc) were scaled by their corresponding monthly series maximum, excluding outliers. The green line with the arrow marker represents the hysteresis pattern generated from a median of mean monthly values. Overall, Fig. 4-4 and 4-5 show that hysteresis can have several defining patterns. The two main patterns are the size and directions. Based on the size, it can be a narrow tight (e.g., Fig. 4-4d and e) or a wide loop (Fig. 4-4a) hysteresis. The direction can be clockwise (e.g., Fig. 4-5) or counterclockwise (i.e., Fig. 4-4). These patterns vary when we look at catchment individually. In the following subsections, we use catchment climatic and hydrologic characteristics indices presented in section 3.3

to explain the factors underlying the hysteresis patterns (Fig 4-4 and 4-5) and the intra-annual variability of GPP-Wetness and GPP-VPD relationship strength (Fig. 4-3).

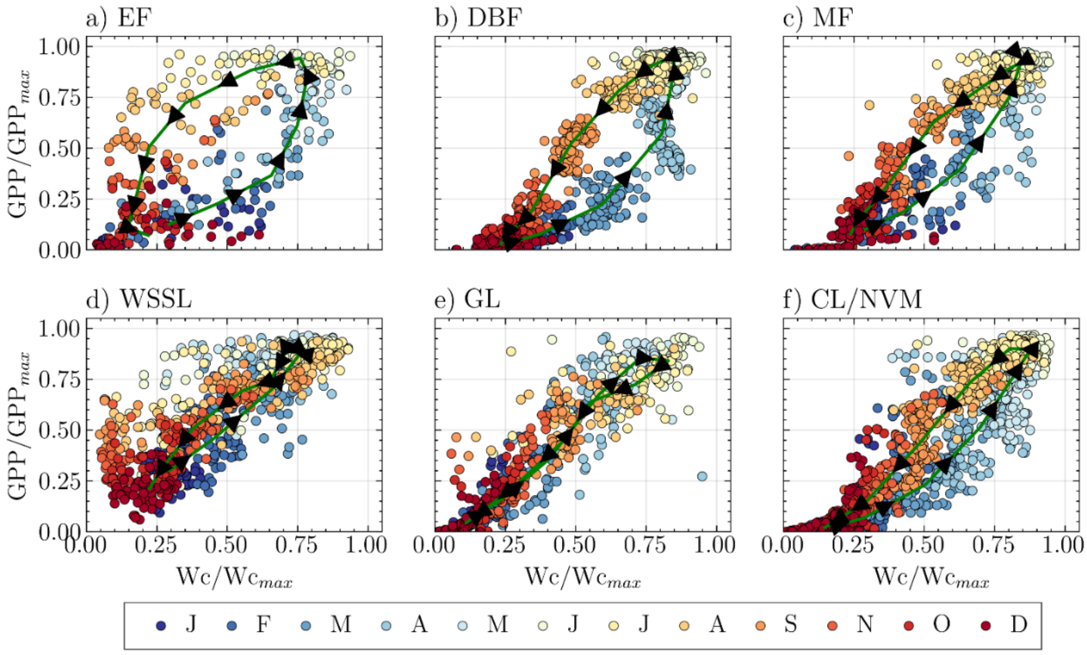


Figure 4-4: The GPP-Wetness hysteresis: GPP and Wc were normalized by the maximum mean monthly values. The line and the arrow represent the median catchments hysteric curves and the direction of hysteresis.

### 4.4.2. Catchment Wetness-GPP and GPP-VPD Hysteresis

Hysteresis, in simple terms, is a phenomenon that arises between two causal variables, in which the change in effect lags changes in the causing variable. We found such a phenomenon between catchment water supply and vegetation productivity (i.e., Wetness and GPP) and atmospheric demand and vegetation productivity (i.e., VPD and GPP). Visual observation of GPP-Wetness hysteresis curves for all our catchments showed that the hysteresis loop ranges from a narrow tight loop (narrow-hysteresis) to a wide loop (wide-hysteresis). To describe the relative size of the loop, we computed the area within the loop for each catchment after scaling the variables (i.e., GPP, Wc, and VPD) with their monthly mean values.

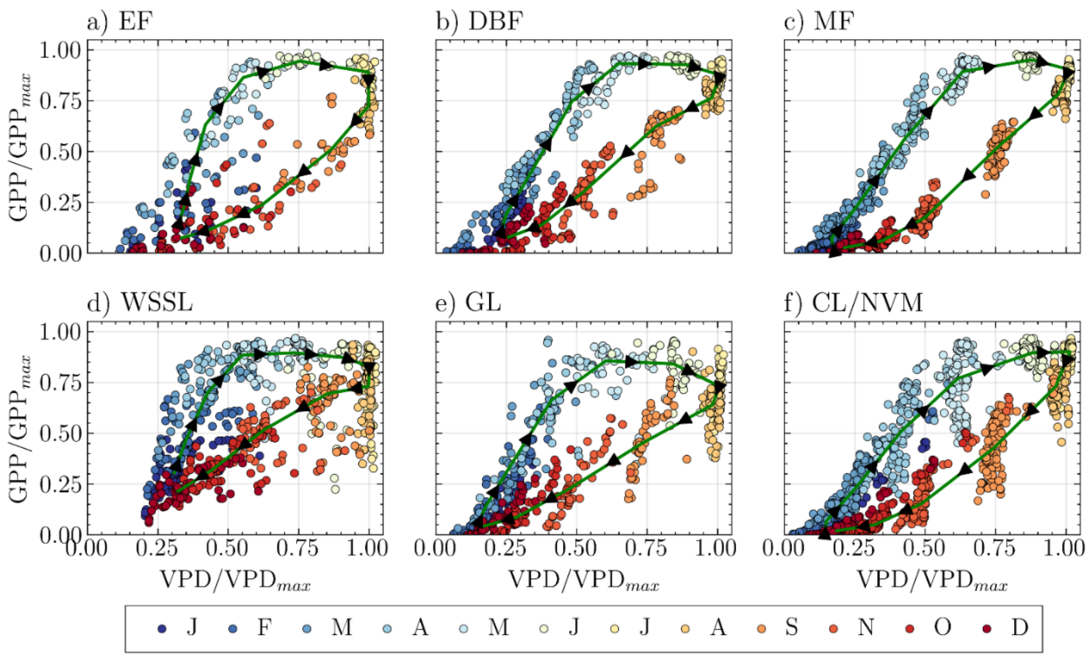


Figure 4-5: The GPP-VPD hysteresis: GPP and VPD were normalized by the maximum mean monthly values. The line and the arrow represent the median catchments hysteric curves and the direction of hysteresis.

Both GPP-Wetness hysteresis loop areas have a strong positive relationship with HI intra-annual variability and a strong negative relationship with annual mean HI (Fig. 4-6a and b). The GPP-VPD hysteresis loop area does not significantly relate to HI; however, it is negatively affected by long-term EAI and low precipitation duration (average dry period duration)(Fig. 4-6c and d). Catchments that are characterized by high and invariable HI at intra-annual, resulting in high annual mean HI (i.e., HI→1) demonstrate a narrow hysteresis (Fig. 4-7a, b, and c). This is a typical characteristic of catchments in a water-limited state throughout the year. The narrowest loop develops when the mean monthly EFI→1 (i.e., mean monthly ET → mean monthly PET) and the mean monthly HI→1(i.e., mean monthly ET → mean monthly Wc) respectively. These are primarily GL and WSSL vegetation types dominated catchments. Wide hysteresis develops in catchments with strong intra-annual EF and HI variability (Fig. 4-7d, e, and f). The widest loop develops when the intra-annual patterns of HI and EF are out of phase. A phenomenon that develops when seasonal patterns of PET and Wc are in phase but the PET >> Wc during the peak atmospheric demand period. The widest hysteresis cures were seen, mainly in EF catchments.

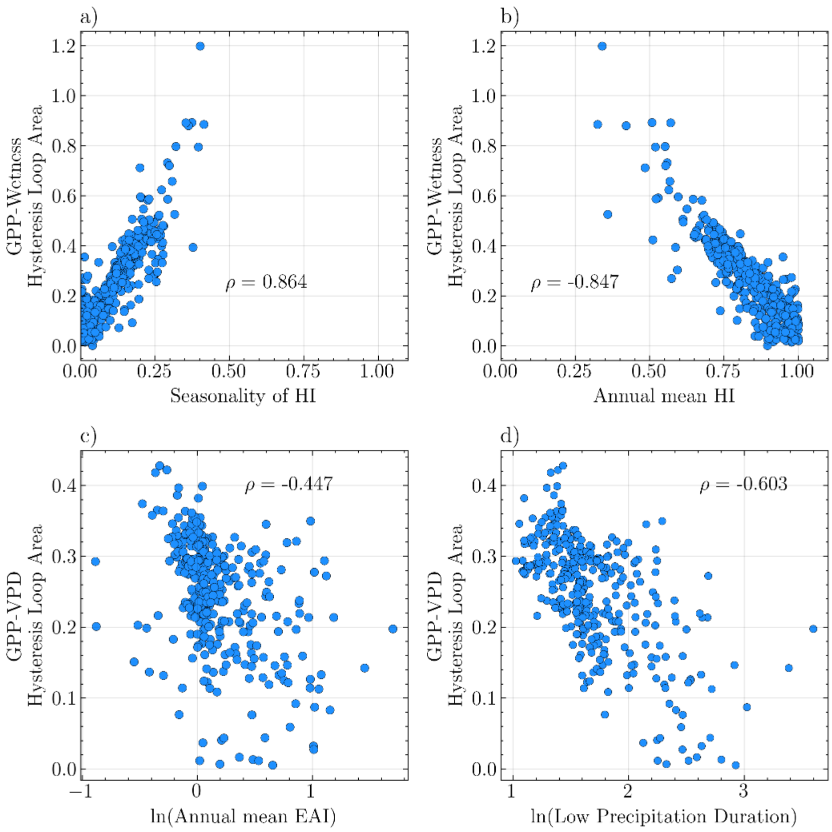


Figure 4-6: Horton Index versus GPP-Wetness Hysteresis: a) Horton Index seasonality versus GPP-VPD hysteresis, b) Annual mean Horton Index versus GPP-VPD hysteresis

The GPP-Wetness and GPP-VPD hysteresis direction is the other primary pattern we found from visually observing individual catchments. The VPD average time of occurrence in general lags GPP by one month. Therefore, plotting GPP = f(VPD) creates a clockwise hysteresis (Fig. 4-7c and f). On the other hand, many of our catchments' mean monthly wetness reaches peak value before GPP; hence GPP = f(Wc) creates a counterclockwise hysteresis (Fig. 4-7b). In contrast, few catchments where peak catchment wetness is attained earlier than GPP produce a clockwise pattern (Fig. 4-7e). These characteristics are primarily driven by catchment EFI, HI, and CUE intra-annual variability. Those catchments with clear clockwise patterns characterize low intra-annual variability of HI and EFI, accompanied by high CUE during the dormant season, which decreases as HI increases.

### 4.4.3. Hydroclimatic Controls on Vegetation Productivity

We explored the intra-annual variability of catchment water supply, atmospheric demand, and vegetation productivity by evaluating relationships among metrics that quantify the climatic dryness/wetness for ecosystem (i.e., EAI), hydrologic dryness/wetness (i.e., HI), and catchment production efficiency (i.e., CUE). The first two metrics make up the Budyko-type Horton Index framework developed by Abeshu & Li (2021). Along with this framework, we use CUE and normalized mean monthly GPP as a third dimension. The patterns created by catchments within the Budyko-space (area bound by water/energy-limit lines) vary with season (Fig. 4-8), which indicates the nonlinear temporal dynamics between EAI, HI, and carbon uptake. The critical pattern from Fig. 4-8 is that catchments are attached to the energy-limit line and hardly productive in carbon uptake during the dormant seasons (e.g., November-February). However, all catchments move upwards along the energy-limit line as the season progresses, and carbon uptake increases from January-Jun. In June-August, most catchments are collected towards a space where HI$\rightarrow$1, EAI$\rightarrow$1 and mean monthly GPP approaches the maximum value. Here, catchments operate at their highest hydrologic and climatic efficiency.

Catchments spread along the water-limit line in August before they started reversing the patterns and finally reached a state where catchments are attached to the energy-limit line and unproductive in December. These patterns are a result of the hysteric relationship between HI and EAI. Along the rising limb of the hysteresis curve (mainly January-August), a contrasting pattern can be seen between Fig. 4-8 and 4-9.

The vegetation carbon uptake increases steadily and reaches maximum vegetation productivity from June to August. In contrast, CUE generally decreases before reaching the minimum efficiency state from June to August. On the falling limb of the hysteresis curve (mainly Sep. – Dec.), total carbon uptake decreases while vegetation uptake efficiency increases. An efficient climatic and hydrologic state for catchment is also a maximum productivity state for catchment vegetation. However, assuming that catchments operate under no nutrient limitations, in terms of available water supply and atmospheric demand, catchments are most efficient in carbon uptake during their dormant periods.

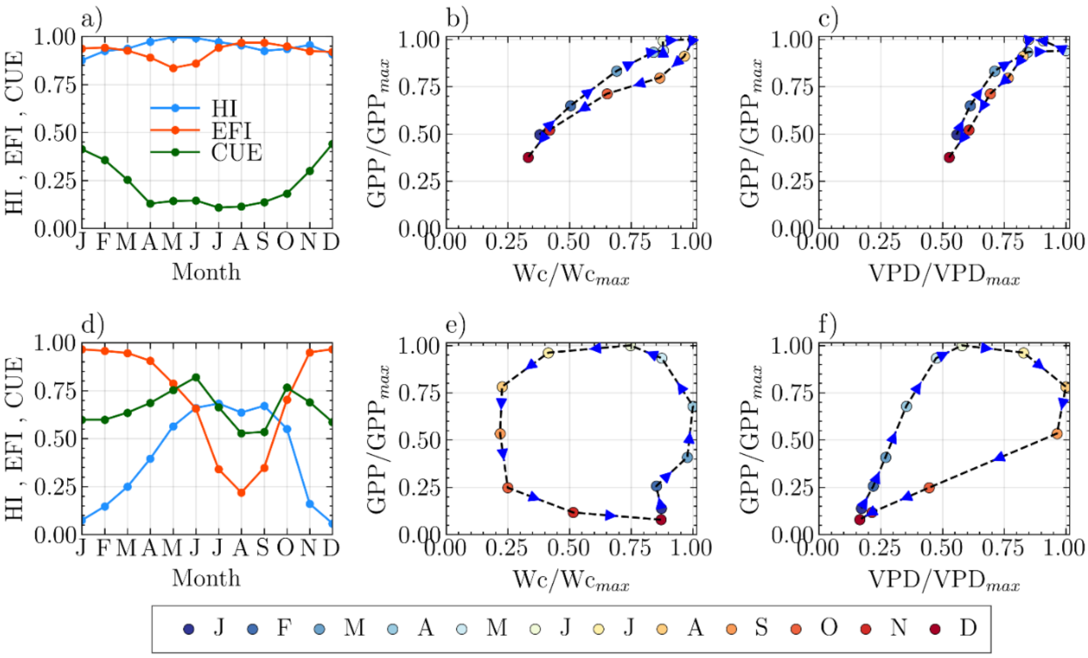


Figure 4-7: Intra-annual variability of HI, EF, and CFE (a, d), GPP-Wetness hysteresis (b, e), and GPP-VPD hysteresis (c, d). The upper row is narrow and clockwise(a,b,c), & the lower is wide and counterclockwise

Catchments that are not in a permanently water-limited state (i.e., HI > EF both intra-annually and annually) (see Fig. 4-7a) switch between water-limited and energy-limited states within a year (see Fig. 4-7d). For instance, from Fig. 4-7d, one can see that the EFI < HI from June-October, which indicates the catchment has switched to a water-limited state. These catchments are under an energy-limited state during the greening up and browning of vegetation. However, they become water-limited catchments during the peak growing periods (mostly June to August). The CUE generally shows a bimodal seasonal pattern in response to these switches between states. The occurrence time of the two peaks depends on the number of months where the catchments stay in a water-limited state. For catchments with a permanent water-limited state, mean monthly HI and EFI have low seasonality and mean monthly HI > mean monthly EFI during most growing months. The corresponding CUE patterns are concave upward. Based on these seasonal patterns, we can generalize that hydrologic variations drive catchment vegetation CUE's seasonality. This suggests that vegetation carbon uptake may be more sensitive to VPD under a water-limited state, as indicated by the poor association of GPP-Wetness and strong negative association of GPP-VPD(Fig.4-3).

## 4.5 Discussions

We investigated the intra-annual variability and connectedness between catchment water supply for vegetation use (Wc), atmospheric dryness (VPD), and vegetation productivity (GPP) using a comparative analysis of 380 catchments distributed across the contagious US.

Our primary aim here is to shed light on three points: i) seasonal characteristics of catchments switching between water-limited and energy-limited states, ii) the cause-effect relationship between hydrologic variation, atmospheric demand, and vegetation productivity, and iii) characterizing catchment vegetation carbon uptake seasonal dynamics with underlying factors. We use mean monthly Wc, VPD, and GPP along with several mean monthly indices, including the HI, EAI, EFI, CUE, and SI.

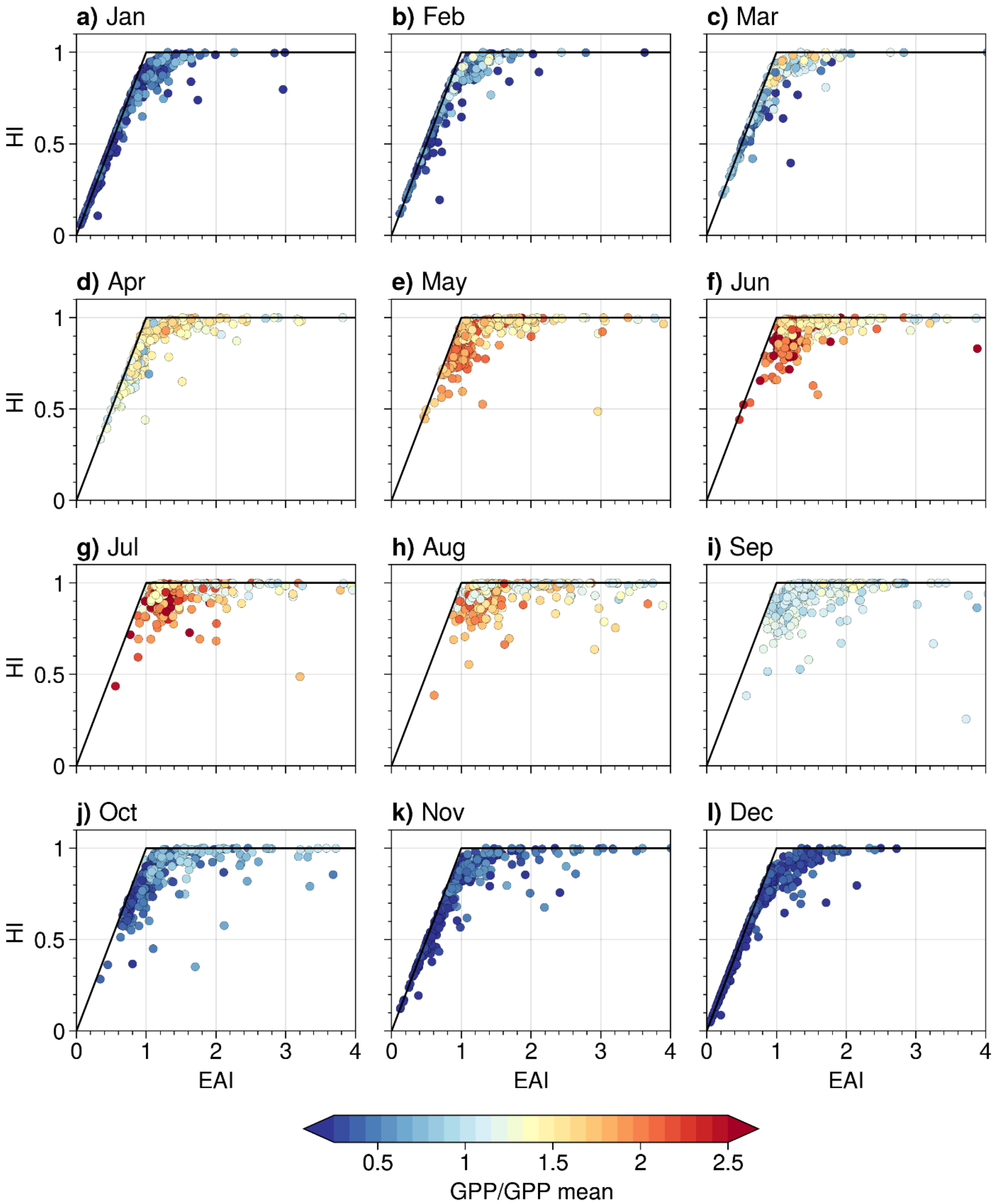


Figure 4-8: Intra annual variability of HI, EAI, and GPP in Budyko-type framework. Each point's scatter plots represent a catchment (380 points per panel). The color bar represents GPP normalized by its climatological mean.

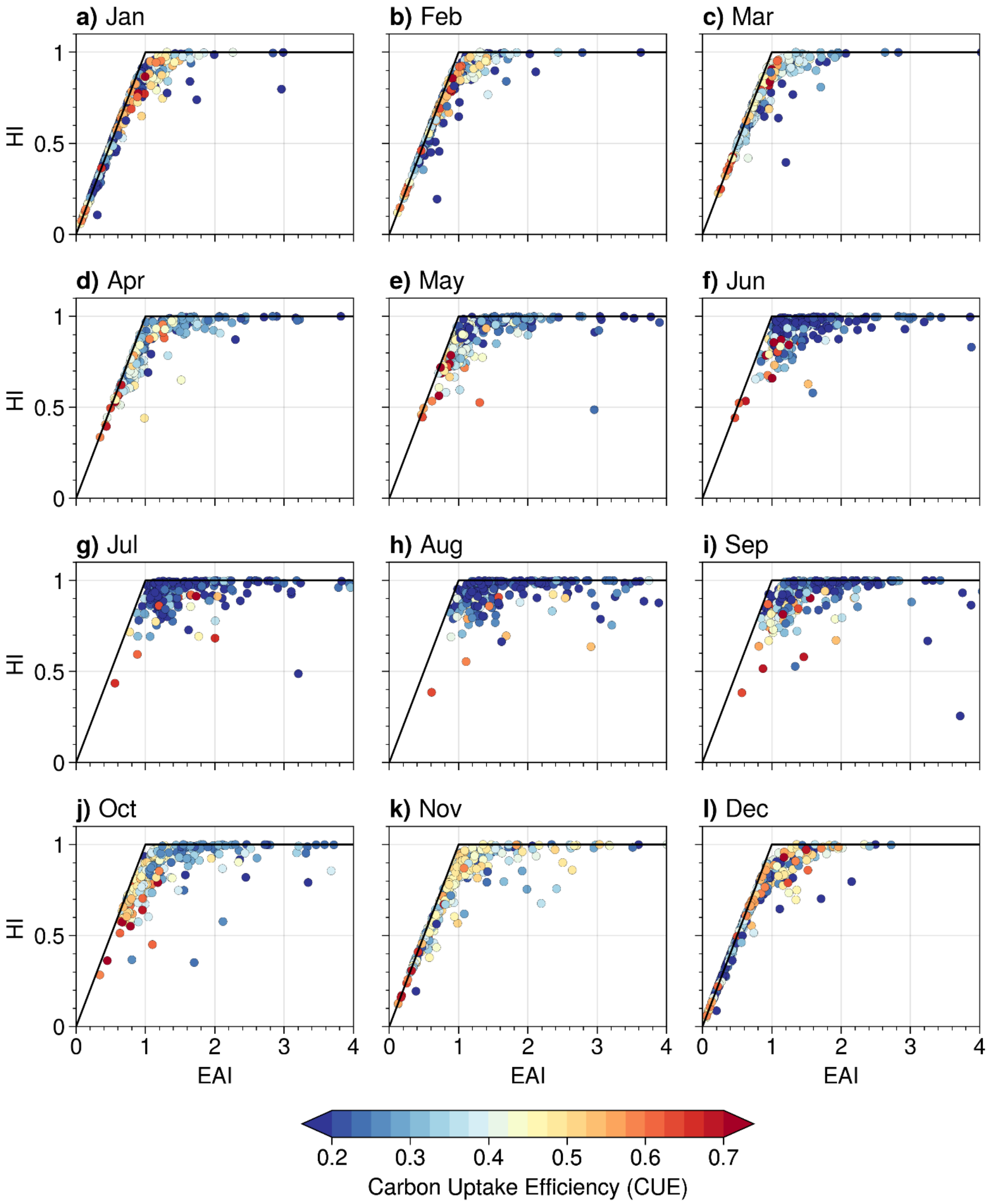


Figure 4-9: Intra annual variability of HI, EAI, and CUE in Budyko-type framework. The color bar is for CUE=GPP/GPPpotential. The scatter plots in each month are 380 points; each point represents a catchment.

Catchment vegetations are under hydrological stress during the peak growing period. This is evident because CUE is generally out-of-phase with hydrologic states (i.e., HI) during the peak carbon uptake period. However, the catchment hydrologic state variations do not explain the periods of hydrologic stress by themselves. It must be interpreted along with catchment energy use efficiency (i.e., EFI). This helps clarify that CUE is inversely related to HI and total carbon uptake for catchments in a water-limited condition, regardless of whether it is permanent or temporary. Catchment becomes more efficient in carbon uptake as it gets drier and drier. In other words, the amount of carbon taken up by vegetation at the expense of one unit of water increases with catchment hydrological stress (i.e., ↑ HI). Seasonally, this is evidenced by the strong association between HI and GPP. However, relative to potential GPP catchment vegetation, carbon uptake efficiency decreases with an increase in HI. This is true for catchments under a permanent water-limited state throughout the year. For other catchments where hydrologic states switch between water-limited and energy-limited within a year, this happens when the catchment is under a water-limited state.

The Wetness-GPP and VPD-GPP causality link accompanied by the lag correlation indicates that the supply-demand-productivity cause and effect process at the catchment scale generally happens in a span of two months. Vegetation responds to the catchment water supply in the same month or at a maximum of one-month lag (Fig. 4-2c). The atmospheric demand lags behind GPP by one month. The time lags between these variables resulted in Wetness-GPP and VPD-GPP hysteric curves (Fig. 4-4 and 4-5). The size of the hysteresis loop (narrow/wide) depends on both intra-annual and long-term hydrologic characteristics. Wetter catchments have wider hysteresis, while narrow hysteresis is typical behavior of dry catchments. Intra-annually, variability of HI accompanied by an out-of-phase pattern with EFI implies a wider hysteresis curve. The narrowness of the hysteresis curve is a signature of a catchment that is efficient in energy and water use but inefficient in carbon uptake relative to the potential. The counterclockwise GPP-Wetness hysteresis is generally expected behavior as water availability drives vegetation growth and response is delayed. However, the clockwise hysteresis curve is counterintuitive. These characteristics are primarily driven by catchment EFI, HI, and CUE. Catchments producing clockwise patterns are characterized by low carbon uptake efficiency, high energy use efficiency, and high water use efficiency (Fig. 7a). Catchments with counterclockwise GPP-Wetness hysteresis show three features (Fig. 7d): i) HI and EFI out-of-phase, ii) CUE in-phase with HI during greening and browning, and iii) CUE in-phase with EFI during peak growing periods.

Climatic and hydrologic factors control catchment vegetation carbon uptake. The collective patterns observed with HI−EAI−GPP (Fig.8) and HI−EAI−CUE (Fig.9) showed that catchment efficiency in water use and energy use does not translate to efficiency in catchment vegetation carbon uptake; rather, it signifies the lowest carbon uptake efficiency state. Catchment hydrologic states are the driving factor when catchment is under an energy-limited state, and climatic factors govern the peak growing periods. The peak period characteristics are more likely to be attributed to increased atmospheric demand, leading to stomatal closures.

## 4.6 Conclusions

This study uses comparative analysis to explore vegetation carbon uptake response to catchment wetness and atmospheric dryness using 380 catchments distributed across the contagious US. Hysteresis patterns between vegetation carbon uptake and catchment wetness and carbon uptake and atmospheric demand are controlled jointly by the seasonal characteristics of the catchment energy and water use. The narrowest hysteresis develops in catchments that operate at their highest hydrologic and climatic efficiency throughout the year, mostly GL and WSSL dominated catchments. Widest hysteresis develops when EFI and HI have strong intra-annual EFI and HI variability and are out of phase. The direction is generally counterclockwise as vegetation response lag behind water availability. However, some catchments show a clockwise pattern. These catchments are dominated by vegetations that respond quickly to water availability but die under increased hydrologic stress, such as grasslands. We also found that vegetation is under seasonal hydrologic stress when the catchment transitions from an energy-limited to water-limited state for catchments not permanently under energy-limited or water-limited. For these catchments, total carbon uptake is strongly positively related to the hydrologic state under an energy-limited condition and inversely associated with atmospheric dryness during a water-limited state. The carbon uptake efficiency follows the patterns of the non-dominant state (i.e., HI during an energy-limited state and EFI during a water-limited state). Catchments that are permanently water-limited are characterized by carbon uptake efficiency of low magnitude and low seasonal variability.  The seasonal patterns of total carbon uptake are opposite to the season carbon uptake efficiency. Vegetation total carbon uptake increases as catchment get drier and uptake efficiency decreases.

# 5 A Simple Empirical Model for Vegetation Carbon Uptake[4]

## 5.1 Introduction

Simple conceptual hydrologic models are often used for catchment process understanding (Berghuijs et al., 2014; Yao et al., 2020; Ye et al., 2012) and as an emulator at a global scale(Liu et al., 2018). These models are preferred because they incorporate essential hydrologic processes and are simple to set up while only requiring limited inputs. Their goal is often to produce hydrologic releases (i.e., runoff and actual evapotranspiration). The model parameters estimations are conducted using observational or reanalysis-based data, commonly streamflow/runoff. Vegetation characteristics are often not represented in this process; if they are, it is usually static characteristics such as vegetation type to aid the runoff simulation. The seasonal dynamics rarely inform the simulated hydrologic releases. Presently, vegetation temporal dynamics data, such as the carbon uptake available through remote sensing or reanalysis-based data for catchment or large scale applications(Jung et al., 2019; Robinson et al., 2018). Hence, taking advantage of these data types, extending simple hydrologic models beyond hydrologic simulation is essential to estimate model parameters and process understanding informed by seasonal vegetation dynamics.

Hydrological models can be fully coupled or partially coupled depending on how they represent vegetation characteristics. Most hydrologic processes models, such as VIC (Liang et al., 1994), HBV (Lindström et al., 1997), Probability Distribution Model (Bartlett et al., 2016a; Moore, 2007), abcd (Martinez and Gupta, 2010), and THREW (Tian et al., 2008), fall under the latter category. They introduce vegetation

[4] This work is in preparation to be submitted for publication to as Abeshu, G. W., & Li, H. Y. A simple dynamic vegetation model underpinned by the generalized proportionality hypothesis.

only to achieve a more realistic simulation of the rainfall-runoff processes, often simply by using vegetation type to estimate potential evapotranspiration. The fully coupled models, on the contrary, can explicitly and simultaneously solve hydrological and vegetation dynamics over space and time. Biome-BGC (Hidy et al., 2016), BEPS-TerrainLab (Govind et al., 2009), Tethys-Chloris (Fatichi et al., 2016), and RHESSys (Tague and Band, 2004) are a few examples of such models. At regional and global scales, most earth system models are capable of process-based dynamic vegetation representations, thus simulating both water and carbon cycle; this includes earth system models like CESM (Hurrell et al., 2013), E3SM (Golaz et al., 2019), LPJ-GUESS (Smith et al., 2001), and ORCHIDEE (Krinner et al., 2005).

Given the spatial heterogeneity across catchments, understanding water-carbon interactions at the seasonal scale is mainly performed using fully coupled models. However, we frequently use lumped and semi-distributed catchment level hydrologic models to understand catchment hydrologic processes (Burnash, 1995; Bartlett et al., 2016b, 2016a; Martinez & Gupta, 2010; Wang, 2018). These models often introduce vegetation types in catchments to obtain a more realistic simulation of the hydrologic characteristics without considering vegetation phenology. Hence, they lack the representations of seasonal vegetation dynamics. Therefore, it is substantial to enhance the capacity of such models. Here, we aim to demonstrate a means for extending the partially coupled model type's capacity to be informed by seasonal vegetation dynamics or simulate seasonal vegetation dynamics.

This study couples the functions developed in Chapters 2 and 3 with a conceptual hydrologic model for a global-scale application. We demonstrate the capacity of the simple hydrologic models to simulate monthly gross primary productivity with limited input variables using the abcd model as a case study. The remainder of this chapter is organized as follows: Section 5.2 presents the data employed, and section 5.3 describes the method. Results and discussion are presented in section 5.4, followed by a summary in section 5.5.

## 5.2 Data

This study uses global climate forcing, actual evapotranspiration, and gross primary productivity data. The climate forcing data are from the WATCH Forcing Data methodology applied to ERA-Interim (WFDEI), which provides daily climate data at a half-degree spatial resolution(Weedon et al., 2014). The data is based on ERA-Interim reanalysis data sets using the Global Precipitation Climatology Centre (GPCC) bias correction target for monthly rainfall and snowfall sums. The WFDEI data set covers the period from 1971 to 2012. The forcing variables employed here include minimum and maximum temperatures, precipitation, snow, short wave solar radiation, and relative humidity (Fig. 5-1). WFDEI data used in this study is obtained from the Inter-Sectoral Impact Model Intercomparison Project (ISIMIP) repository. The actual evapotranspiration and gross primary productivity (GPP) are from FluxCom(Jung et al., 2019). FluxCom provides GPP and ET data produced from remote sensing using machine learning trained with and without inputs from climate forcing. We use the RS+METEO product generated from an ensemble of three machine learning methods, including random forest, artificial neural network, and multivariate adaptive regression spline (Jung et al., 2019). FluxCom product is also available for different climate forcing datasets, including CERES_GPCP, CRUNCEP_v8, GSWP3, and WFDEI. Here, for consistency, we use GPP and ET data produced with inputs from WFDEI climate forcing variables (Fig. 5-2). Both WFDEI and FluxCom data were extracted for the land cells. For calibrating the ***abcd*** parameters, we also use gridded runoff data simulated by the VIC model.

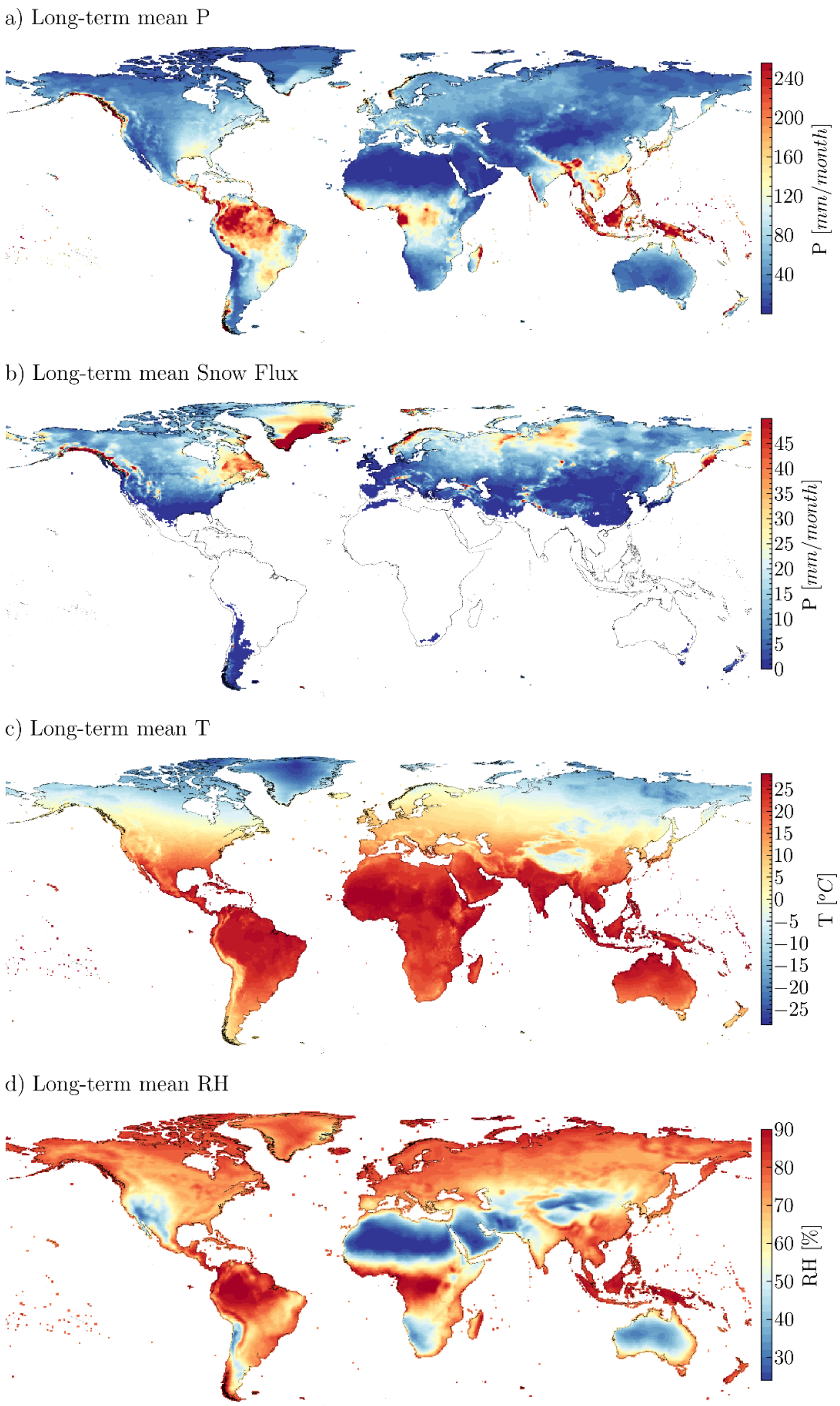


Figure 5-1: Long-term mean of WFDEI climate forcing data at 0.5-degree spatial resolution and monthly temporal resolution: a) precipitation, b) snow flux, c) mean temperature and d) relative humidity.

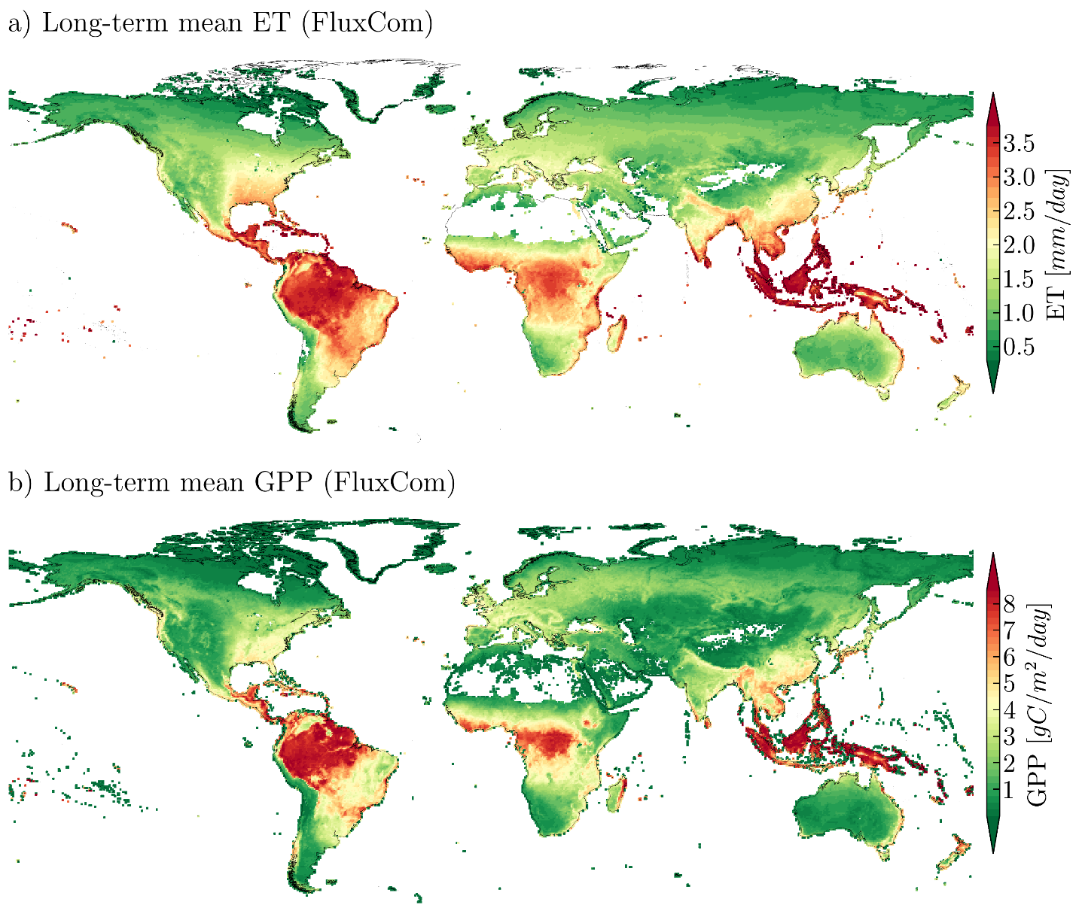


Figure 5-2: Long-term mean ET and GPP computed from FluxCom dataset at 0.5-degree spatial and monthly temporal resolution.

## 5.3 Methods

### 5.3.1 The *abcdm* Model

We couple the GPP-ET function developed in Chapter 3 with a simple water balance model for a global-scale application, the **abcd** model (Martinez and Gupta, 2010), adopted for global scale runoff generation in Xanthos(Liu et al., 2018). Xanthos is a global hydrologic model which provides hydrological estimation for GCAM (see. Chapter 5 for details ). Though the function is simple enough to be coupled with any hydrologic models outputting ET, the ***abcd*** is preferred because it incorporates essential hydrologic processes and is simple to set up while only requiring a few inputs, including air temperature, precipitation, and potential evapotranspiration. The goal for these models is to produce hydrologic releases (i.e., runoff and actual evapotranspiration).

Here, we extend them to simulate carbon uptake. The following subsections provide a general overview and structure of the model for completeness. We refer readers to Martinez and Gupta (2010) and Liu et al. (2018) for a detailed understanding.

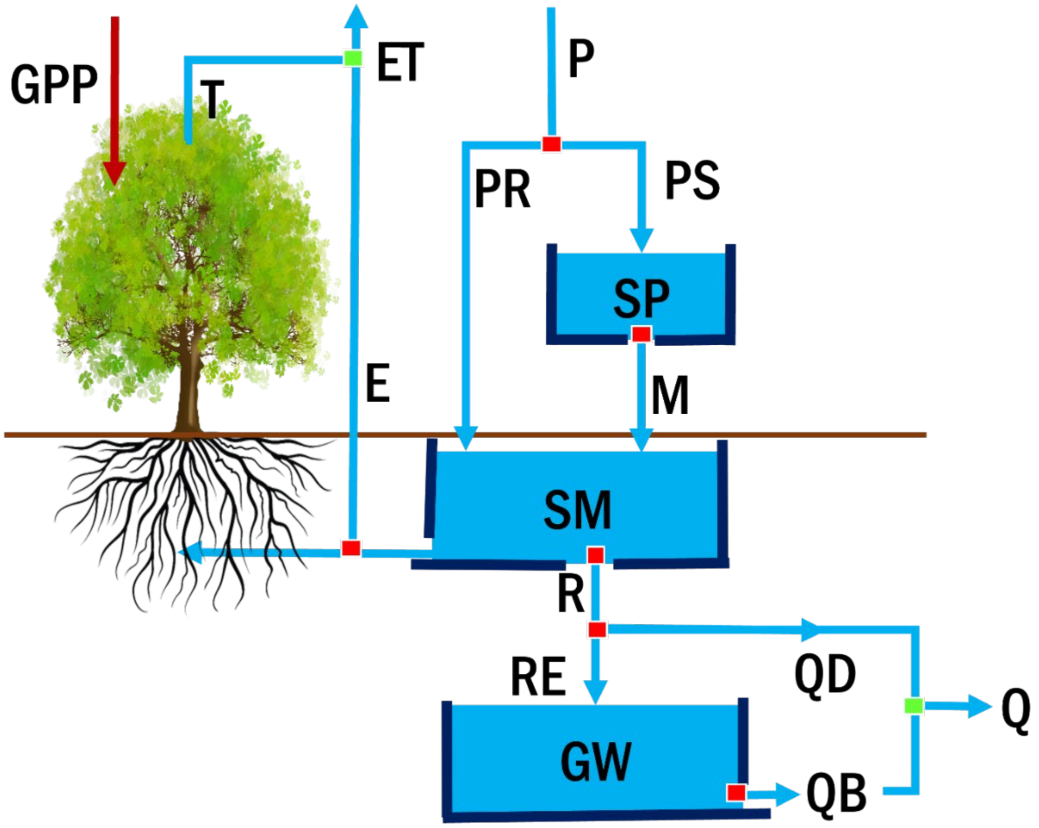


Figure 5-3: Conceptual diagram for coupled abcd model and the two-parameter GPP functional equation.

The ***abcdm*** is a spatially lumped model which depicts a catchment or grid as a collection of three storage buckets arranged in series. The incoming total precipitation first partitions into snow and rain components. The snow component joins the first storage bucket, while rain directly joins the second bucket. The second bucket characterizes the soil water storage, and its incoming flux is liquid precipitation (i.e., rain plus snowmelt from the first bucket). The outgoing fluxes are direct runoff, recharge, and evapotranspiration. The recharge component joins the groundwater storage (the third bucket), and baseflow is a leakage from the groundwater storage. The total runoff is the sum of baseflow and direct runoff. The model has five parameters;

parameters ***a*** and ***b*** describe the soil water storage bucket, ***c*** and ***d*** characterize the groundwater storage bucket, and parameter ***m*** characterizes the first bucket (Fig. 5-3). The acronyms in Figure 5-3 are defined as follows: PR and PS are rain and snow precipitation; SP is snowpack, M is melt, SM is soil moisture, GW is groundwater, ET evapotranspiration, R is water available, QD is fast runoff, QB is the slow runoff, and Q is total runoff

### 5.3.2 Coupling GPP-ET Function with Hydrologic Models

The ***abcd*** model is a framework for simulating hydrologic releases (i.e., evapotranspiration and discharge). We extend its capacity to simulate seasonal vegetation dynamics, specifically carbon uptake (Fig. 5-3). This has two main advantages. First, the model vertical (evapotranspiration) and horizontal (runoff) release temporal characteristics can be informed by vegetation dynamics even for such a simplified model structure. Secondly, it extends the capacity of simple traditional hydrologic models beyond just simulating hydrologic processes. We use the GPP−ET functional relationship developed in Chapter 3, which is given by $GPP_m = \beta E_m + \alpha\overline{E}$. Where $\overline{GPP}$ and $\overline{ET}$ are long-term mean GPP and ET, respectively. β and α are the parameters of the GPP−ET function corresponding to slope and intercept coefficient of the linear relationship. The upper and lower bounds for β and α were determined using global GPP and ET long-term data. Unlike Chapter 3, where we determined the parameters bound for different vegetation groups, we use single upper and lower bounds for all grids regardless of their cover type. To obtain the bounds, we first determined the long-term mean ecosystem water use efficiency (EWUE), a ratio of long-term mean GPP to long-term mean ET at each grid. The 97.5$^{th}$ percentile of global gridded EWUE was then taken as the maximum global value to avoid outliers, which yielded 3.7. We rounded this value to 4.0 and defined the bounds of the parameters as $0 < \beta \leq 4.0$ and $-4.0 \leq \alpha \leq 4.0$.

The ***abcdm*** model ET is estimated with a generic equation that determines ET as an exponential function of potential evapotranspiration. The equation abcd model used to estimate evapotranspiration opportunity has a similar functional form as conceptual functions with generalized proportionality background (Wang and Tang, 2014). Hence, we repace the ET equation with the Horton Index framework developed by Abeshu & Li (2021), where for grid-scale catchment, wetness is substituted with the ET opportunity.ET opportunity is defined as the summation of actual evapotranspiration during month *m* and soil water storage at the end of month *m*. Substituting ET opportunity for catchment wetness comes with an underlaying assumption that groundwater discharge from a grid is relatively small.

### 5.3.3 Determination of the Coupled Models Parameters

The coupled model has seven parameters, five being ***abcd*** parameters and two being GPP−ET function parameters. We determine these parameters in two stages using the Shuffled Complex Evolution (SCE-UA) method(Duan et al., 1992; Houska et al., 2015). The first stage aims to determine the two GPP−ET function parameters using ET and GPP data from FluxCom. We use a single objective function to calibrate GPP over 25 years (1979 to 2001). For this stage, the calibration is performed at each land grid. The second stage calibration is a multiobjective and aimed at estimating the ***abcd*** model parameters. One of the objective functions is for ET and the second one corresponds to runoff. Xanthos has 235 basins globally; these basins are created for the convenience of studies on the GCAM platform. For the ***abcd*** model parameter calibration, we use these basins for calibration. Calibrating a model at each land grid at a global scale consumes computational resources and time. Therefore, we calibrate the parameters at the basin scale. In other words, the abcd parameters are constant across grids of a given basin. The objective function is obtained from basin total, i.e., basin total ET and basin total runoff. Using the optimal parameter sets from both stages, we simulated monthly GPP from 2002 to 2013 and evaluated it against FluxCom GPP. The 2002 – 2013 data is unused in the parameters estimation process.

### 5.3.4 GPP-ET Functional Parameter Estimation from Climate Variables

Chapter three demonstrates that the GPP-ET functional relationship parameters at the catchment scale can be estimated a priori from catchment climate variables. We repeated this procedure for the gridded dataset. Figure 5-3 depicts the climate variable and the indices used in the analysis, computed as follows.

1) *Vapor pressure deficit(VPD)*: Using Magnu's formula(Parish and Putnam, 1977), we computed daily maximum and minimum saturation vapor pressure ($e_s$) from maximum and minimum temperatures, respectively. From the mean daily $e_s$ (i.e., mean of daily maximum and minimum $e_s$) and relative humidity, VPD is computed as $(1 - RH) * e_s$. We then computed the mean monthly VPD to depict the long-term mean seasonal characterstics. We use the mean and minimum of mean monthly VPD for estimating the parameters (Fig. 5-4a).
2) *Annual mean snow fraction (Sf)*: is the ratio of annual mean snow flux to the annual mean total precipitation. It ranges between 0 and 1, indicating regions with no snow contribution and liquid precipitation, respectively (Fig. 5-4b).
3) *Precipitation seasonality index (SIp)*: is the sum of the absolute deviations of the mean monthly precipitation from the monthly mean divided by the annual mean precipitation (Walsh & Lawler, 1981). It summarizes the monthly precipitation degree of variability within a year. The smallest value, zero, indicates that

precipitation is uniformly distributed throughout the year, whereas the maximum value, 1.833, indicates that only one month contributed to the annual total (Fig. 5-4c).

4) *Annual mean shortwave solar radiation ($R_s$)*: The mean monthly $R_s$ at each grid represent the regime curve for available photosynthetic radiation. The two essential characteristics we use are the mean and minimum of the regime curve (Fig. 5-4d).

We applied two methods in estimating the parameter values a priori: the multivariable linear regression and machine learning, specifically the boost. The multivariable linear regression sufficiently predicted the two parameters GPP−ET function at the catchment level (see Chapter 3). However, the sample size was insufficient to apply a machine learning method. Here, we apply a selected machine learning method in addition to multivariable linear regression for two reasons. First, the multivariable regression in Chapter 3 is based on CONUS data only; therefore, there is no guarantee that one can obtain a similar sufficiency level at the global scale. Secondly, more than 50000 land cells are available globally, which allows an efficient implementation of machine learning techniques. Given the accessibility and low computational requirements, several machine learning approaches can be easily applied to such datasets. We use an eXtreme Gradient Boosting (XGBoost) method, a gradient tree-boost algorithm widely used for its high efficiency and performance (Abeshu et al., 2022; Chen and Guestrin, 2016). XGBoost is a scalable end-to-end tree boosting system, a framework that develops strong learners by combining weak learners sequentially(Chen and Guestrin, 2016).

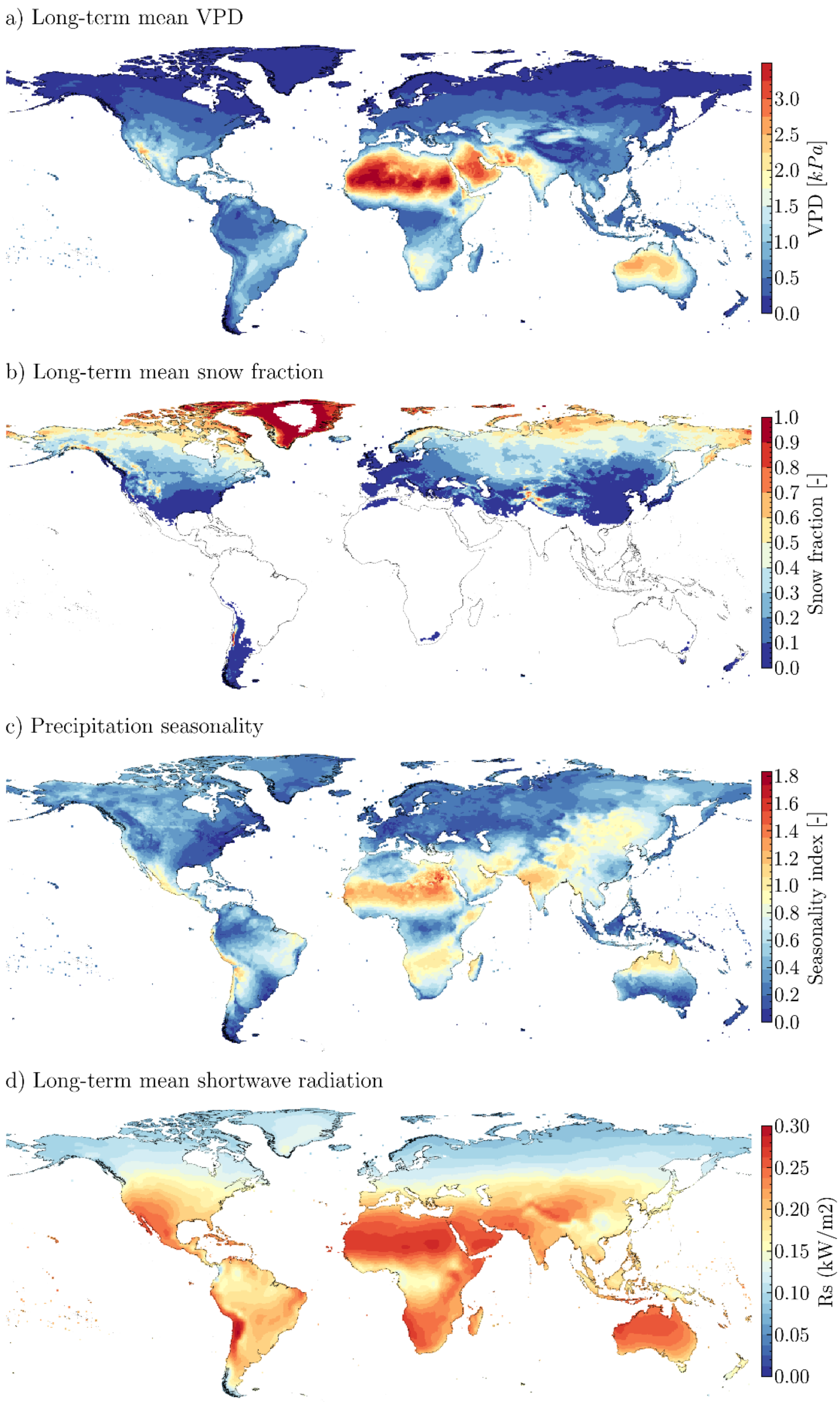


Figure 5-4: Long-term mean of WFDEI climate forcing data at 0.5-degree spatial resolution and monthly temporal resolution: a) precipitation, b) snow flux, c) mean temperature and d) relative humidity.

We determine the XGBoost hyperparameters using Optuna, an optimization framework designed specifically for machine learning objectives(Akiba et al., 2019), and the

Nondominated Sorting Genetic Algorithm II (NSGAII) parameter sampler(Deb et al., 2002) is used to generate the parameters. For a detailed procedure for the XGBoost application, we refer the readers to Abeshu et al. (2022). We use ten-fold cross-validation, 70% of the dataset for training and 30% for testing.

### 5.3.5 Statistical Analysis

We use several statistical metrics to quantify the degree of agreement between our dataset and predicted magnitudes. This includes the Kling-Gupta Efficiency (KGE)(Gupta et al., 2009), coefficient of correlation (R), and normalized root mean squared error (NRMSE). KGE ranges between $-\infty$ to 1.0, where 1.0 indicates perfect agreement. For reference, if the predicted value is constant throughout the study period and equal to the monthly mean, it yields KGE equal to -0.41. R ranges between -1 and +1; the magnitude indicates the degree of agreement, while the sign implies whether it is direct (+) or inverse (-). For XGBoost optimization, we use a coefficient of determination, $R^2$.

## 5.4 Results and Discussions

The first calibration stage aims to obtain $\beta$ and $\alpha$ values using FluxCom GPP and ET data. Figure 5-5 depicts the estimated $\beta$ and $\alpha$ values (Fig. 5-5c and d) and the GPP−ET functional model performance (Fig. 5-5c and d). The GPP-ET function performed reasonably well; ignoring non-vegetated lands such as the Sahara desert and Green land, we obtained ~57200 land grids. KGE $\geq$ 0.5 and $\geq$ 0.8 at 98.5% and 88.4% of the grids during the validation period, respectively. This implies that the slope ($\beta$) and intercept coefficients ($\alpha$) are estimated at a reasonable degree of accuracy and can be employed for future GPP estimation given ET. The slope coefficient spatial patterns generally correspond with vegetation patterns across the globe, showing higher magnitudes in forested ecosystems and lower dry places. While it is mostly > 0 in lower latitude grids, the $\alpha$ becomes < 0 in higher latitude grids, generally similar to snow fraction global patterns. Given that the snows dominate the dormant vegetation period vegetation, and the intercept of the GPP-ET function also corresponds to this period, the pattern is reasonable.

The second stage calibration estimates the ***abcd*** model parameters at 235 Xanthos basins. These parameters are uniform across a given basin. Figure 5-6 shows basin-level performances with the optimal parameter sets. KGE is ≥ 0.5 for ~85% and ≥ 0.8 for ~ 55% of the 235 basins, indicating that the model can reliably simulate ET for input into the GPP-ET function. These results are at the basin scale, and the number of grids within the 235 basins ranges from 5 to 3514. Hence, the basin level calibration does not guarantee good performance across all grids. Specifically, in some of the largest basins like the Amazon (2002 grids), Yenisey (1723 grids), Ob (1555 grids), and Congo (1234 grids) basins, the basin-scale performances may not translate to the grid. Note that these are not the top four basins. Since many of the basins in Xanthos have made-up names, after ranking them based on the number of grids within them, we chose four widely known river basins among the top ten. This is essentially one of the drawbacks of the basin-level calibration strategy. Overall, the second stage calibration reasonably captured the basin's temporal characteristics with all its drawbacks and merits.

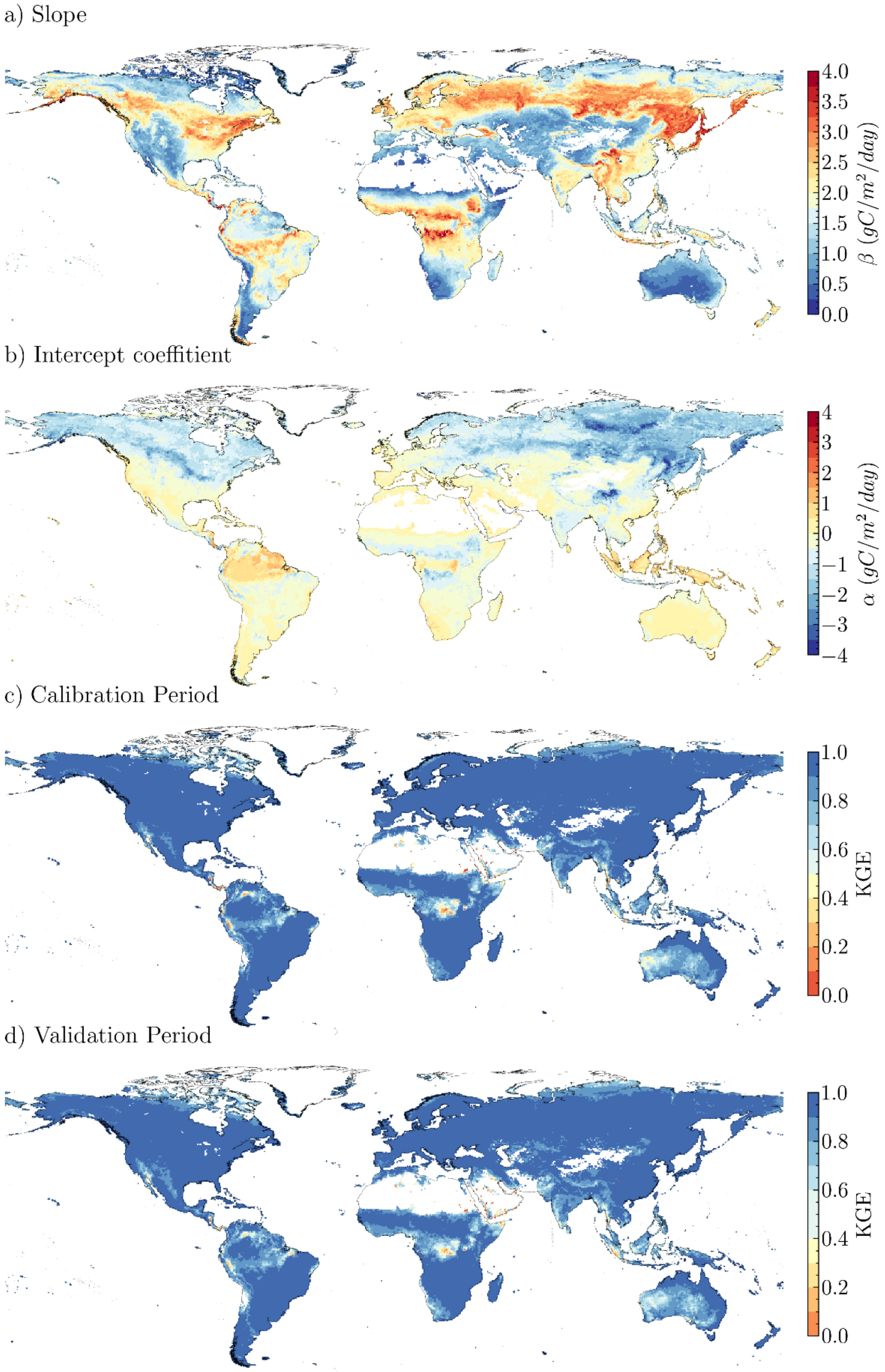


Figure 5-5 : Slope and intercept coefficients for the two-parameter GPP functional equation (a, b).The two-parameter GPP function performance: c) calibration (1979-2000) and d) validation (2001-2013) period.

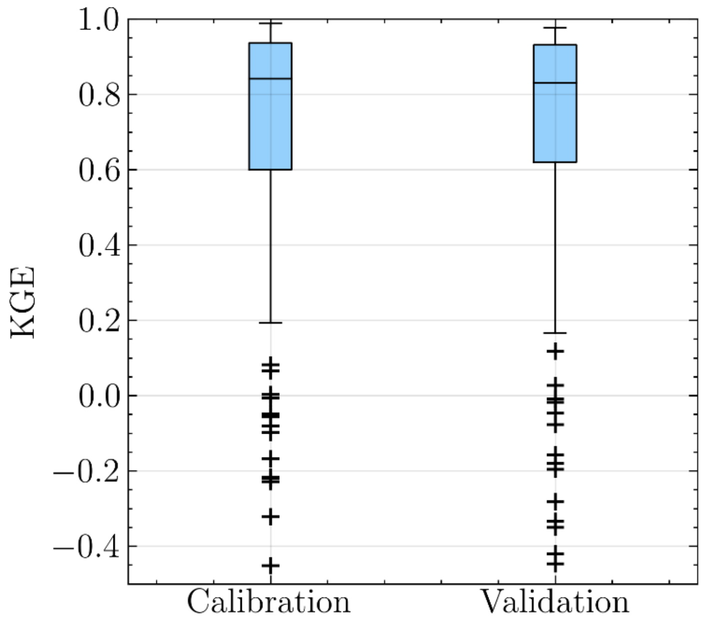

Figure 5-6: Performance of the abcd model

We used the two parameters estimated from the first stage and the five parameters estimated from the second stage calibrations to simulate monthly GPP between 2002 to 2013. Figures 5-6 to 5-7 show the grid level long-term mean, R, and NRMSE. R is used to evaluate if the simulation captures the timing of seasonal GPP patterns, while NRMSE is used to measure the magnitude difference. More than 77 % of the grids showed $R \geq 0.6$, and about 69% have $NRMSE < 0.5$, indicating substantial agreement with the FluxCom GPP. The simulated GPP performed reasonably well with most of the grids, while there are also areas it performed poorly. For instance, near the equator towards the south show negative R, indicating that the simulated GPP and FluxCom GPP are out of sync. These problems are specifically noticeable in the Amazon basin and the Congo basin. First, the issue may result from climatic forcing as it tends to show some systematic spatial pattern along a longitudinal direction below the equator. Secondly, it may result from the lumped basin parameter estimation discussed earlier.

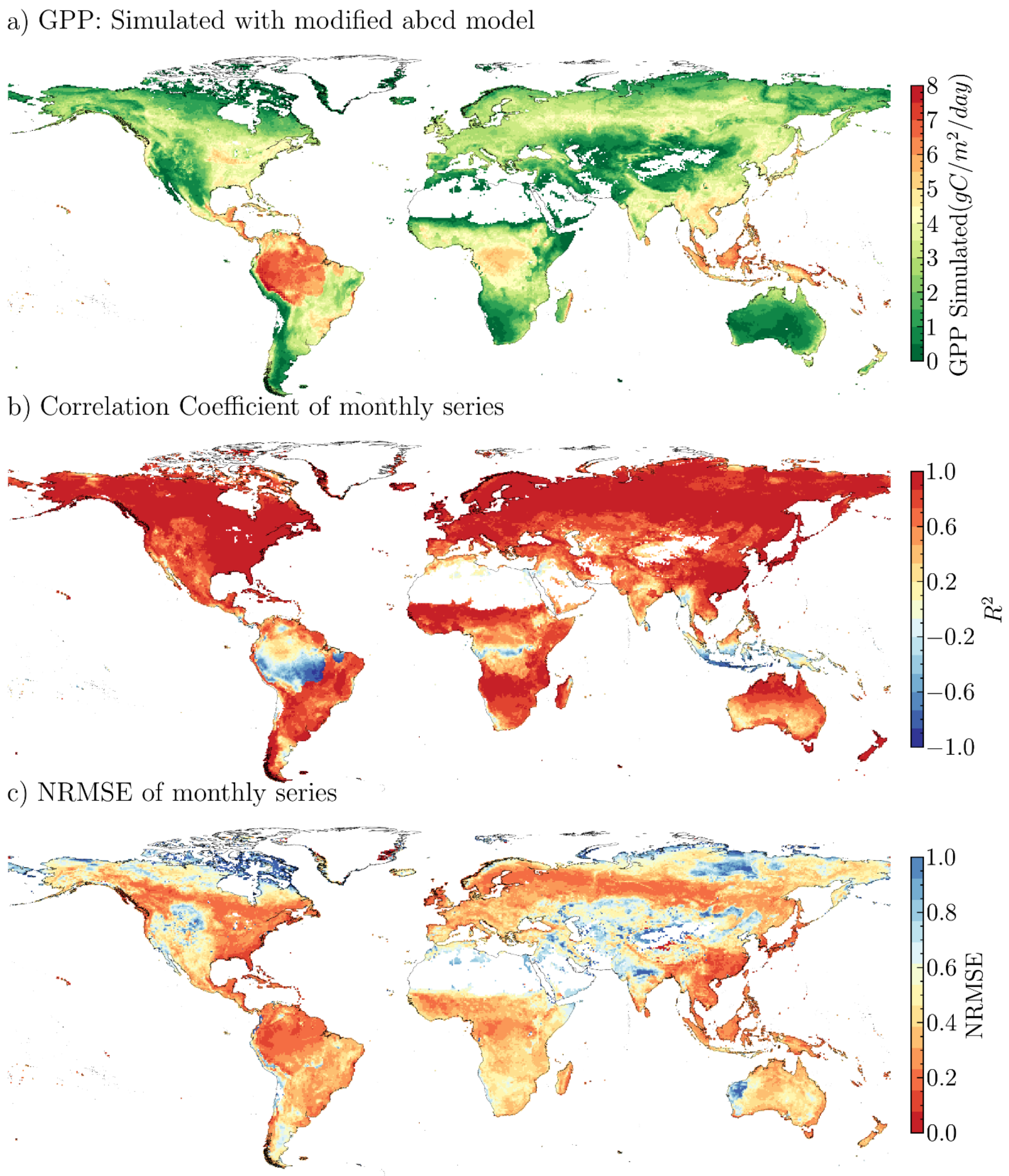


Figure 5-7: Evaluation of GPP simulated with coupled ***abcd*** and two-parameter GPP function against FluxCom GPP product at a global scale.

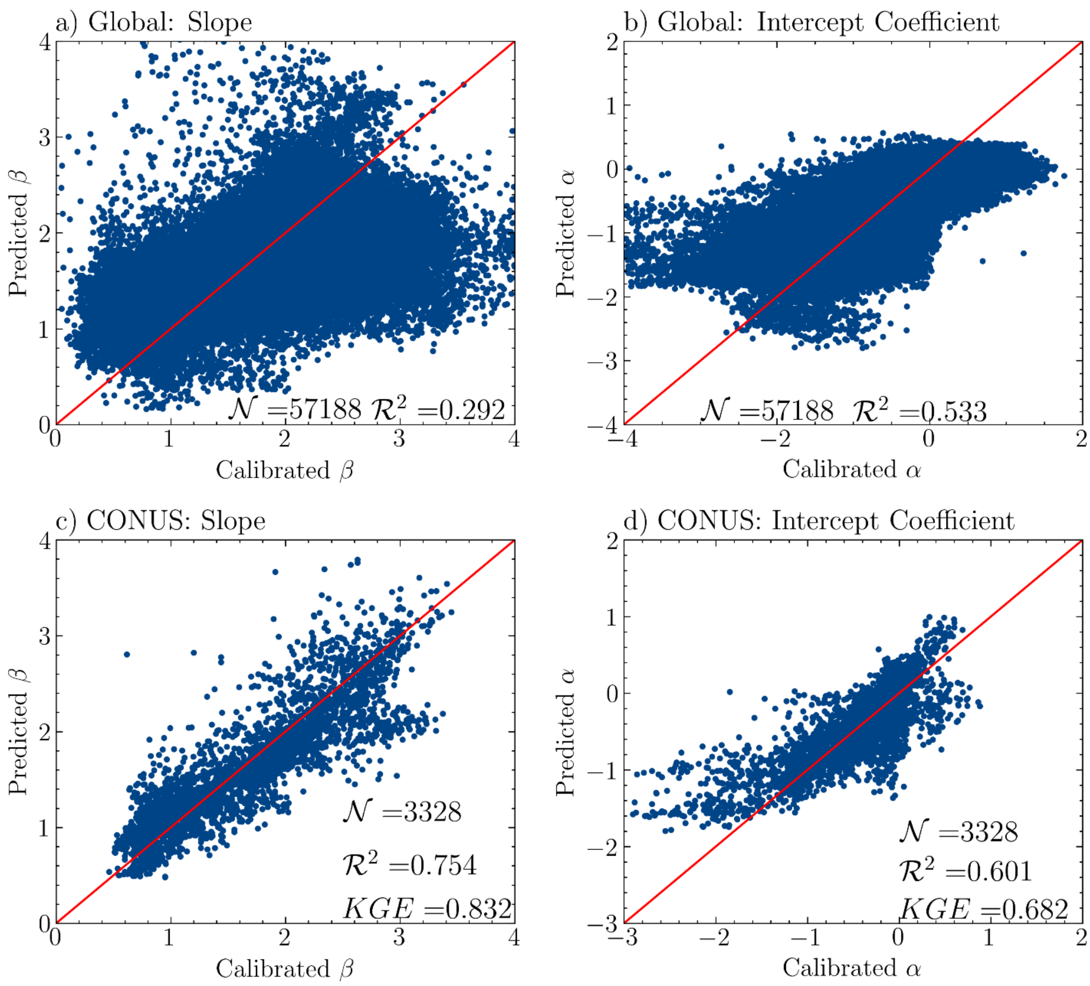


Figure 5-8: Slope and intercept coefficients predicted from climate variables versus those estimated through calibration: a) and b) are global slope and intercept coefficient, c) and d) are CONUS slope and intercept coefficient.

Further, we explored if the first stage parameters can be determined from climatic variables on a global scale. Initially, we developed multivariable regression using the four climatic indicators described in section 5.3.4. We used monthly mean VPD, monthly mean Rs, precipitation seasonality index, and long-term mean snow fraction for the slope parameter. For the intercept coefficient, monthly mean values of VPD and Rs were replaced with the minimum mean monthly values.

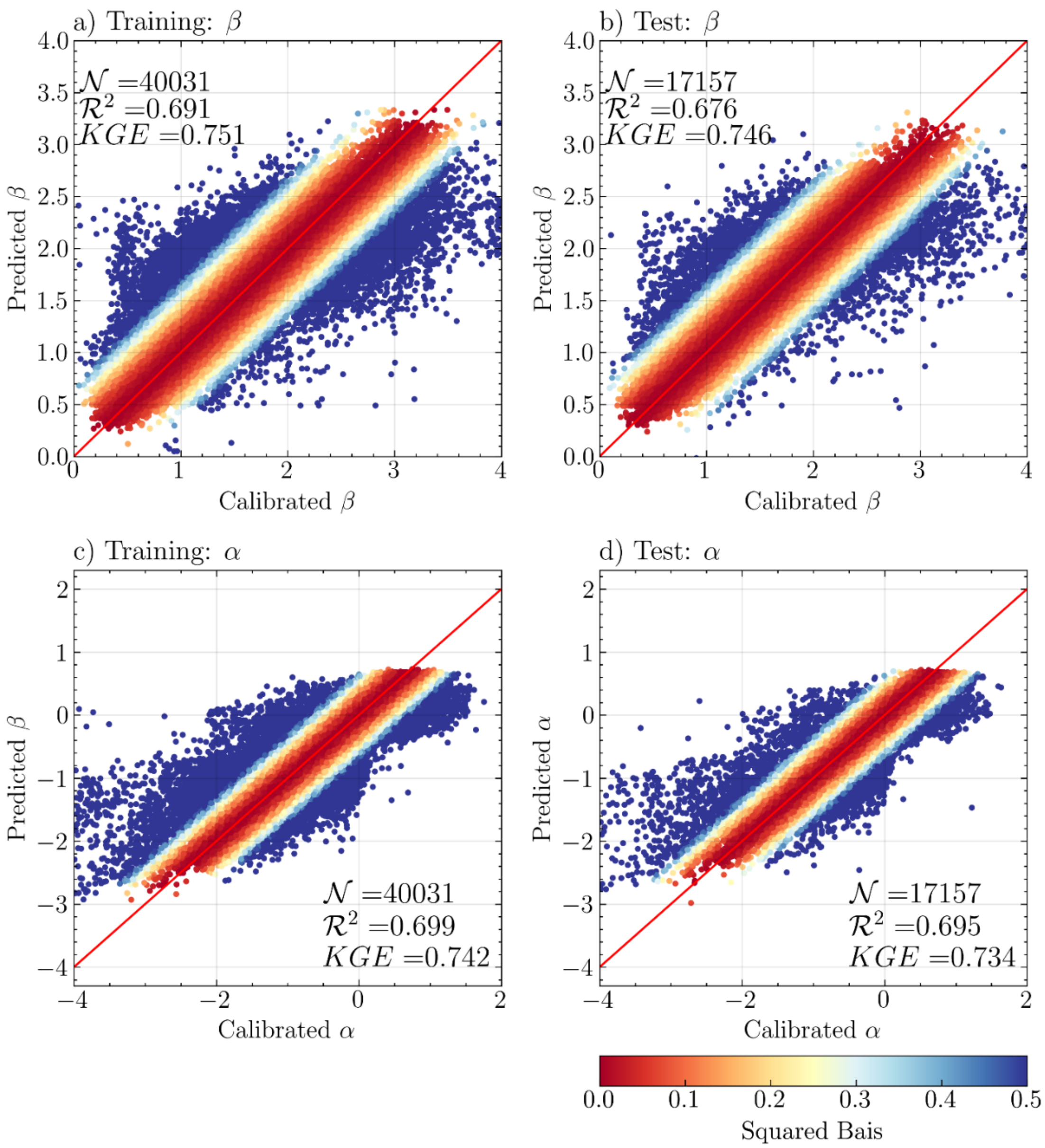


Figure 5-9: XGBoost results for β and α during training and testing. N is the number of samples. The squared bais is the square of the difference between actual and predicted results.

The global scale linear regression performance is very poor for both parameters (Fig. 5-8a and b); therefore, it cannot be used for prediction purposes. We then extracted grids within the continental United States (CONUS) and repeated the procedure (Fig. 5-8c and d). The result showed KGE = 0.832 and $R^2$ = 0.754 for β, and KGE=0.682 and $R^2$ = 0.601 for α. This supports the results presented in Chapter 3. Since the global multi regression function performed poorly, we applied a machine learning technique

(XGBoost) using the same climatic variables. The result shows that these variables can reasonably predict the GPP-ET functional relationship parameters (Fig. 5-9). Hence, although the multi regression method has failed to detect these parameters as factors controlling the GPP-ET relationship across the globe, the performance of the machine learning method shows that climatic factors determine the type of linear relationship between GPP-ET. In other words, whether the linear relationship is steep, moderate, or mild is determined by climatic characteristics.

## 5.5 Summary

This study aims to demonstrate how we can extend conceptual hydrologic models' capacity beyond simulating the hydrologic process only. Specifically, the objective is to couple the GPP-ET function developed in Chapter 3 with Xanthos (a global hydrologic model developed based on ***abcd***). Xanthos has five parameters, and the GPP-ET function has two parameters. The calibration is performed in two stages, where the first stage estimates the slope and intercept coefficient of the GPP-ET function, and the second stage estimates the Xanthos parameters. The first stage calibration is at grid level using GPP and ET data from FluxCom, while the second stage is performed at basin level using WFDEI forcing data and FluxCom ET. We also applied a multilinear regression model and XGBoost (a machine learning technique) to evaluate climatic variables' capability to predict the type of GPP-ET functional relationship.

The first stage calibration performed reasonably well globally, with high KGE values in most grids. The slope parameters showed spatial patterns which correspond to global vegetation patterns. On the other hand, the intercept coefficient is generally $< 0$ in high latitude regions. The second stage calibration also produced basin-level ET reasonably well. The monthly GPP was simulated by combining parameters from both stages to be evaluated against FluxCom GPP. The results showed that the simulated GPP and FluxCom GPP temporal patterns agree reasonably well, except for regions just below the equator where it shows opposite patterns. This is likely attributed to the bais in forcing data, an issue with basin level second stage calibration, which is amplified in large basins or both. In terms of magnitude, the simulated GPP compared reasonably well in most grids, as indicated by lower NRMSE values. The multilinear regression between climatic variables and GPP-ET parameters (i.e., β and α) performed poorly on a global scale but reasonably well for CONUS. However, applying the machine learning technique to the global dataset showed that the climatic variables can reasonably predict β and α. Like findings in Chapter 3, this indicates that at the global scale, long-term climatic characteristics, including VPD, precipitation seasonality, snow fraction, and solar radiation determine the type linear relationship (i.e., steep, moderate, or mild slope) between GPP and ET. Our analysis concludes that the GPP-ET functional relationship applies globally and can be coupled with simple hydrologic models and simulate monthly GPP reasonably well.

# 6 Implications of Soil Water Storage Variations on Streamflow Mediated by Water Management[5]

## 6.1 Introduction

Reservoirs are pivotal in fulfilling society's water demands in multiple sectors, including irrigation, hydropower production, flood control, industrial and domestic water supply, navigation, and recreation. There are 6,862 large reservoirs included in the Global Reservoir and Dam (GRanD) dataset (Lehner et al., 2011). Based on their primary purposes, 1,789 are irrigation reservoirs with a total storage capacity of ~1,100 billion $m^3$; 1,541 are hydropower reservoirs with a total storage capacity of ~3,880 billion $m^3$; 542 are flood-control reservoirs with a total storage capacity of ~502 billion $m^3$; and the rests are water supply, navigation, or recreation reservoirs.

Following an approach initially implemented by Hanasaki et al. (2006), most Global Hydrologic Models (GHMs) treat reservoirs as either irrigation or non-irrigation reservoirs (Best et al., 2011; Döll et al., 2009; Hanasaki et al., 2008; Pokhrel et al., 2012; Schaphoff et al., 2018; Voisin et al., 2013; Wisser et al., 2010). This approach requires lumping all reservoirs where irrigation is not a primary purpose into a single category. Several other studies have employed this approach with some modifications, including H08 (Hanasaki et al., 2008), MATSIRO-TRIP (Pokhrel et al., 2012), WaterGAP2 (Döll et al., 2009), WBMPlus (Wisser et al., 2010), and LPJmL4 (Schaphoff et al., 2018). GHMs like ORCHIDEE (Guimberteau et al., 2012) only include representations of irrigation reservoirs. The level of difference one may observe in the representation of irrigation reservoirs across GHMs mainly arises from a lack of consensus on the appropriate approach for delineating the spatial extent that is

[5] This work is in preparation to be submitted for publication to Journal of Hydrology as: Abeshu, G.W., Fuqiang Tian, F., Hongchang Hu, H., Yuan Zhuang, Y., Hejazi, M., Sean Turner, S., Thomas Wild, T., Mengqi Zhao, M., Chowdhury, K., Vernon, C., and Li, H., A new water management module for global hydrologic models

dependent on a particular reservoir for meeting water demands (Biemans et al., 2011; Hanasaki et al., 2006).

Non-irrigation reservoirs within most GHMs are treated like flood-control reservoirs. The inflow, minimum pool level, and maximum static full level are the only significant factors controlling the magnitude and timing of water release (Hanasaki et al., 2006; Yassin et al., 2019). However, this approach poses challenges because, among non-irrigation reservoirs, hydropower reservoirs are typically operated differently from flood-control reservoirs. An essential difference between them is that the primary function of a hydropower reservoir, in terms of water supply, is to reliably exceed a pre-determined minimum storage level at all times (Loucks and van Beek, 2017). The minimum and maximum releases corresponding to the minimum and maximum storage levels are also pre-determined. Conversely, an essential feature of flood-control reservoirs is to provide a reliable capacity to retain a predicted or unforeseen future flooding event by emptying existing reservoir storage. The objective is to reduce peak flow magnitude, and storage level is only a concern when there is an incoming flood event (Votruba and Broza, 1989). This strategy translates to a direct loss of benefit for hydropower reservoirs (Loucks & van Beek, 2017; Turner et al., 2017).

Whist, the understanding of the difference between flood-control and hydropower reservoirs is evident at the individual reservoir level; it remains unclear whether this difference still manifests noticeably or significantly at the regional or larger scales. Most of the GHMs nevertheless focus on the water dynamics at the regional or global scale (Best et al., 2011; Döll et al., 2009; Hanasaki et al., 2008; Pokhrel et al., 2012; Schaphoff et al., 2018; Voisin et al., 2013; Wisser et al., 2010). It is, therefore, worthwhile to investigate whether the aforementioned difference between individual flood-control and hydropower reservoirs has sufficiently significant impacts on the water dynamics at the regional or global scales.

This study aims to incorporate the above advances in GHMs to enhance Xanthos, a global hydrology model designed to interact with the Global Change Analysis Model (GCAM) framework (Hejazi et al., 2013a, 2013b; Li et al., 2017). GCAM is a leading integrated assessment model that coherently represents the individual dynamics and connections among five systems: the economy, energy system, climate system, water system, and agriculture and land-use system (Calvin et al., 2019). Aided by Xanthos, GCAM allows for a consistent global water supply analysis (i.e., surface water, groundwater, and desalinated water) and demand across multiple sectors. Hejazi et al. (2013b, 2013a) and Li et al. (2017) introduced Xanthos as a simple surface water availability model consisting of a monthly water balance scheme and a cell-to-cell river routing scheme. Liu et al. (2018) further improved Xanthos by introducing a new monthly water balance module based on the ***abcd*** model (Martinez and Gupta, 2010). Xanthos can be run as a distributed (i.e., gridded) model, but Liu et al. (2018) also developed a lumped version of the water balance module. In the lumped version, each river basin was treated as a single spatial unit to avoid the high computational cost and complex parameter calibration, allowing 100,000 simulations to be completed within two minutes on a standard computing workstation. Nevertheless, Xanthos focused on representing the natural global water balance without human interventions such as reservoirs (Hejazi et al., 2013; Liu et al., 2018). However, reservoirs play a crucial role in regulating streamflow by mediating water availability and demand (Wan et al., 2018, 2017; Zhang et al., 2020, 2019, 2018). For convenience, we denote the current version of Xanthos as ***Xanthos-original***.

Table 6-1: List of global hydrological models with reservoir representations.

| S.No | Model Name | Domain | Water Use/ Reservoirs | Reservoir Classification | Representations | Reference | Website |
|---|---|---|---|---|---|---|---|
| 1 | H08 (H07) | Globe | Yes/Yes | Irrigation/ Non-Irrigation | 1) Irrigation Reservoir release is based on demand<br>2) Non-Irrigation: is treated as flood control where releases are adjustments to the mean annual inflow based on storage level | Hanasaki et al., (2008)<br>Boulange et al., (2021)<br>Yoshida et al., (2022) | http://h08.nies.go.jp/h08/index.html |
| 2 | WaterGAP | Globe | Yes/Yes | Irrigation/ Non-Irrigation | Modified H07 | Döll et al., (2009)<br>Schmied et al., (2021) | www.watergap.de |
| 3 | WBMplus | Globe | Yes/Yes | Irrigation/ Non-Irrigation | Modified H07 | Wisser et al., (2010)<br>Grogan et al., (2022) | https://wsag.unh.edu/wbm.html |

Table 6-1 Continued

| | | | | | | | |
|---|---|---|---|---|---|---|---|
| 4 | PCR-GLOBWB | Globe | Yes/Yes | No | Uses default strategy aimed at passing the average discharge while maintaining levels between a minimum and maximum storage. For irrigation, release based on downstream water demand is possible for an elaborate release strategy. | Sutanudjaja et al, (2018)<br><br>Shen et al, (2022) | www.globalhydrol ogy.nl |
| 5 | LISFLOOD | Europe, Globe | Yes/Yes | None | It uses a simple general reservoir operation scheme, simulated as an outflow function between three storage limits: minimum outflow, non-damaging outflow, and normal outflow | De Roo et al., (2000)<br><br>van der Knijff et al., (2010)<br><br>Hirpa et al., (2018) | https://ec-jrc.github.io/lisflood-model/3_03_optLISFLOOD_reservoirs/ |
| 6 | MATSIRO | Globe | Yes/Yes | Irrigation/<br><br>Non-Irrigation | H08(H07) | Pokhrel et al., (2012)<br><br>Pokhrel et al., (2015)<br><br>Telteu et al., (2021) | http://hydro.iis.u-tokyo.ac.jp/~sujan/research/models/matsiro.html |

Table 6-1 Continued

| | | | | | | | |
|---|---|---|---|---|---|---|---|
| 7 | LPJmL | Globe | Irrigation only/Yes | Irrigation/<br><br>Non-Irrigation | 1) Irrigation reservoirs are assumed to release their water proportionally to gross irrigation water demand downstream.<br>2) Other purposes (hydropower, flood control and others) are assumed to be designed for releasing a constant water volume throughout the year | Schaphoff et al, (2018)<br><br>Telteu et al, (2021) | http://www.pik-potsdam.de/research/projects/activities/biosphere-water-modelling/lpjml |
| 8 | CWatM | Globe | Yes/Yes | None | It adopts LISFLOOD generic reservoir operation method. Reservoirs are simulated as outflow functions between three storage limits (conservative, normal, flood) and three outflow functions (minimum, normal, non-damaging) | Burek et al., (2020) | https://cwatm.iiasa.ac.at/modeldesign.html |
| 9 | MOSART-WM | Globe | Yes/Yes | Irrigation/<br><br>Flood control/ Combination of<br><br>flood control and irrigation, and others | The operating rules are determined based on historical long-term mean monthly inflow, reservoir characteristics, and reservoir purpose | T. Zhou et al., (2020) | https://im3.pnnl.gov/model?model=MOSART-WM |

The main objectives of this study are thus threefold: 1) to enhance Xanthos by adding a new water management module, where irrigation, hydropower, and flood-control reservoirs are treated differently (this enhanced Xanthos is denoted as ***Xanthos-enhanced***); 2) to evaluate the performance of the enhanced Xanthos in terms of reproducing observed streamflow variability, particularly under water scarcity conditions; and 3) to understand the impacts of difference between individual flood-control and hydropower reservoirs at the regional scale. The rest of this paper is organized as follows. Section 6.2 introduces the theoretical underpinnings of the modeling framework. Section 6.3 describes the design and execution of numerical experiments that constitute the first global application of this new modeling framework, an evaluation of its performance, and sensitivity analysis of key model parameters. Section 6.4 summarizes the major conclusions and discusses potential future directions.

## 6.2 Methodology

Xanthos is a distributed GHM with a spatial resolution of 0.5 degrees. By accounting for both reservoir operation and local water withdrawal, Xanthos now consists of three modules: runoff generation, river routing, and water management, as shown in Figure 6-1. This section focuses on the water management module and briefly summarizes the runoff and river routing components for completeness. For more details on the runoff and river routing components, please refer to Li et al. (2017), Liu et al. (2018), and Vernon et al. (2019).

### 6.2.1 Runoff Generation Module

Simple water balance models effectively capture key hydrologic processes, and their interactions, in diverse climatic and landscape settings (Martinez and Gupta, 2011; Ye et al., 2012). These models often rely on partitioning incoming water mass into subcomponents, such as partitioning precipitation into rain and snow or partitioning rain into infiltration and surface runoff. The ***abcd*** model is one such model, first developed by Thomas (1981) and further improved (with respect to process representation) by Martinez and Gupta (2010). Liu et al. (2018) introduced the ***abcd*** model into Xanthos as its runoff module, simulating direct runoff, baseflow, and soil moisture at the monthly time step (Fig. 6- 1a). The sum of direct runoff and baseflow is denoted as total runoff, which feeds into the river module (Fig. 6- 1b). Table 1 lists the five parameters in the ***abcd*** model. The parameters ***a*** and ***b*** pertain to runoff characteristics, while ***c*** and ***d*** relate to shallow soil moisture and deeper groundwater storage. The fifth parameter is a snowmelt coefficient, denoted as ***m***.

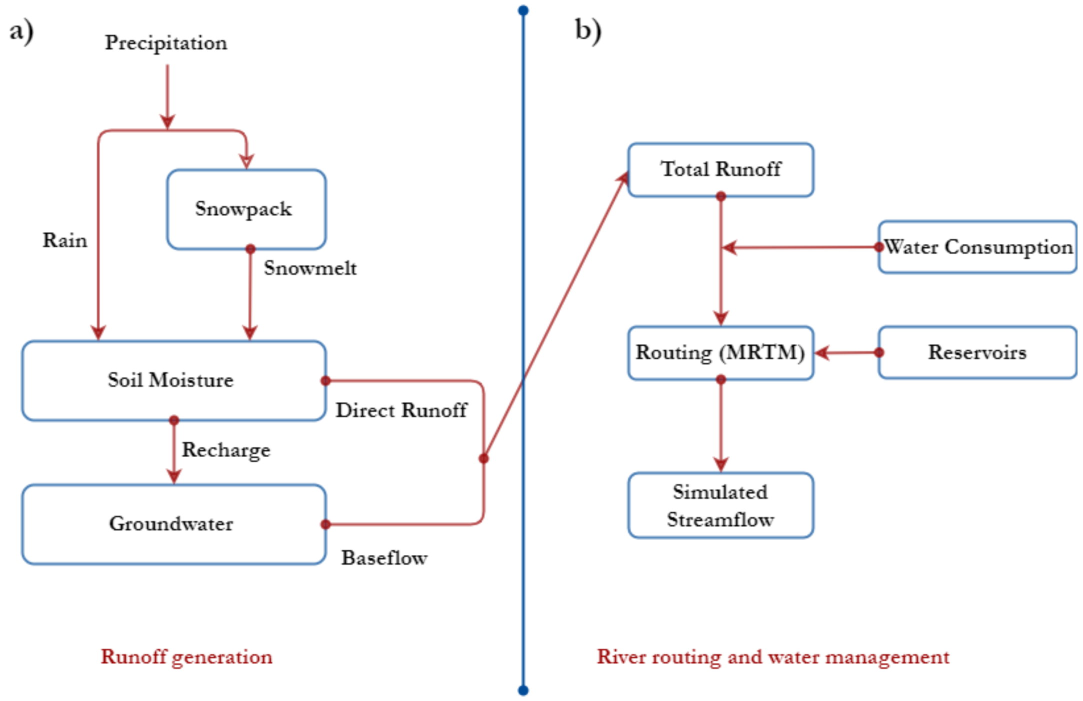


Figure 6-1: Schematic diagram of the enhanced Xanthos. a) runoff generation module, b) river routing and water management modules.

### 6.2.2 River Routing Module

In Xanthos, the routing of water through river networks is simulated using a simple cell-to-cell river routing scheme, a modified version of the River Transport Model (Branstetter and Erickson, 2003), hereinafter denoted as MRTM. MRTM is essentially based on the linear reservoir routing method. The channel flow rate is estimated as a function of channel water storage, channel velocity, and flow distance from one grid cell to another (Zhou et al., 2015). MRTM uses spatially variable but temporally constant channel velocities, which were derived by averaging the long-term channel velocity simulations from Li et al. (2015). The flow distance values were derived by tracing the natural dominant river channel between grid cells to account for the meanders (Wu et al., 2011). Here we add a channel velocity adjustment coefficient (Table 5-2) to account for the uncertainties in our channel velocity field. For more details about MRTM, please refer to Zhou et al. (2015).

### 6.2.3 Water Management Module

To enhance Xanthos, we add a water management module on top of the river module (Fig. 6- 1b). The water management module represents the two most common surface water management activities: local surface water extraction and reservoir operation. Local surface water extraction is water that is locally consumed within a particular grid cell. For example, thermal power plants use water for cooling purposes, and some of this water may evaporate and effectively be unavailable for use in a given grid cell. This local consumptive water use is subtracted from the total runoff from the ***abcd*** model (Fig. 6- 1b). The remaining runoff is then discharged into the channels and routed downstream using MRTM. In a grid, if the consumptive water use is greater than the total runoff, the remaining runoff is zero. This grid is considered to either have unmet water demand or access to supply from other external sources such as desalination or groundwater pumping, which are not represented in Xanthos. If there is a reservoir in a grid, local runoff and upstream inflow are first intercepted and stored in the reservoir. Reservoir operation is then invoked to estimate the release from the reservoir to the downstream grids. A reservoir operation rule is defined for each reservoir based on its primary purpose. Here we consider four main types of reservoirs: irrigation, flood-control, hydropower, and others. Next, we provide more details on how each reservoir type is treated.

#### 6.2.3.1 Irrigation Reservoirs

Irrigation reservoirs are represented by adapting Hanasaki et al. (2006) approach, which determines the reservoir release based on the upstream inflow and the total water demand from the downstream areas. More specifically, for each irrigation reservoir, the provisional release is given as

$$R'_{m,y} = \begin{cases} \frac{i_{mean}}{2} * \left(1 + \frac{demand_{m,\ y}}{d_{mean}}\right) & , d_{mean} \geq 0.5 * i_{mean} \\ i_{mean} + demand_{m,\ y} - d_{mean}\ , & < 0.5 * i_{mean} \end{cases} . \tag{6-1}$$

Where $R'_{m,y}$ is the provisional monthly reservoir release ($m^3s^{-1}$) in month $m$ and year $y$; *demand* is the total monthly demand from downstream areas that are dependent on this reservoir; $d_{mean}$ is the mean annual total water demand of the reservoir ($m^3s^{-1}$); $i_{mean}$ is the mean annual inflow from upstream ($m^3s^{-1}$). The subscripts m and y represent month and year, respectively.

Though deterministic by nature, the provisional release equation for irrigation reservoirs is demand-driven. $d_{mean}$ is calculated based on the delineated downstream dependent grids. If $d_{mean}$ is greater than or equal to 50% of the mean annual inflow $i_{mean}$, 50% of $i_{mean}$is considered a baseline release, and the seasonal dynamics are accounted for by the relative contribution of monthly demand to $d_{mean}$. If $d_{mean}$ is less than 50% of the mean annual inflow $i_{mean}$, the provisional release can be estimated as the mean annual inflow modified by the seasonal variation of demand around the mean annual demand.

The provisional release is further adjusted based on the degree of regulation (γ) determined by the ratio of reservoir storage capacity (C) to annual total inflow in cubic meters per year ($I_{mean}$), initial storage at the beginning of y^th operational year ($S_{first,y}$) and reservoir capacity reduction factor ($\kappa$). $\kappa$ ranges in 0~1 and is a non-dimensional constant to reduce the total reservoir capacity magnitudes reported in GranD to account for the dead and surcharge storage or storage reduction due to sediment accumulation. $\alpha$ approaching 0 means the reservoir capacity may have been significantly reduced by sediment accumulation. The final release is estimated as,

$$R_{m,y} = \begin{cases} \left(\frac{S_{first,y}}{\kappa C}\right) * R'_{m,y} & \gamma \geq 0.5 \\ \left(\frac{\gamma}{0.5}\right)^2 * \left(\frac{S_{first,y}}{\kappa C}\right) * R'_{m,y} + \left\{1 - \left(\frac{\gamma}{0.5}\right)^2\right\} i_{m,y} & 0 \leq \gamma < 0.5. \end{cases} \quad (6\text{-}2)$$

Where $R_{m,y}$ is the monthly release ($m^3s^{-1}$); $i_{m,y}$ is the monthly inflow ($m^3s^{-1}$); and $I_{mean}$ is the annual inflow ($m^3yr^{-1}$). The general logic behind the two sets of final release conditions in equation (2) can be interpreted as the influence of reservoir degree of regulation on release decisions. The $\alpha$ and $\gamma$ parameters are used to adjust the behavior of irrigation reservoir operating policies.

The GranD reservoirs can be classified into relatively large and small storage reservoirs based on the degree of regulation. Suppose a reservoir's total storage capacity is less than 50% of its mean annual inflow. In that case, it is considered here to be a relatively small storage reservoir, whereas greater than 50% indicates a relatively large storage reservoir. In relatively small reservoirs, releases are dependent on their monthly inflows, while in relatively large reservoirs, releases are relatively independent of their monthly inflows (Hanasaki et al., 2006).

The total water demand for each reservoir is estimated by summing up water demand values from grids within the reservoir's downstream dependent area. The reservoir-dependent area is determined following Hanasaki et al. (2006), Haddeland et al. (2006), and Biemans et al. (2011). Specifically, the downstream spatial extent of reservoir dependency along the main stem is determined based on an average stream velocity and the study's temporal interval (monthly). Assuming an average velocity of 0.5 m/s, total travel distance of water in one month is 0.5m/s x 30 x 24 x 3600s = 1296 km/month. Therefore, the dependent downstream grids along the main stem are roughly 20 grids (0.5x0.5 degrees) downstream. If there are other reservoirs located within this travel distance, we assume the dependency on the current reservoir stops and is taken over by the other reservoir. We then delineate a buffer zone within four–grid ranges from the main stem. Finally, assuming water movement is by gravity only, those grids with a mean elevation lower than that of the reservoir are identified as the reservoir's dependent grids within the buffer zone.

#### 6.2.3.2 Hydropower Reservoirs

We represent the operation of hydropower reservoirs using a stochastic dynamic programming (SDP) approach ( Loucks et al., 1981, 2017; Turner et al., 2017). The SDP approach was pioneered by Loucks et al. (1981), extending the dynamic programming approach to account for the uncertain nature of reservoir inflows explicitly (Loucks and van Beek, 2017). It executes sequential decisions for temporal stages with nonlinear objectives while considering reservoir inflows as random variables (Loucks and van Beek, 2017). For a known inflow $i_{m,y}$ and hydrologic state variables in the current period, the SDP formulation estimates the expected benefit, $f_{m,y}$, resulting from each release decision $R_{m,y}$ as,

$$f_{m,y}(S_{m,y}, i_{m,y}) = max_{R_{m,y}} E\{B_{m,y}(S_{m,y}, i_{m,y}, R_{m,y}) + [f_{m+1,y}(S_{m+1,y}, i_{m,y})]\},$$

$$\forall S_{m,y}, i_{m,y} \;\; m \in \{1, \dots, T\}. \qquad (6\text{-}3)$$

Where $T$ is the current system period ($T$ = 12 for a monthly operating scheme). The reservoir state at each decision-making time step, i.e., month $m$ in year $y$, is described by the storage $S_{m,y}$ and the current inflow $i_{m,y}$. For each state and time step, the release decision $R_{m,y}$ is selected to minimize the current benefit $B_{m,y}(S_{m,y}, i_{m,y}, R_{m,y})$ plus future benefit expectation $f_{m+1,y}(S_{m+1,y}, i_{m,y})$, which depends on the resultant state of the system at time step $m+1$, i.e., the succeeding month.

The method for simulating the hydropower reservoir operation is adopted from ***reservoir***, R package that contains several reservoir release decision-making tools, including the SDP techniques (Turner et al., 2016). The method was later employed for the global-scale study of hydroelectric plants' vulnerability to climate change (Turner et al., 2017). We integrated the SDP approach from this package, presented in Turner et al. (2016, 2017), into Xanthos for hydropower release simulation. Here the SDP approach is first trained using the naturalized inflow of each reservoir to represent hydrological uncertainty, which we obtain by running MRTM without the water management option. The objective function is set to maximize hydropower production over the long term. The SDP procedure is executed to develop an optimal release policy for each month as a function of storage levels. We discretize storage into 1000 levels and generate the corresponding expected release for all 12 months. If the release is unavailable or less than 10% of the mean annual inflow, the monthly release was set to environmental flow, 10% of the mean annual inflow. When a storage level is at the reservoir's maximum storage capacity, release equals the maximum turbine flow corresponding to the power plant's installed capacity.

#### 6.2.3.3 Flood-control Reservoirs and Others

The primary purpose of flood-control reservoirs is to redistribute the floodwater from a flood season to a non-flood season. The operation of flood-control reservoirs is also estimated following Hanasaki et al. (2006) with

$$R_{m,y} = \begin{cases} \left(\frac{S_{first,y}}{\alpha C}\right) * i_{mean} & \gamma \geq 0.5 \\ \left(\frac{\gamma}{0.5}\right)^2 \left(\frac{S_{first,y}}{\alpha C}\right) * i_{mean} + \left\{1 - \left(\frac{\gamma}{0.5}\right)^2\right\} i_{m,y}, & 0 \leq \gamma < 0.5 \end{cases} \tag{6-4}$$

where $R_{m,y}$ is the monthly is release (m$^3$s$^{-1}$); and $i_{m,y}$ is the monthly inflow (m$^3$s$^{-1}$). In this study, release for reservoirs categorized as "others" is also determined as a function of inflow and storage characteristics only, thus similar to the flood-control reservoirs. The logical reasoning for the set of equations employed here is in line with equation (1). For instance, as with irrigation reservoirs, the $\alpha$ and $\gamma$ parameters are used to adjust the behavior of flood-control reservoirs.

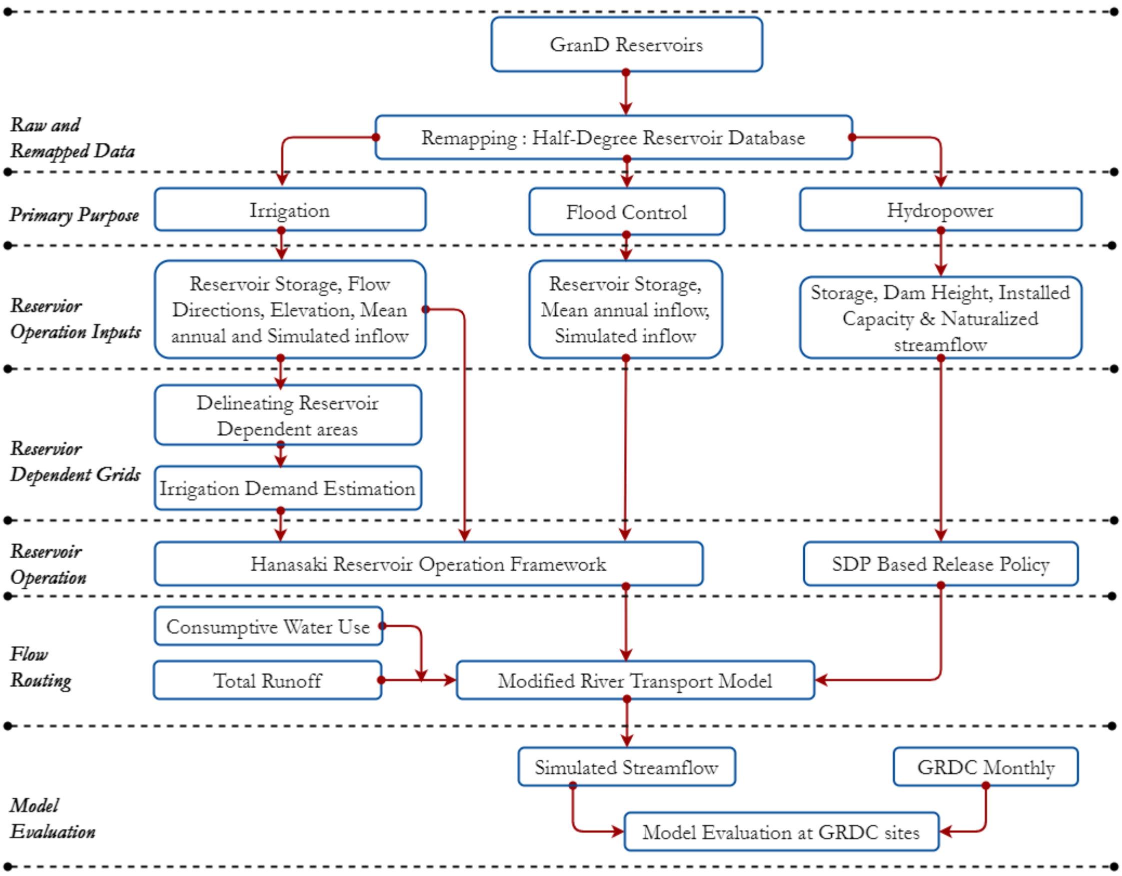


Figure 6-2. Reservoir representation in Xanthos.

### 6.2.4 Model Parameter Determination Strategy

In total, there are seven parameters in the enhanced Xanthos. Typically, there are two strategies for determining the parameter values in a hydrologic model: calibration and estimation a priori. Parameter calibration is computationally expensive and only feasible for those computationally cheap models. The Xanthos runoff module can run separately at the monthly time step and is computationally cheap. However, the

Xanthos river routing and water management modules have to run at a three-hour time step for numerical stability, and thus computationally too expensive for a traditional parameter calibration approach. Furthermore, most hydrological models are subject to the equifinality issue since the number of parameters, in most cases, far exceeds the number of observational variables available for calibration (Beven, 2006). Parameter estimation a priori requires each parameter to be physically meaningful and have robust relationships with the existing climate or landscape data. These relationships, however, are not readily available and have to be identified via good prior knowledge (e.g., Li et al., 2015) or machine-learning techniques (e.g., Abeshu et al., 2022; Li et al., 2022).

Table 6-2:List of model parameters.

| **Parameter** | **Description** | **Range** | **Type** |
|---|---|---|---|
| | ***Distributed-Regulated Model*** | | |
| *a* | Propensity of runoff to occur before the soil is fully saturated | 0–1 | runoff |
| *b* | Upper limit on the sum of evapotranspiration and soil moisture storage | 0–8000 | runoff |
| c | Degree of recharge to groundwater | 0–1 | runoff |
| d | Release rate of groundwater to baseflow | 0–1 | runoff |
| m | Snowmelt coefficient | 0–1 | runoff |
| $\upsilon$ | Velocity adjustment coefficient | 0–10 | routing |
| $\kappa$ | Reservoir capacity reduction factor | 0.85 | reservoir |

This study proposes a new parameter determination strategy to overcome the limitations mentioned above. Note that the runoff and river modules in Xanthos can run sequentially, i.e., first running the runoff module at a monthly time step, which then provides inputs to the river and water management modules which run at a 3-hour time step. Correspondingly, our new parameter strategy consists of two stages. This strategy applies each of the seven parameters listed in Table 6-2 uniformly to all the grid cells in a river basin. For any river basin involved in the parameter determination, we also need at least one river station where observed monthly streamflow data are available with reasonable quality.

The 1st stage is to determine a small set of optimal parameters for the runoff module in four steps: 1) We generate a million runoff parameter combinations using a Latin Hypercube Sampling (LHS). The LHS method ensures a good representation of the whole parameter space. 2) For each of these runoff parameter combinations, we run the runoff module to produce the simulated monthly total runoff time series at each grid cell in the study period. 3) We take the simulated annual runoff at each grid cell. We then take the spatial average across the grid cells within the upstream drainage area of a river station where the observed streamflow data is available, denoted as $Q_{sim\_annual}$ [mm/year]. 4) At the river station, we take the long-term mean of observed streamflow and divide it by the drainage area, $Q_{obs\_annual}$. We then select the top 100 runoff parameter combinations that give the smallest root mean square error between $Q_{sim\_annual}$ and $Q_{obs\_annual}$. These 100 runoff parameter combinations are passed onto the 2nd stage.

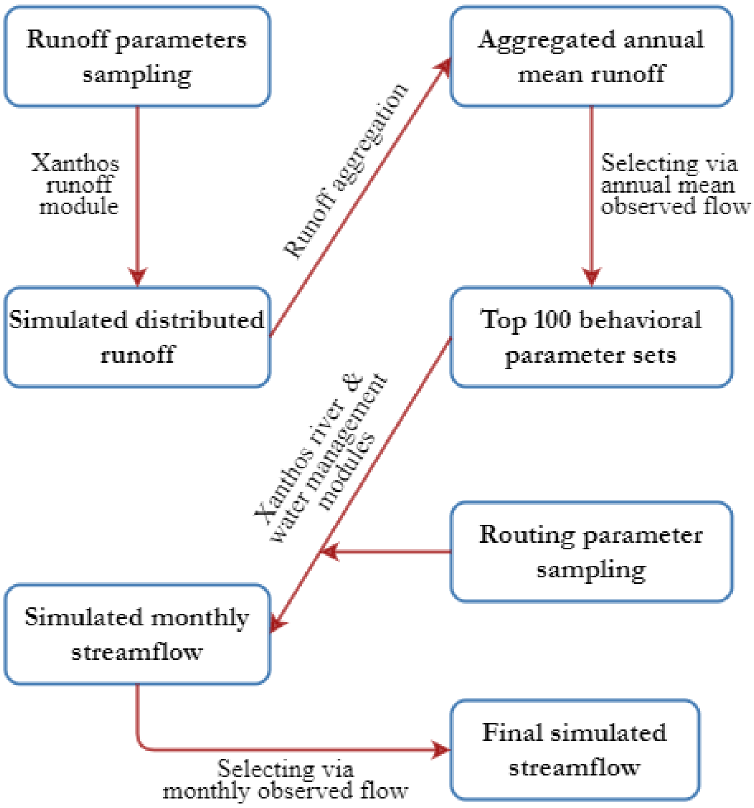


Figure 6-3. Runoff parameters selection strategy for Xanthos.

In the 2nd stage, we determine the final optimal parameter set in four steps: 1) We set the reservoir capacity reduction factor ($\boldsymbol{\kappa}$) as 0.85, following Hanasaki et al. (2006). 2) For the channel velocity adjustment coefficient ($\boldsymbol{\upsilon}$), we sample it in a relatively uniform manner within the range of 0.1~10.0. In total, there are 19 possible $\boldsymbol{\upsilon}$ values to be considered. For each of 100 selected runoff parameter combinations, we use the corresponding simulated runoff time series as the inputs and run the river and water management modules 19 times (each time corresponds to one of the 19 $\boldsymbol{\upsilon}$ values and $\kappa$ =0.85) at a 3-hour time step. 4) The simulated streamflow time series at the grid cell where the river station is located was validated against the observed monthly streamflow time series using the Kling–Gupta efficiency (KGE) (Gupta et al., 2009) given by

$$KGE = 1 - \sqrt{(r-1)^2 + \left(\frac{\sigma_{Sim}}{\sigma_{Obs}} - 1\right)^2 + \left(\frac{\mu_{Sim}}{\mu_{Obs}} - 1\right)^2} \tag{6-5}$$

where $\sigma_{sim}, \sigma_{obs}, \mu_{sim}, and\ \mu_{obs}$ are the standard deviation in simulations, the standard deviation in observations, the simulation mean, and the observation mean values. Higher KGE indicates a better degree of agreement between the simulated and observed variables, and a KGE value of 1.0 indicates perfect agreement. From Step (3), there are 1900 simulations for each basin, each corresponding to a combination of five runoff and routing parameters (**a**, ***b***, ***c***, ***d***, ***m*****,** and ***υ***). The final optimal parameter set is the one that gives the best KGE value.

This new strategy has several benefits: 1) It largely alleviates, if not eliminates, the equifinality issue by exploring the whole parameter space. For each of the six parameters, its theoretical range is fully accounted. 2) It reduces the computational load to a reasonable level. For each river basin, we will have 1million runs for the runoff module at the monthly time step, and another 1900 runs for the river routing and water management modules at the three-hour time step. We suggest that this new strategy applies to those hydrologic modeling frameworks where 1) some module(s) is computationally much cheaper than the others and 2) these modules can run sequentially instead of simultaneously. The demonstration of this parameter determination strategy is provided in section 6.3.

### 6.2.5 Water Availability Signature

In addition to KGE, we also assess how well our model captures water availability variations under extreme events like droughts. Hence, we examine Xanthos' capacity to simulate hydrological droughts. A hydrologic drought is defined here as the streamflow value at a specific month (e.g., January) lower than the long-term average streamflow for that month. We quantify hydrologic droughts using the Standardized Discharge Index (SDI). SDI is analogous to the Standardized Precipitation Index (SPI) (Lloyd-Hughes and Saunders, 2002), but the SDI uses streamflow data instead of precipitation data. Note that we do not use SDI in our parameter calibration but rather use it as a signature to help diagnose the model's capacity to reproduce drought conditions when water availability from river systems faces more pressure than during normal conditions.

The SDI is first computed with six- different distribution fitting methods (Gumble, Lognormal, Generalized Logistic, Generalized Extreme Value, Pearson Type III, and Generalized Pareto) to diagnose any systematic dependency on the fitting method. From the analysis, we find no significant dependency on the model performance in selecting the distributions in terms of the correlation coefficients between the observed and simulated SDI time series. Therefore, following Vicente-Serrano et al. (2012), we use the Generalized Extreme Value (GEV) distribution for SDI calculation. We define a drought event as a period (usually several months) when the SDI values are continuously no more than -1. We identify each drought event by determining the starting and ending months from the calculated SDI time series.

## 6.3 Results

We apply the enhanced Xanthos modeling framework over the global domain at a 0.5-degree resolution and monthly time step. The study period is 1971-1990 based on the availability of forcing and observed streamflow data over all the basins. We divide the study period into a calibration period, 1971-1980, and a validation period, 1981-1990.

### 6.3.1 Data and Numerical Experiments

For this study, gridded global monthly climatic data, including precipitation, maximum temperature, and minimum temperature, are obtained from the WATer and global CHange (WATCH; Weedon et al., 2011) dataset from 1971 to 2001. Global reservoir data are obtained from the GRanD dataset (Lehner et al., 2011) (Fig. 6-4a). Monthly water demand and consumptive water use data for various sectors at a 0.5-degree resolution are from Huang et al. (2018a, 2018b), which are available from 1971 to 2010 (Fig. 6-4b). Observed streamflow data for model parameter identification and validation are obtained from the Global Runoff Data Center (GRDC) (https://www.bafg.de/GRDC). We adjust the GRDC gauge station coordinates to Xanthos grids and compare the corresponding MRTM upstream area in Xanthos with the GRDC gauge contributing area. Here, only gauges within ±20% in area difference (3097 GRDC gauges) are retained for further use in this study. Temporal filtering of these gauges with the availability of 20 years (1971-1990) of continuous data reduced the number of stations to 1178. These gauge stations are located within 91 of the 235 Xanthos basins. For model validation purposes, we select the GRDC gauge with the largest upstream area within each basin, i.e., 91 GRDC gauges in total (Fig. 6- 4c).

The GRanD database we use here only considers reservoirs with storage capacity values greater than 0.1 $km^3$. Reservoirs with missing storage capacity and those identified with purposes such as tide control are dropped, reducing the total GranD reservoirs from 6862 to 6847. For any grid cell with more than one reservoir in it, we aggregate all of the reservoirs located locally (i.e., within the grid cell) into a single reservoir with a storage capacity equivalent to that of the local reservoirs combined. To determine this aggregated reservoir's primary purpose, we first divide all reservoirs into three different categories based on their primary purposes: irrigation, hydropower, and flood-control and others. In each category, we sum up the reservoir storage capacities. Lastly, the aggregated reservoir's primary purpose is assigned to the category with the largest summed storage capacity. After this treatment, the 6847 GranD reservoirs are remapped into 3790 reservoirs. Among the 3790 reservoirs, 1095, 598, and 2097 are categorized as irrigation, hydropower, and flood-control and others, respectively.

With the data mentioned above, we carry out three global simulations to demonstrate the enhanced Xanthos: 1) A simulation with the enhanced Xanthos, denoted as *Distributed-Regulated*, where we run the runoff, river routing, and water management modules with the parameter values determined following the new strategy as outlined in Section 2.4; 2) A simulation with the distributed version of the original Xanthos by Liu et al. (2018), i.e., without water management, denoted as *Distributed-Natural*, where the *Distributed-Natural* simulated flow is obtained by routing calibrated runoff data generated by Liu et al. (2018) with calibrated *abcd* model parameters; 3) A simulation similar to *Distributed-Regulated*, but treating all the hydropower reservoirs as flood-control reservoirs, denoted as *Distributed-Regulated-II*. By comparing *Distributed-Regulated* with *Distributed-Natural*, we isolate the net effects of the water management module on the model performance. By comparing *Distributed-Regulated* with *Distributed-Regulated-II*, we isolate the net difference between simulating hydropower reservoirs based on Eqn. (6-3) and the traditional way, i.e., treating hydropower reservoirs as flood-control based on Eqn. (6-4).

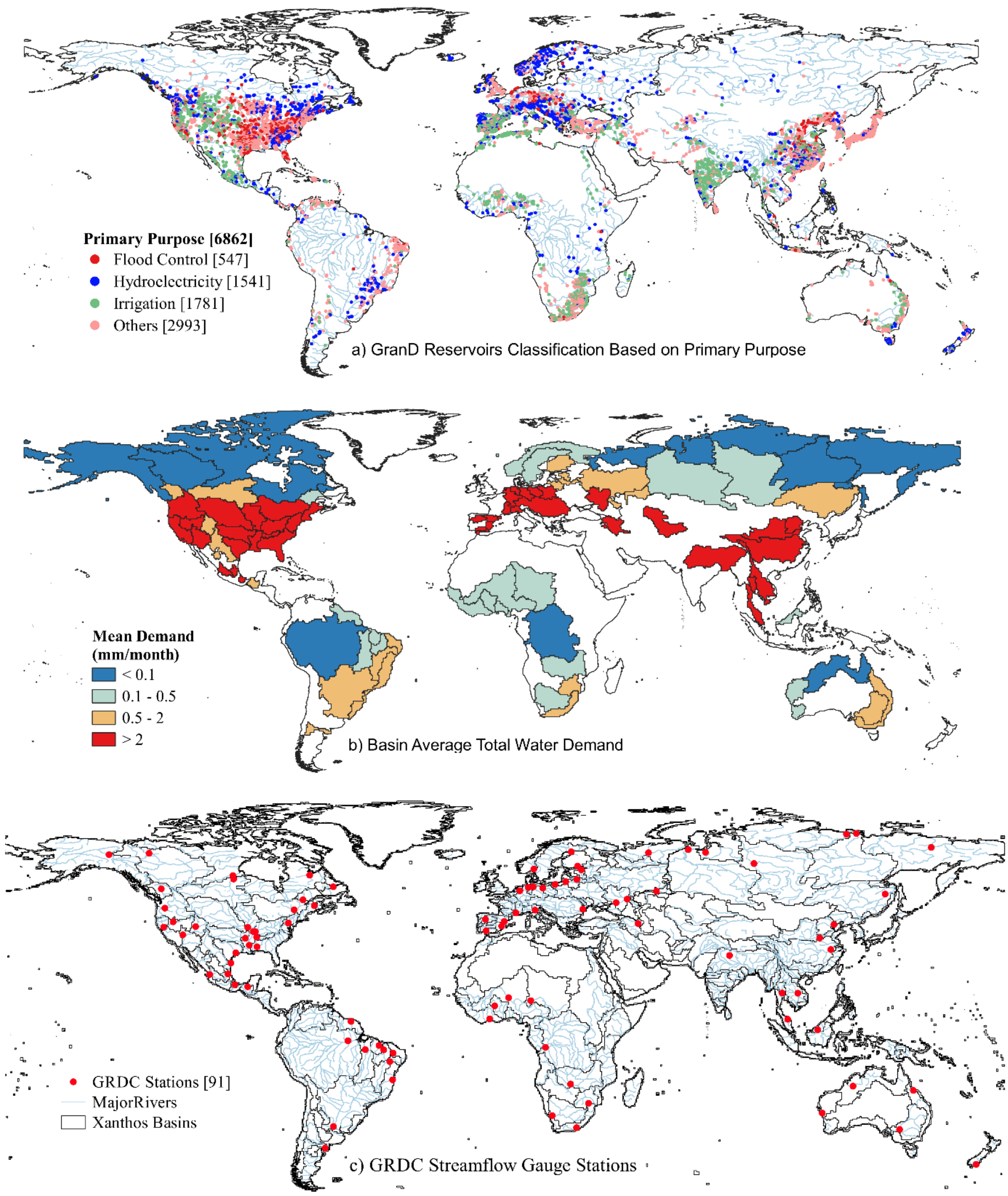


Figure 6-4. Global distribution of 6862 reservoirs from the GranD database classified based on primary purpose (a), basin average water demand for 94 river basins (b), and GRDC stream gauge stations in 94 basins(c).

### 6.3.2 Parameter Determination

Latin hypercube sampling (LHS) is a statistical method for multidimensional parameter space sampling. This approach ensures that all portions of the sampling space are represented through its stratified sampling strategy (McKay et al., 1979). The user decides on the required number of parameter combinations and individual parameters' upper and lower bounds. Based on that, LHS simultaneously stratifies on all input dimensions. The upper and lower bounds of all runoff parameters are 0 and 1, respectively, except for the parameter ***b***, which has a lower bound of zero and an upper bound of 8m. We decided on generation 1million parameter combinations to sufficiently cover all parameter spaces. The generated parameters are uniformly distributed between their corresponding bounds (Fig. 6-5).

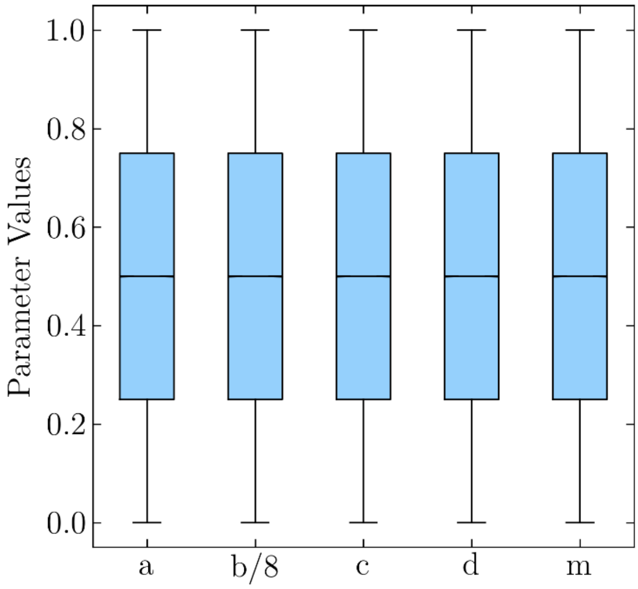

Figure 6-5 : Sampling runoff generation parameters using the LHS method

The runoff parameters generated by LHS were passed to the Xanthos runoff module to generate gridded runoff at monthly time series. We spatially average runoff at grids upstream of observed flow stations and computed NRMSE between the simulated and observed annual series (Fig. 6-6a). We then selected the top 100 parameter combinations that resulted in the smallest NRMSE for use in the second stage of parameter selection. The runoff generated by the top 100 parameters was further evaluated at the mean monthly scale to confirm that the selected parameters produced reasonable runoff relative to observed flow magnitude and timing (Fig. 6-6b). We specifically evaluate two essential characteristics. First, the mean monthly runoff employed here is a simple spatial average with no sense of routing; therefore, the peak time for mean monthly runoff is expected to be earlier than the streamflow peak time (Fig. 6-6b). Secondly, one would also expect the peak time difference (i.e., GRDC mean monthly peak flow time subtract runoff peak flow time) for the selected parameters to be among the best of the 1million (Fig. 6-6c). The distribution of the final selected parameters for this stage is shown in Fig. (6-6d).

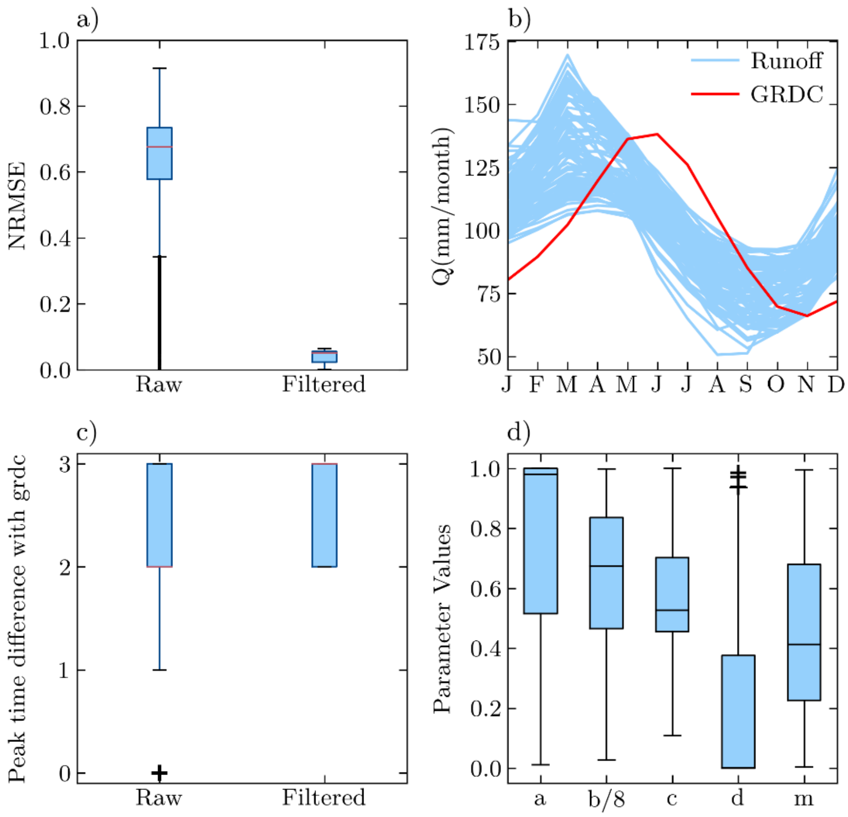


Figure 6-6: Two-stage parameter selection over the Amazon River basin

### 6.3.3 Global Evaluation

Overall, Xanthos' performance has improved after adding the water management module, as shown in Figure 6-7~6-9. Figure 6-7 shows the boxplots of KGE between the GRDC monthly observed streamflow and those simulated from the *Distributed-natural* and *Distributed-regulated* simulations for the 91 basins during the calibration (Fig. 6-7a) and validation (Fig. 6-7b) periods, respectively. In most cases, during both calibration and validation periods, the Distributed-regulated simulation's

KGE values are consistently higher than those of the *Distributed-natural* simulation. Moreover,

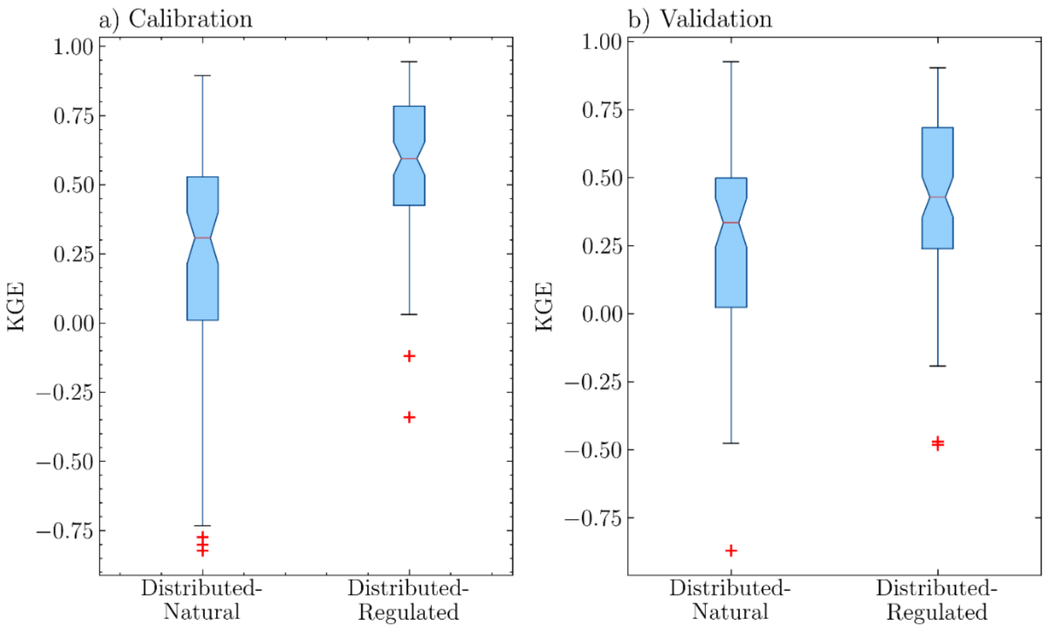


Figure 6-7: Boxplots of the Kling-Gupta Efficiency (KGE) values for the Distributed-natural and Distributed-regulated simulations during the calibration (1971-1980) and validation (1981-1990) periods, respectively.

As shown in Figure 6-8, out of the 91 basins, the KGE values have been improved in 75 basins (KGE values increased no less than 0.05) and worsened in 7 basins (KGE values decreased no less than 0.05) and not changed significantly in 9 basins. This worsened performance is likely due to 1) the uncertainties in the climate forcing data and GRDC streamflow observations and 2) the lack of spatial variability in the estimated parameters.

To further examine Xanthos' performance in more detail, Figure 6-9 shows the monthly time series of model-simulated and observed streamflow at six out of 91 GRDC stations with the highest average annual water demand (Po, Rhine, Ziya He Interior, Ganges-Brahmaputra, Mid Atlantic and Chao Phraya). Compared to the original version of Xanthos, the enhanced (i.e., Distributed-regulated) version better captures the seasonal variations of streamflow, i.e., more closely matching the observed streamflow during the high-flow and low-flow periods. This implies the importance of the reservoir regulation effect (e.g., reducing high-flow and enhancing low-flow) that has not been captured by the original version of Xanthos.

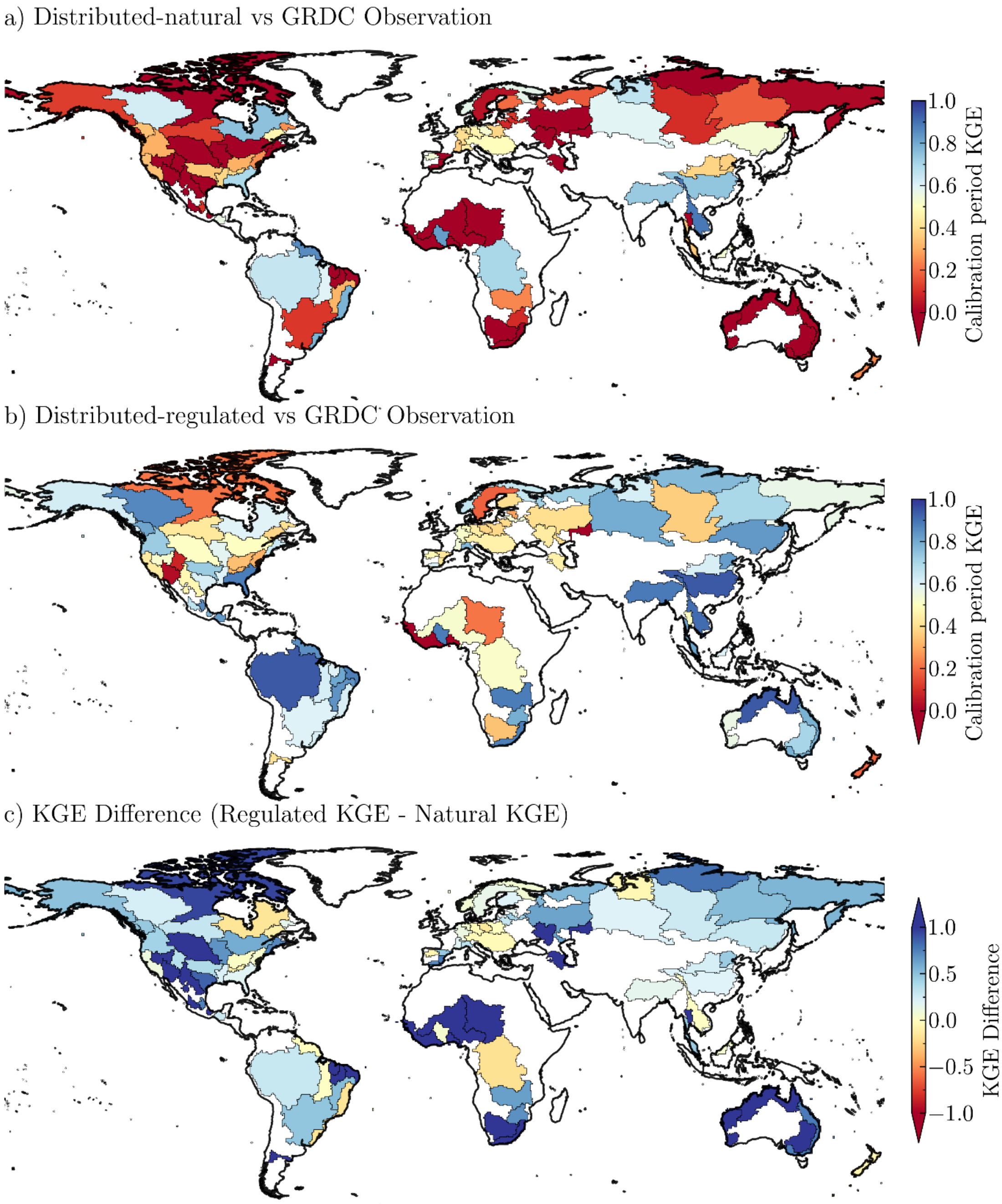


Figure 6-8: Spatial maps of KGE between the monthly GRDC observed streamflow and simulated streamflow from (a) Distributed-natural, (b) Distributed-regulated, and c) Difference (Regulated KGE – Natural KGE).

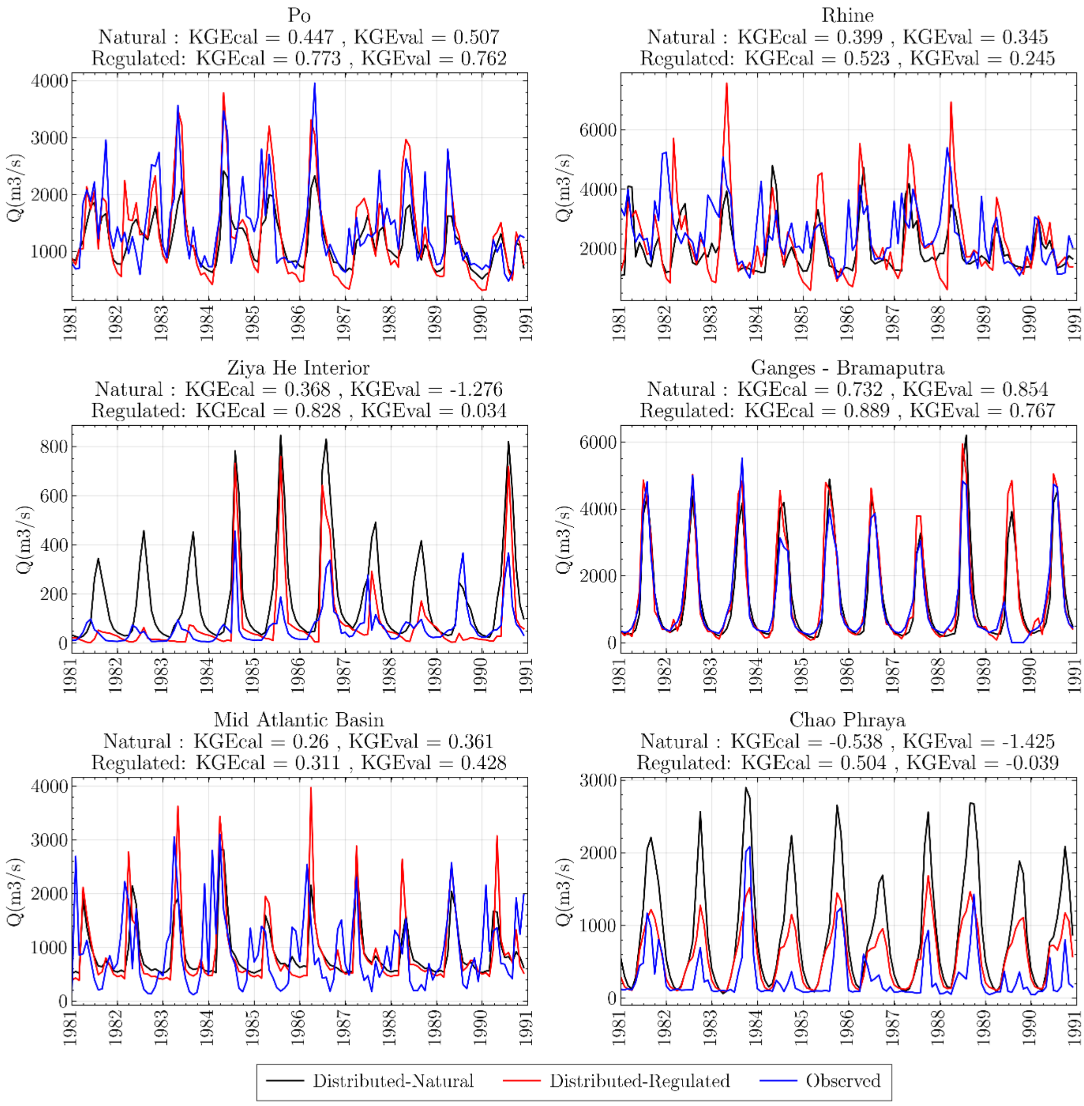


Figure 6-9: Simulated and observed monthly streamflow for six basins with the highest water demand in the validation period.

To assess how well the enhanced model captures water availability variations under drought events, Figure 6-10 shows the time series of SDI values (for the period 1981-1990) for the same six basins in Figure 6-9. Drought events are characterized by clusters of negative SDI values, which indicate below-normal streamflow conditions but not necessarily low flow conditions. The model cannot reasonably capture significant drought events in all basins except for the Po basins. Although the model can reproduce hydrologic drought conditions in some instances, overall, it performed poorly. Therefore, a more rigorous diagnostic evaluation is needed to identify the causes of the biases in basins for potential use. This presents a future area in which to improve Xanthos further.

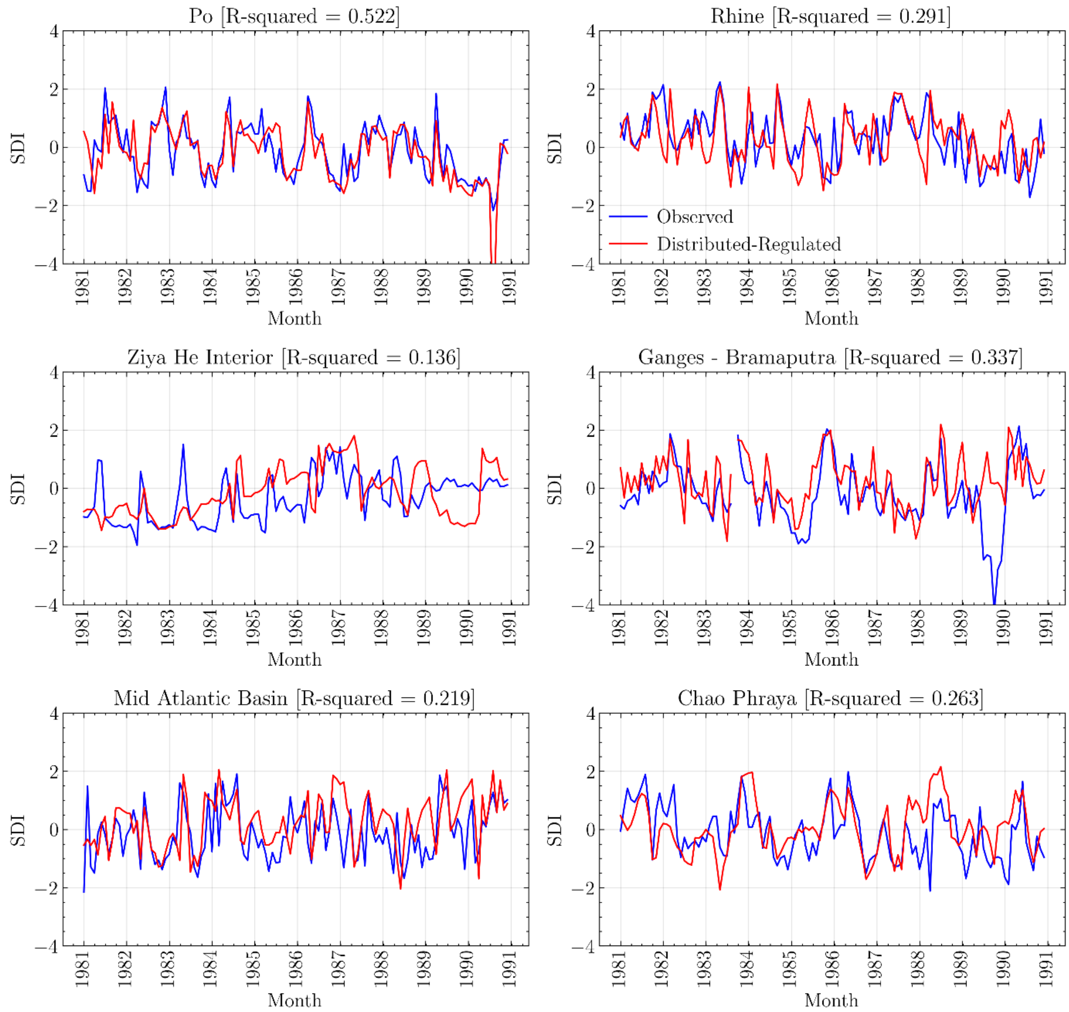


Figure 6-10. Comparison of simulated and observed SDI time series for the period 1981-1990 for the six selected basins with the highest water demand.

### 6.3.4 Parameter Sensitivity Analysis

To identify which parameters are most critical (i.e., contribute most to variance in key model outputs), we evaluate the model's sensitivity to the parameter changes, as shown in Figure 6-11. Note here that we use the correlation coefficient for the sensitivity analysis because the objective is to evaluate the correlation between the change in parameter values and model performances. The correlation coefficient is computed between model parameters and model performance for the runoff simulated with the one million parameter sets (Fig. 6-11a). The results show a significant relationship (correlation coefficient > |± 0.4|) only for parameters ***a*** (represent the propensity of runoff to occur before the soil is fully saturated) and ***b*** (represent an upper limit on the sum of evapotranspiration and soil moisture storage), which indicates that the model performance is sensitive to these two parameters.

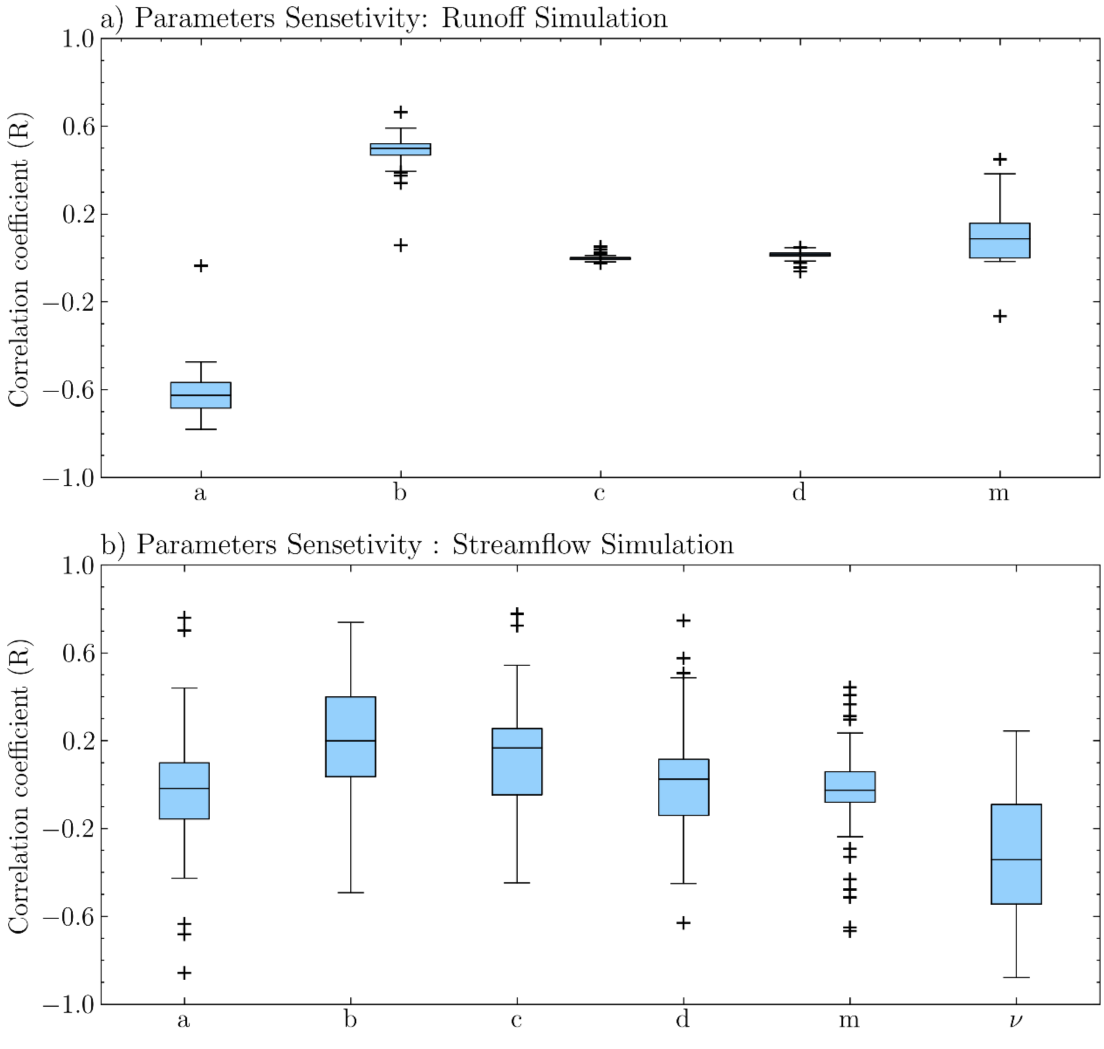


Figure 6-11: Parameter sensitivity analysis for the distributed version of enhanced Xanthos in the form of the correlation coefficient between parameter values and KGE.

A similar analysis is made for the set of parameters generated by combining the hundred best ***abcdm*** parameters set with the velocity adjustment parameter (υ) (Fig. 6-11b). Here, it appears that the model performance is more correlated with υ than the other parameters. This is expected because all the difference between the 100 selected runoff parameter combinations is supposed to be small.

### 6.3.5 Hydropower Reservoirs

Among the 91 basins, 75 of them have one or more hydropower reservoirs included in GRanD and hence in our simulations. In total, there are 296 such hydropower reservoirs in these 75 selected basins and 598 globally. At each of the 296 reservoirs, the simulated release and storage time series from *Distributed-regulated-II* are compared with those from *Distributed-regulated*. In order to observe the difference in the timing of the simulated reservoir behavior (between *Distributed-regulated-II* and *Distributed-regulated)* and the difference in the magnitude separately, here we use the coefficient of determination ($R^2$) to measure the difference in the timing and normalized-root-mean-square (NRMSE) to measure the difference in the magnitude, respectively. NRMSE here is the root mean square error normalized by the long-term mean.

Figure 6-12 shows a spatial map for the reservoirs and release comparisons between *Distributed-regulated-II* and *Distributed-regulated*. For the release comparison, the NRMSE is > 0.25 for ~ 45 % of the 296 reservoirs and while the $R^2$ is < 0.5 for ~28% of the reservoirs. Similarly, the comparison between storages time series for the two scenarios show NRMSE > 0.25 and $R^2$ < 0.5 for ~44% and ~90% of the 296 reservoirs, respectively. This indicates that the storage patterns have a very significant disagreement across almost all of the reservoirs; at the same time, the releases showed at least a satisfactory agreement for most of the reservoirs. The correlation between reservoir capacity and NSE is close to zero, indicating that the dissimilarity or lack thereof in release and storage patterns are unrelated to reservoir size. To the very least, the observed characteristics, in general, imply that simulating hydropower reservoirs as a flood control is another source of uncertainty in water management representation in global hydrological models. The approach we implement for simulating hydropower reservoirs should be treated as a baseline for representing hydropower reservoirs in global hydrological models. Future investigation is thus needed to shed more light on the comparison between hydropower and flood-control reservoirs.

We further select the Yenisey basin to look into more details. In Yenisey, the upstream area of the GRDC station is dominated by hydropower reservoirs, i.e., four hydropower reservoirs and two flood-control, as shown in Figure 6-13a. Note that one of the two flood-control reservoirs is located downstream of the hydropower reservoirs (Figure 6-13a). This spatial arrangement allows us to evaluate the effects of simulating hydropower reservoirs as flood-control without interference from the third purpose (i.e., in cases like an irrigation reservoir is located downstream of a hydropower reservoir). Figure 6-13b shows the total simulated storage (sum of all six reservoirs) from *Distributed-regulated-II* and *Distributed-regulated*. The difference in the magnitude of total simulated storage between the two simulations is very significant. In *Distributed-regulated-II,* where all reservoirs are simulated as flood-control, the storage is relatively more variable, likely because the release aims to maintain mean annual flow, which leads to release greater than inflow during the drier seasons and quick fill up during the wet seasons. The streamflow comparison at the GRDC site (Fig. 6- 13c) indicates that the difference in the simulated reservoir releases is significant as well. The KGE values drop from 0.366 to 0.152 during the calibration period (1971-1980) and from 0.293 to 0.008 during the validation period (1981-1990) when simulating the hydropower reservoirs as flood-control.

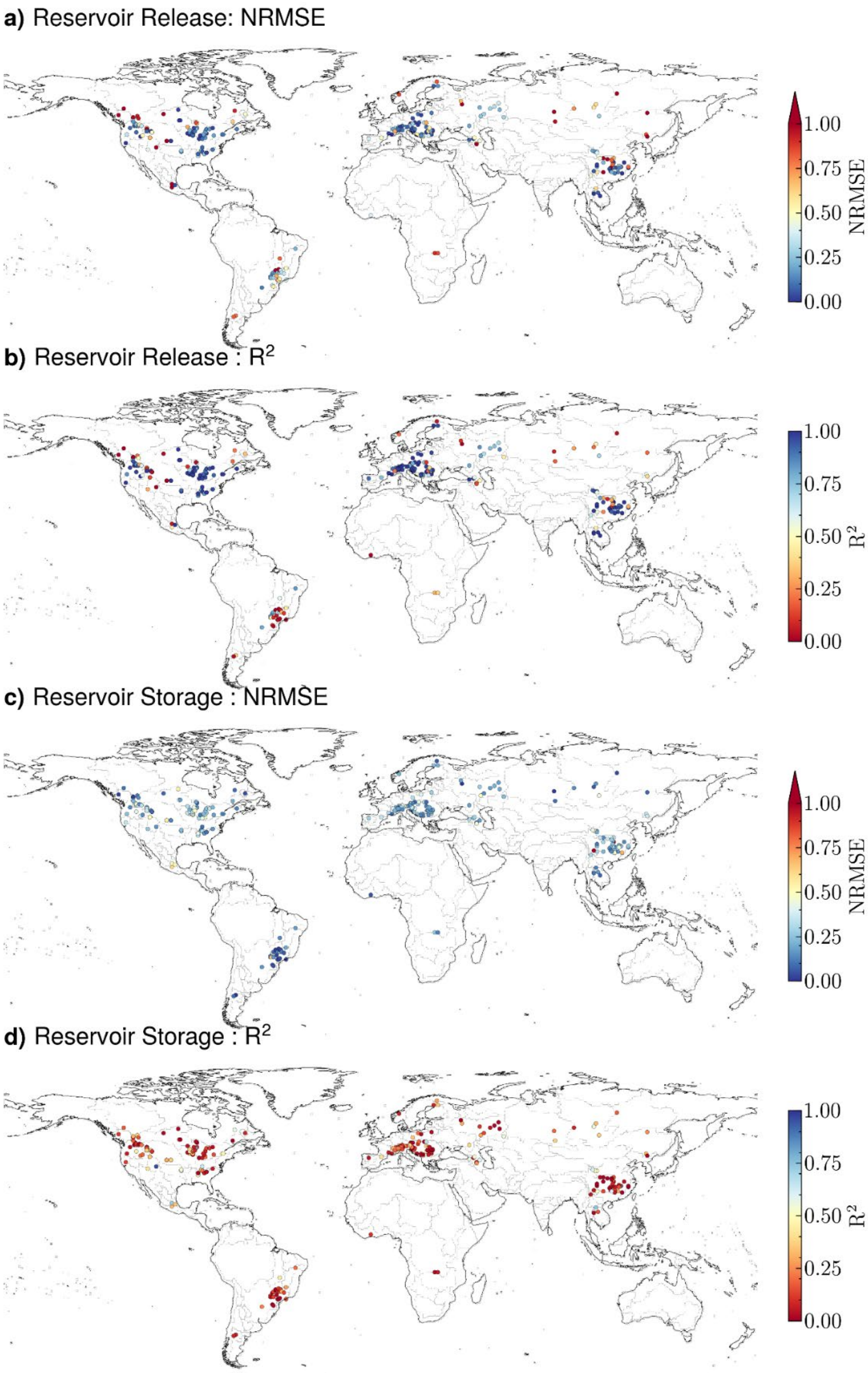


Figure 6-12: Difference between reservoir release time series between those simulated as hydropower reservoirs and those simulated as flood control reservoirs.

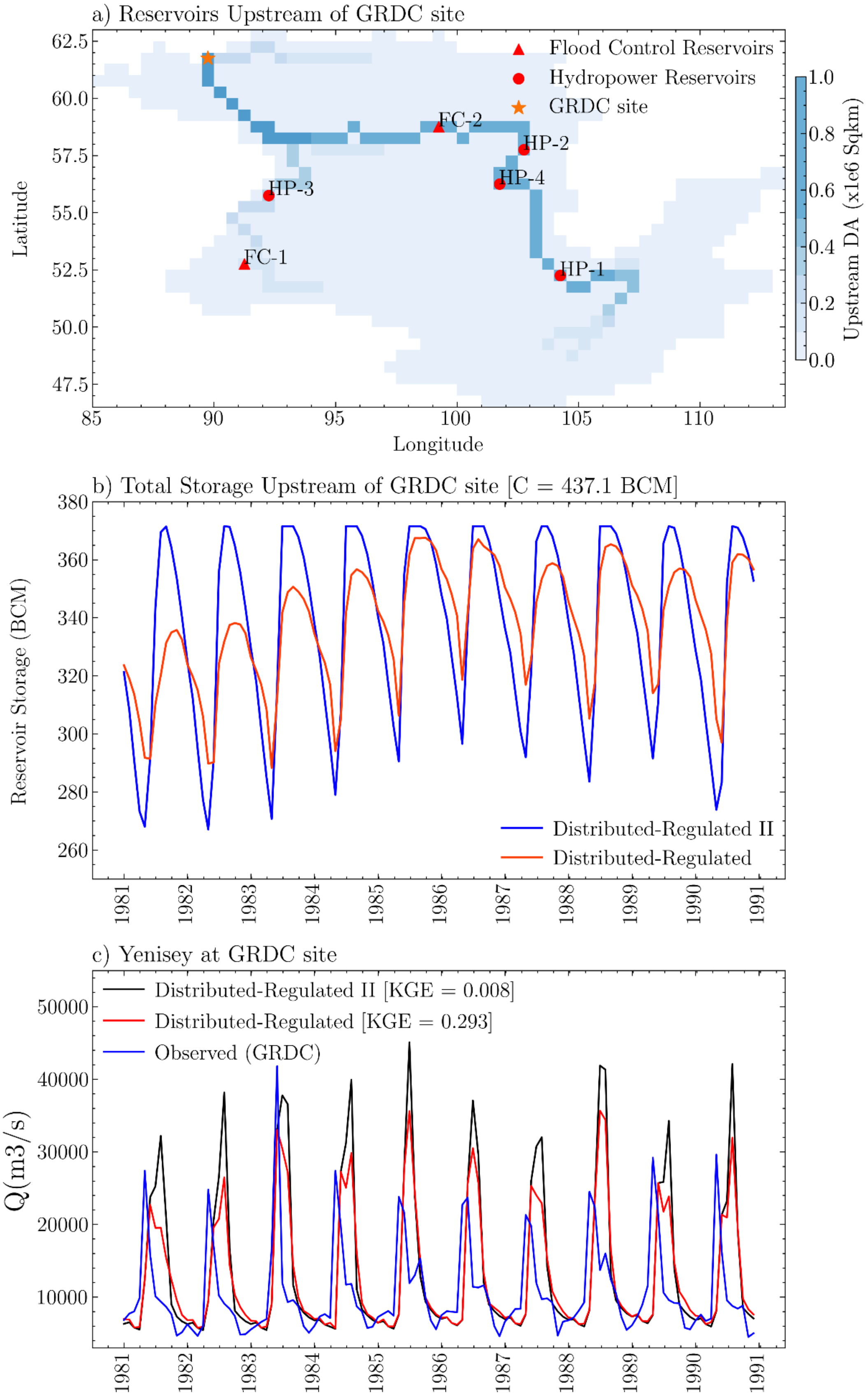


Figure 6-13: Yenisey basin reservoirs upstream of GRDC site (a), total reservoir storage upstream (b), streamflow at GRDC site (c). DA is the upstream drainage area, and C is the total capacity of reservoirs upstream.

Figure 6-14 depicts the temporal variability of simulated storage at each individual reservoir in Yenisey. When simulated as hydropower, reservoirs generally maintain high storage than when simulated as flood control. This can be attributed to the release policy we employ for hydropower simulation, which targets maximum long-term revenue where reservoir storage level is an essential component. Reservoirs downstream of hydropower reservoirs are also influenced by the change of reservoir purpose from hydropower to flood-control (Fig. 6-13c).

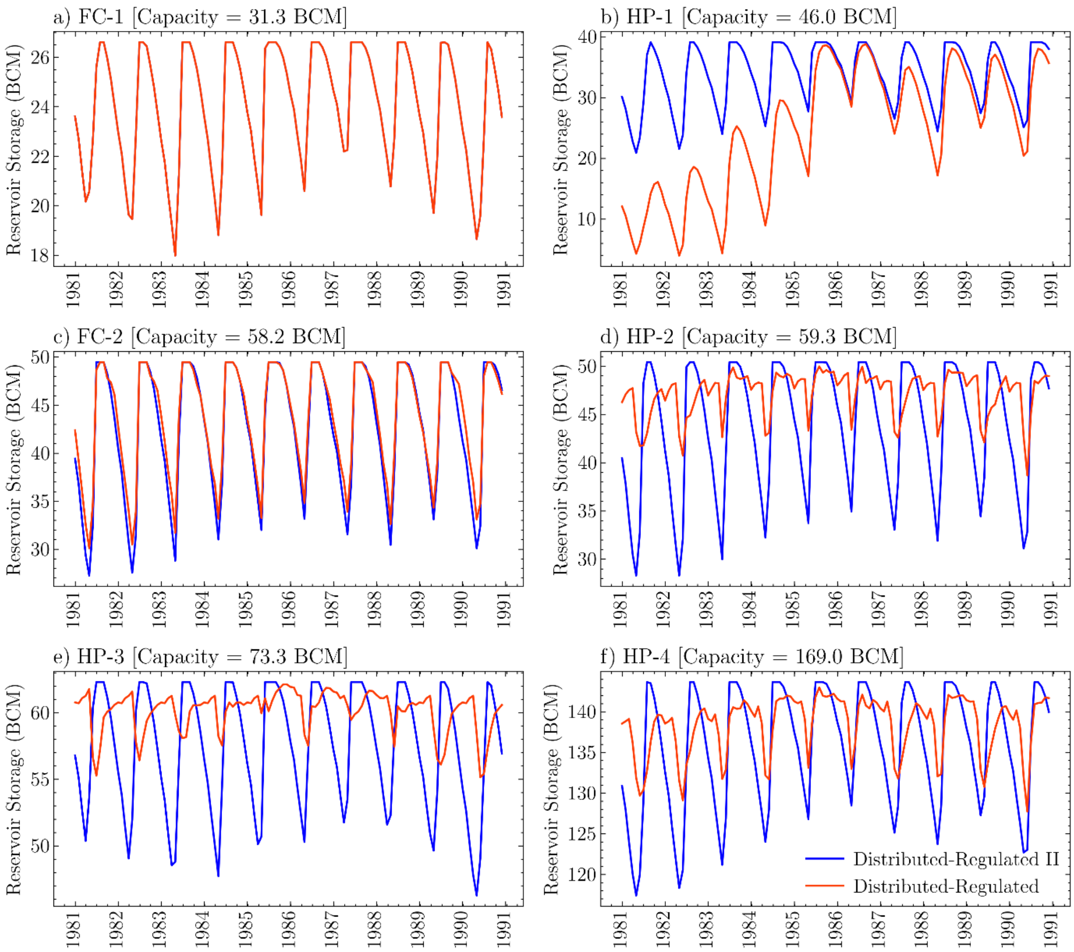


Figure 6-14: Simulated storage characteristics for reservoirs located upstream of Yenisey basin GRDC station for the last ten years of our simulation. Four are hydropower (a, d, e, and f), and two are flood control (b and c) reservoirs.

Figure 6- 15 shows the difference between the simulated monthly releases in the peak and low flow periods. On the one hand, the release from the flood control

reservoirs is high during peak flow periods because they aim to create space for the next flood event. On the other hand, the release from the hydropower reservoirs can only go up to the maximum turbine flow plus spillover. The Hanasaki approach readjusts the mean annual flow depending on the reservoir's degree of regulation (i.e., the ratio of capacity to mean annual inflow). Therefore, in Xanthos, given that the readjusted mean annual flow is greater than the environmental flow (10% of the mean annual flow), it remains a constant value. For hydropower reservoirs, low flow releases are determined by a release policy intended to maximize revenue. Because of the changes in reservoir purpose, downstream reservoir releases are also modified.

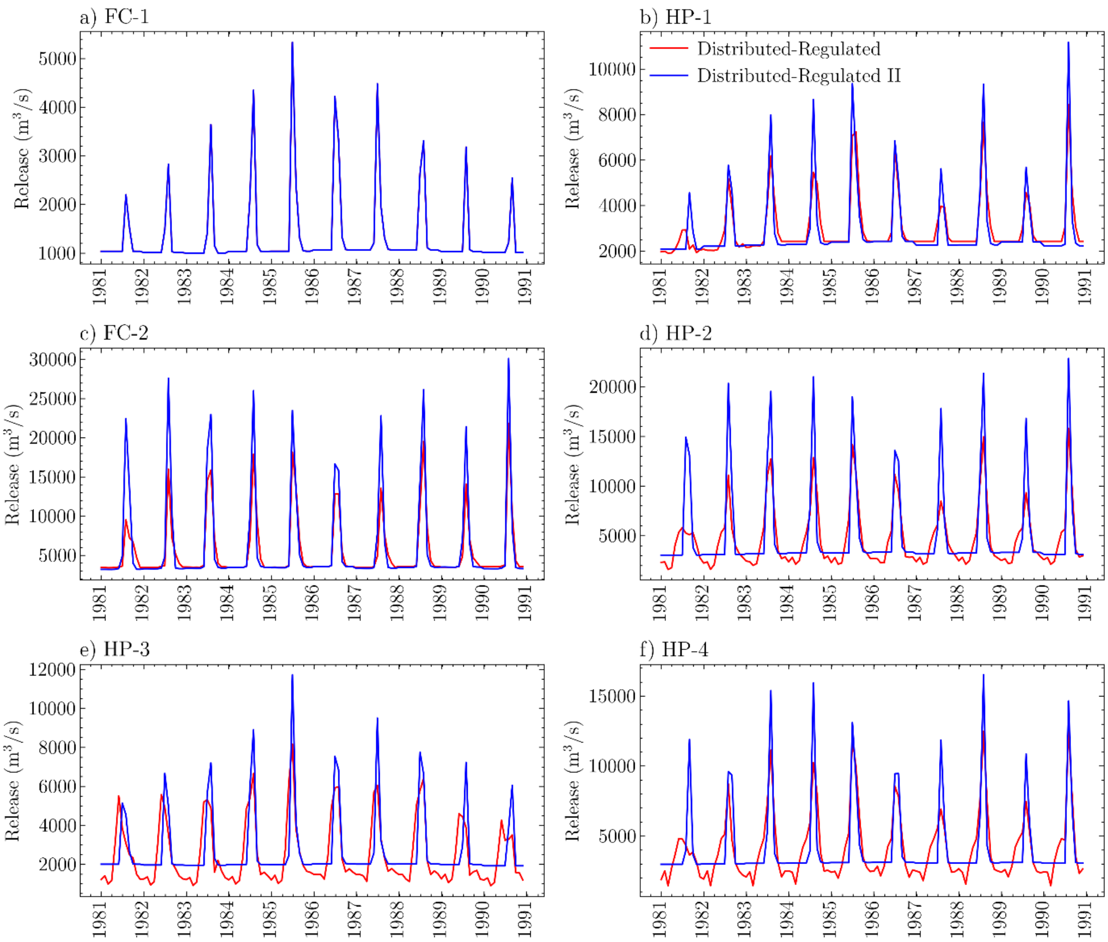

Figure 6-15: Similar to Figure 6-14, except for simulated releases.

Overall, hydropower and flood-control reservoirs behave very differently under the same climate and upstream conditions. Nevertheless, we note that it is premature to conclude from the above analysis that treating hydropower reservoirs as flood-control leads to poor hydrological simulations. Many reservoirs, particularly those large ones, are multi-purposed, and multiple factors control their behavior. This study takes the same simplification strategy adopted by all the existing GHMs, i.e., treating all the reservoirs as single-purpose. Overcoming this simplification in a GHM setting is beyond the scope of this study and left for the future.

## 6.4 Summary and Conclusions

This study adds a new water management module into Xanthos to improve its representation of global hydrological systems. The new water management module enhances Xanthos mainly by introducing reservoir regulation and local surface water withdrawal. We represent three categories of reservoirs in different ways: irrigation, hydropower and flood-control and others. We apply the enhanced Xanthos globally at a 0.5-degree spatial resolution and monthly time step. Validation against the observed streamflow at 91 river stations suggests the improved performance over the original version of Xanthos. At the individual reservoir level, we show that hydropower and flood-control reservoirs indeed behave quite differently, particularly in terms of reservoir storage variations. At the regional level, we show that treating hydropower reservoirs as flood-control leads to at least noticeable impacts on the simulated streamflow. We also show that the new model can reasonably capture drought dynamics in managed river systems. This new feature can improve the analysis of finer-scale energy-water-land dynamics within frameworks capable of ingesting Xanthos outputs to capture water sector supply-demand dynamics (e.g., Khan et al., 2020).

There are several opportunities to improve the river system modeling further. First, the groundwater storage (both above and below confined aquifers) could be represented more explicitly, which will enable the integration of groundwater pumping as an additional water supply. Second, natural lakes could be added in addition to reservoirs. Second, lakes are an essential source of water supply, although they are not as heavily managed as reservoirs. They also significantly impact the regional climate through their water and energy exchanges with the atmosphere. Third, hydrologically small reservoirs (i.e., those with a storage capacity less than 0.1 $km^3$) (Lehner et al., 2011) are currently not accounted for due to data limitations, but they potentially play an essential role in the regional and global water supply. Last but not least, the representation of reservoirs could be enhanced by accounting for reservoir sedimentation, given that reservoir storage is being lost globally at a rate of 0.5% per year (Mahmood, 1987; White, 2001). Relatively simple, empirically-based approaches to capture these dynamics for reservoirs globally have been shown to be effective and can be borrowed from other open-source modeling frameworks (e.g., Wild et al., 2021).

Even with the above limitations, the water management module we introduce here offers a more realistic representation of river systems in global hydrologic models like Xanthos. The model has the potential to provide insight into the competition between changes in water availability (primarily affected by climate variability) and water demand (controlled mainly by human activities) at regional or global scales and support decision making in a complex socio-economic system setting under various future climate change and management scenarios.

# 7 Conclusions, Implications, and Future work

## 7.1 Conclusions

Motivated by the need for simplified and falsifiable approaches for linking catchment water balance with vegetation dynamics, most of this dissertation chapters aimed to develop and implement such macroscopic functional frameworks. The inspiration was to look for patterns and functions among a population of catchments, not to analyze a particular watershed in isolation. Hence, a Darwinian approach has been adopted to develop simple, falsifiable, and sufficiently exact functions. For this purpose, a population of near-natural catchments distributed across climatic and landscape gradients of the continental United States was employed. The developed functional frameworks and generated understanding were integrated into a global hydrological model. The objective was to extend the hydrological model capacity beyond simulating hydrologic releases. This was followed by developing an approach for implementing the representation of water management infrastructure (i.e., reservoirs) in the same global hydrological model. The study domain for the reservoir representation is global and limited to reservoirs with a storage capacity larger than 0.1 $km^3$. The significant contributions of this dissertation are recited below,

1) A conceptual framework for exploring multi-scale links between catchment water balance and vegetation dynamics was developed theoretically based on the generalized proportionality hypothesis and successfully validated at near-pristine catchments distributed across the continental United States. The functional framework (i.e., Horton Index (HI)) has one parameter and two variables representing potential supply (i.e., catchment wetness) and demand (i.e., potential evapotranspiration). The parameter is an indicator for catchment wetting partitioning. A space-time similarity between the regional (inter-catchment) and

intra-annual variability (within catchment) was detected from observation data. The function can explain these space-time similarity patterns in a unified way. Under water-limited conditions, HI approaches its theoretical maximum of 1.0, and its variability decreases; this is true for both within-catchment and inter-catchment cases, shedding light on the HI's constancy property (Horton, 1933; Troch et al., 2009). This study also extended the use of HI to intra-annual, which is traditionally inter-annual.

2) A hypothesis was tested on the linearity of the relationship between gross primary production (GPP) and the water balance (i.e., ET) at the catchment scale. It was confirmed that the GPP-ET linear relationships reported at the plant or patch scale hold at the catchment level. Motivated by this understanding, a simple two-parameter functional relationship linking catchment water balance and vegetation carbon uptake was developed and successfully validated at catchments distributed across climate, vegetation type, and topographic gradients. This function was then used to demonstrate how one can reliably simulate seasonal vegetation dynamics at the monthly scale. The two parameters are estimated a priori as a function of climate and landscape conditions. Furthermore, the function is valuable for estimating transpiration at the catchment scale.

3) Vegetation carbon uptake response to catchment water supply and atmospheric dryness was analyzed using indices summarizing climatic, hydrologic, and vegetation characteristics. The lag between seasonal water supply carbon uptake and carbon uptake and atmospheric dryness creates a hysteresis. Both hysteresis curve patterns are controlled jointly by the seasonal characteristics of the catchment energy and water use. The narrowest hysteresis develops in catchments that operate at their highest hydrologic and climatic efficiency throughout the year. Widest hysteresis develops when energy and water use efficiency have strong intra-annual variability and are out of phase. The direction is generally

counterclockwise as vegetation response lag behind water availability. However, some catchments show a clockwise pattern. These catchments are dominated by vegetation that responds quickly to water availability but dies under increased hydrologic stress, for instance, grasslands. For catchments oscillating between energy-limited and water-limited states, it was found that vegetation is under seasonal hydrologic stress when catchment transitions into water-limited. Catchments that are permanently water-limited are characterized by carbon uptake efficiency of low magnitude and low seasonal variability. The seasonal patterns of total carbon uptake are opposite to the season carbon uptake efficiency. Vegetation total carbon uptake increases as catchment get drier and uptake efficiency decreases.

4) The developed HI analytical framework and the functional relationship between GPP and ET were used to extend Xanthos model capacity beyond simulating hydrologic releases. The monthly GPP simulated by the coupled model performed reasonably well against another global dataset. This study finding also showed that at the global scale, long-term climatic characteristics, including vapor pressure deficit, precipitation seasonality, snow fraction, and solar radiation determine the type of linear relationship between GPP and ET. It also concluded that the GPP-ET functional relationship applies globally and can be coupled with simple hydrologic models and simulate monthly GPP reasonably well.

5) A new water management module was developed for Xanthos. The aim was to improve the model's representation of global river systems. The module enhances Xanthos mainly by introducing reservoir regulation and local surface water withdrawal. Three reservoir types were represented: hydropower, irrigation, and flood control. The reservoir operation rules are simulated based on purposes and storage characteristics. The inclusion of reservoirs improved the model simulation performances significantly, as shown by comparison against the observed streamflow. It is the first attempt to represent hydropower reservoirs in a global hydrologic model. This work also uses a novel model parameter estimation which helps in reducing the equifinality issues.

## 7.2 Implications

The dissertation presented two groups of study. The first three chapters (2 – 4) adopted a Darwinian approach to investigate the links between catchment vegetation dynamics and water balance. The last two chapters (5 & 6) focus on enhancing Xanthos' capacity, a global hydrological model. The implications of the findings presented in each chapter were recited as follows.

1) The developed Horton index analytical framework paves the way for many exciting opportunities to advance our understanding of water-plant interactions. The framework can be used as a first-order constraint when simulating ecological and hydrological responses using hydrological, land surface, and earth system models. It can also help improve the parameterization of hydrologic models to better estimate the runoff, for instance, according to dominant vegetation cover. The emergent space-time similarity patterns may be used as empirical evidence to advance our understanding of Horton's hypothesis that vegetation practices maximization of productivity relative to available water (Horton, 1933).
2) The GPP-ET functional relationship directly links catchment water balance to terrestrial vegetation productivity; hence, it can be used as a diagnostic tool for coupled water-carbon simulations at the catchment, regional or larger scales. Coupled with simple hydrologic models such as the ***abcd*** (Martinez and Gupta, 2010; Thomas, 1981) and the probability distribution type models (Moore, 2007; Wang, 2018), the function can enhance their capacity by linking them to vegetation dynamics. The function can also simulate catchment, grid, or larger scale transpiration contributions to total evapotranspiration.

3) The findings from the links between GPP and two major abiotic factors, catchment water available for vegetation use and atmospheric dryness, establish a need to develop a functional framework between catchment water supply, atmospheric demand, and vegetation productivity. A framework that can help track normal and extreme hydrologic and climatic signal's impact on catchment vegetation and vice versa. Further understanding of the three-way connection (i.e., water supply – vegetation – atmospheric demand) can be a starting place for what vegetation does between and within storm periods.
4) The promising performance obtained evaluating GPP simulated from the coupling ***abcd*** model with the HI and GPP-ET function implies that enhanced hydrologic models can simulate vegetation dynamics reasonably well without too many detailed representations. Thus, this approach can be employed for diagnosing hydrologic models with vegetation dynamics information.
5) The water management module introduced in Xanthos offers a more realistic representation of river systems. The model has the potential to provide insight into the competition between changes in water availability (primarily affected by climate variability) and water demand (controlled mainly by human activities) at regional or global scales and support decision making in a complex socio-economic system setting under various future climate change and management scenarios. It will allow for assessing future reservoir development and management from a coupled human-natural system perspective. It also affirms the need for representing hydropower reservoirs in global hydrologic models.

## 7.3 Future work

The was dissertation focused on the hydrological-ecological and hydrological-human systems independently. The intersection between the three systems, the water-vegetation-human nexus, is an exciting arena that deserves more attention, particularly in an urban setting. In part, the sustainability of urban systems hinges on the co-dynamics and resilience of these three systems. Exploring novel ways to achieve sustainable, adaptable, and resilient infrastructure from an ecohydrological perspective is an exciting arena. The future works of this dissertation will focus on the following two areas.

1) Present-day activities to establish a sustainable urban system through building eco-cities and green infrastructures are often guided by the functionalities of the gray infrastructures, and plants are frequently treated as aesthetic features, simply there to improve urban wellbeing. However, humans and vegetation are alike in that they both demand water from the hydrologic system. The main difference is that despite the height of our knowledge and technologies, we face a water management crisis in many corners of the world with fast-rising demands and depreciating freshwater resources. Plants do not have such capacities or forecast future water supply or demand, but they are continually aware of available resources. They cope with prolonged water shortages and changes around them and survive severe environmental conditions. They harmonize with their environment and maximize productivity relative to available water. Hence, there are vital lessons humans can learn from plants, and this could be essential for a step toward understanding the urban ecohydrological system resilience.

2) Urban ecohydrological systems continue to change due to the rapidly evolving dynamic spatial expansions of urban areas to accommodate the growing urban dwellers. Trends indicate that climate change is likely to exacerbate the odds of natural hazards such as drought and flood in urban settings. While these hazards are generally unavoidable for all communities, resilience to the resulting risk is significantly lower in socially vulnerable populations. The latest ASCE Americas Infrastructure report shows that the number of high-hazard-potential reservoirs in the US has doubled over the last two decades, mainly due to encroachment into the downstream areas of the previously rural reservoirs. Similarly, about 45% of the US population is exposed to high- to very high-risk levee systems. Historical evidence shows that communities residing or working in such risk regions are predominantly people of color. The emerging drought impact patterns across many US cities also echo similar phenomena. The resilience of the vulnerable community is a baseline for urban infrastructure resilience success. Hence, addressing the needs of the disproportionately impacted community is essential for improving the overall resilience. The critical step in this direction is understanding the underlying process of human-flood and human-drought interactions in low-income communities through theoretical analysis and modeling to inform policymakers.

## References

Abeshu, G.W., Li, H.Y., 2021. Horton Index: Conceptual Framework for Exploring Multi-Scale Links Between Catchment Water Balance and Vegetation Dynamics. Water Resour. Res. 57, 1–24. https://doi.org/10.1029/2020WR029343

Abeshu, G.W., Li, H.Y., Zhu, Z., Tan, Z., Leung, L.R., Li, H.Y., 2022. Median bed-material sediment particle size across rivers in the contiguous US. Earth Syst. Sci. Data 14, 929–942. https://doi.org/10.5194/essd-14-929-2022

Adams, W.W., Zarter, C.R., Ebbert, V., Demmig-Adams, B., 2004. Photoprotective Strategies of Overwintering Evergreens. Bioscience 54, 41–49. https://doi.org/10.1641/0006-3568(2004)054[0041:psooe]2.0.co;2

Addor, N., Newman, A.J., Mizukami, N., Clark, M.P., 2017. The CAMELS data set: Catchment attributes and meteorology for large-sample studies. Hydrol. Earth Syst. Sci. 21, 5293–5313. https://doi.org/10.5194/hess-21-5293-2017

Akiba, T., Sano, S., Yanase, T., Ohta, T., Koyama, M., 2019. Optuna: A Next-generation Hyperparameter Optimization Framework, in: Proceedings of the ACM SIGKDD International Conference on Knowledge Discovery and Data Mining. ACM, New York, NY, USA, pp. 2623–2631. https://doi.org/10.1145/3292500.3330701

Alexander, L.C., Fritz, K.M., Schofield, K.A., Autrey, B.C., DeMeester, J.E., Golden, H.E., Goodrich, D.C., Kepner, W.G., Kiperwas, H.R., Lane, C.R., LeDuc, S.D., Leibowitz, S.G., McManus, M.G., Pollard, A.I., Ridley, C.E., Vanderhoof, M.K., Wigington, P.J., 2018. Featured Collection Introduction: Connectivity of Streams and Wetlands to Downstream Waters. J. Am. Water Resour. Assoc. 54, 287–297. https://doi.org/10.1111/1752-1688.12630

Amenu, G.G., Kumar, P., 2008. A model for hydraulic redistribution incorporating coupled soil-root moisture transport. Hydrol. Earth Syst. Sci. 12, 55–74. https://doi.org/10.5194/hess-12-55-2008

Arciniega-Esparza, S., Breña-Naranjo, J.A., Troch, P.A., 2017. On the connection between terrestrial and riparian vegetation: the role of storage partitioning in water-limited catchments. Hydrol. Process. 31, 489–494. https://doi.org/10.1002/hyp.11071

Baldocchi, D., Falge, E., Gu, L., Olson, R., Hollinger, D., Running, S., Anthoni, P., Bernhofer, C., Davis, K., Evans, R., Fuentes, J., Goldstein, A., Katul, G., Law, B., Lee, X., Malhi, Y., Meyers, T., Munger, W., Oechel, W., Paw, U.K.T., Pilegaard, K., Schmid, H.P., Valentini, R., Verma, S., Vesala, T., Wilson, K., Wofsy, S., 2001. FLUXNET: A New Tool to Study the Temporal and Spatial Variability of Ecosystem-Scale Carbon Dioxide, Water Vapor, and Energy Flux Densities. Bull. Am. Meteorol. Soc. 82, 2415–2434. https://doi.org/10.1175/1520-0477(2001)082<2415:FANTTS>2.3.CO;2

Bartlett, M.S., Parolari, A.J., McDonnell, J.J., Porporato, A., 2016a. Framework for event-based semidistributed modeling that unifies the SCS-CN method, VIC, PDM, and TOPMODEL. Water Resour. Res. 52, 7036–7052. https://doi.org/10.1002/2016WR019084

Bartlett, M.S., Parolari, A.J., McDonnell, J.J., Porporato, A., 2016b. Beyond the SCS-CN method: A theoretical framework for spatially lumped rainfall-runoff response. Water Resour. Res. 52, 4608–4627. https://doi.org/10.1002/2015WR018439

Beer, C., Ciais, P., Reichstein, M., Baldocchi, D., Law, B.E., Papale, D., Soussana, J.F., Ammann, C., Buchmann, N., Frank, D., Gianelle, D., Janssens, I.A., Knohl, A., Köstner, B., Moors, E., Roupsard, O., Verbeeck, H., Vesala, T., Williams, C.A., Wohlfahrt, G., 2009. Temporal and among-site variability of inherent water use efficiency at the ecosystem level. Global Biogeochem. Cycles 23. https://doi.org/10.1029/2008GB003233

Berghuijs, W.R., Sivapalan, M., Woods, R.A., Savenije, H.H.G., 2014. Patterns of similarity of seasonal water balances: A window into streamflow variability over a range of time scales. Water Resour. Res. 50, 5638–5661. https://doi.org/10.1002/2014WR015692

Best, M.J., Pryor, M., Clark, D.B., Rooney, G.G., Essery, R.. L.H., Ménard, C.B., Edwards, J.M., Hendry, M.A., Porson, A., Gedney, N., Mercado, L.M., Sitch, S., Blyth, E., Boucher, O., Cox, P.M., Grimmond, C.S.B., Harding, R.J., 2011. The Joint UK Land Environment Simulator (JULES), model description – Part 1: Energy and water fluxes. Geosci. Model Dev. 4, 677–699. https://doi.org/10.5194/gmd-4-677-2011

Biemans, H., Haddeland, I., Kabat, P., Ludwig, F., Hutjes, R.W.A., Heinke, J., Von Bloh, W., Gerten, D., 2011. Impact of reservoirs on river discharge and irrigation water supply during the 20th century. Water Resour. Res. 47, 1–15. https://doi.org/10.1029/2009WR008929

Blöschl, G., Sivapalan, M., Wagener, T., Viglione, A., Savenije, H., 2011. Runoff prediction in ungauged basins: Synthesis across processes, places and scales, Runoff Prediction in Ungauged Basins: Synthesis Across Processes, Places and Scales. https://doi.org/10.1017/CBO9781139235761

Bonan, G.B., Doney, S.C., 2018. Climate, ecosystems, and planetary futures: The challenge to predict life in Earth system models. Science (80-. ). 359. https://doi.org/10.1126/science.aam8328

Bonan, G.B., Patton, E.G., Harman, I.N., Oleson, K.W., Finnigan, J.J., Lu, Y., Burakowski, E.A., 2018. Modeling canopy-induced turbulence in the Earth system: A unified parameterization of turbulent exchange within plant canopies and the roughness sublayer (CLM-ml v0). Geosci. Model Dev. 11, 1467–1496. https://doi.org/10.5194/gmd-11-1467-2018

Boulange, J., Hanasaki, N., Yamazaki, D., Pokhrel, Y., 2021. Role of dams in reducing global flood exposure under climate change. Nat. Commun. 12, 1–7. https://doi.org/10.1038/s41467-020-20704-0

Branstetter, M.L., Erickson, D.J., 2003. Continental runoff dynamics in the Community Climate System Model 2 (CCSM2) control simulation. J. Geophys. Res. Atmos. 108, 1–17. https://doi.org/10.1029/2002jd003212

Brooks, J.R., Meinzer, F.C., Coulombe, R., Gregg, J., 2002. Hydraulic redistribution of soil water during summer drought in two contrasting Pacific Northwest coniferous forests. Tree Physiol. 22, 1107–1117. https://doi.org/10.1093/treephys/22.15-16.1107

Brooks, P.D., Troch, P.A., Durcik, M., Gallo, E., Schlegel, M., 2011. Quantifying regional scale ecosystem response to changes in precipitation: Not all rain is created equal. Water Resour. Res. 47, 1–13. https://doi.org/10.1029/2010WR009762

Budyko, M.I., 1974. Climate and Life. Academic Press, New York.

Burek, P., Satoh, Y., Kahil, T., Tang, T., Greve, P., Smilovic, M., Guillaumot, L., Zhao, F., Wada, Y., 2020. Development of the Community Water Model (CWatM v1.04)

- A high-resolution hydrological model for global and regional assessment of integrated water resources management. Geosci. Model Dev. 13, 3267–3298. https://doi.org/10.5194/gmd-13-3267-2020

Byrne, M.P., O'Gorman, P.A., 2013. Link between land-ocean warming contrast and surface relative humidities in simulations with coupled climate models. Geophys. Res. Lett. 40, 5223–5227. https://doi.org/10.1002/grl.50971

Calvin, K., Patel, P., Clarke, L., Asrar, G., Bond-Lamberty, B., Yiyun Cui, R., Di Vittorio, A., Dorheim, K., Edmonds, J., Hartin, C., Hejazi, M., Horowitz, R., Iyer, G., Kyle, P., Kim, S., Link, R., Mcjeon, H., Smith, S.J., Snyder, A., Waldhoff, S., Wise, M., 2019. GCAM v5.1: Representing the linkages between energy, water, land, climate, and economic systems. Geosci. Model Dev. 12, 677–698. https://doi.org/10.5194/gmd-12-677-2019

Chen, T., Guestrin, C., 2016. XGBoost: A scalable tree boosting system, in: Proceedings of the ACM SIGKDD International Conference on Knowledge Discovery and Data Mining. ACM, New York, NY, USA, pp. 785–794. https://doi.org/10.1145/2939672.2939785

Cohen, M.J., Creed, I.F., Alexander, L., Basu, N.B., Calhoun, A.J.K., Craft, C., D'Amico, E., DeKeyser, E., Fowler, L., Golden, H.E., Jawitz, J.W., Kalla, P., Kirkman, L.K., Lane, C.R., Lang, M., Leibowitz, S.G., Lewis, D.B., Marton, J., McLaughlin, D.L., Mushet, D.M., Raanan-Kiperwas, H., Rains, M.C., Smith, L., Walls, S.C., 2016. Do geographically isolated wetlands influence landscape functions? Proc. Natl. Acad. Sci. U. S. A. https://doi.org/10.1073/pnas.1512650113

De Roo, A.P.J., Wesseling, C.G., Van Deursen, W.P.A., 2000. Physically based river basin modelling within a GIS: The LISFLOOD model. Hydrol. Process. 14, 1981–1992. https://doi.org/10.1002/1099-1085(20000815/30)14:11/12<1981::aid-hyp49>3.0.co;2-f

Deb, K., Pratap, A., Agarwal, S., Meyarivan, T., 2002. A fast and elitist multiobjective genetic algorithm: NSGA-II. IEEE Trans. Evol. Comput. 6, 182–197. https://doi.org/10.1109/4235.996017

Dingman, S.L., 2015. Physical Hydrology.

Döll, P., Fiedler, K., Zhang, J., 2009. Global-scale analysis of river flow alterations due to water withdrawals and reservoirs. Hydrol. Earth Syst. Sci. 13, 2413–2432. https://doi.org/10.5194/hess-13-2413-2009

Duan, Q., Sorooshian, S., Gupta, V., 1992. Effective and Efficient Global Optimization for Conceptual Rainfall-Runoff Models 28, 1015–1031.

Eagleson, P.S., 2002. Ecohydrology : Darwinian Expression of Vegetation Form and Function, Ecohydrology. Cambridge University Press, Cambridge. https://doi.org/10.1017/CBO9780511535680

Evans, J.D., 1996. Straightforward statistics for the behavioral sciences. Thomson Brooks/Cole Publishing, Pacific Grove, CA.

Fan, Y., Miguez-Macho, G., Jobbágy, E.G., Jackson, R.B., Otero-Casal, C., 2017. Hydrologic regulation of plant rooting depth. Proc. Natl. Acad. Sci. U. S. A. 114, 10572–10577. https://doi.org/10.1073/pnas.1712381114

Fatichi, S., Pappas, C., Ivanov, V.Y., 2016. Modeling plant–water interactions: an ecohydrological overview from the cell to the global scale. Wiley Interdiscip. Rev. Water 3, 327–368. https://doi.org/10.1002/wat2.1125

Fisher, N.I., 1993. Statistical analysis of circular data.

https://doi.org/10.1017/cbo9780511564345

France, P.W., 1981. Water resource systems planning and analysis, Advances in Water Resources. Prentice-Hall., Englewood Cliffs, New Jersey. https://doi.org/10.1016/0309-1708(81)90046-4

Fu, B.P., 1981. On the calculation of the evaporation from land surface. Sci. Atmos. Sin 5, 23–31.

Gentine, P., Green, J.K., Guérin, M., Humphrey, V., Seneviratne, S.I., Zhang, Y., Zhou, S., 2019. Coupling between the terrestrial carbon and water cycles - A review. Environ. Res. Lett. 14. https://doi.org/10.1088/1748-9326/ab22d6

Glinski, J., Lipiec, J., 2018. Soil physical conditions and plant roots, Soil Physical Conditions and Plant Roots. CRC Press. https://doi.org/10.1201/9781351076708

Golaz, J.C.J.-C., Caldwell, P.M.P.M., Van Roekel, L.P.L.P., Petersen, M.R., Tang, Q., Wolfe, J.D.J.D., Abeshu, G., Anantharaj, V., Asay-Davis, X.S.X.S., Bader, D.C.D.C., Baldwin, S.A.S.A., Bisht, G., Bogenschutz, P.A.P.A., Branstetter, M., Brunke, M.A.M.A., Brus, S.R.S.R., Burrows, S.M.S.M., Cameron-Smith, P.J.P.J., Donahue, A.S.A.S., Deakin, M., Easter, R.C., Evans, K.J.K.J., Feng, Y., Flanner, M., Foucar, J.G.J.G., Fyke, J.G.J.G., Griffin, B.M.B.M., Hannay, C., Harrop, B.E.B.E., Hoffman, M.J.M.J., Hunke, E.C.E.C., Jacob, R.L.R.L., Jacobsen, D.W.D.W., Jeffery, N., Jones, P.W.P.W., Keen, N.D.N.D., Klein, S.A.S.A., Larson, V.E.V.E., Leung, L.R.R., Li, H.Y.H.-Y., Lin, W., Lipscomb, W.H.W.H., Ma, P.L.P.-L., Mahajan, S., Maltrud, M.E.M.E., Mametjanov, A., McClean, J.L., McCoy, R.B.R.B., Neale, R.B.R.B., Price, S.F.S.F., Qian, Y., Rasch, P.J.P.J., Reeves Eyre, J.E.J.E.J., Riley, W.J.W.J., Ringler, T.D.T.D., Roberts, A.F.A.F., Roesler, E.L.E.L., Salinger, A.G.A.G., Shaheen, Z., Shi, X., Singh, B., Tang, J., Taylor, M.A.M.A., Thornton, P.E.P.E., Turner, A.K.A.K., Veneziani, M., Wan, H., Wang, H., Wang, S., Williams, D.N.D.N., Wolfram, P.J.P.J., Worley, P.H.P.H., Xie, S., Yang, Y., Yoon, J.-H.J.H., Zelinka, M.D.M.D., Zender, C.S.C.S., Zeng, X., Zhang, C., Zhang, K., Zhang, Y., Zheng, X., Zhou, T., Zhu, Q., 2019. The DOE E3SM Coupled Model Version 1: Overview and Evaluation at Standard Resolution. J. Adv. Model. Earth Syst. 11, 2089–2129. https://doi.org/10.1029/2018MS001603

Golden, H.E., Creed, I.F., Ali, G., Basu, N.B., Neff, B.P., Rains, M.C., McLaughlin, D.L., Alexander, L.C., Ameli, A.A., Christensen, J.R., Evenson, G.R., Jones, C.N., Lane, C.R., Lang, M., 2017. Integrating geographically isolated wetlands into land management decisions. Front. Ecol. Environ. 15, 319–327. https://doi.org/10.1002/fee.1504

Gomyo, M., Kuraji, K., 2016. Effect of the litter layer on runoff and evapotranspiration using the paired watershed method. J. For. Res. 21, 306–313. https://doi.org/10.1007/s10310-016-0542-5

Good, S.P., Noone, D., Bowen, G., 2015. Hydrologic connectivity constrains partitioning of global terrestrial water fluxes. Science (80-. ). 349, 175–177. https://doi.org/10.1126/science.aaa5931

Govind, A., Chen, J.M., Margolis, H., Ju, W., Sonnentag, O., Giasson, M.A., 2009. A spatially explicit hydro-ecological modeling framework (BEPS-TerrainLab V2.0): Model description and test in a boreal ecosystem in Eastern North America. J. Hydrol. 367, 200–216. https://doi.org/10.1016/j.jhydrol.2009.01.006

Granger, C.W.J., 1969. Investigating Causal Relations by Econometric Models and Cross-spectral Methods. Econometrica 37, 424. https://doi.org/10.2307/1912791

Green, J.K., Seneviratne, S.I., Berg, A.M., Findell, K.L., Hagemann, S., Lawrence, D.M., Gentine, P., 2019. Large influence of soil moisture on long-term terrestrial carbon uptake. Nature 565, 476–479. https://doi.org/10.1038/s41586-018-0848-x

Grogan, D.S., Zuidema, S., Prusevich, A., Wollheim, W.M., Glidden, S., Lammers, R.B., 2022. WBM : A scalable gridded global hydrologic model with water tracking functionality. Geosci. Model Dev. 08, 1–54.

Grossiord, C., Buckley, T.N., Cernusak, L.A., Novick, K.A., Poulter, B., Siegwolf, R.T.W., Sperry, J.S., McDowell, N.G., 2020. Plant responses to rising vapor pressure deficit. New Phytol. 226, 1550–1566. https://doi.org/10.1111/nph.16485

Guardiola-Claramonte, M., Troch, P.A., Ziegler, A.D., Giambelluca, T.W., Durcik, M., Vogler, J.B., Nullet, M.A., 2010. Hydrologic effects of the expansion of rubber (Hevea brasiliensis) in a tropical catchment. Ecohydrology 3, 306–314. https://doi.org/10.1002/eco.110

Guimberteau, M., Laval, K., Perrier, A., Polcher, J., 2012. Global effect of irrigation and its impact on the onset of the Indian summer monsoon. Clim. Dyn. 39, 1329–1348. https://doi.org/10.1007/s00382-011-1252-5

Gupta, H. V., Kling, H., Yilmaz, K.K., Martinez, G.F., 2009. Decomposition of the mean squared error and NSE performance criteria: Implications for improving hydrological modelling. J. Hydrol. 377, 80–91. https://doi.org/10.1016/j.jhydrol.2009.08.003

Haddeland, I., Skaugen, T., Lettenmaier, D.P., 2006. Anthropogenic impacts on continental surface water fluxes. Geophys. Res. Lett. 33, 2–5. https://doi.org/10.1029/2006GL026047

Hanasaki, N., Kanae, S., Oki, T., 2006. A reservoir operation scheme for global river routing models. J. Hydrol. 327, 22–41. https://doi.org/10.1016/j.jhydrol.2005.11.011

Hanasaki, N., Kanae, S., Oki, T., Masuda, K., Motoya, K., Shirakawa, N., Shen, Y., Tanaka, K., 2008. An integrated model for the assessment of global water resources - Part 1: Model description and input meteorological forcing. Hydrol. Earth Syst. Sci. 12, 1007–1025. https://doi.org/10.5194/hess-12-1007-2008

Harper, A.B., Cox, P.M., Friedlingstein, P., Wiltshire, A.J., Jones, C.D., Sitch, S., Mercado, L.M., Groenendijk, M., Robertson, E., Kattge, J., Bönisch, G., Atkin, O.K., Bahn, M., Cornelissen, J., Niinemets, Ü., Onipchenko, V., Peñuelas, J., Poorter, L., Reich, P.B., Soudzilovskaia, N.A., Van Bodegom, P., 2016. Improved representation of plant functional types and physiology in the Joint UK Land Environment Simulator (JULES v4.2) using plant trait information. Geosci. Model Dev. 9, 2415–2440. https://doi.org/10.5194/gmd-9-2415-2016

Harte, J., 2002. Toward a synthesis of the Newtonian and Darwinian worldviews. Phys. Today 55, 29–34. https://doi.org/10.1063/1.1522164

Hatfield, J.L., Prueger, J.H., 2015. Temperature extremes: Effect on plant growth and development. Weather Clim. Extrem. 10, 4–10. https://doi.org/10.1016/j.wace.2015.08.001

Hejazi, M.I., Edmonds, J., Clarke, L., Kyle, P., Davies, E., Chaturvedi, V., Eom, J., Wise, M., Patel, P., Calvin, K., 2013a. Integrated assessment of global water scarcity over the 21st century – Part 2: Climate change mitigation policies. Hydrol. Earth Syst. Sci. Discuss. 10, 3383–3425. https://doi.org/10.5194/hessd-10-3383-2013

Hejazi, M.I., Edmonds, J., Clarke, L., Kyle, P., Davies, E., Chaturvedi, V., Wise, M., Patel, P., Eom, J., Calvin, K., 2013b. Integrated assessment of global water scarcity over the 21st century – Part 1: Global water supply and demand under extreme radiative forcing. Hydrol. Earth Syst. Sci. Discuss. 10, 3327–3381. https://doi.org/10.5194/hessd-10-3327-2013

Hidy, D., Barcza, Z., MarjanoviÄ, H., Sever, M.Z.O., Dobor, L., Gelybó, G., Fodor, N., Pintér, K., Churkina, G., Running, S., Thornton, P., Bellocchi, G., Haszpra, L., Horváth, F., Suyker, A., Nagy, Z., 2016. Terrestrial ecosystem process model Biome-BGCMuSo v4.0: Summary of improvements and new modeling possibilities. Geosci. Model Dev. 9, 4405–4437. https://doi.org/10.5194/gmd-9-4405-2016

Hirpa, F.A., Salamon, P., Beck, H.E., Lorini, V., Alfieri, L., Zsoter, E., Dadson, S.J., 2018. Calibration of the Global Flood Awareness System (GloFAS) using daily streamflow data. J. Hydrol. 566, 595–606. https://doi.org/10.1016/j.jhydrol.2018.09.052

Hooshyar, M., Wang, D., 2016. An analytical solution of Richards' equation providing the physical basis of SCS curve number method and its proportionality relationship. Water Resour. Res. 52, 6611–6620. https://doi.org/10.1002/2016WR018885

Horton, R.E., 1933. The Role of infiltration in the hydrologic cycle. Eos, Trans. Am. Geophys. Union 14, 446–460. https://doi.org/10.1029/TR014i001p00446

Houska, T., Kraft, P., Chamorro-Chavez, A., Breuer, L., 2015. SPOTting model parameters using a ready-made python package. PLoS One 10, 1–22. https://doi.org/10.1371/journal.pone.0145180

Huang, Zhongwei; Hejazi, Mohamad; Li, Xinya; Tang, Qiuhong; Vernon, Chris; Leng, Guoyong; Liu, Yaling; Döll, Petra; Eisner, Stephanie; Gerten, Dieter; Hanasaki, Naota; Wada, Y., 2018. Global gridded monthly sectoral water use dataset for 1971-2010: v2. Zenodo. https://doi.org/10.5281/ZENODO.1209296

Huang, Z., Hejazi, M., Li, X., Tang, Q., Vernon, C., Leng, G., Liu, Y., Döll, P., Eisner, S., Gerten, D., Hanasaki, N., Wada, Y., 2018. Reconstruction of global gridded monthly sectoral water withdrawals for 1971-2010 and analysis of their spatiotemporal patterns. Hydrol. Earth Syst. Sci. 22, 2117–2133. https://doi.org/10.5194/hess-22-2117-2018

Hufkens, K., Keenan, T.F., Flanagan, L.B., Scott, R.L., Bernacchi, C.J., Joo, E., Brunsell, N.A., Verfaillie, J., Richardson, A.D., 2016. Productivity of North American grasslands is increased under future climate scenarios despite rising aridity. Nat. Clim. Chang. 6, 710–714. https://doi.org/10.1038/nclimate2942

Hurrell, J.W., Holland, M.M., Gent, P.R., Ghan, S., Kay, J.E., Kushner, P.J., Lamarque, J.-F., Large, W.G., Lawrence, D., Lindsay, K., Lipscomb, W.H., Long, M.C., Mahowald, N., Marsh, D.R., Neale, R.B., Rasch, P., Vavrus, S., Vertenstein, M., Bader, D., Collins, W.D., Hack, J.J., Kiehl, J., Marshall, S., 2013. The Community Earth System Model: A Framework for Collaborative Research. Bull. Am. Meteorol. Soc. 130204122247009. https://doi.org/10.1175/bams-d-12-00121

Huxman, T.E., Smith, M.D., Fay, P.A., Knapp, A.K., Shaw, M.R., Lolk, M.E., Smith, S.D., Tissue, D.T., Zak, J.C., Weltzin, J.F., Pockman, W.T., Sala, O.E., Haddad, B.M., Harte, J., Koch, G.W., Schwinning, S., Small, E.E., Williams, D.G., 2004. Convergence across biomes to a common rain-use efficiency. Nature 429, 651–654. https://doi.org/10.1038/nature02561

Joiner, J., Yoshida, Y., 2020. Satellite-based reflectances capture large fraction of variability in global gross primary production (GPP) at weekly time scales. Agric. For. Meteorol. 291, 108092. https://doi.org/10.1016/j.agrformet.2020.108092

Jung, M., Koirala, S., Weber, U., Ichii, K., Gans, F., Camps-Valls, G., Papale, D., Schwalm, C., Tramontana, G., Reichstein, M., 2019. The FLUXCOM ensemble of global land-atmosphere energy fluxes. Sci. Data 6, 1–14. https://doi.org/10.1038/s41597-019-0076-8

Kamphorst, E.C., Jetten, V., Guérif, J., Pitk a ¨ nen, J., Iversen, B. V., Douglas, J.T., Paz, A., 2000. Predicting Depressional Storage from Soil Surface Roughness. Soil Sci. Soc. Am. J. 64, 1749–1758. https://doi.org/10.2136/sssaj2000.6451749x

Katul, G.G., Oren, R., Manzoni, S., Higgins, C., Parlange, M.B., 2012. Evapotranspiration: A process driving mass transport and energy exchange in the soil-plant-atmosphere-climate system. Rev. Geophys. 50. https://doi.org/10.1029/2011RG000366

Khan, Z., Wild, T.B., Silva Carrazzone, M.E., Gaudioso, R., Mascari, M.P., Bianchi, F., Weinstein, F., Pérez, F., Pérez, W., Miralles-Wilhelm, F., Clarke, L., Hejazi, M., Vernon, C.R., Kyle, P., Edmonds, J., Muoz Castillo, R., 2020. Integrated energy-water-land nexus planning to guide national policy: An example from Uruguay. Environ. Res. Lett. 15. https://doi.org/10.1088/1748-9326/ab9389

Krinner, G., Viovy, N., de Noblet-Ducoudré, N., Ogée, J., Polcher, J., Friedlingstein, P., Ciais, P., Sitch, S., Prentice, I.C., 2005. A dynamic global vegetation model for studies of the coupled atmosphere-biosphere system. Global Biogeochem. Cycles 19, 1–33. https://doi.org/10.1029/2003GB002199

Kukal, M.S., Irmak, S., 2018. U.S. Agro-Climate in 20th Century: Growing Degree Days, First and Last Frost, Growing Season Length, and Impacts on Crop Yields.

Sci. Rep. 8, 1–14. https://doi.org/10.1038/s41598-018-25212-2

L'vovich, M.I., 1979. World Water Resources and Their Future, Special Publications Series. American Geophysical Union, Washington, D. C. https://doi.org/10.1029/SP013

Lane, C.R., Leibowitz, S.G., Autrey, B.C., LeDuc, S.D., Alexander, L.C., 2018. Hydrological, Physical, and Chemical Functions and Connectivity of Non-Floodplain Wetlands to Downstream Waters: A Review. J. Am. Water Resour. Assoc. 54, 346–371. https://doi.org/10.1111/1752-1688.12633

Lehner, B., Liermann, C.R., Revenga, C., Vorosmarty, C., Fekete, B., Crouzet, P., Doll, P., Endejan, M., Frenken, K., Magome, J., Nilsson, C., Robertson, J.C., Rodel, R., Sindorf, N., Wisser, D., 2011. Global Reservoir and Dam Database, Version 1 (GRanDv1): Reservoirs, Revision 01 [WWW Document]. NASA Socioecon. Data Appl. Cent. https://doi.org/10.7927/H4N877QK

Levia, D.F., Carlyle-Moses, D.E., Tanaka, T., 2011. Forest Hydrology and Biogeochemistry : Synthesis of Past Research and Future Directions, Ecological Studies, Ecological Studies. Springer Netherlands, Dordrecht. https://doi.org/10.1007/978-94-007-1363-5

Li, H.Y., Leung, L.R., Getirana, A., Huang, M., Wu, H., Xu, Y., Guo, J., Voisin, N., 2015. Evaluating global streamflow simulations by a physically based routing model coupled with the community land model. J. Hydrometeorol. 16, 948–971. https://doi.org/10.1175/JHM-D-14-0079.1

Li, X., Vernon, C.R., Hejazi, M.I., Link, R.P., Feng, L., Liu, Y., Rauchenstein, L.T., 2017. Xanthos – A Global Hydrologic Model. J. Open Res. Softw. 5, 0–6. https://doi.org/10.5334/jors.181

Liang, X., Lettenmaier, D.P., Wood, E.F., Burges, S.J., 1994. A simple hydrologically based model of land surface water and energy fluxes for general circulation models. J. Geophys. Res. Atmos. 99, 14415–14428. https://doi.org/10.1029/94JD00483

Lindström, G., Johansson, B., Persson, M., Gardelin, M., Bergström, S., 1997. Development and test of the distributed HBV-96 hydrological model. J. Hydrol. 201, 272–288. https://doi.org/10.1016/S0022-1694(97)00041-3

Liu, L., Gudmundsson, L., Hauser, M., Qin, D., Li, S., Seneviratne, S.I., 2020. Soil moisture dominates dryness stress on ecosystem production globally. Nat. Commun. 11, 1–9. https://doi.org/10.1038/s41467-020-18631-1

Liu, Y., Hejazi, M., Li, H., Zhang, X., Leng, G., 2018. A hydrological emulator for global applications-HE v1.0.0. Geosci. Model Dev. 11, 1077–1092. https://doi.org/10.5194/gmd-11-1077-2018

Liz Pástor, Zoltán Botta-Dukát, Gabriella Magyar, Tamás Czárán, G.M., 2016. Theory-Based Ecology: A Darwinian Approach.

Lloyd-Hughes, B., Saunders, M.A., 2002. A drought climatology for Europe, in: International Journal of Climatology. pp. 1571–1592. https://doi.org/10.1002/joc.846

Loucks, D.P., van Beek, E., 2017. Water resource systems planning and management: An introduction to methods, models, and applications, Water Resource Systems Planning and Management: An Introduction to Methods, Models, and Applications. Springer International Publishing, Cham. https://doi.org/10.1007/978-3-319-44234-1

Luke Smallman, T., Williams, M., 2019. Description and validation of an intermediate complexity model for ecosystem photosynthesis and evapotranspiration: ACM-GPP-ETv1. Geosci. Model Dev. 12, 2227–2253. https://doi.org/10.5194/gmd-12-2227-2019

Mahmood, K., 1987. Reservoir sedimentation: impact, extent, and mitigation. Technical paper. United States.

Markham, C.G., 1970. Seasonality of Precipitation in the United States. Ann. Assoc. Am. Geogr. 60, 593–597. https://doi.org/10.1111/j.1467-8306.1970.tb00743.x

Martínez-Vilalta, J., Poyatos, R., Aguadé, D., Retana, J., Mencuccini, M., 2014. A new look at water transport regulation in plants. New Phytol. 204, 105–115. https://doi.org/10.1111/nph.12912

Martinez, G.F., Gupta, H. V., 2011. Hydrologic consistency as a basis for assessing complexity of monthly water balance models for the continental United States. Water Resour. Res. 47, 1–18. https://doi.org/10.1029/2011WR011229

Martinez, G.F., Gupta, H. V., 2010. Toward improved identification of hydrological models: A diagnostic evaluation of the "abcd" monthly water balance model for the conterminous United States. Water Resour. Res. 46, 1–21. https://doi.org/10.1029/2009WR008294

Massmann, A., Gentine, P., Lin, C., 2019. When Does Vapor Pressure Deficit Drive or Reduce Evapotranspiration? J. Adv. Model. Earth Syst. 11, 3305–3320. https://doi.org/10.1029/2019MS001790

Maxwell, R.M., Condon, L.E., 2016. Connections between groundwater flow and transpiration partitioning. Science (80-. ). 353, 377–380. https://doi.org/10.1126/science.aaf7891

McAdam, S.A.M., Brodribb, T.J., 2015. The evolution of mechanisms driving the stomatal response to vapor pressure deficit. Plant Physiol. 167, 833–843. https://doi.org/10.1104/pp.114.252940

Miralles, D.G., Gash, J.H., Holmes, T.R.H., De Jeu, R.A.M., Dolman, A.J., 2010. Global canopy interception from satellite observations. J. Geophys. Res. Atmos. 115, 1–8. https://doi.org/10.1029/2009JD013530

Miralles, D.G., Jiménez, C., Jung, M., Michel, D., Ershadi, A., McCabe, M.F., Hirschi, M., Martens, B., Dolman, A.J., Fisher, J.B., Mu, Q., Seneviratne, S.I., Wood, E.F., Fernández-Prieto, D., 2016. The WACMOS-ET project – Part 2: Evaluation of global terrestrial evaporation data sets. Hydrol. Earth Syst. Sci. 20, 823–842. https://doi.org/10.5194/hess-20-823-2016

Moore, R.J., 2007. The PDM rainfall-runoff model. Hydrol. Earth Syst. Sci. 11, 483–499. https://doi.org/10.5194/hess-11-483-2007

Müller Schmied, H., Caceres, D., Eisner, S., Flörke, M., Herbert, C., Niemann, C., Asali Peiris, T., Popat, E., Theodor Portmann, F., Reinecke, R., Schumacher, M., Shadkam, S., Telteu, C.E., Trautmann, T., Döll, P., 2021. The global water resources and use model WaterGAP v2.2d: Model description and evaluation. Geosci. Model Dev. 14, 1037–1079. https://doi.org/10.5194/gmd-14-1037-2021

Nathan, R.J., McMahon, T.A., 1990. Evaluation of automated techniques for base flow and recession analyses. Water Resour. Res. 26, 1465–1473. https://doi.org/10.1029/WR026i007p01465

Neter, J., Wasserman, W., Michael, K.H., 1983. John Neter_Applied Linear Regression Models.pdf.

Newman, A.J., Clark, M.P., Sampson, K., Wood, A., Hay, L.E., Bock, A., Viger, R.J., Blodgett, D., Brekke, L., Arnold, J.R., Hopson, T., Duan, Q., 2015. Development of a large-sample watershed-scale hydrometeorological data set for the contiguous USA: Data set characteristics and assessment of regional variability in hydrologic model performance. Hydrol. Earth Syst. Sci. 19, 209–223. https://doi.org/10.5194/hess-19-209-2015

Nolan, R.H., Tarin, T., Fairweather, K.A., Cleverly, J., Eamus, D., 2017. Variation in photosynthetic traits related to access to water in semiarid Australian woody species. Funct. Plant Biol. 44, 1087–1097. https://doi.org/10.1071/FP17096

Novick, K.A., Biederman, J.A., Desai, A.R., Litvak, M.E., Moore, D.J.P., Scott, R.L., Torn, M.S., 2018. The AmeriFlux network: A coalition of the willing. Agric. For. Meteorol. 249, 444–456. https://doi.org/10.1016/j.agrformet.2017.10.009

Ol'dekop, E.M., 1911. On evaporation from the surface of river basins, Transactions on meteorological observations. Tartu, Estonia.

Oleson, K.W., Lawrence, D.M., Bonan, G.B., Flanner, M.G., Kluzek, E., Lawrence, P.J., Levis, S., Swenson, S.C., Thornton, P.E., Dai, A., Decker, M., Dickinson, R., Feddema, J., Heald, C.L., Hoffman, F., Jean-Francois Lamarque, N.M., Niu, G.-Y., Qian, T., Randerson, J., Running, S., Sakaguchi, K., Slater, A., Stöckli, R., Wang, A., Yang, Z.-L., Zeng, Xiaodong, Zeng, Xubin, 2010. Technical Description of version 4.0 of the Community Land Model (CLM). Boulder, Colorado.

Öquist, G., Huner, N.P.A., 2003. Photosynthesis of Overwintering Evergreen Plants. Annu. Rev. Plant Biol. 54, 329–355. https://doi.org/10.1146/annurev.arplant.54.072402.115741

Parish, O.O., Putnam, T.W., 1977. Equations for Determination of Humidity from Dewpoints and Psychrometric Data. Edwards, California, US, California, US.

https://doi.org/NASA TN D-8401

Pastorello, G., Trotta, C., Canfora, E., Chu, H., Christianson, D., Cheah, Y.W., Poindexter, C., Chen, J., Elbashandy, A., Humphrey, M., Isaac, P., Polidori, D., Ribeca, A., van Ingen, C., Zhang, L., Amiro, B., Ammann, C., Arain, M.A., Ardö, J., Arkebauer, T., Arndt, S.K., Arriga, N., Aubinet, M., Aurela, M., Baldocchi, D., Barr, A., Beamesderfer, E., Marchesini, L.B., Bergeron, O., Beringer, J., Bernhofer, C., Berveiller, D., Billesbach, D., Black, T.A., Blanken, P.D., Bohrer, G., Boike, J., Bolstad, P. V., Bonal, D., Bonnefond, J.M., Bowling, D.R., Bracho, R., Brodeur, J., Brümmer, C., Buchmann, N., Burban, B., Burns, S.P., Buysse, P., Cale, P., Cavagna, M., Cellier, P., Chen, S., Chini, I., Christensen, T.R., Cleverly, J., Collalti, A., Consalvo, C., Cook, B.D., Cook, D., Coursolle, C., Cremonese, E., Curtis, P.S., D'Andrea, E., da Rocha, H., Dai, X., Davis, K.J., De Cinti, B., de Grandcourt, A., De Ligne, A., De Oliveira, R.C., Delpierre, N., Desai, A.R., Di Bella, C.M., di Tommasi, P., Dolman, H., Domingo, F., Dong, G., Dore, S., Duce, P., Dufrêne, E., Dunn, A., Dušek, J., Eamus, D., Eichelmann, U., ElKhidir, H.A.M., Eugster, W., Ewenz, C.M., Ewers, B., Famulari, D., Fares, S., Feigenwinter, I., Feitz, A., Fensholt, R., Filippa, G., Fischer, M., Frank, J., Galvagno, M., Gharun, M., Gianelle, D., Gielen, B., Gioli, B., Gitelson, A., Goded, I., Goeckede, M., Goldstein, A.H., Gough, C.M., Goulden, M.L., Graf, A., Griebel, A., Gruening, C., Grünwald, T., Hammerle, A., Han, S., Han, X., Hansen, B.U., Hanson, C., Hatakka, J., He, Y., Hehn, M., Heinesch, B., Hinko-Najera, N., Hörtnagl, L., Hutley, L., Ibrom, A., Ikawa, H., Jackowicz-Korczynski, M., Janouš, D., Jans, W., Jassal, R., Jiang, S., Kato, T., Khomik, M., Klatt, J., Knohl, A., Knox, S., Kobayashi, H., Koerber, G., Kolle, O., Kosugi, Y., Kotani, A., Kowalski, A., Kruijt, B., Kurbatova, J., Kutsch, W.L., Kwon, H., Launiainen, S., Laurila, T., Law, B., Leuning, R., Li, Yingnian, Liddell, M., Limousin, J.M., Lion, M., Liska, A.J., Lohila, A., López-Ballesteros, A., López-Blanco, E., Loubet, B., Loustau, D., Lucas-Moffat, A., Lüers, J., Ma, S., Macfarlane, C., Magliulo, V., Maier, R., Mammarella, I., Manca, G., Marcolla, B., Margolis, H.A., Marras, S., Massman, W., Mastepanov, M., Matamala, R., Matthes, J.H., Mazzenga, F., McCaughey, H., McHugh, I., McMillan, A.M.S., Merbold, L., Meyer, W., Meyers, T., Miller, S.D., Minerbi, S., Moderow, U., Monson, R.K., Montagnani, L., Moore, C.E., Moors, E., Moreaux, V., Moureaux, C., Munger, J.W., Nakai, T., Neirynck, J., Nesic, Z., Nicolini, G., Noormets, A., Northwood, M., Nosetto, M., Nouvellon, Y., Novick, K., Oechel, W., Olesen, J.E., Ourcival, J.M., Papuga, S.A., Parmentier, F.J., Paul-Limoges, E., Pavelka, M., Peichl, M., Pendall, E., Phillips, R.P., Pilegaard, K., Pirk, N., Posse, G., Powell, T., Prasse, H., Prober, S.M., Rambal, S., Rannik, Ü., Raz-Yaseef, N., Reed, D., de Dios, V.R., Restrepo-Coupe, N., Reverter, B.R., Roland, M., Sabbatini, S., Sachs, T., Saleska, S.R., Sánchez-Cañete, E.P., Sanchez-Mejia, Z.M., Schmid, H.P., Schmidt, M., Schneider, K., Schrader, F., Schroder, I., Scott, R.L., Sedlák, P., Serrano-Ortíz, P., Shao, C., Shi, P., Shironya, I., Siebicke, L., Šigut, L., Silberstein, R., Sirca, C., Spano, D., Steinbrecher, R., Stevens, R.M., Sturtevant, C., Suyker, A., Tagesson, T., Takanashi, S., Tang, Y., Tapper, N., Thom, J., Tiedemann, F., Tomassucci, M., Tuovinen, J.P., Urbanski, S., Valentini, R., van der Molen, M., van Gorsel, E., van Huissteden, K., Varlagin, A., Verfaillie, J., Vesala, T., Vincke, C., Vitale, D., Vygodskaya, N., Walker, J.P., Walter-Shea, E., Wang, H., Weber, R., Westermann, S., Wille, C., Wofsy, S., Wohlfahrt, G., Wolf, S., Woodgate, W., Li, Yuelin, Zampedri, R., Zhang, J., Zhou, G., Zona, D., Agarwal, D., Biraud, S., Torn, M., Papale, D., 2020. The FLUXNET2015 dataset and the ONEFlux processing pipeline for eddy covariance data. Sci. data 7, 225. https://doi.org/10.1038/s41597-020-0534-3

Pokhrel, Y., Hanasaki, N., Koirala, S., Cho, J., Yeh, P.J.F., Kim, H., Kanae, S., Oki, T., 2012. Incorporating anthropogenic water regulation modules into a land surface model. J. Hydrometeorol. 13, 255–269. https://doi.org/10.1175/JHM-D-11-013.1

Pokhrel, Y.N., Koirala, S., Yeh, P.J.-F., Hanasaki, N., Longuevergne, L., Kanae, S., Oki, T., 2015. Incorporation of groundwater pumping in a global Land Surface Model with the representation of human impacts. Water Resour. Res. 51, 78–96. https://doi.org/10.1002/2014WR015602

Poncea, V.M., Shetty, A. V., 1995a. A conceptual model of catchment water balance: 1. Formulation and calibration. J. Hydrol. 173, 27–40. https://doi.org/10.1016/0022-1694(95)02739-C

Poncea, V.M., Shetty, A. V., 1995b. A conceptual model of catchment water balance: 2. Application to runoff and baseflow modeling. J. Hydrol. 173, 41–50. https://doi.org/10.1016/0022-1694(95)02745-B

Porporato, A., Rodriguez-Iturbe, I., 2013. From random variability to ordered structures: a search for general synthesis in ecohydrology. Ecohydrology 6, 333–342. https://doi.org/10.1002/eco.1400

Prieto, I., Armas, C., Pugnaire, F.I., 2012. Water release through plant roots: New insights into its consequences at the plant and ecosystem level. New Phytol. https://doi.org/10.1111/j.1469-8137.2011.04039.x

Purdy, A.J., Fisher, J.B., Goulden, M.L., Colliander, A., Halverson, G., Tu, K., Famiglietti, J.S., 2018. SMAP soil moisture improves global evapotranspiration. Remote Sens. Environ. 219, 1–14. https://doi.org/10.1016/j.rse.2018.09.023

Rajib, A., Golden, H.E., Lane, C.R., Wu, Q., 2020. Surface Depression and Wetland

Water Storage Improves Major River Basin Hydrologic Predictions. Water Resour. Res. 56, 1–19. https://doi.org/10.1029/2019WR026561

Rasmussen, C., 2012. Thermodynamic constraints on effective energy and mass transfer and catchment function. Hydrol. Earth Syst. Sci. 16, 725–739. https://doi.org/10.5194/hess-16-725-2012

Robinson, N.P., Allred, B.W., Smith, W.K., Jones, M.O., Moreno, A., Erickson, T.A., Naugle, D.E., Running, S.W., 2018. Terrestrial primary production for the conterminous United States derived from Landsat 30 m and MODIS 250 m. Remote Sens. Ecol. Conserv. 4, 264–280. https://doi.org/10.1002/rse2.74

Rore, C.W., Stern, W.R., 1967. Determination of Withdrawal of Water from Soil by Crop Roots as a Function of Depth and Time. J. Agric. Meteorol. 23, 130–130137. https://doi.org/10.2480/agrmet.23.130

Roth, B.E., Slatton, K.C., Cohen, M.J., 2007. On the potential for high-resolution lidar to improve rainfall interception estimates in forest ecosystems. Front. Ecol. Environ. 5, 421–428. https://doi.org/10.1890/060119.1

Running, S.W., Zhao, M., 2015. User's Guide Daily GPP and Annual NPP (MOD17A2/A3) Products, NASA Earth Observing System MODIS Land Algorithm.

Sakaguchi, K., Zeng, X., 2009. Effects of soil wetness, plant litter, and under-canopy atmospheric stability on ground evaporation in the Community Land Model (CLM3.5). J. Geophys. Res. Atmos. 114, 1–14. https://doi.org/10.1029/2008JD010834

Savenije, H.H.G., 2004. The importance of interception and why we should delete the term evapotranspiration from our vocabulary. Hydrol. Process. 18, 1507–1511.

https://doi.org/10.1002/hyp.5563

Schaefli, B., Van Der Ent, R.J., Woods, R., Savenije, H.H.G., 2012. An analytical model for soil-atmosphere feedback. Hydrol. Earth Syst. Sci. 16, 1863–1878. https://doi.org/10.5194/hess-16-1863-2012

Schaphoff, S., Von Bloh, W., Rammig, A., Thonicke, K., Biemans, H., Forkel, M., Gerten, D., Heinke, J., Jägermeyr, J., Knauer, J., Langerwisch, F., Lucht, W., Müller, C., Rolinski, S., Waha, K., 2018. LPJmL4 - A dynamic global vegetation model with managed land - Part 1: Model description. Geosci. Model Dev. 11, 1343–1375. https://doi.org/10.5194/gmd-11-1343-2018

Schenk, H.J., Jackson, R.B., 2002a. The global biogeography of roots. Ecol. Monogr. 72, 311–328. https://doi.org/10.1890/0012-9615(2002)072[0311:TGBOR]2.0.CO;2

Schenk, H.J., Jackson, R.B., 2002b. Rooting depths, lateral root spreads and below-ground/above-ground allometries of plants in water-limited ecosystems. J. Ecol. 90, 480–494. https://doi.org/10.1046/j.1365-2745.2002.00682.x

Schlesinger, W.H., Jasechko, S., 2014. Transpiration in the global water cycle. Agric. For. Meteorol. 189–190, 115–117. https://doi.org/10.1016/j.agrformet.2014.01.011

SCS, 1985. National engineering handbook. Section 4, Hydrology.

Shen, Y., Ruijsch, J., Lu, M., Sutanudjaja, E.H., Karssenberg, D., 2022. Random forests-based error-correction of streamflow from a large-scale hydrological model: Using model state variables to estimate error terms. Comput. Geosci. 159, 105019. https://doi.org/10.1016/j.cageo.2021.105019

Sivapalan, M., 2005. Pattern, Process and Function: Elements of a Unified Theory of

Hydrology at the Catchment Scale. Encycl. Hydrol. Sci. https://doi.org/10.1002/0470848944.hsa012

Sivapalan, M., Thompson, S.E., Harman, C.J., Basu, N.B., Kumar, P., 2011a. Water cycle dynamics in a changing environment: Improving predictability through synthesis. Water Resour. Res. 47, 1–7. https://doi.org/10.1029/2011WR011377

Sivapalan, M., Yaeger, M.A.A., Harman, C.J.J., Xu, X., Troch, P.A.A., 2011b. Functional model of water balance variability at the catchment scale: 1. Evidence of hydrologic similarity and space-time symmetry. Water Resour. Res. 47, 1–12. https://doi.org/10.1029/2010WR009568

Smallman, T.L., Moncrieff, J.B., Williams, M., 2013. WRFv3.2-SPAv2: Development and validation of a coupled ecosystem-atmosphere model, scaling from surface fluxes of CO2 and energy to atmospheric profiles. Geosci. Model Dev. 6, 1079–1093. https://doi.org/10.5194/gmd-6-1079-2013

Smith, B., Prentice, I.C., Sykes, M.T., 2001. Representation of vegetation dynamics in the modelling of terrestrial ecosystems: Comparing two contrasting approaches within European climate space. Glob. Ecol. Biogeogr. 10, 621–637. https://doi.org/10.1046/j.1466-822X.2001.00256.x

Song, J., Willmott, C.J., Hanson, B., 1997. Simulating the surface energy budget over the Konza Prairie with a mesoscale model. Agric. For. Meteorol. 87, 105–118. https://doi.org/10.1016/S0168-1923(97)00023-3

Spielmann, F.M., Wohlfahrt, G., Hammerle, A., Kitz, F., Migliavacca, M., Alberti, G., Ibrom, A., El-Madany, T.S., Gerdel, K., Moreno, G., Kolle, O., Karl, T., Peressotti, A., Delle Vedove, G., 2019. Gross Primary Productivity of Four European Ecosystems Constrained by Joint CO2 and COS Flux Measurements.

Geophys. Res. Lett. 46, 5284–5293. https://doi.org/10.1029/2019GL082006

Stokes, P.A., Purdon, P.L., 2017. A study of problems encountered in Granger causality analysis from a neuroscience perspective. Proc. Natl. Acad. Sci. U. S. A. 114, E7063–E7072. https://doi.org/10.1073/pnas.1704663114

Sun, X., Wilcox, B.P., Zou, C.B., Stebler, E., West, J.B., Wyatt, B., 2021. Isotopic partitioning of evapotranspiration in a mesic grassland during two wetting–drying episodes. Agric. For. Meteorol. 301–302. https://doi.org/10.1016/j.agrformet.2021.108321

Sutanudjaja, E.H., Van Beek, R., Wanders, N., Wada, Y., Bosmans, J.H.C., Drost, N., Van Der Ent, R.J., De Graaf, I.E.M., Hoch, J.M., De Jong, K., Karssenberg, D., López López, P., Peßenteiner, S., Schmitz, O., Straatsma, M.W., Vannametee, E., Wisser, D., Bierkens, M.F.P., 2018. PCR-GLOBWB 2: A 5 arcmin global hydrological and water resources model. Geosci. Model Dev. 11, 2429–2453. https://doi.org/10.5194/gmd-11-2429-2018

Tague, C.L., Band, L.E., 2004. RHESSys: Regional Hydro-Ecologic Simulation System—An Object-Oriented Approach to Spatially Distributed Modeling of Carbon, Water, and Nutrient Cycling. Earth Interact. 8, 1–42. https://doi.org/10.1175/1087-3562(2004)8<1:rrhsso>2.0.co;2

Tang, Y., Wang, D., 2017. Evaluating the role of watershed properties in long-term water balance through a Budyko equation based on two-stage partitioning of precipitation. Water Resour. Res. 53, 4142–4157. https://doi.org/10.1002/2016WR019920

Telteu, C.E., Müller Schmied, H., Thiery, W., Leng, G., Burek, P., Liu, X., Boulange, J.E.S., Andersen, L.S., Grillakis, M., Gosling, S.N., Satoh, Y., Rakovec, O., Stacke, T., Chang, J., Wanders, N., Shah, H.L., Trautmann, T., Mao, G., Hanasaki, N., Koutroulis, A., Pokhrel, Y., Samaniego, L., Wada, Y., Mishra, V., Liu, J., Döll, P., Zhao, F., Gädeke, A., Rabin, S.S., Herz, F., 2021. Understanding each other's models An introduction and a standard representation of 16 global water models to support intercomparison, improvement, and communication. Geosci. Model Dev. 14, 3843–3878. https://doi.org/10.5194/gmd-14-3843-2021

Thomas, HA., 1981. Improved Methods for National Water Assessment. Water Resources Contract: WR15249270. 3, 59.

Thompson, S.E., Harman, C.J., Troch, P.A., Brooks, P.D., Sivapalan, M., 2011. Spatial scale dependence of ecohydrologically mediated water balance partitioning: A synthesis framework for catchment ecohydrology. Water Resour. Res. 47, 1–20. https://doi.org/10.1029/2010WR009998

Tian, F.Q., Hu, H.P., Lei, Z.D., 2008. Thermodynamic watershed hydrological model: Constitutive relationship. Sci. China, Ser. E Technol. Sci. 51, 1353–1369. https://doi.org/10.1007/s11431-008-0147-0

Trenberth, K.E., Dai, A., van der Schrier, G., Jones, P.D., Barichivich, J., Briffa, K.R., Sheffield, J., 2014. Global warming and changes in drought. Nat. Clim. Chang. 4, 17–22. https://doi.org/10.1038/nclimate2067

Troch, P., Dwivedi, R., Liu, T., Meira Neto, A.A., Roy, T., Valdés-Pineda, R., Durcik, M., Arciniega-Esparza, S., Breña-Naranjo, J.A., 2018. Catchment-scale groundwater recharge and vegetation water use efficiency. Hydrol. Earth Syst. Sci. Discuss. 1–46. https://doi.org/10.5194/hess-2018-449

Troch, P.A., Martinez, G.F., Pauwels, V.R.N., Durcik, M., Sivapalan, M., Harman, C., Brooks, P.D., Gupta, H., Huxman, T., 2009. Climate and vegetation water use efficiency at catchment scales. Hydrol. Process. 23, 2409–2414. https://doi.org/10.1002/hyp.7358

Turner, S., Ng, J.Y., Galelli, S., Maintainer, ], 2016. Package “reservoir” Title Tools for Analysis, Design, and Operation of Water Supply Storages.

Turner, S.W.D., Ng, J.Y., Galelli, S., 2017. Examining global electricity supply vulnerability to climate change using a high-fidelity hydropower dam model. Sci. Total Environ. 590–591, 663–675. https://doi.org/10.1016/j.scitotenv.2017.03.022

van der Knijff, J.M., Younis, J., de Roo, A.P.J., 2010. LISFLOOD: A GIS-based distributed model for river basin scale water balance and flood simulation. Int. J. Geogr. Inf. Sci. 24, 189–212. https://doi.org/10.1080/13658810802549154

Vernon, C.R., Hejazi, M.I., Turner, S.W.D., Liu, Y., Braun, C.J., Li, X., Link, R.P., 2019. A global hydrologic framework to accelerate scientific discovery. J. Open Res. Softw. 7, 1–7. https://doi.org/10.5334/jors.245

Vicente-Serrano, S.M., López-Moreno, J.I., Beguería, S., Lorenzo-Lacruz, J., Azorin-Molina, C., Morán-Tejeda, E., 2012. Accurate Computation of a Streamflow Drought Index. J. Hydrol. Eng. 17, 318–332. https://doi.org/10.1061/(asce)he.1943-5584.0000433

Voepel, H., Ruddell, B., Schumer, R., Troch, P.A., Brooks, P.D., Neal, A., Durcik, M., Sivapalan, M., 2011. Quantifying the role of climate and landscape characteristics on hydrologic partitioning and vegetation response. Water Resour. Res. 47, 1–13. https://doi.org/10.1029/2010WR009944

Voisin, N., Li, H., Ward, D., Huang, M., Wigmosta, M., Leung, L.R., 2013. On an improved sub-regional water resources management representation for integration into earth system models. Hydrol. Earth Syst. Sci. 17, 3605–3622. https://doi.org/10.5194/hess-17-3605-2013

Votruba, L., Broza, V., 1989. C Flood-control Function of Reservoirs, in: WATER MANAGEMENT IN RESERVOIRS. Elsevier, pp. 295–296. https://doi.org/10.1016/S0167-5648(08)70640-3

Walsh, R.P.D., Lawler, D.M., 1981. Rainfall Seasonality: Description, Spatial Patterns and Change Through Time. Weather 36, 201–208. https://doi.org/10.1002/j.1477-8696.1981.tb05400.x

Wan, W., Zhao, J., Li, H.Y., Mishra, A., Hejazi, M., Lu, H., Demissie, Y., Wang, H., 2018. A Holistic View of Water Management Impacts on Future Droughts: A Global Multimodel Analysis. J. Geophys. Res. Atmos. 123, 5947–5972. https://doi.org/10.1029/2017JD027825

Wan, W., Zhao, J., Li, H.Y., Mishra, A., Ruby Leung, L., Hejazi, M., Wang, W., Lu, H., Deng, Z., Demissisie, Y., Wang, H., 2017. Hydrological Drought in the Anthropocene: Impacts of Local Water Extraction and Reservoir Regulation in the U.S. J. Geophys. Res. Atmos. 122, 11,313-11,328. https://doi.org/10.1002/2017JD026899

Wang, D., 2018. A new probability density function for spatial distribution of soil water storage capacity leads to SCS curve number method. Hydrol. Earth Syst. Sci. Discuss. 22, 1–31. https://doi.org/10.5194/hess-2018-32

Wang, D., Tang, Y., 2014. A one-parameter Budyko model for water balance captures emergent behavior in darwinian hydrologic models. Geophys. Res. Lett. 41, 4569–4577. https://doi.org/10.1002/2014GL060509

Wang, D., Wang, G., Anagnostou, E.N., 2007. Evaluation of canopy interception schemes in land surface models. J. Hydrol. 347, 308–318. https://doi.org/10.1016/j.jhydrol.2007.09.041

Wang, D., Zhao, J., Tang, Y., Sivapalan, M., 2015. A thermodynamic interpretation of Budyko and L'vovich formulations of annual water balance: Proportionality Hypothesis and maximum entropy production. Water Resour. Res. 51, 3007–3016. https://doi.org/10.1002/2014WR016857

Wang, L., Good, S.P., Caylor, K.K., 2014. Global synthesis of vegetation control on evapotranspiration partitioning. Geophys. Res. Lett. 41, 6753–6757. https://doi.org/10.1002/2014GL061439

Weedon, G.P., Balsamo, G., Bellouin, N., Gomes, S., Best, M.J., Viterbo, P., 2014. Data methodology applied to ERA-Interim reanalysis data. Water Resour. Res. 50, 7505–7514. https://doi.org/10.1002/2014WR015638.Received

Weedon, G.P., Gomes, S., Viterbo, P., Shuttleworth, W.J., Blyth, E., ÖSterle, H., Adam, J.C., Bellouin, N., Boucher, O., Best, M., 2011. Creation of the WATCH forcing data and its use to assess global and regional reference crop evaporation over land during the twentieth century. J. Hydrometeorol. 12, 823–848. https://doi.org/10.1175/2011JHM1369.1

White, R., 2001. Evacuation of sediments from reservoirs, Evacuation of sediments from reservoirs. Thomas Telford Publishing. https://doi.org/10.1680/eosfr.29538

Wild, T.B., Birnbaum, A.N., Reed, P.M., Loucks, D.P., 2021. An open source reservoir and sediment simulation framework for identifying and evaluating siting, design, and operation alternatives. Environ. Model. Softw. 136, 104947. https://doi.org/10.1016/j.envsoft.2020.104947

Wisser, D., Fekete, B.M., Vörösmarty, C.J., Schumann, A.H., 2010. Reconstructing

20th century global hydrography: A contribution to the Global Terrestrial Network- Hydrology (GTN-H). Hydrol. Earth Syst. Sci. 14, 1–24. https://doi.org/10.5194/hess-14-1-2010

Wu, H., Kimball, J.S., Mantua, N., Stanford, J., 2011. Automated upscaling of river networks for macroscale hydrological modeling. Water Resour. Res. 47, 1–18. https://doi.org/10.1029/2009WR008871

Wu, Q., Lane, C.R., Wang, L., Vanderhoof, M.K., Christensen, J.R., Liu, H., 2019. Efficient Delineation of Nested Depression Hierarchy in Digital Elevation Models for Hydrological Analysis Using Level-Set Method. J. Am. Water Resour. Assoc. 55, 354–368. https://doi.org/10.1111/1752-1688.12689

Yao, L., Libera, D.A., Kheimi, M., Sankarasubramanian, A., Wang, D., 2020. The Roles of Climate Forcing and Its Variability on Streamflow at Daily, Monthly, Annual, and Long-Term Scales. Water Resour. Res. 56, 1–23. https://doi.org/10.1029/2020WR027111

Yao, L., Wang, D., 2022. Hydrological Basis of Different Budyko Equations: The Spatial Variability of Available Water for Evaporation. Water Resour. Res. 58, 1–14. https://doi.org/10.1029/2021WR030921

Yassin, F., Razavi, S., Elshamy, M., Davison, B., Sapriza-Azuri, G., Wheater, H., 2019. Representation of Water Management in Hydrological and Land Surface Models. Hydrol. Earth Syst. Sci. Discuss. 1–35. https://doi.org/10.5194/hess-2019-7

Ye, S., Yaeger, M., Coopersmith, E., Cheng, L., Sivapalan, M., 2012. Exploring the physical controls of regional patterns of flow duration curves Part 2: Role of seasonality, the regime curve, and associated process controls. Hydrol. Earth Syst. Sci. 16, 4447–4465. https://doi.org/10.5194/hess-16-4447-2012

Yoshida, T., Hanasaki, N., Nishina, K., Boulange, J., Okada, M., Troch, P.A., 2022. Inference of Parameters for a Global Hydrological Model: Identifiability and Predictive Uncertainties of Climate-Based Parameters. Water Resour. Res. 58. https://doi.org/10.1029/2021WR030660

Yu, F., Harbor, J.M., 2019. The effects of topographic depressions on multiscale overland flow connectivity: A high-resolution spatiotemporal pattern analysis approach based on connectivity statistics. Hydrol. Process. 33, 1403–1419. https://doi.org/10.1002/hyp.13409

Zapata-Rios, X., Brooks, P.D., Troch, P.A., McIntosh, J., Guo, Q., 2016. Influence of terrain aspect on water partitioning, vegetation structure and vegetation greening in high-elevation catchments in northern New Mexico. Ecohydrology 9, 782–795. https://doi.org/10.1002/eco.1674

Zeng, X., 2001. Global Vegetation Root Distribution for Land Modeling. J. Hydrometeorol. 2, 525–530. https://doi.org/10.1175/1525-7541(2001)002<0525:gvrdfl>2.0.co;2

Zhang, X., Li, H.Y., Deng, Z.D., Leung, L.R., Skalski, J.R., Cooke, S.J., 2019. On the variable effects of climate change on Pacific salmon. Ecol. Modell. 397, 95–106. https://doi.org/10.1016/j.ecolmodel.2019.02.002

Zhang, X., Li, H.Y., Deng, Z.D., Ringler, C., Gao, Y., Hejazi, M.I., Leung, L.R., 2018. Impacts of climate change, policy and Water-Energy-Food nexus on hydropower development. Renew. Energy 116, 827–834. https://doi.org/10.1016/j.renene.2017.10.030

Zhang, X., Li, H.Y., Leung, L.R., Liu, L., Hejazi, M.I., Forman, B.A., Yigzaw, W., 2020. River Regulation Alleviates the Impacts of Climate Change on U.S.

Thermoelectricity Production. J. Geophys. Res. Atmos. 125. https://doi.org/10.1029/2019JD031618

Zhang, Y., Xiao, X., Guanter, L., Zhou, S., Ciais, P., Joiner, J., Sitch, S., Wu, X., Nabel, J., Dong, J., Kato, E., Jain, A.K., Wiltshire, A., Stocker, B.D., 2016a. Precipitation and carbon-water coupling jointly control the interannual variability of global land gross primary production. Sci. Rep. 6, 39748. https://doi.org/10.1038/srep39748

Zhang, Y., Xiao, X., Zhou, S., Ciais, P., McCarthy, H., Luo, Y., 2016b. Canopy and physiological controls of GPP during drought and heat wave. Geophys. Res. Lett. 43, 3325–3333. https://doi.org/10.1002/2016GL068501

Zhao, M., Heinsch, F.A., Nemani, R.R., Running, S.W., 2005. Improvements of the MODIS terrestrial gross and net primary production global data set. Remote Sens. Environ. 95, 164–176. https://doi.org/10.1016/j.rse.2004.12.011

Zhou, S., Park Williams, A., Berg, A.M., Cook, B.I., Zhang, Y., Hagemann, S., Lorenz, R., Seneviratne, S.I., Gentine, P., 2019a. Land–atmosphere feedbacks exacerbate concurrent soil drought and atmospheric aridity. Proc. Natl. Acad. Sci. U. S. A. 116, 18848–18853. https://doi.org/10.1073/pnas.1904955116

Zhou, S., Yu, B., Huang, Y., Wang, G., 2014. The effect of vapor pressure deficit on water use efficiency at the subdaily time scale. Geophys. Res. Lett. 41, 5005–5013. https://doi.org/10.1002/2014GL060741

Zhou, S., Yu, B., Zhang, Y., Huang, Y., Wang, G., 2016. Partitioning evapotranspiration based on the concept of underlying water use efficiency. Water Resour. Res. 52, 1160–1175. https://doi.org/10.1002/2015WR017766

Zhou, S., Zhang, Y., Williams, A.P., Gentine, P., 2019b. Projected increases in intensity, frequency, and terrestrial carbon costs of compound drought and aridity events. Sci. Adv. 5, 1–9. https://doi.org/10.1126/sciadv.aau5740

Zhou, T., Leung, L.R., Leng, G., Voisin, N., Li, H.Y., Craig, A.P., Tesfa, T., Mao, Y., 2020. Global Irrigation Characteristics and Effects Simulated by Fully Coupled Land Surface, River, and Water Management Models in E3SM. J. Adv. Model. Earth Syst. 12, 1–18. https://doi.org/10.1029/2020MS002069

Zhou, Y., Hejazi, M., Smith, S., Edmonds, J., Li, H., Clarke, L., Calvin, K., Thomson, A., 2015. A comprehensive view of global potential for hydro-generated electricity. Energy Environ. Sci. 8, 2622–2633. https://doi.org/10.1039/c5ee00888c